Surface Modification of Stainless Steel for Cavitation Environment through Microwave Cladding

A Dissertation
Submitted In the Fulfilment of
The Requirements for the Degree of

Master of Engineering
In
Production Engineering

By

Jonty Mago

Registration No.: 801785006

Under the Supervision of

Dr. Dheeraj Gupta
Associate Professor
MED,TIET, Patiala

Dr. Vivek Jain
Associate Professor
MED, TIET, Patiala

THAPAR INSTITUTE
OF ENGINEERING & TECHNOLOGY
(Deemed to be University)

DEPARTMENT OF MECHANICAL ENGINEERING
THAPAR INSTITUTE OF ENGINEERING &TECHNOLOGY,
PATIALA-147004, INDIA

July, 2019

I Would Like To Dedicate My Thesis to My Beloved Family, Virtuous Teachers, and Treasured Friends……

Declaration

I hereby declares that the thesis entitled "***Surface Modification of Stainless Steel for Cavitation Environment through Microwave Cladding***" submitted to the ***Department of Mechanical Engineering*** at ***Thapar Institute of Engineering & Technology, Patiala*** for the award of the degree of ***Master of Engineering in Production Engineering***, is a record of original bonafide research work carried out by me under the supervision of ***Dr. Dheeraj Gupta and Dr. Vivek Jain.*** All the requirements for the submission of this thesis have been fulfilled as per institute norms.

No part of the matter embodied in this report has been submitted to any other university or institute for the award of any degree.

Jonty

Date: 14/8/19 **Jonty Mago**

It is certified that the above statement made by the student is correct to the best of our knowledge and belief.

Dr. Dheeraj Gupta
Associate Professor
Mechanical Engineering Department
TIET, Patiala-147004, India
dheeraj.gupta@thapar.edu

Dr. Vivek Jain
Associate Professor
Mechanical Engineering Department
TIET, Patiala-147004, India
vivek.jain@thapar.edu

Acknowledgement

First and foremost, I wish to thank my supervisors ***Dr. Dheeraj Gupta*** and ***Dr. Vivek Jain*** for their unwavering support, supervision, guidance, and belief in me. I am thankful for the positive suggestions and meticulous guidance that helped me to improve my scientific writing and carry out the new research. I feel motivated and honoured to work under their supervision throughout my entire M.E thesis work.

I gratefully acknowledge the funding for this work through the ***Science & Engineering Research Board (SERB), India***, under the project titled ***"Development of Microwave Processed Cavitation Erosion Resistant Cladding"*** File no.: EMR/2016/007964.

A special thanks to the office of the Mechanical Engineering Department for providing all the facilities required for research work. Thanks to all my lab mates, seniors, and friends for their support and a very special & sincere thanks to Mr. Sandeep Bansal who had helped me a lot during my research work. I am thankful to the office staff of the Mechanical Engineering Department at Thapar Institute of Engineering & Technology, Patiala for their help and cooperation throughout my study.

A huge thanks go to the whole family, who always encouraged me and stood by me. I thank all my family and relatives who had supported and cared for me during my research work. I am grateful to all those who have helped me directly or indirectly in this journey of my life.

Finally, I bow and thank the Almighty, without whom I could not have completed this journey of completing my research work.

Jonty

Jonty Mago

Abstract

The problem of cavitation in hydropower plant components is the major challenge. Surface modification is the most economical method to enhance material resistance for the cavitation prone components. However, poor adhesion, cracks, and porosity of cladding/coating deposited on the substrate material is the main limitation of the commonly used surface modification techniques. Cladding via microwave route is a potential surface modification technique to mitigate these defects. In the present study, the composite clads of Ni-based/40Cr_3C_2 and Ni-based/20Cr_3C_2-20Mo were successfully developed on SS-316 substrate via microwave cladding route after optimizing the processing parameters at 2.45 GHz frequency and 900 W power in a domestic microwave oven.

The prepared clads were examined for microstructure, phase quality and quantity, porosity, microhardness, flexural strength (bonding strength) and cavitation erosion resistance at different parametric conditions. Whereas, the microstructural examination of the developed clads has been carried out by using scanning electron microscopy, the phase investigation has been carried by using X-ray diffraction (XRD), the microhardness measurement has been performed using Vicker's microhardness tester. Whereas the porosity analysis, flexure strength test and cavitation erosion study have been performed as per *ASTM-B276-05, ASTM-C1161-13 and ASTM-G32-16* standards, respectively.

The microstructure analysis reveals that the composite clads of 600 µm and 750 µm thicknesses were developed and the developed clads are free from all type of visible cracks and pores. The stripe-like Cr_3C_2 and rib-like or net-like Mo precipitate were found through microstructural investigation. The results of porosity analysis show that the developed Ni-based/40Cr_3C_2 and Ni-based/20Cr_3C_2-20Mo composite clads possesses only 1.67 % and 0.26 %, which is significantly less as compared to conventionally used cladding/coatings processes. The XRD analysis confirms the presence of various possible intermetallics (Ni_3Cr_2, Ni_3Fe, FeCr, FeMoCr, $MoNi_4$) and hard carbide ($Cr_{23}C_6$, Cr_3Ni_2SiC, SiC, $NiMo_4C$, Mo_2C) phases in the clad region. The formation of various carbides, silicides and intermetallics during microwave hybrid heating led to higher microhardness of the developed composite clads. The

microhardness of the developed Ni-based/40Cr_3C_2 and Ni-based/20Cr_3C_2-20Mo composite clad is come out to be 605±80 $HV_{0.3}$ and 681±30 $HV_{0.3}$, respectively, which is 3 and 3.5 times higher than that of the substrate (SS-316) respectively. The presence of high strength carbides and intermetallics in the microwave processed composite clads resulted in the higher flexural strength of these clads. The value of flexural strength in case of Ni-based/40Cr_3C_2 composite clad was 813.229 MPa. On the other hand, in case of Ni-based/20Cr_3C_2-20Mo, the flexural strength was 708.76 MPa.

The functional characterization (in terms of vibratory cavitation erosion testing at varying test parameters) results revealed that cavitation erosion resistance (CER) of the developed composite clads is higher than the SS-304 substrate. The Ni-based/20Cr_3C_2-20Mo composite exhibited better CER than all other developed clads. The overall results led to the conclusions that the microwave energy was successfully utilized to develop the CER clads of various materials. The microwave processed composite clads can be successfully used in hydropower plant applications.

Keywords: *Microwave Cladding; Characterization; ASTM-G32; Cavitation Erosion Resistance; Flexure Strength; Fractographic Analysis.*

Table of Content

List of Figures

List of Tables

List of Abbreviations

Abbreviations		Full-Form
Al_2O_3	=	Alumina
AMP	=	Amplitude
APS	=	Air Plasma Spraying
ASTM	=	American Society for Testing & Material
BCC	=	Body Centre Cubic
BSE	=	Backscatter Image
CER	=	Cavitation Erosion Rate
CI	=	Cavitation Inducer
CML	=	Cumulative Mass Loss
Cr_3C_2	=	Chromium Carbide
CVD	=	Cathodic Vapour Deposition
CVL	=	Cumulative Volume Loss
DC	=	Direct Current
EDS	=	Energy Dispersive Spectroscopy
EM	=	Electromagnetic
FCC	=	Face Centre Cubic
FGM	=	Functionally Graded Materials
FSP	=	Friction Stir Processing
HEA	=	High Energy Entropy Alloy
HT	=	Heat Transfer
HVOF	=	High-Velocity Oxy-Fuel
IBT	=	Incubation Time
IEA	=	International Energy Agency
IMD	=	Immersion Depth
ISO	=	International Standards Organization
JIS	=	Japanese Industrial Standards
JCPDS	=	Joint Committee on Powder Diffraction Standards
MDE	=	Mean Depth for Erosion
MDER	=	Mean Erosion Rate

MHH	=	Microwave Hybrid Heating
MMC	=	Metal Matrix Composites
Mo	=	Molybdenum
MSS	=	Martensitic Stainless Steel
MW	=	Microwaves
NaCl	=	Sodium Chloride
NCER	=	Normalised Cavitation Erosion Rate
Nd: YAD	=	Neodymium-doped Yttrium Aluminium Garnet
NIR	=	Normalised Intensity Ratio
OM	=	Optical Microscopy
PTA	=	Plasma Tungsten Arc
PVD	=	Physical vapour Deposition
PH	=	Pouvoir Hydrogene
SAED	=	Selected Area Electron Diffraction
SEM	=	Scanning Electron Microscopy
SEI	=	Secondary Electron Image
SMAW	=	Submerged Arc Welding
SOD	=	Standoff Distance
SPE	=	Solid Particle Erosion
SS	=	Stainless Steel
TEM	=	Transmission Electron Microscopy
TIG	=	Tungsten Inert Gas
TMP	=	Thermo Mechanical Processing
UTM	=	Universal Testing Machine
WC	=	Tungsten Carbide
XRD	=	X-ray Diffraction

List of Symbols

Symbol		Meaning
∘	=	Degree
°C	=	Degree Centigrade
μ'	=	Magnetic Constant
μ_0	=	Magnetic Permeability
μm	=	Micrometre
μ_r	=	Relative Permeability
A	=	Ampere
cm	=	Centimetre
D_p	=	Depth of Penetration
D_s	=	Skin Depth
f	=	Frequency
g/cm^3	=	Grams Per Centimetre Cube
GHz	=	Giga-Hertz
GPa	=	Giga-Pascal
GW	=	Giga-Watt
HV	=	Vickers Hardness
j	=	Polarization
K	=	Kelvin
kg/m^3	=	Kilogram Per Metre Cube
kHz	=	Kilo-Hertz
kV	=	Kilo-Volt
kW	=	Kilo-Watt
l/h	=	Litre Per Hour
l/min	=	Litre Per Min
m	=	Metre
m/s	=	Metre Per Min
m^3/h	=	Metre Cube Per Hour
mg/h	=	Milligram Per Hour
MHz	=	Mega-Hertz

mm	=	Millimetres
mm/min	=	Millimetres Per Min
mm/s	=	Millimetres Per Seconds
MPa	=	Mega Pascal
N	=	Newton
nm	=	Nanometre
Pa	=	Pascal
rpm	=	Revolution Per Min
S^{-1}	=	Per Seconds
$tan\delta$	=	Tangent Loss
µm/h	=	Micrometre Per Hours
V	=	Voltage
W	=	Watt
W/mK	=	Watt Per Metre Kelvin
ε'	=	Electrical Permittivity
ε''	=	Dielectric Loss Factor
ε_o	=	Electric Permittivity
ω	=	Angular Frequency
$\boldsymbol{\lambda}_o$	=	Wavelength

Chapter 1

Introduction

1.1 Origin of the Research Problem

In the 21st Century, Energy plays a vital role in the process of growth, development, and survival of the Economy. Inconsistency in its supply can affect the functionality of a country; specifically, it has an adverse effect on the developing countries. Majority of developing countries like China, India, Indonesia, Brazil, Afghanistan, Bangladesh, and Srilanka are currently facing a shortage of energy because of a growing population and technological advancements [1], their fossil fuels have been rapidly depleting due to rising demand for electricity due to the growing population. The excessive use of non-renewable resources should be immediately stopped not only because they are depleting, yet in addition, the burning of fossil fuels (non-renewable resources) causes environmental pollution.

In 2018, the World Energy Outlook yearly edition, published by the International Energy Agency (IEA) estimated that global energy-related CO_2 emissions would increase by around 50% by 2030 [2]. In reaction to these, global warming and threats to climate change have forced industries to use energy more efficiently, while greenhouse gasses emissions have become the most attractive topic of our decade. Therefore, research and development efforts, in the field of renewable energy technologies, are of great importance for finding solutions to these ecological challenges by offering clean and reliable energy sources. The share of renewable energy sources, in other world energy sources, has increased in the last few years and is expected to increase in the near future. In 2007, 1000 GW of renewable energy was installed, and so far, the total global capacity of renewable energy sources has reached 2017 GW [3]. The Figure 1.1 presents a total of six of the largest countries capacity in renewable electricity. As it is shown, the leading countries, in terms of total installed capacity of non-renewable energy, are China, U.S.A, and Germany, followed by Japan, India, and Italy. Moreover, it can be seen that hydro energy has been extensively utilized by the top six countries [4] as it has the enormous potential to be a sustainable system that reduces emissions and becomes an essential asset for the global supply of renewable energy.

India is the seventh-largest hydropower producer in the world and has tremendous potential for generating hydropower [5]. The hydropower is the second-largest energy source in the Indian energy sector.

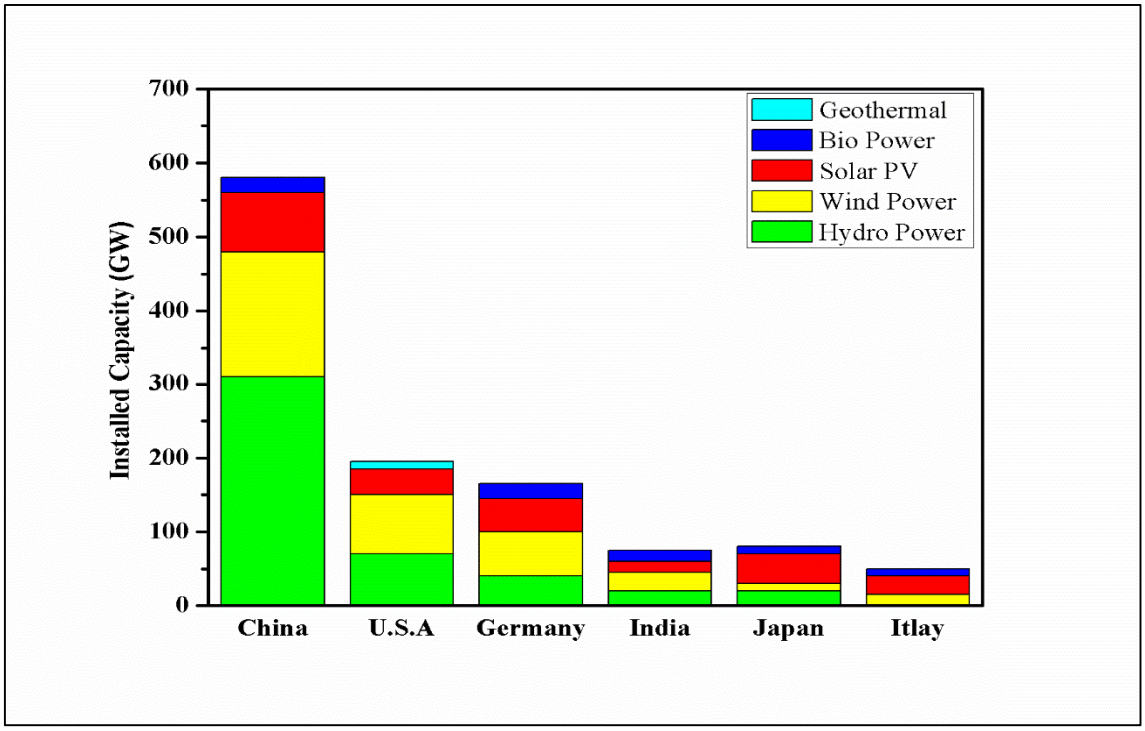

Figure 1.1: Six leading countries with a total installed renewable energy capacity [4]

The values in Figure 1.2, 1.3 confirms the importance of hydroelectric power versus all other non-renewable and renewable energy production methods, such as geothermal, marine, solar, wind, coal, diesel, nuclear and biomass. A hydroelectric plant may, however, be subjected to various design, operational, and maintenance problems that may reduce the capacity of the power plant.

In addition, a hydropower plant can suffer tremendous revenue losses due to several teething problems that ultimately prolong the downtime of the power plant. The performance and workability of the plant highly depend upon the satisfactory working of the hydro turbine and its associated components [6]. Hydraulic turbines are severely damaged due to the some following main reasons:

i. Cavitation
ii. Erosion
iii. Fatigue
iv. Material defect

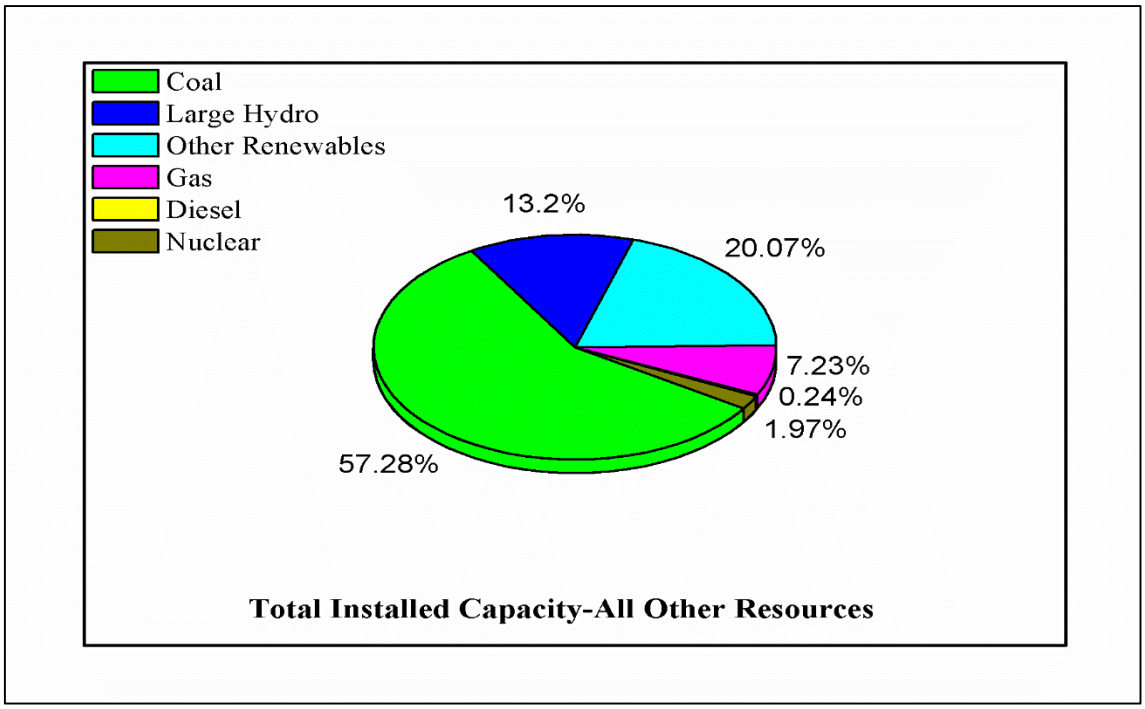

Figure 1.2: Percentage contribution of all energy sources in total installed capacity in India as on 31/05/18 (Statistics by Ministry of Power) [7]

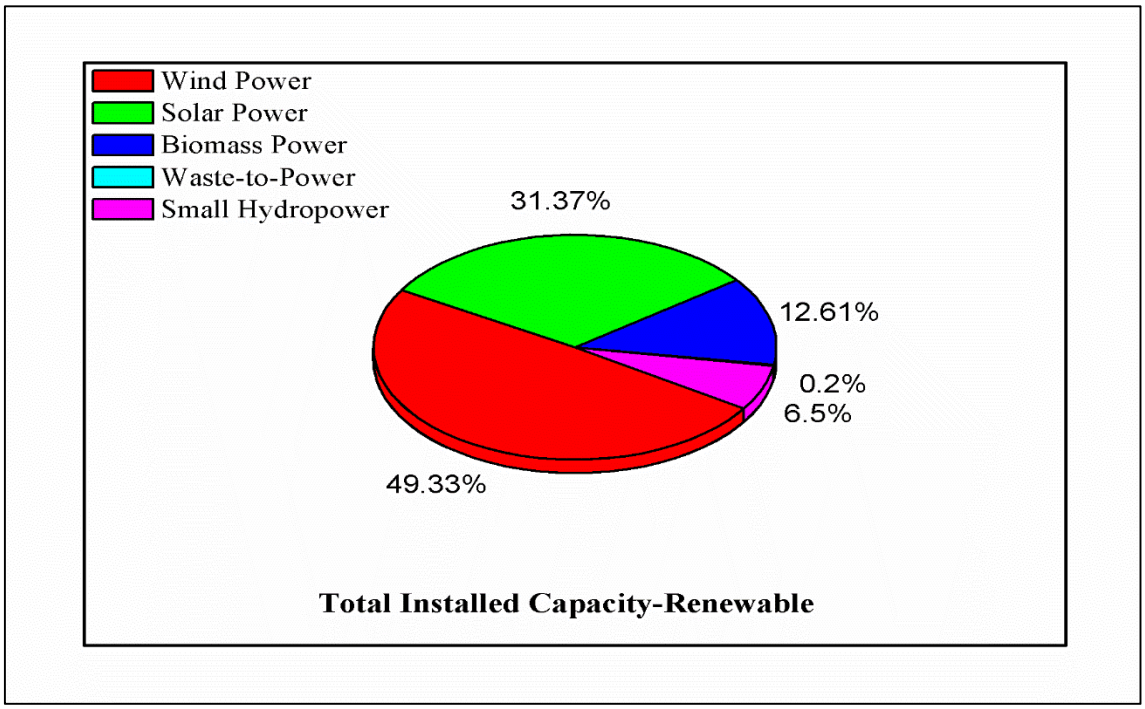

Figure 1.3: Percentage contribution of different renewable energy sources in total installed renewable capacity in India as on 28/02/16 (Statistics by Ministry of Renewable Energy) [8]

i. **Cavitation:** Water flowing into the hydraulic turbines, undergoes pressure, and velocity variation. Such variation can change in flow characteristics with consequences for turbine efficiency and service life. Cavitation failure can be results of such changes affecting turbine in-service life. The repetitive formation and disintegration of these vapor bubbles during the fluid flow aggravate the surface of the turbine parts by pitting action [9]. The area of cavitation erosion of the Kaplan turbine blade is as shown in Figure 1.4. The severity of the cavitation is explained in most famous Research article titled "*Tiny Bubble Challenges Giant Turbines: Three Gorges Puzzle*" [10] of case study on hydraulic turbines failure in very next year after its commission of world largest hydropower plant Three Gorges due to cavitation. Whereas the hydraulic turbines of this plant were manufactured by world top manufacturing companies Alstom, GE, and Siemens.

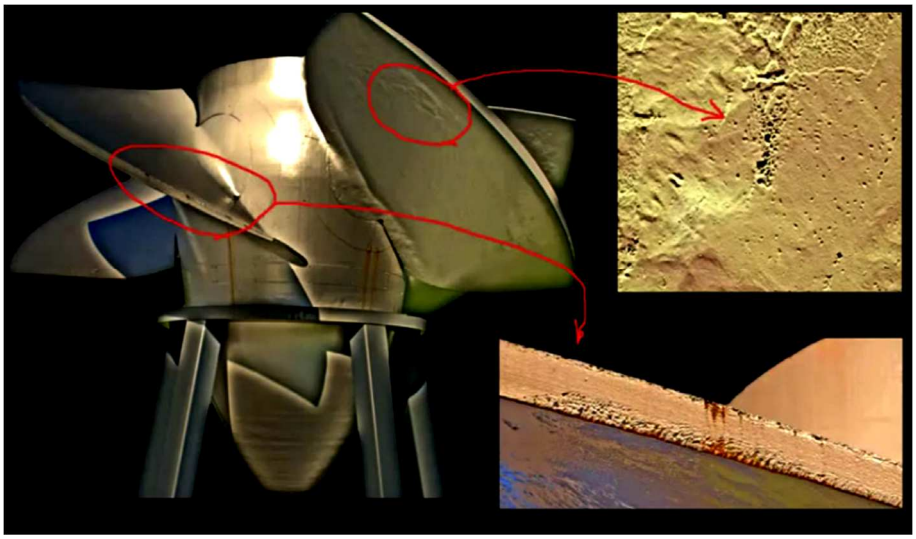

Figure 1.4: The damaged surface of the Kaplan turbine due to cavitation & its pitting action [9]

ii. **Erosion:** The Erosive wear of the hydraulic turbine and its components is occurring due to the presence of the silt and sediments particles in the water. When the hard abrasive sediments impinge on the surface of the turbine blades with a high velocity that causes instantaneous destruction of the temporary oxide film and the formation of surface irregularities on surfaces that direct the flow and generate cavitation type effects to the turbine component [11]. Besides, to this, the sediment erosion also causes noise and vibration in the hydraulic turbines components, and that increases the probability of the failure on the component and is directly proportional to the

size of the sediment. However, the erosion rate depends on the various properties like size, shape, and concentration of the sediments.

However, Sediment erosion is a severe problem, especially in the countries of South Asia belonging to the Himalayan regions (such as China, India, and Nepal). One of the main reasons is the presence of large amounts of quartz in the silt (Fe_2O_3, Al_2O_3, SiO_2, CaO, and MgO), especially during the monsoon seasons. The quartz material is known, because of its extremely high hardness (On Moh's scale-7 versus Diamond on Moh's Scale 10), can quickly wear out the components of the hydraulic turbine during operation **[12].** Therefore, it is crucial that countries such as India, Nepal, and China focus on cavitation and sediment-assisted erosion, as much of the water-energy in these countries is extracted from the Himalayan Rivers which contain an excessive amount of sediment.

iii. **Fatigue:** Fatigue of the material is another form of failure of the turbine. The hydro turbine components, which are repeatedly subjected to cyclic loading above material yield stress, may gradually fail due to cracks development and their growth rate. Hydraulic turbines are made up of multiple interconnected elements as a result of the vibrations of one element being transferred to another, that cause deformation of all linked components **[13].** Also, the additional load on the affected parts can lead to a sudden onset element failure. Few of the analysis of the flow through the turbine blades **[14]** showed that the eddy current formation is the leading cause for vibrations as well as stress generation.

iv. **Materials Defects:** The studies available on turbine failure mechanisms and of damaged turbine components in hydropower plants concluded that the main reasons for turbine failure are combined effect of sediment erosion, cavitation, and corrosion. The turbine parts failures due to material defects that occur during the installation phase are infrequent in the literature **[10].** The disadvantages are generally controlled during the production phase of the turbine and its components; so that the turbine parts to be manufactured and also they meet the standards required by a hydroelectric plant. One of the common defects that occurred during the production phase is sensitization of stainless steel.

1.2 Cavitation Phenomena

Cavitation erosion is the most common type of surface degradation process occurs in the components of the hydropower plants **[10].** However, it happens due to sudden fluctuation in the pressure in the flowing liquid. At the boundaries when the pressure of the flowing liquid falls below its vapor pressure, the formation of empty cavities known as bubbles takes place **[15].** Further, when the pressure starts rising, the growth of the bubbles start reversing, and at high pressure, it collapses. This collapsing process generates the shock waves and micro jets repeatedly, which exert tremendous stresses on the surface of the components. This ultimately led to surface fatigue, material removal, and pit formation. In the end, the functionality of the component is completely lost **[16].** The steps involved in pit formation on hydraulic turbine component due to cavitation are illustrated in Figure 1.5.

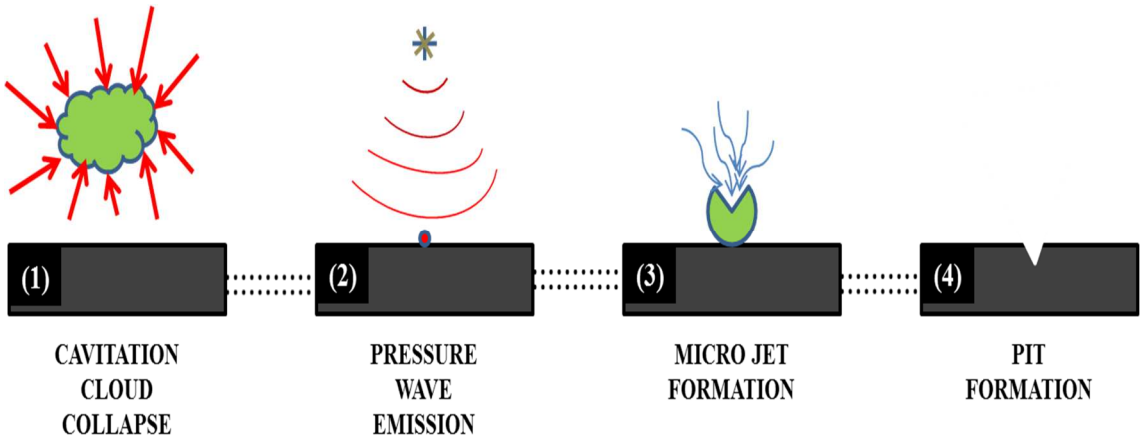

Figure 1.5: Pit formation due to cavitation phenomena

The parts of the hydro turbine, which are prone to degrade due to the cavitation phenomenon, are listed in Table 1.1:

Table 1.1: Various components of hydraulic turbines which are prone to cavitation [6]

Classification of Hydraulic Turbines	**Type of turbine**	**Parts Prone to Cavitation Damage**
Reaction	Francis	1.The Trailing edge of the blade 2. The leading edge of the blade 3.Wicket gates guide vanes 4. Draft tubes
	Kaplan	Guide vanes, Blades
Impulse	Pelton	Bucket
	Bulb	Blades

1.3 Cavitation and Sediment Erosion Prevention Methods

A review of the literature revealed that the phenomenon of cavitation might not be removed entirely from all turbines. The cavitation problem in the hydroelectric power plant could be minimized by keeping the load fluctuation to a minimum. However, in some of the cases, the cavitation could be avoided altogether. If: the draft tube is designed to operate in the forward whirl, pressure distribution at the back side of the turbine is improved, and computational fluid dynamics studies of the fluid flow along the surface of the hydraulic component carried out in advance [17]. However, at the operational level, the vulnerable effects of cavitation and sediment erosion can be minimized by using some of the following methods [18] as illustrated in Figure 1.6 and Figure 1.7, respectively. According to the literature review, the bulk material modification and surface modification are most extensively used methods to enhance cavitation and sediment erosion resistance of the components [11]. The latter i.e., surface modification was found as a better option and more economical.

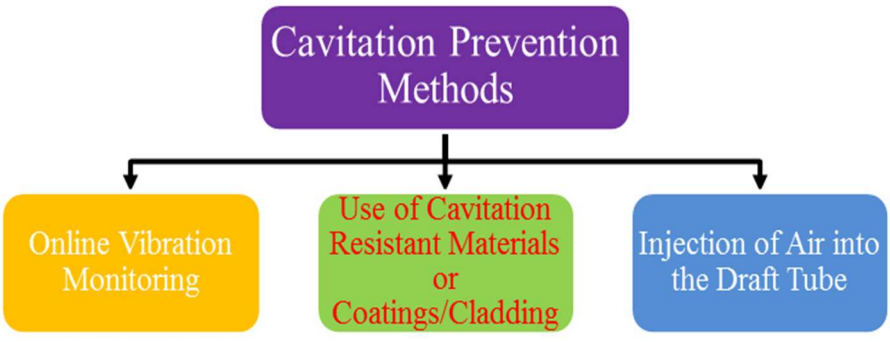

Figure 1.6: The methods to prevent cavitation erosion

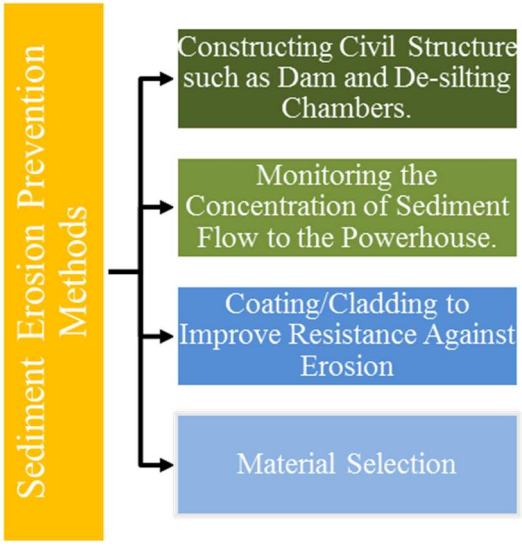

Figure 1.7: The methods to minimize sediment erosion

1.4 Surface Engineering

The deterioration of engineering components mostly initiates from the surface because, in most of the applications, surfaces are in direct contact, resulting in maximum stress at the surface. Hence, the surface improvement is the most primary concern in most of the engineering applications. Surface engineering is defined as a method or tool which is designed to alter/tailored the properties of the metallic and non-metallic surface of constituents to be used for functional or decorative purposes **[19].** The surface engineering can provide the solution for the various problems mentioned below:

i. Wear Resistance
ii. Corrosion Resistance
iii. Frictional energy loses
iv. High-temperature oxidation resistance
v. Aesthetic appearance
vi. Electrical Properties improvement
vii. Thermal Properties improvement

This is important in terms of components in-service life and frequent interruption of plant performance **[20].** The area of surface engineering is broadly divided into three categories, which are surface chemistry; surface metallurgy and surface coatings & associated various processes that come under these categories are illustrated in

Figure 1.8. A brief comparison based on some essential parameters of different coating/cladding processes is shown in Table 1.2.

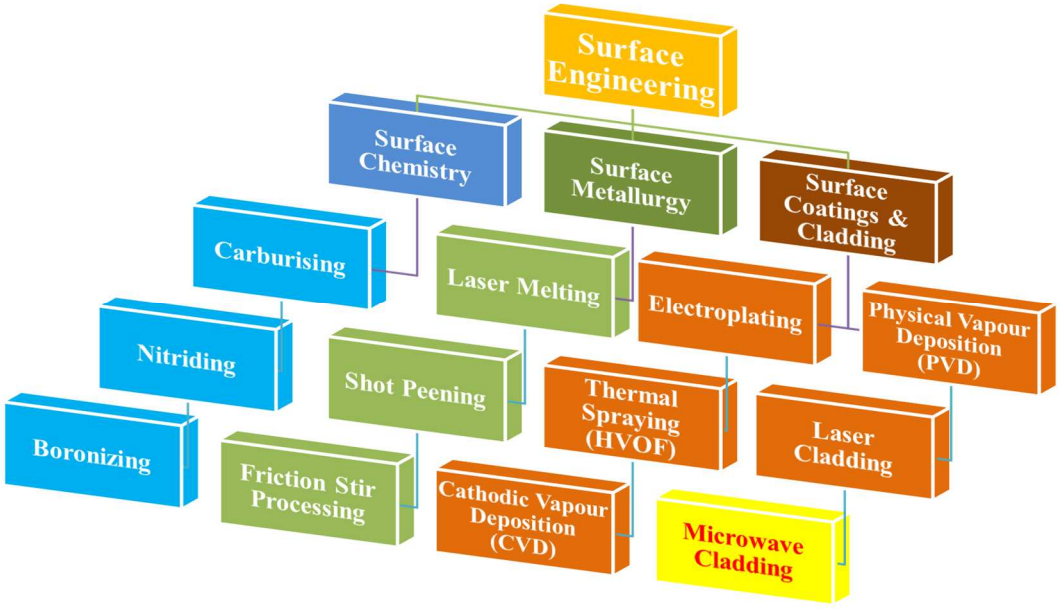

Figure 1.8: Types of the surface engineering process

Table 1.2: Comparison of various surface coatings/cladding on multiple parameters [19]

Process Characteristics	**Gaseous State Processes**		**Solution Process**	**Molten or Semi-Molten State Processes**		
	PVD	CVD	Electroplating	Laser Cladding	Thermal Spraying	Welding
Deposition Rate (Kg/h)	Up to 0.5 Per Source	Up to 1 Per Source	0.1-0.5	0.1	0.1-10	3.0-50
Coating Thickness (µm)	0.1-1000	0.5-2000	10-500	50-2000	50-1000	1000-100000
Substrate Deposition or Treatment Temperature (°C)	50-500	150-12000	25-100	200-2000	100-800	500-1200
Uniformity of Coating	Good	Very Good	Fair/Good	Fair	Variable	Variable
Bonding Mechanism	Atomic	Atomic	-	Metallurgical	Mechanical	Metallurgical

Thermal spraying (HVOF-High Velocity Oxy-Fuel), arc spray welding, and laser cladding are the most commonly used techniques to produce composite coatings/cladding on the metallic substrate. Spraying techniques are highly efficient, but they don't provide metallurgical bonding between the substrate and hard particles **[21].** Because of weak metallurgical bonding and high porosity in these coatings, they have weak flexural strength (peel of strength) and fracture toughness. Moreover, due to low flexural strength and fracture toughness of coatings produced with the spraying technique are don't withstand against cavitation impact energy for a long time. This is due to the fact that during cavitation phenomena, the loosely bonded hard particle easily detaches from the substrate **[22-23].** Whereas in the case of conventional welding processes, the dilution of clad materials is very high, the substrate also gets severely deformed and solidification cracking problems. Moreover, due to those cracks and high dissolution of materials, there is comprehensively reduction in the mechanical properties and Cavitation Erosion Resistance (CER) of the cladding **[24-25].**

In summary, during coating/cladding formation, the problems arise due to the heating source (laser beam in laser cladding, flame/arc in spraying and welding). The heat energy transferred from heating source to material through conventional mode (radiation, conduction, and convection) and developed coating/cladding solidified rapidly solidified with a high thermal gradient. The significant limitations of the frequently used surface modification processes to improve CER are summarized in Table 1.3. Where, the kinetics of heat transfer mainly depends on physical properties (thermal conductivity, specific heat, convective heat transfer coefficient, thermal diffusivity) of materials which governed the quality of cladding.

Table 1.3: The limitations of the frequently used surface modification processes for CER [26]

S.no	Surface Coating Techniques	Limitations
1	CVD and PVD	1. PVD and CVD processes operate at high vacuums and temperatures, which requires skilled operators. 2. The rate at which the coating is deposited is usually quite slowing in addition to these appropriate cooling systems is also required as the process involves a large amount of heat.
2	Electroless deposition	1. Coating thickness limits up to 1-100 µm.
3	Electrolytic deposition	1. A conducting substrate is required. 2. DC power supply is generally required.
4	Thermal spraying	1. It does not produce metallurgically bonded coatings. 2. There are various hard spots left in a coating layer which leads to high abrasion. 3. Defects like porosity are high in this process.
5	Laser surface treatment	1. High initial setup cost and high power requirements. 2. Thermal distortion, residual stress, and thermal gradient on the substrate due to a highly intense heat source. 3. Crack formation at the clad top surface and interface due to high cooling rate.

1.5 Factors for Efficient Material Processing

The first and foremost concern of the industries, researchers, and technologists is the effectiveness and efficiency of the material processing method. As the demand for energy is growing at an alarming rate, cleaner, more sustainable, and greener technologies need to be developed. Some of the critical factors for effective material processing are shown in Figure 1.9. All of these factors contribute to an efficient and sustainable process. Therefore, these factors could get the most attention while developing a new production process, so that all the limitations of traditional processes can be overcome.

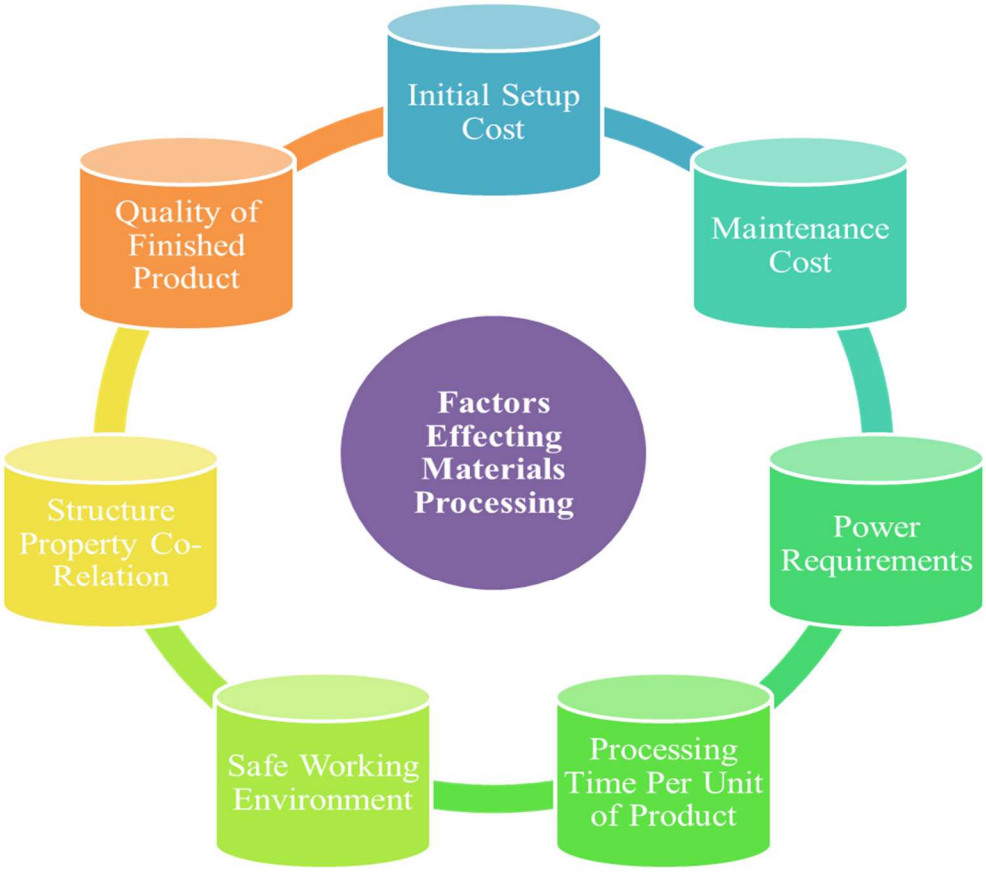

Figure 1.9: Factor affecting an efficient material processing method

Recently, the processing of materials with microwaves proved to be an innovative technique of surface treatment to develop a coating on metallic surfaces **[27-30].** The microwave coating/cladding covers almost all the limitations of conventional surface coating/cladding techniques. This leads to uniform heating of the volume, thereby reducing residual stresses, heat gradient, and thermal deformation in the target material and helps to obtain a metallurgically bonded surface layer without cracking. Therefore, this new technique has a promising future, because it offers many advantages over conventional surface coating/cladding techniques.

1.6 Microwave Irradiation as an Unconventional Energy Source

Microwaves are consisting of magnetic and electric waves which propagate perpendicular to each other and having wavelengths varying from 1 m to 1 mm in the air, as shown in Figure 1.10. These wavelengths belong to the electromagnetic spectrum, having a frequency range of 300MHz to 300GHz **[31].** Before 1945, microwave radiations applications were limited to communications systems, including

satellite, radio, and television communications. In 1945, American physicist and inventor, Percy Spencer [32] investigated the thermal effects of microwave radiation and patented the microwave technology used for heating purposes, which is known as a microwave oven. In India, the microwave frequency range of 2.45 GHz is allocated for domestic microwave oven. However, in microwave heating furnaces, different frequencies range of 915 MHz to 18 GHz are used [33-34].

Microwaves are used in many applications, including food processing, medical purposes, communication systems, industrial heating and material processing due to these ranges of frequencies.

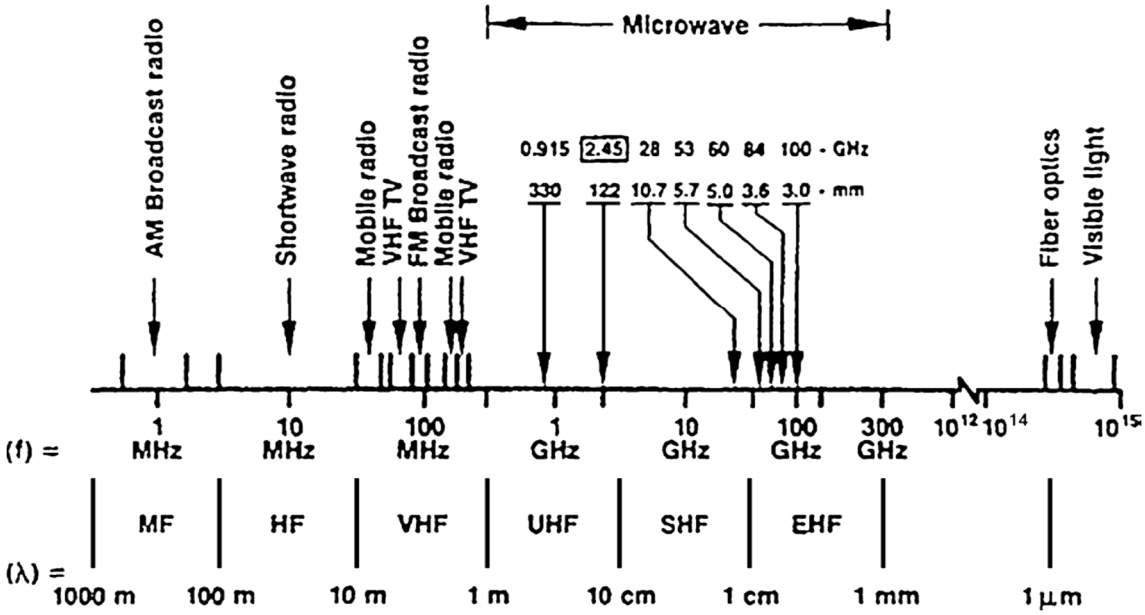

Figure 1.10: An electromagnetic spectrum of wavelength and frequencies for microwave processing [31]

Microwave applications in the field of heating were investigated by scientists [35-36] in the field of material processing, such as rubber vulcanization, steel production, processing of ceramic and metallic materials, alternative sources of energy recovery [37]. The main features of the microwave material processing [38] are shown in Figure 1.11.

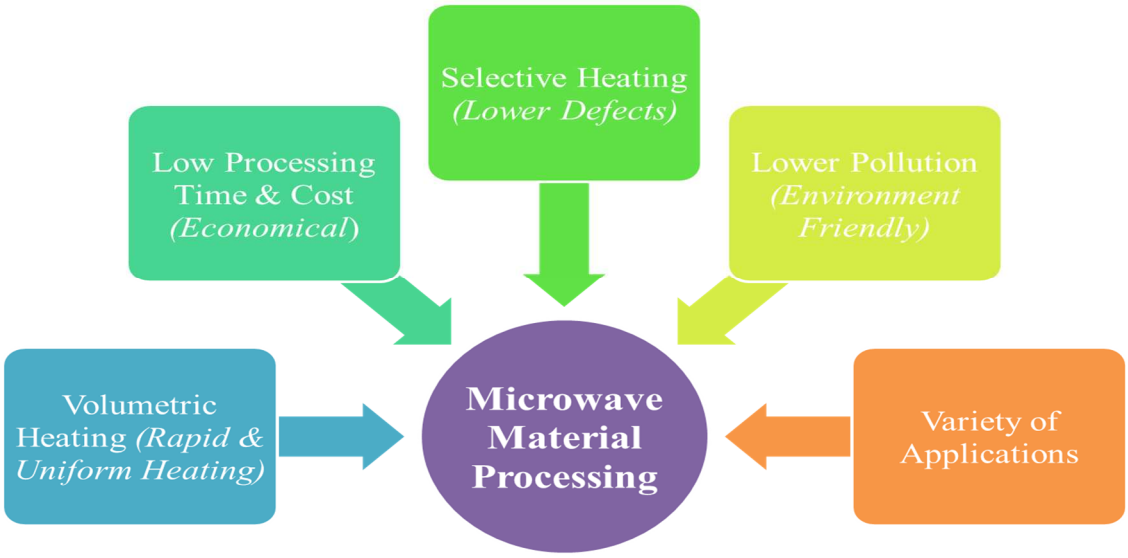

Figure1.11: Favourable characteristics of microwave materials processing

In microwave absorbent (which start absorbing microwaves at room temperature) materials, direct microwave absorption at the atomic level results in volumetric heating of the material. This further provides rapid heating rates with a lower thermal gradient in the material to be processed. The volumetric heating function causes a fast heating rate to reduce processing time, resulting in lower power consumption compared to conventional heating **[39-41].** During microwave treatment, substantial energy savings and processing time were achieved.

1.7 Historical Development of Microwave Processing

The historical or chronological progress in the field of microwave heating & metallic material processing illustrated in Figure 1.12 and 1.13 respectively, which shows the chronological order of the numerous developments taking place in this filed **[42].** Microwave applications used to be based on low-temperature applications until 1960, which were further explored for high-temperature applications such as ceramic material processing. Mostly ceramics materials are readily coupled with microwave radiations of frequency 2.45 GHz.

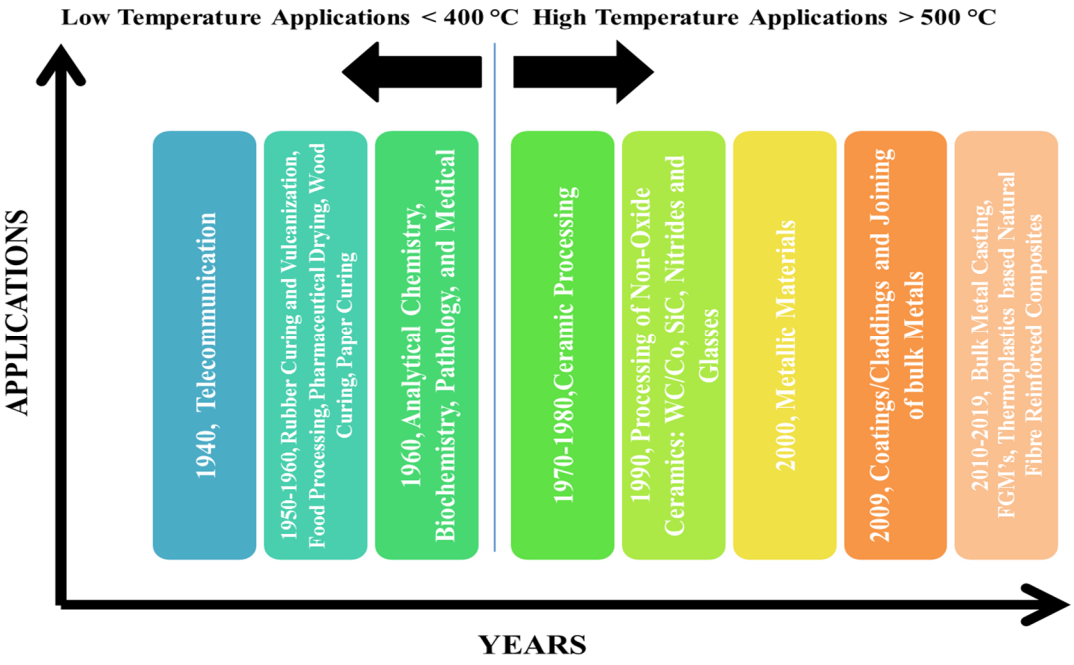

Figure 1.12: Historical developments of microwave radiations in the various fields

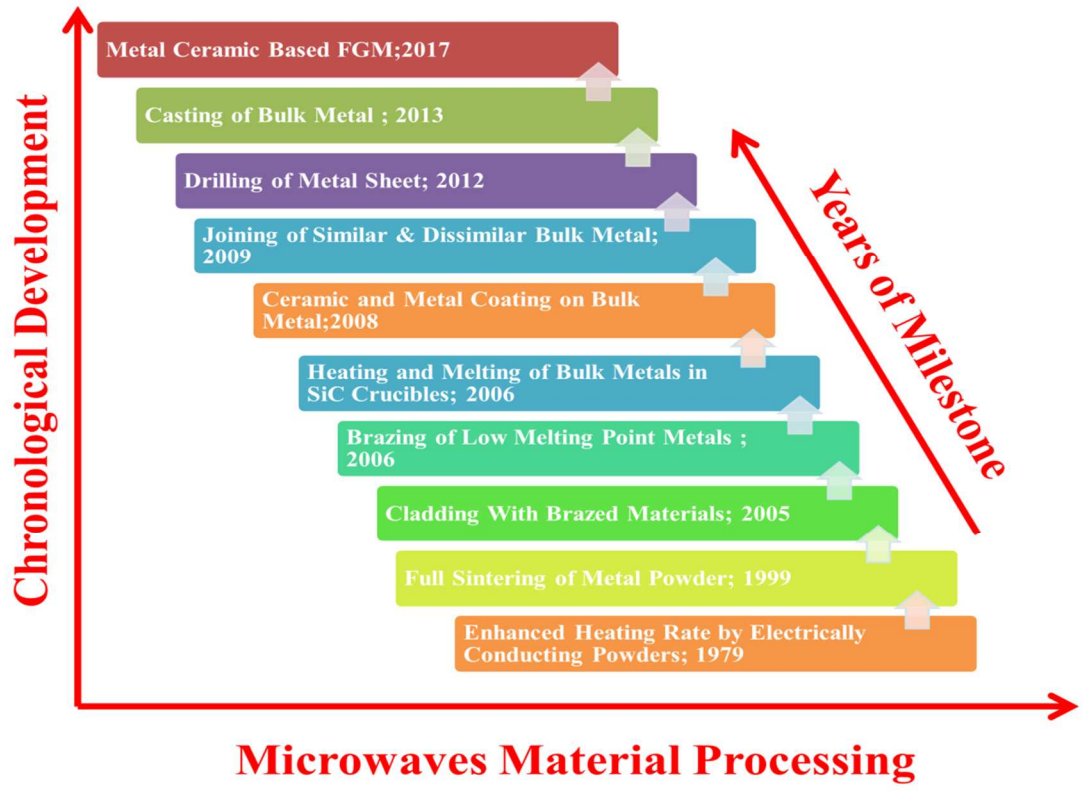

Figure 1.13: Chronological developments in microwave processing of metallic materials

However, bulk metallic materials reflect the incoming microwave radiation of low frequency of 2.45 GHz at room temperature, as a result of which the processing of such

materials was complicated, and further scientists conducted numerous experiments, and in 1999, Roy et al. [43] reported the successful sintering of metallic powders, which further explored the possibility of coupling microwaves with metallic materials in the form of fine powders. These studies prompted scientists to consider the processing of metallic powders utilizing microwaves [44-46]; which were later successfully achieved. In the year 2009, Srinath et al. [47] successfully joined the bulk copper with copper powder using a domestic microwave oven. These works have led to the use of microwaves in the field of high-temperature applications. In 2010, using microwave hybrid heating (MHH) Gupta and Sharma patented the method of cladding on the metallic substrate of metallic and non-metallic powder [48]. In which they have successfully deposited the layer of copper powder on a stainless steel substrate [49]. In recent years, applications of microwaves at high temperatures have been evolved, and many works have been carried out in the field of coating materials, joining, casting, and in-situ casting [50-53]. Recently, Kaushal et al. in 2017 [54] reported the development of functionally graded materials (FGM) using the MHH technique. Moreover, Singh et al. in 2019 [55] developed the natural fibers reinforced composites with microwaves assisted compression moulding.

1.8 Basics of Microwave Material Processing

1.8.1 Microwave Material Interaction

The material interaction with any electromagnetic (EM) radiation depends upon the EM radiation properties like phase angle, amplitude, electric and magnetic field components, ability to propagate & transfer energy from one point to another point and electrical & magnetic properties like dielectric constant, tangent loss, resistivity etc. of material under radiation exposure [56]. The interaction of microwave irradiation with the material is categorized into three types:

i. **Transparent:** The material which transmits all the microwave energy without absorbing any energy component. Materials have low dielectric loss factor come under this category. Few examples are alumina (Al_2O_3), quartz, and thermosetting plastics [57]. The behaviour of the transparent material in response to incident microwave irradiation is illustrated in Figure 1.14 (a).

ii. **Opaque:** The material which reflects the incident microwave energy without absorbing any energy component or negligible penetration into the material. Most of the conductors are opaque to microwave irradiations. Sometime in opaque material accumulation of extra negative charge cause sparking at the surface. Few examples are Steel, carbon nanotubes, and aluminium [58]. The behaviour of the opaque material in response to incident microwave irradiation is illustrated in Figure 1.14 (b).

iii. **Absorbent:** The material which absorbed some component of incident microwave energy and converts into heat and help in increasing the material temperature. Materials with high dielectric loss factor are known for suitable microwave absorbent materials. Few examples are charcoal, and ceramics [59]. The behaviour of the absorbent material in response to incident microwave irradiation is illustrated in Figure 1.14 (c).

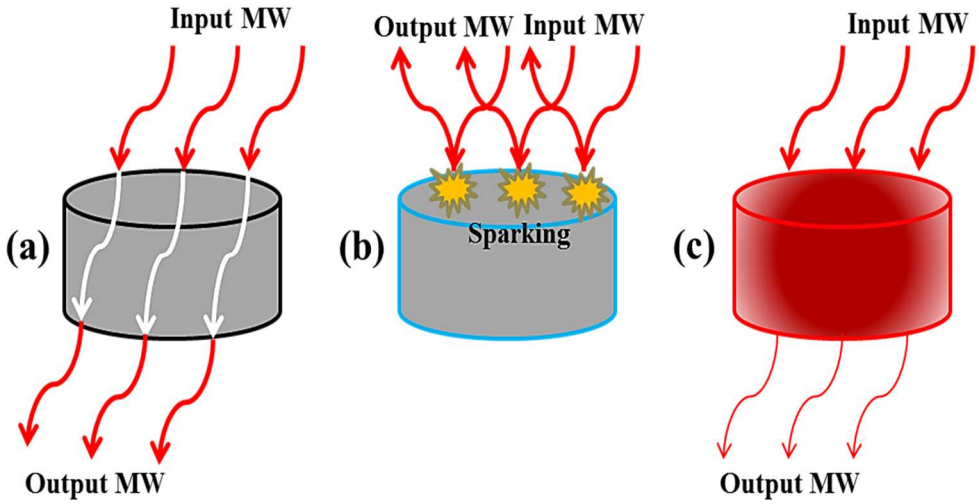

Figure 1.14: Representation material response to incident microwave radiation
(a) Transparent (b) Opaque (c) Absorbent

1.8.2 Microwave Heating Mechanisms

During microwave material interaction, the microwave radiations alternate its direction billion times in a minute. There are various kinds of microwave absorbing materials. The physical mechanism of converting microwave radiation energy into heat was different for different materials. Scientists reported the four types of mechanism to date. The microwave heating mechanisms are dielectric heating, electromagnetic heating,

resistive heating, and bipolar rotation [56]. Brief details of the microwave heating mechanism in different materials are mentioned below:

i. **Bipolar Rotation:** It occurs when positive and negative charges of polar molecules are separated. In the microwave field, in the direction of increasing amplitude, these dipoles rotate. As a result of this rotation, friction between molecules occurs uniformly and generates heat throughout the material.
ii. **Resistive Heating:** It occurs in the materials having a large number of free electrons or high ability to receive ions so that current can be generated. These materials are conductors or semiconductors with high electrical conductivity.
iii. **Electromagnetic Heating:** This type of heating may be referred to as the rotation of the magnetic pole to analogous material for the rotation of polar molecules in oscillating electric fields. It occurs in materials with magnetic properties like high susceptible to external electromagnetic fields as induced by microwave radiation.
iv. **Dielectric Heating:** This mechanism is predominant in the case of ceramics materials. Moreover, its combination of both resistive and bipolar rotation. Resistive heating due to the presence of free electrons and ions and bipolar rotation in the present dipoles.

1.8.3 Conventional, Microwave and Microwave Hybrid Heating

In case of conventional heating, heat is supplied via conduction, convection, and radiation modes from the outer surface and transferred to the material inner core, while processing material with microwave heating, the heating profile is inverted i.e., and heating starts from the core of material and moves towards outward direction. However, In the case of microwave heating, the heating of material takes place at the molecular level. Also, In the case of conventional heating, there is a significant thermal gradient at the surfaces lead to poor microstructures of the surface [60]. However, in the case of microwave heating, the presence of thermal runways in the core leads to microstructure distortion and cracking [61]. To overcome this differential heating phenomenon at cores and surface, the theory of microwave hybrid heating has been proposed by various researchers. In the case of MHH, a combination of both conventional heating and microwave heating are used so that both directional heating can be utilized to reduce the temperature gradient between the core and the surface. Metallic materials are opaque (reflect microwaves) to microwave radiations under normal conditions of 2.45 GHz

frequency. However, at an elevated temperature, these materials start absorbing microwaves. In the case of MHH, a suitable susceptor like charcoal powder is placed on the metallic powder separated by the separator sheet of graphite as shown in Figure 1.15 (a). As the susceptor absorbs microwaves at room temperature, when it has been exposed to microwaves, the temperature starts increasing. As shown in Figure 1.15 (b). As the metallic powder is in contact with the susceptor, its temperature rises, and it starts absorbing microwaves at high temperature [62]. Thus microwave heating starts within the material**,** as shown in Figure 1.15 (c).

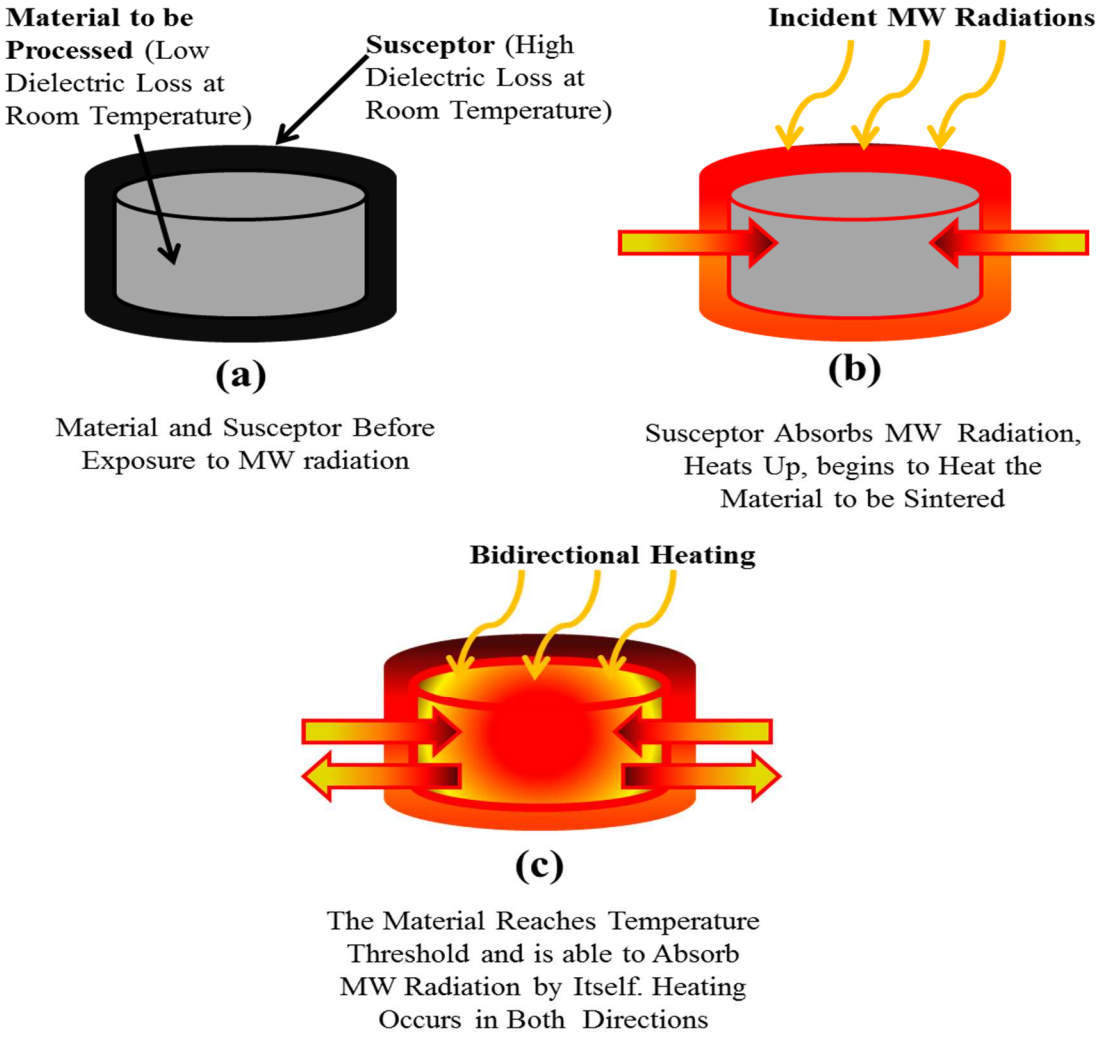

Figure 1.15: Steps involved in bidirectional or hybrid heating (a) Material and susceptor before MW exposure (b) Heating of susceptor by MW radiation (c) Material temperature reaches threshold and MW radiation absorption by itself begins

The microstructures produced are better in case of MHH due to uniform and rapid heating results into considerable savings in the energy consumptions and processing times [42]. The comparisons of the different heating phenomenon are shown in figure 1.16.

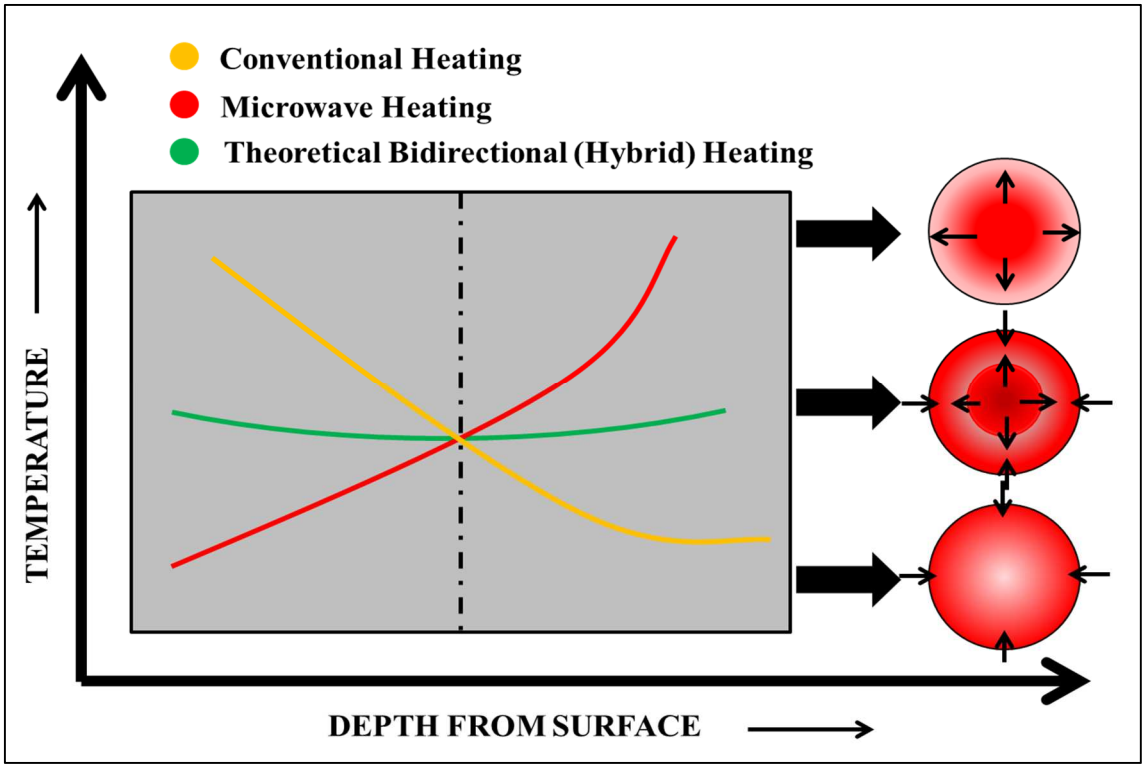

Figure 1.16: Temperature distribution in various heating mechanism [42]

1.8.4 Properties Affecting Microwave Materials Processing

Microwave radiations don't similarly penetrate in all material. Many physical properties of the materials are a noteworthy part of the microwave material processing. Some of the properties are essential to be known before microwave material processing. Complex relative permittivity and loss tangent are few of them [42]. Loss tangent can be calculated from Equation (1.1):

$$\tan\delta = \frac{\varepsilon''}{\varepsilon'} \text{ ----------(1.1)}$$

Where ε'' is dielectric loss factor (F/m), it is known as the ability of a material to convert microwave energy into heat. Moreover, ε' is an electrical permittivity in the medium (F/m). Complex relative permittivity (ε-(F/m)) gives more exact information about the

microwave interaction with the material **[63].** That can be calculated from equation (1.2):

$$\varepsilon = \varepsilon_0(\varepsilon' - j\varepsilon'') = \varepsilon_0\varepsilon'(1 - j\tan\delta) \text{----------(1.2)}$$

ε_0 = Electrical permittivity in space (F/m)

j = Electrical Polarization

The interaction of the material with microwave is further described by the significant parameter known as Depth of Penetration (D_p) in mm, in case of non-metallic materials and Skin Depth (D_s) in mm, in case of metallic materials. Depth of penetration is function of angular frequency of electromagnetic radiation (ω-s^{-1}), Magnetic Permeability or Absolute Permeability (μ_0-(H/m)), Magnetic Constant (μ′-(H/m)), permittivity in Air (ε_0-(F/m)), Dielectric Constant (ε′-(F/m)) and Dielectric Loss Factor (ε″-(F/m)). Whereas skin depth can be computed form two equations, and it is a function of Resistivity of material (ρ-(Ω-m)), Frequency of Microwaves (f-GHz), Magnetic Permeability (μ-(H/m)), and Relative Permeability (μ_r) **[64].** The theoretical calculations of the depth of penetration and skin depth can be done by using Equations (1.3) and Equation (1.4) respectively.

$$D_p = \frac{1}{\omega\sqrt{\left[0.5\,\mu_0\mu'\varepsilon_0\varepsilon'\left\{\sqrt{\left(1+\left(\frac{\varepsilon''_{eff}}{\varepsilon'}\right)^2\right)}-1\right\}\right]}} \text{---------- (1.3)}$$

$$D_s = \sqrt{\frac{\rho}{\pi f\mu_r\mu_0}} = 0.029(\rho\lambda_0)^{0.5} \text{---------- (1.4)}$$

1.9 Advantages of Microwave Processing of Materials

The main advantages of material processing with microwaves are associated with its characteristics of a higher heating rate of target materials, combined with lower energy consumption and shorter processing time. As compared with conventional heating, microwave heating produces better microstructures, higher efficiency with less energy consumption, fewer defects, and lower heating costs.

1.9.1 Properties and Microstructure Enhancement by Microwave Processing

The properties and microstructure of metallic/non-metallic can be enhanced by microwave processing. The sintering process requires uniform thermal gradient, higher heating rates, high temperatures, and uniform thermal distribution in the specimen. These properties cannot be achieved by using conventional sintering pathways that, limits scientists to remain compact for longer processing times and higher temperatures. The low heating rates, along with longer processing times, lead to heterogeneous microstructures with several inhomogeneities and defects like cracks and porosity **[65].** These problems can be reduced by the microwave sintering of materials, which ensures a homogeneous microstructure with reduced energy consumption and improved properties.

1.9.2 Improved Densification Parameter

It has been reported that 100% of dense processed material can be obtained by microwave processing, allowing better material properties. Figure 1.17 shows the work of Mondel et al. **[65]** in the densification of tungsten alloys, which clearly shows that higher densities are obtained in microwave processing than in conventional processing. The density of the W-10Cu composite was increased by about 13% and, during microwave processing; almost completely dense composites were obtained in comparison with conventional processing**.**

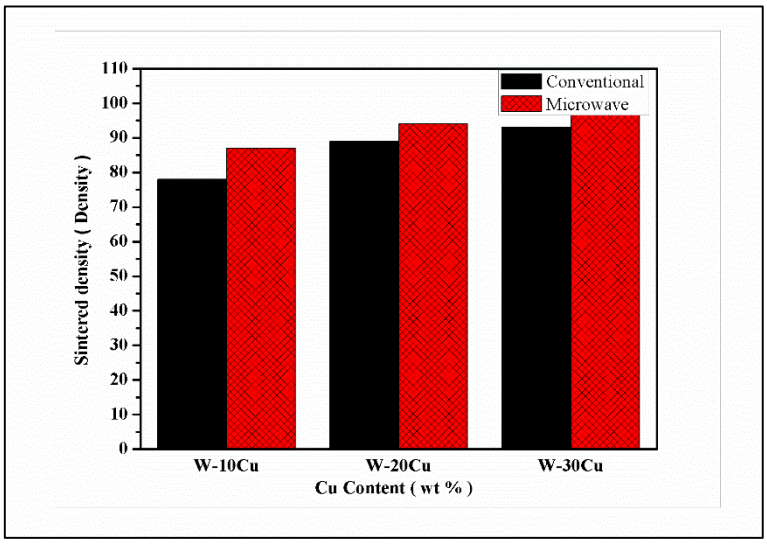

Figure 1.17: Comparison between the theoretical sintered density of W-Cu composites by conventional and microwave sintering **[65]**

1.9.3 Power Consumptions in Microwave Processing

Due to higher processing times, higher energy consumption, and poor characteristics of process components, the traditional methods of material manufacturing and processing become obsolete or modernized by new or new hybrid processes. These limitations have forced scientists to find alternative and new material and production methods for processing advanced materials such as ceramics, functionally graded materials, cermet, and metal matrix composites, and so on. Microwave material processing has emerged over the years as one of the new materials processing methods, in the production of a better product at a lower cost and processing time. Mondel et al. **[65]** in their work, they reported that sintering W-Cu alloys using microwaves takes less time compared to the conventional muffle furnaces method. Figure 1.18 shows a comparison of processing times, which shows a reduction in processing time by a factor of six. Panda et al. **[66]** described in his article that microwave processing consumes 10 to 200 times less energy and 10 to 100 times less energy than conventional routes.

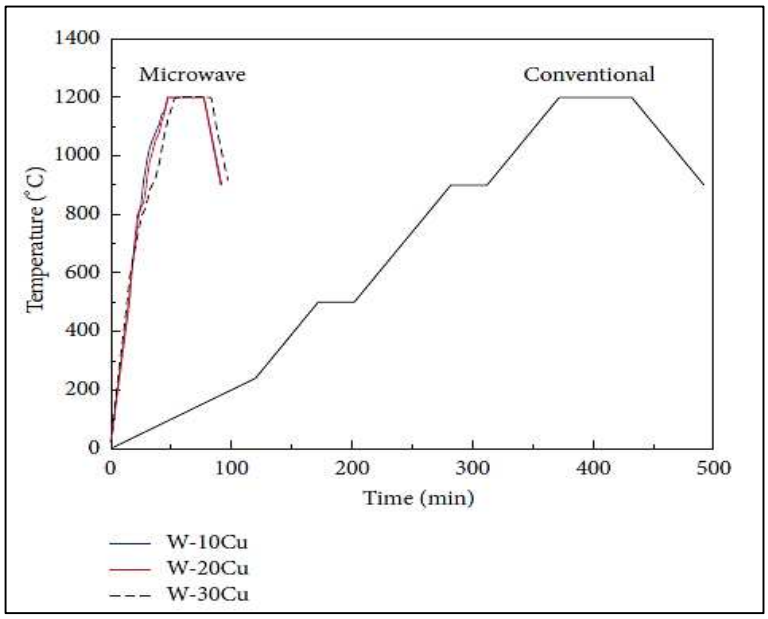

Figure 1.18: Comparison of processing times for microwave and conventional heating for W-Cu alloys **[65]**

1.10 Limitation of the Microwave Heating

Microwave material processing method has gained importance over the conventional material processing methods in the last few years. This process is still under research phase. Although microwave material processing has many advantages, there are some limitations also which make this process a challenging task. The most widely found limitations are:

i. Poor interaction of metallic material with microwave irradiations at room temperature.
ii. The uncontrollable temperature inside the microwave cavity.
iii. Difficulties in the processing of complex geometries.
iv. Microwave radiation leakage is harmful to the human body which limits its use in industries yet.

Chapter 2

Literature Review

2.1 Introduction to Chapter

In this chapter, the broad literature survey related to different surface modification methods that have been evolved and more emphasis has been given to the methods used for coating/cladding (specifically stainless steels substrate) for improving cavitation erosion-resistant (CER) has been enlisted. The various well-matured techniques are in use to increase the resistance to cavitation erosion, like, HVOF (high velocity oxy-fuel), double glow discharge plasma sputtering, filtered arc deposition, laser cladding, arc spraying, plasma spraying, physical vapour deposition (PVD), cathodic vapour deposition (CVD), conventional welding processes like shielded metal arc welding (SMAW), friction stir processing (FSP), and hard facing. This chapter also contains the literature summary of post-processing or heat treatment method used to enhance the cavitation erosion resistance of prepared coating/cladding by reducing the processing defects of prepared coating/claddings. In the last, literature consists of breakthrough and development in the field of cladding with microwave hybrid heating has been also discussed.

2.2 Literature Survey of at Present Available Methods for Improvement of Cavitation Erosion Resistance

2.2.1 Cavitation Erosion Resistance Coatings by Using Arc Spraying Technique

Lin et al. (2019) [67] have evaluated the CER of coatings based on amorphous/ nanocrystalline iron, deposited on austenitic stainless steel AISI 321 by using arc spraying technique. The X-ray diffraction (XRD) examination of the deposited coating exhibits the co-existence of the nanocrystalline & amorphous phase, which is further confirmed by transmission electron microscopy (TEM) analysis. The Figure 2.1 (a) shows the scanning electron microscopy (SEM) micrograph of complete coating cross-section and Figure 2.1 (b) reveals the defects like pores, micro-cracks, un-melted particles, and an oxides layer in developed coating. It was found that these defects have a negative effect on the corrosion and cavitation erosion behaviour of the developed

coatings. FeNiCrBSiNbW coating exhibited better CER in 3.5% NaCl (sodium chloride) solution as compared to 316L coating. Brittle mode of failure was observed in FeNiCrBSiNbW coating during cavitation testing. The cumulative weight loss in the coating was increased with the increase of cavitation erosion testing time.

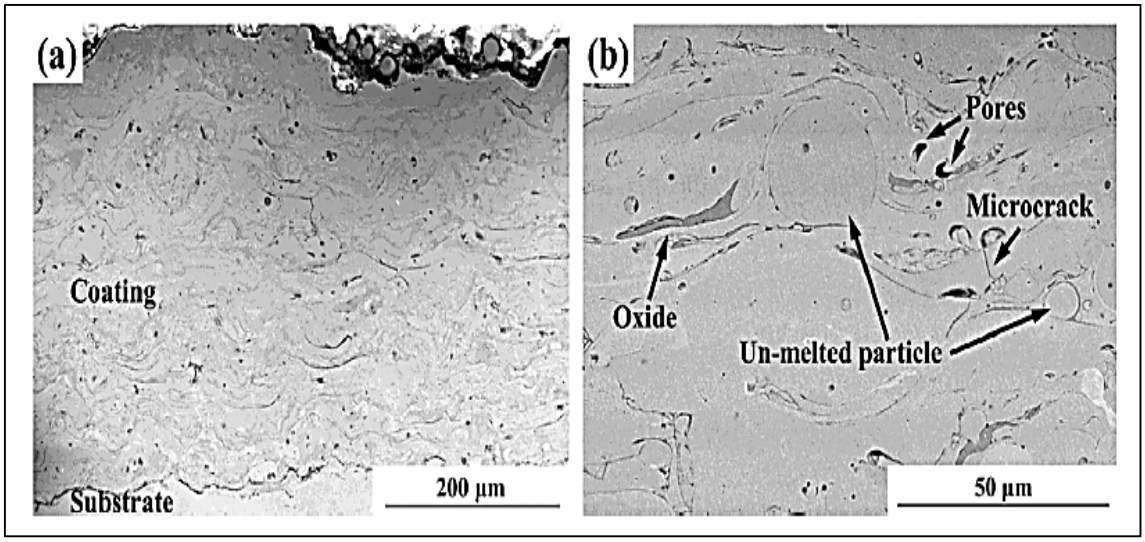

Figure 2.1: SEM micrograph of a cross-sectional view arc sprayed coating showing (a) Transverse section (b) Enlarged view [67]

Lin et al. (2014) [68] have successfully developed the FeNiCrBSiNbW and 316L amorphous coating by using twin-wire arc spraying technology. The mean hardness of FeNiCrBSiNbW coatings was 919±49 $HV_{0.1}$, approximately five times much harder than 316L coating (239±19 $HV_{0.1}$). The developed coatings were investigated for cavitation erosion behaviour in distilled water using vibratory cavitation test equipment at peak amplitude of 60±5 µm and immersion depth of 3 mm. The FeNiCrBSiNbW coating was superior to the 316L coating, in both terms the higher resistance to cavitation erosion and higher hardness. Fractographic analysis of worn-out FeNiCrBSiNbW coating reveals that during cavitation erosion cracks was initiated from the location of pores and area near to un-melted particles.

2.2.2 Cavitation Erosion Resistance Coatings by Using Cathodic Arc Evaporation

Krella et al. (2013) [69] have deposited TiN and CrN coating of varying thickness from 3.9 µm to 7.8 µm on X39Cr13 and X6CrNiTi 18-10 steel via cathodic arc evaporation technique. Whereas all the substrates were heat treated (tempering) at various

temperatures (400°C and 600°C) to achieve the different mechanical and metallurgical properties. All coatings were deposited at a bias voltage of -100 V and at 350°C. Developed coatings were tested for adhesion with the substrate, hardness, and young modulus. For the adhesion evaluation, scratch adhesion test was performed. In both of the coatings materials, a significant increase in hardness was observed with the increase in coating thickness. TiN and CrN Coating with 7.8 µm thickness have the highest hardness and best adhesion with the substrate. The cavitation testing was carried out for 600 min in cavitation tunnel apparatus, an inlet pressure of 1000 kPa and outlet pressure of 130 kPa. The deposited coating has high CER than the substrate despite the thickness of the coating. The coatings with the highest thickness have best CER. The deterioration of the coating was in the form of spalling.

Krella et al. (2011) [70] have developed TiN coating on X6CrNiTi 18-10 steel via cathodic arc deposition method at varying deposition parameters, the substrate bias voltage (-300 V, -100 V, and 0 V) and substrate temperature (200°C, 350°C, and 500°C) both were varied at three levels. TiN-12 Coating (-100 V bias voltage & 350°C substrate temperature) have highest hardness (27.4 GPa), highest young modulus (525 GPa), lowest H/E ratio (0.052) and best adhesion (30 N) with the substrate as compared to a coating deposited at other deposition parameters. The developed coatings were examined for cavitation resistance with cavitation tunnel apparatus in hard tap water. The author concluded that till the incubation period, the whole cavitation impact energy was utilized in phase transformation after then the material loss begins. The mass loss due to cavitation erosion is an active function of adhesion and ductility of the coating. The microscopic observations showed that the first micro-cracks appeared on top of microfilm and at delamination spot.

2.2.3 Cavitation Erosion Resistance Coatings by Using by Using Filtered Arc Deposition

Yang et al. (2009) [71] have investigated the cavitation performance of NiTi thin films deposited on SS-316 by filtered arc deposition. The coating deposition was performed at a different substrate surface temperature of 130°C, 300°C, 430°C and 600°C. The coating thickness of 1.88 µm was achieved at 125 A deposition current, the bias voltage of 80 V in 7 minutes. The films deposited at 300°C showed very broad XRD spectrum, i.e. considered to be amorphous. Whereas coating deposited at 430°C showed the

preferred order crystalline phase and monoclinic martensitic phase in the XRD spectrum, which was further confirmed by TEM analysis. The substrate temperature during coating deposition has a significant effect on FADP coatings microstructure. The crystalline NiTi films deposited at 600°C showed 2.5 times higher cavitation erosion resistance as a result of faster phase transformation and higher thermo elastic reversibility.

2.2.4 Surface Modification for CER by Using Friction Stir Processing

Hajjan et al. (2014) [72] have worked on the FSP of the stainless steel 316L surface. The specimens were processed at a constant linear travel speed of 30 mm/min and two different rotational speeds of 200 rpm and 315 rpm. The initial grain size of SS-316L was 14.8 µm, SEM images as shown in Figure 2.2 (a), whereas after friction stir processing the very fine grain structure of 4.6 µm and 1.7 µm is achieved as shown in Figure 2.2 (b) and (c) respectively. The cavitation testing on vibratory cavitation test apparatus is carried out for 20 hours at 50 µm amplitude, 20 kHz frequency and the specimen is placed at 0.5 mm distance from the tip of the horn. The cavitation resistance of friction stir processed material was improved by 3-6 times. It was observed that the deterioration of fine grain structure takes place more homogenously than coarse grain structure. The EBDS results show that the cavitation damage is governed by several mechanism grain boundary destruction, micro cracking and fatigue crack propagation.

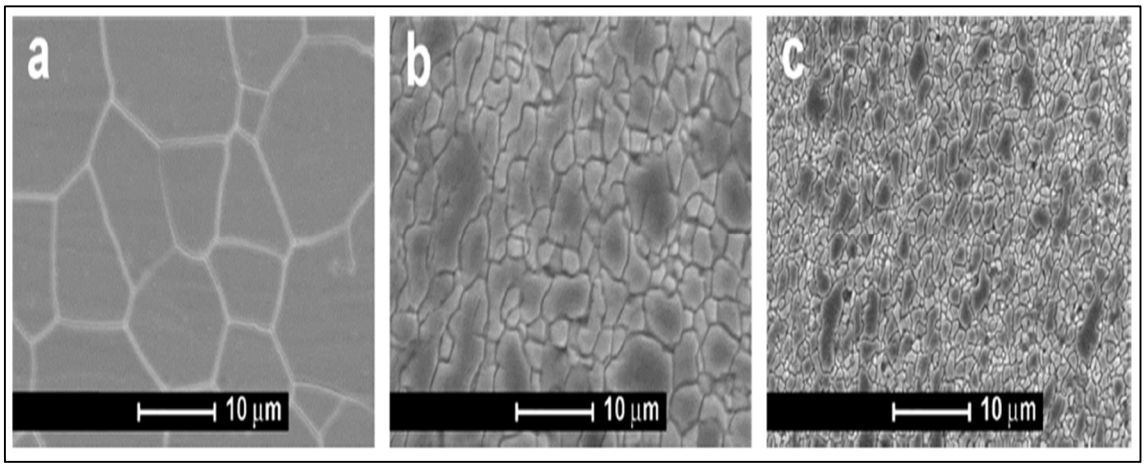

Figure 2.2: SEM images showing grain structure of (a) SS316L before FSP (b) SS316L after FSP at 200 rpm (c) SS316L after FSP at 315 rpm [72]

Grewal et al. (2012) [73] have worked on the FSP of the CA6NM hydro turbine steels. The processing was carried out at table feed of 20 mm/min, 0.3 mm tool pressure, -20°C cooling temperature, and 2500 rpm spindle speed. The XRD examination shows the formation of hard $Cr_{23}C_7$ phase. Microstructure examination reveals that unprocessed samples have an average grain size of 30 µm, whereas after FSP sample the average grain size reduced was to 2.5 µm. The EBDS analysis shows that the processed sample has nearly 15% of grains in the nano range. After FSP, the hardness of the substrate surface was increased by 160%. The cavitation erosion resistance of the FSP specimen was found 60% higher than the unprocessed sample. The increase in hardness of the substrate was responsible for higher CER. The similar erosion mechanism was observed in both of the specimens, but the severity of damage is very different.

2.2.5 Cavitation Erosion Resistance Coatings by Using High-Velocity Oxy-Fuel Spraying Technique

Ding et al. (2018) [74] have studied the effect of different size WC particles on CER of HVOF deposited WC-Co Coatings. NC-Nanostructured (50-500 nm), MC-multimodal, and CC-conventional (10-45 µm) WC-12Co coatings were developed on SS304. The Spray parameters used for coating process were horizontal velocity 500 mm/s, spray distance 380 mm, oxygen flow 53.2 m^3/h and fuel flow 0.20 m^3/h. The coating thickness of the 400±20 µm has been achieved. The microhardness of prepared coatings is 1541±80 $HV_{0.2}$ for NC, 1523±157 $HV_{0.2}$ for MC and 1034± 77.5 $HV_{0.2}$ for CC. The porosity in the prepared coatings is 1.76±0.27% with CC, 1.18±0.21% with MC, and 0.63±0.11% in NC. The nanostructured WC-12Co particles allow sufficient growth for denser structure coatings and decreasing porosity. The XRD analysis of deposited coating shows that serious decarburization occurred in the nanostructured coating, free metallic W was observed. All the developed coatings showed higher fracture toughness. The CER of nanostructured coating is 65% more than conventional coating and 40% more than multimodal coating. Densification and strong, cohesive strength were reported as the main factor in CER improvement.

Amarendra et al. (2018) [75] have studied the combined slurry and CER of thermal sprayed 70Ni-Cr coatings deposited on SS-410. The surface hardness of the received specimen was 220 HV, and the modified specimen was 264 HV. The thickness of the

developed coating was approximately 67 µm. The peel-off test with ASTM C633 has confirmed that deposited coatings have good adhesion strength. The combined outcome of slurry and cavitation erosion was investigated by slurry pot tester coupled with CI (cavitation inducers). The slurry erosion testing was performed with a slurry of two different sand particles sizes of 200 µm and 300 µm. Moreover, with the increase in sand particle size, the increase in mass loss was observed. The thermal spray coating has increased the slurry erosion, cavitation erosion, and combined slurry erosion resistance of SS-410.

Ding et al. (2017) [76] have deposited the micro-nano structure WC-10Co4Cr coating on SS-316 using HVOF technology. Mechanical, metallurgical and electrochemical characterisations of developed coatings were carried out. The thickness of the developed coating was approximately 450±20 µm. The fracture toughness of MC is 65% more than that of CC. There was no large difference between the microhardness of the micro-nano coatings (1345±136 HV) and conventional coatings (1322±181 HV). The porosity in MC (micro-nano) coating was 0.26±0.077%, whereas in CC (conventional coating) was 0.43±0.12%. The XRD patterns of both coatings show similar results, whereas the intensity of the crystalline phase was more in MC and no serious decarburization was observed in WC. Moreover, MC possesses higher corrosion resistance during electrochemical testing. The cavitation erosion testing of developed coatings was carried out in 3.5 wt% NaCl for 18 hours. The results show that MC coating has 50% more CER than SS-316 and 12.5% more CER than CC.

Qiao et al. (2017) [77] have prepared Fe-based amorphous/nanocrystalline coatings on stainless steel 321 substrate by using HVOF technique. Taguchi L9 array was utilised to optimise the spray parameters (carrier gas flow rate, fuel flow rate, and nozzle stand-off distance). The ANOVA was employed to identify the significance of spray parameters on performance characteristics (porosity, hardness and cavitation erosion resistance). The flow of fuel (kerosene) in HVOF coating process came out as the most crucial process parameter, followed by nozzle stand-off distance (spray distance) and carrier gas flow rate (oxygen). The Fe-based coating deposited at optimised spray parameters (Kerosene flow rate - 28 l/h, spray distance-300 mm and oxygen flow-963 l/min) was very dense and excellent adhesion with the substrate. The average thickness of the developed coating was 300 µm. The hardness and porosity of the best coating are

1121±53 $HV_{0.2}$ and 1.21±0.71%. The deposited coating consisted of an amorphous phase with few amounts of hard Fe_2B, Fe_3B, CrB and Cr_2B. CER of the coatings increases with the increase in hardness and decreases with an increase in porosity. The CER of the Fe-based thermal sprayed coatings was significantly higher than AISI 321.

Lavigne et al. (2017) [78] have investigated the CER of Fe-based cavitec coating, Co-based stellite-6 coating and WC based WC-CoCr coating deposited by HVOF technique on SS-304. Four different variations were used for cavitec coatings, that are UM-LV (unmilled-low velocity), UM-HV (UM-LV (unmilled-high velocity), M6-LV (milled 6 hours-low velocity), and M6-HV (milled 6 hours-high velocity). The thickness and hardness of the developed coatings were in the range of 85 µm to 350 µm and 4.6 to 121 GPa respectively. The cavitec M6-HV coating has the best bonding with the substrate due to higher deposition velocity. XRD examination shows that the after ball milling the cavitec powder underwent a phase transformation from the austenitic phase to the martensitic phase. However, the maximum phase of the austenite was recovered after deposition of the coating. The vibratory cavitation testing was carried out for 8 hours in distilled water at 50 µm amplitude and 20 kHz frequency; the specimen was placed at 0.5 mm distance from the horn tip. The UM–LV ultimately failed after 2 hours of cavitation exposure. The best HVOF coating was M6-HV, it has equivalent CER to the well-known stellite 6 and WC-CoCr Coatings. The comparison of erosion rate and incubation time various coatings are shown in Figure 2.3.

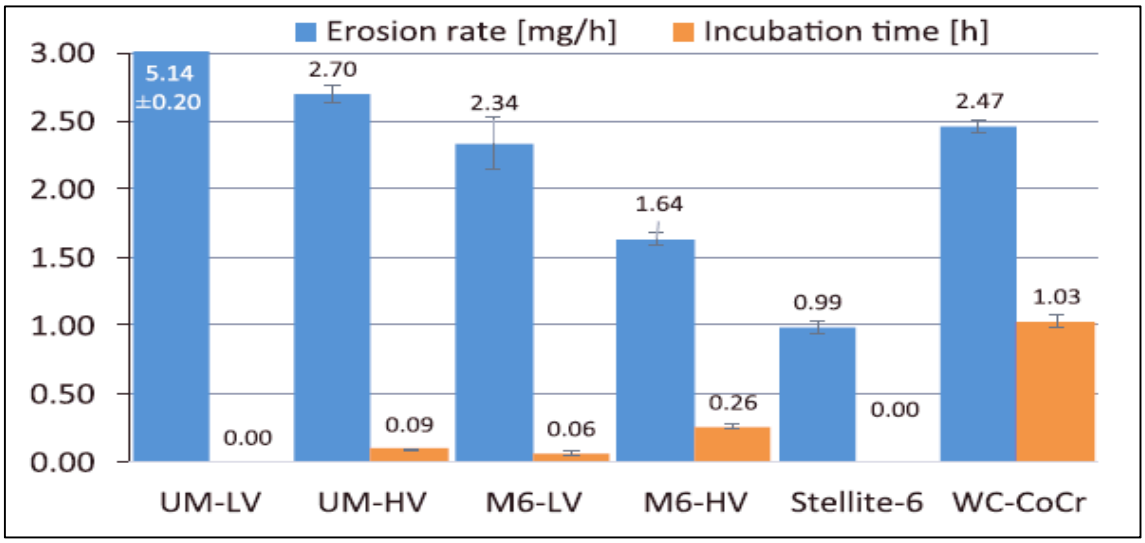

Figure 2.3: Cavitation erosion characteristics of HVOF coatings [76].

Kumar et al. (2016) [79] have investigated the effect of spray particle velocity on the CER of HVAF (high-velocity air-fuel), and HVOF processed 86WC-10Co4Cr coatings on SS-410. The coatings of 410 µm thicknesses were deposited at spray velocities of 680 m/s for HVOF, 865 m/s (AF-1), 960 m/s (AF-2) and 1010 m/s (AF-3) for HVAF. The properties such as microhardness, fracture toughness, and porosity were investigated. The HVAF coatings exhibit higher hardness, lower porosity and better resistance to nanoindentation than HVOF coatings at same spray particles velocity. The best HVAF coating was AF1 having hardness 1473±40 HV and porosity 0.52±0.13%. Whereas, the scratch test shows that the scratch depth in HVAF coatings was 35% less than HVOF. Cavitation erosion testing reveals that AF1 coating has three times higher CER than of HVOF coating. The erosion mechanism of the HVOF coating during cavitation comprises of microcracking of matrix phase, propagation of cracks along the WC grain boundaries, further pulling of WC particles from the matrix and at the end delamination of the coatings. The author concluded that the CoCr matrix phase formed in the HVAF provides higher crack-resistant to the matrix. Also, the higher WC cohesiveness further increases the CER of HVAF coatings by manifolds.

Hong et al. (2015) [80] have examined the CER of nanostructured WC-10Co-4Cr coatings in 3.5% NaCl solution deposited via HVOF technique on 1Cr18Ni9Ti steel. The prepared coatings were analysed in various aspects like microstructure and tribological. The microstructural analysis reveals that highly dense and 200 µm thick coating was deposited and porosity in the coating was less than 1%. TEM images shown in Figure 2.4 (a) confirms the presence of nanostructured WC having hexagonal structure in SAED (selected area electron diffraction) as shown in Figure 2.4 (b) surrounded by the amorphous matrix visible in Figure 2.4 (c) and Figure 2.4 (d), shows the SAED pattern of the amorphous phase. The cavitation test has been carried out as per ASTM G32-10 standards for 10 hours; the specimen was attached to the free end of the ultrasonic horn and immersed 3 mm below in the test liquid. The HVOF coating exhibits 1.27 times CER as compared to steel. The reasons for coating superior CER were good fracture toughness, high hardness and presence of amorphous phase. The coating failure mechanism was micro cracking in soft binder phases or matrix, ploughing of hard phases and formation pits due to corrosion.

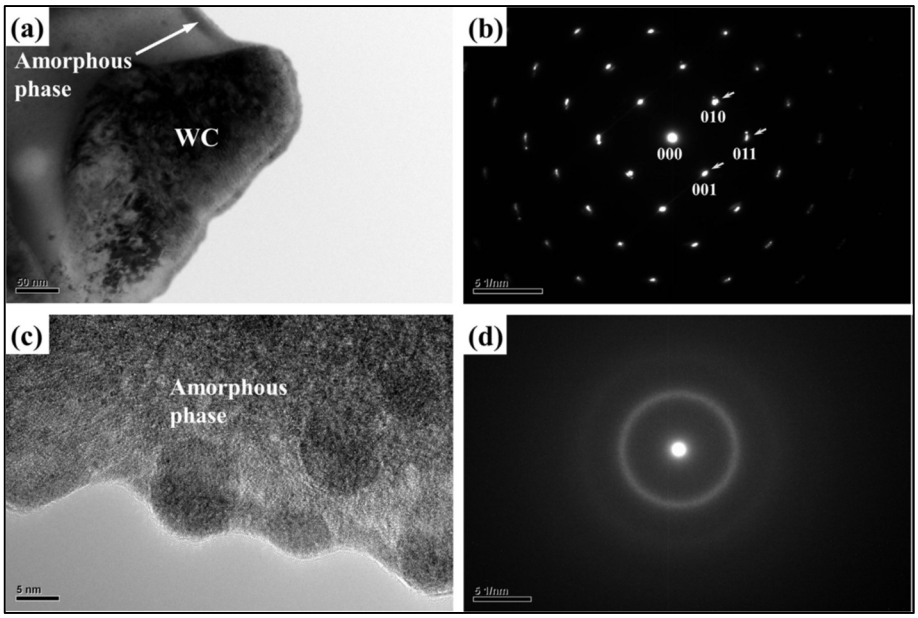

Figure 2.4 TEM images of (a) Nanostructured WC phases covered by amorphous phase (b) WC phase SAED pattern (c) Amorphous matrix (d) Amorphous phase SAED pattern [80]

Kekes et al. (2014) [81] have deposited the WC-Co/Cr and NiCrFeBSiC composite Coatings on stainless steel 304 by using the HVOF technique. The five coating combinations (0% WC-Co/Cr, 25% WC-Co/Cr, 50% WC-Co/Cr, 75% WC-Co/Cr and 100% WC-Co/Cr) were used. The microhardness of the developed coatings was varied in the range 800 $HV_{0.2}$ to 1400 $HV_{0.2}$, depending upon the percentage of the reinforcement. The developed coatings were tested for CER for 10 hours on vibratory cavitation apparatus, schematic as shown in Figure 2.5 and the testing has been carried out in distilled water at 30 µm amplitude, 20 kHz frequency, 50 mm immersion depth and the specimen was placed at the distance of 1 mm from the horn tip. The average roughness of 0.5±0.1 µm was maintained on every specimen before testing, due to the high initial surface roughness of the deposited coatings. The coating with 50% WC-Cr/Co has higher CER and coating with 100% WC-Cr/Co has worst CER. In the case of 100% metallic coating, the failure of coating is only due to plastic deformation without being fractured. However, in 100% cermet coating, the entire coating detaches from the substrate due to poor cohesion during cavitation testing. Whereas, the erosion in the composite coating, due to the local stress, which results in micro-cracks initiation in carbide, propagation of cracks in weak boundaries and at the end material loss.

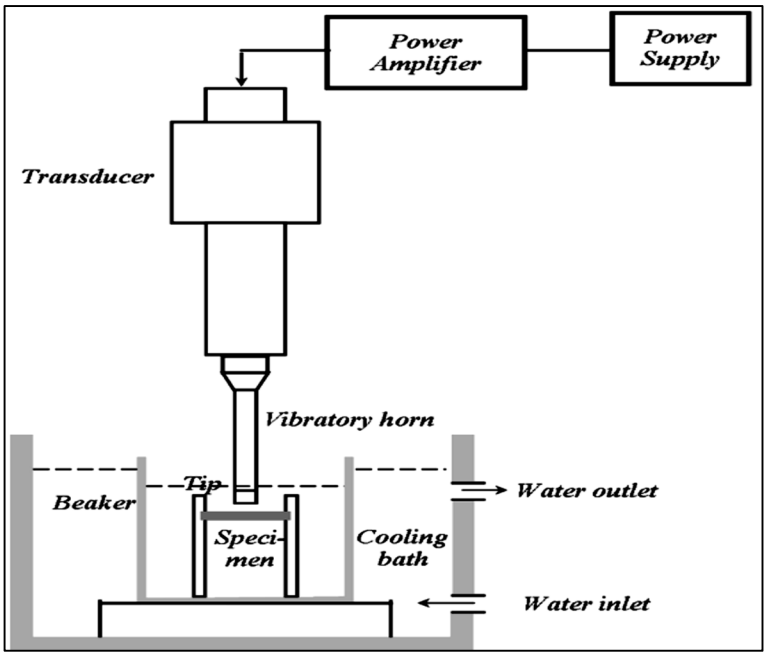

Figure 2.5: Schematic of vibratory cavitation apparatus [81]

Santa et al. (2009) [82] studied the cavitation and slurry erosion of six (nickel-1, nickel-2, chromium oxide, tungsten carbide, chromium carbide and Ni-WC/Co composite) HVOF deposited coatings and compared with the uncoated martensitic stainless steel. Nickel-1 coating was composed of 14.6± 1.2% Al_2O_3, Nickel-2 coating was composed of Ni-Fe-Mo-W-Si, and Ni-WC/Co coating was consisting of a 46±2% Ni-Fe-Cr. The average thickness of the deposited coatings was 40 µm. The hardness, porosity, average thickness and other essential details of the deposited coatings were summarized in Table 2.1.

Table 2.1: Properties of the developed HVOF coatings [82]

S.no	Coating	Hardness in Metallic Region	Hardness in Ceramics Region	Porosity (%)	Average Coating Thickness (µm)	Other Details
1	Ni-1	191 $HV_{300g, 15s}$	1533 $HV_{25gf, 15s}$	2.9±1.2	650	Non-crystalline phases
2	Ni-2	385 $HV_{50gf, 15s}$	701 $HV_{50gf, 15s}$	4.4±1.5	760	Non-crystalline phases
3	WC/Co-Ni	639 $HV_{300g, 15s}$	1211 $HV_{300g, 15s}$	13.7±3.8	820	Co_4W_2C partially crystalline phase was found
4	Cr_2O_3	-	1853 $HV_{300g, 15s}$	30	450	Surface cracks, poor cohesion with the substrate

5	WC/Co	-	-	2	85	Number of crystalline phases
6	CrC	-	-	-	40	Heterogeneous coating thickness, XRD spectrum shows substrate related peaks due to less thickness of the coating and high x-ray penetration

The CER of all the HVOF coatings was lower than the uncoated 13-4 stainless steel, because of low cohesion, high porosity and initial cracks. However, the HVOF coatings possess higher slurry erosion resistance as compare to 13-4 steel. The best coating was WC/Co-Ni composite coating. The brittle failure of hard phase and fatigue of the ductile region in HVOF coatings during cavitation was observed. In slurry erosion, the primary wear mechanism was the detachment of the hard phase and micro-cutting and micro-ploughing of matrix phases.

2.2.6 Cavitation Erosion Resistance Coatings by Using Double Glow Discharge Plasma Technique

Jiang et al. (2016) [83] have developed the nanocrystalline Cr_3Si film by using double glow discharge plasma technology on SS-304 specimen. The coating of 5 µm thickness was achieved in 3 hours at an electrode bias voltage of –900 V, the substrate bias voltage of -300 V, working pressure 35 Pa, substrate temperature 800°C, airflow rate 35 cc/s and distance between substrate and electrode 15 mm. The SEM micrograph reveals that deposited coating is free from pores and microcracks and partially bonded with the substrate as shown in Figure 2.6, which was further confirmed by scratch test. The bonding strength of the developed nanocrystalline Cr_3Si film was 80 N. The XRD analysis of deposited coating exhibits the presence of single Cr_3Si phases. The hardness of the deposited coating was 26 GPa, i.e. 10 times higher than of SS304 substrate. After vibratory cavitation testing of 30 hours, the weight loss of the deposited coating was 60% lesser than SS-304 substrate. The cause's erosion of the deposited film was poor bonding strength of the film with the substrate and brittle characteristics of the silicide's present in deposited coatings.

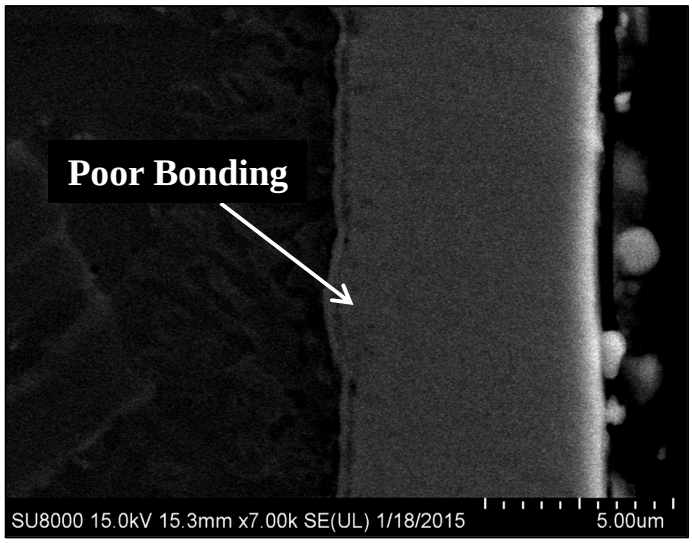

Figure 2.6: SEM micrograph of nanocrystalline Cr_3Si film deposited via a double cathode glow discharge technique [83]

2.2.7 Cavitation Erosion Resistance Coatings by Using Physical vapour deposition (PVD)

Momeni et al. (2016) [84] have developed the single layer NiTi coating, bilayer NiTi/TiCN composite coatings of varying thickness from 3 to 4 µm on X38CrMoV51 hot work tool steel. The various combination of coatings was in the ratio of $(NiTi/TiCN)_2$, $(NiTi/TiCN)_1$, and $(NiTi/TiCN)_{0.5}$. The sputtering process parameters were 300°C substrate temperature and 9.5 KW power. The mechanical properties of deposited coatings like hardness, young modulus and critical load sustained by coatings during the scratch test are tabulated in Table 2.2. The XRD patterns exhibit that the intensity of the crystalline TiCN phase increases with the decrease of NiTi layer thickness. The coatings were tested for CER on ultrasonic vibratory cavitation apparatus for 12 hours at 40 µm amplitude in distilled water. The $(NiTi/TiCN)_{0.5}$ coating has the highest cavitation erosion resistance, followed by $(NiTi/TiCN)_1$, $(NiTi/TiCN)_2$ and NiTi. The adhesion strength between the coating and substrate was the critical factor for the superior CER.

Table 2.2: Mechanical properties of the PVD coatings [84]

S.no	Coating	Hardness (GPa)	Young Modulus (GPa)	Critical load (N)
1	NiTi	5	30	25
2	$(NiTi/TiCN)_2$	13	58	50
3	$(NiTi/TiCN)_1$	12.5	54	30
4	$(NiTi/TiCN)_{0.5}$	15	50	20

2.2.8 Cavitation Erosion Resistance Cladding by Using Submerged Arc Welding (SMAW)

Romo et al. (2012) [85] have investigated the slurry erosion and cavitation erosion of the stellite6 claddings developed on 13-4 steel by using submerged arc welding. Before the cladding steel specimens were homogenized at 1050°C for 1 hour, after that cooled in room temperature and then tempered at 620°C for 1 hour. The welding parameters selected for the coating process were 90-120 A welding current, 10-15° travel angle and 90° work angle. The average hardness of the developed coating was 456 HV. The specimens were tested for cavitation erosion resistance using ASTM-G32 standards and slurry erosion resistance using jet erosion tester at different angles (15°,30°, 45°, 60° and 90°) with slurry of SiO_2 mixed with tap water. The CER of SMAW deposited stellite6 was 7.8 times higher than that of 13-4 steel. Also, slurry erosion resistance of the developed claddings was 50% more than 13-4 steel at 15° impingement angle, whereas only 18 to 23% better for impingement angles between 30 to 90°. The primary failure mechanism of cladding during cavitation was reported, surface fatigue due to the impact of shock waves, whereas during slurry erosion micro-cutting and micro ploughing was observed.

2.2.9 Cavitation Erosion Resistance Claddings by Using Tungsten Inert Gas (TIG) Welding

Cheng et al. (2003) [86] has deposited the NiTi cladding on stainless steel 316 by using the TIG welding process. The developed cladding has good adhesive strength, was verified by nanoindentation tester. The microhardness of the developed cladding was 700 HV, which was approximately 3.5 times higher than the substrate (200 HV). During SEM analysis, few pores of size, less 20 µm was observed. The porosity of the developed claddings was less than 1%. The XRD examination reveals the presence of

following phases NiTiFeCr, (Ni,Fe)Ti. The NiTiFeCr phase confirms the interfacial bonding between the substrate and the cladding. The vibratory cavitation erosion testing was carried out at 100 µm amplitude and 20 kHz frequency in 3.5% NaCl solution. The specimen was placed at a distance of 0.5 mm for the horn tip. The CER of the NiTi-TIG cladding was 9 times higher than the AISI316 steel. The reason attributed to the cavitation erosion resistance was the higher hardness of the cladding and super elasticity of the NiTi phase.

2.2.10 Surface Modification for CER by Using Hard Facing

Sreedhar et al. (2015) [87] have evaluated the effect cavitation erosion on hard-faced Ni-based colmonoy5 and Co-based stellite6 coatings deposited on 316L austenitic stainless steel in liquid sodium at varying temperature (200°C, 250°C and 300°C) for 2 hours. The average deposit thickness was 1.5 mm for both coatings. The hardness of the developed coatings was 369 HV and 393 HV for stellite6 and colmonoy5 respectively. The fracture toughness of the developed coatings was 35.6±2.5 MPa$\sqrt{m}$ and 15.9±3 MPa$\sqrt{m}$ for stellite6 and colmonoy5, respectively. The CER of both of the developed coatings was higher than 316L in sodium liquid. However, the Co-based stellite6 have better CER than Ni-based colmonoy5 because cobalt has lower SFE (stacking fault energy) as compared to nickel. Also, the fracture toughness of the Co-based coating was higher than Ni-based coatings. It was concluded that the cavitation damage in SS316L was uniform over the entire surface. However, in hard faced coatings damage begin from the matrix phase as well as from other intermetallic phases.

2.2.11 Enhancement of CER of Bulk material with Addition to Casting

Li et al. (2017) [88] have investigated the effect of adding molybdenum in SS-316L casting on CER in 3.5% NaCl solution. The four combination of casting were prepared with varying percentage of molybdenum (2.5% - specimen-1, 4% - specimen-2, 6%-specimen-3 and 8%-specimen). The specimens of ø16 mm were tested for CER by using vibratory cavitation test apparatus for 120 min. The electrode potential of all specimens was measured after that data was utilized for the Mott-Schottky plot. From the Mott-Schottky Plot, it was found that the specimen with 8% Mo has the highest negative flat band potential. The micro particles present in the test liquid, which increases the severity of the cavitation damage. However, when the substrate has a

negative charge layer, during the micro-bubbles explosion microjet which carrying a negative charge micro particles start moving towards the substrate surface, but that was repelled by the highly accumulated negative charge of the substrate surface. Also, molybdenum has a high negative potential, therefore with an increase in Mo%, the repelling by the substrate surface will increases. Hence, the specimen with 8% Mo has the highest CER.

2.2.12 Cavitation Erosion Resistance Coatings by Using Plasma Spray Technique

Bitzer et al. (2015) [89] have deposited NiTi coatings on 42CrMo4 steel by using LPPS (low-pressure plasma spraying). The coatings were deposited at two different sets (Set A & Set B) of process parameters. The CER was investigated; the relation was developed between the LPPS process parameters, coating thickness and surface treatment like electrolytically polishing (for reduction of surface roughness). The comparison of NiTi coating with Fe based alloy UTP730 was carried out. The coatings of thickness 60 µm, 360 µm, 800 µm, and 1000 µm were deposited. The coatings were also characterized for of the microstructure, surface roughness and phase transformation. The roughness of LPPS coatings at set A and set B was 14 µm and 13 µm respectively. The one specimen from each set of prepared coatings was electrolytically polished before the cavitation erosion testing. The electrolytically polished coatings developed at parameters set B have highest CER. The increase of CER was observed with increase in coatings thickness. The microstructural study of the coatings after cavitation exposure reveals that pores and higher surface roughness influence material removal. Whereas the XRD examination exhibits that phase transformation of NiTi coatings from austenite to martensite was the cause of weight loss in later stages.

2.2.13 Cavitation Erosion Resistance Coatings by Using Plasma Transferred Arc (PTA) Welding

Zhang et al. (2017) [90] has deposited the NiCrBSiW (colomonoy88) and 41WC-36Ni7.5CrSiB (colomonoy75) alloy coatings on the 316L substrate by PTA (plasma tungsten arc) welding. The PTA welding selected parameters values was 140 A of main arc current, 27 V main arc voltage, 10 g/min powder feed rate, 12 l/min shielding gas flow rate, shielding gas flow rate, 40 mm/min travel speed, 40 mm oscillation width, 1.5

l/min arc gas flow rate. The study of CE and corrosion-erosion behavior was carried out by using vibratory cavitation and jet erosion apparatus respectively in 3.5% NaCl solution. The microstructural study via SEM reveals that deposited coatings have non-uniform grain size and cellular dendritic structure. The XRD analysis exhibits that deposited coatings were composed of γ-Ni, $Cr_{23}C_6$, WC, W_2C, $FeNi_3$, and Fe_3W_3B phases. The microhardness of the colomonoy88 (1519 HV) was 7.5 times more than SS316L (200 HV). However, the microhardness of the colomonoy88 was less than colomonoy75 due to smaller WC particle size. The PTA welded alloy coatings colomonoy75, and colomonoy88 have 3 times and 12 times CER & 8 times and 31 times erosion-corrosion resistance, respectively.

2.2.14 Surface Modification for CER by Using Laser Cladding

Singh et al. (2014) [91] have studied the cavitation erosion and solid particle erosion (SPE) performance of the stellite6 claddings deposited on 13Cr - 4Ni steel by laser cladding process at varied laser energy densities (32, 37, 46 and 52 J/mm^2). The cavitation erosion and solid particle erosion study was carried out as per ASTM-G32-07 and ASTM-G76-07, respectively. The effect of laser energy densities on microstructure, dilution, microhardness and cladding geometry was investigated via SEM, EDS, XRD and Vickers microhardness. The cladding of an average thickness of 1 mm was deposited at all laser energy density. The microhardness of developed claddings was 705 HV at 32 J/mm^2, 630 HV at 37 J/mm^2, 641 HV at 46 J/mm^2, and 615 at 52 J/mm^2. The minimum dilution (4.48%) of stellite6 was observed in the specimen, which was prepared at an energy density of 32 J/mm^2, dilution percentage increase sharply with the increase in energy density. The increase in Ni and Fe and decrease in Cr, W and Co were observed with the increment in laser energy density. The cladding developed at 32 J/mm^2 exhibits highest cavitation erosion and SPE resistance. The CER of 13Cr-4Ni steel in 3.5% NaCl was increased more than 90% with stellite6 laser cladding. The surface topography of specimens after cavitation testing for 40 hours is shown in Figure 2.7. The reason attributed to the CER was the higher elastic recovery of the stellite6 clads.

Paul et al. (2014) [92] have developed Mecto41C (iron base alloy), stellite6 (Co-based alloy), and Colmonoy5 (nickel base alloy) claddings on AISI 316L by a using laser cladding process. The four process parameters (laser power, scan speed, powder feed

rate and gas flow rate) was varied at four levels each to find the optimum processing conditions. Developed claddings were characterized by using SEM, XRD and Vickers microhardness tester.

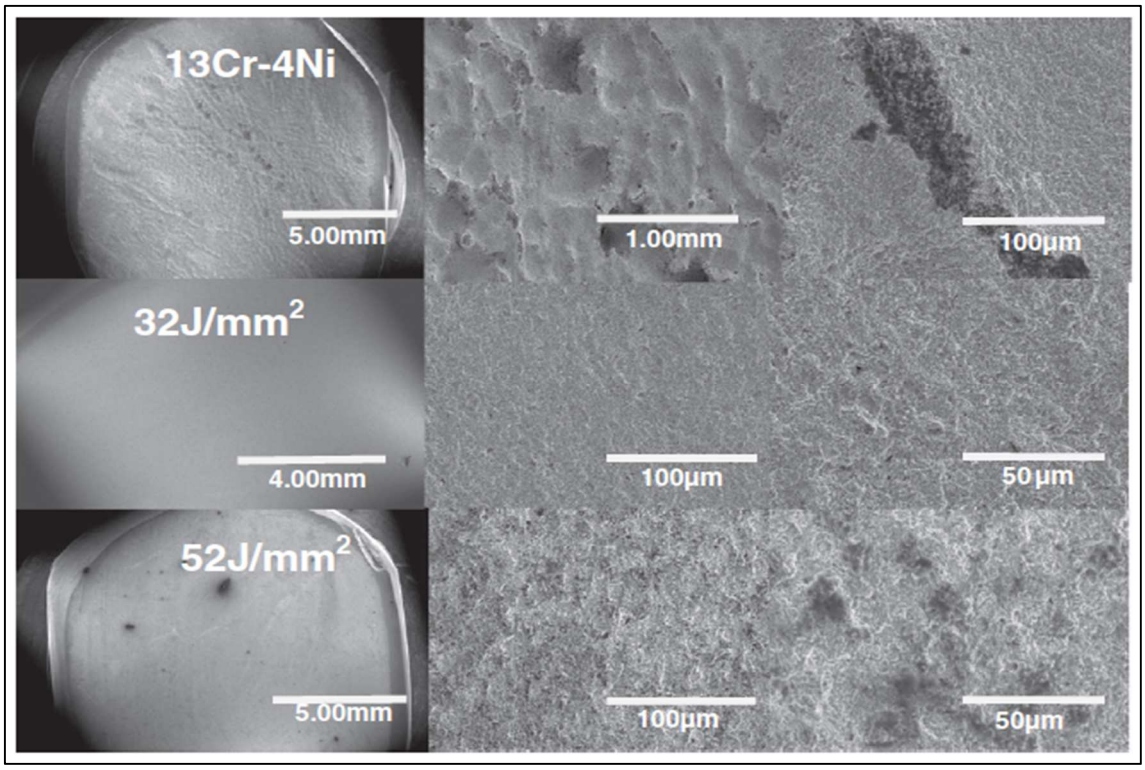

Figure 2.7: Surface topography of specimens after cavitation testing for 40 hours [91]

Both single layer and double layer clads were fabricated. The microhardness with both single and double layer cladding was the same. However, the dilution and bonding with a single layer were inadequate. The final experiments were carried out at optimized process parameters (laser power- 1.6 kW, powder feed rate- 8 g/min, and scan speed- 0.6 m/min). The microstructure investigation reveals that a very fine columnar dendritic structure was formed at optimized process parameters. Many types of carbide, borides and silicide phases were found through XRD analysis of colmonoy-5 clads, whereas γ-Fe and FeO phases were found in XRD analysis of Metco-41C clad and Co, CrC_3 and W_2C were found through XRD analysis of stellite6 clads. The microhardness of the developed claddings of Metco-41C, stellite6 and colmonoy5 were found in the range of 225-250 HV, 475-500 HV and 500-550 HV, respectively. Laser cladding with stellite-6, Metco-41C, and colmonoy-5 on stainless steel 316L enhances the CER by 4.1, 3.7, and 1.6 times, respectively as compared to AISI 316L substrate. The higher hardness of

stellite6 and Metco41C claddings during the later stages was the reason for higher CER. The mode of failure during cavitation of SS316L was plastic deformation; however, the mechanism of failure in claddings was surface fatigue, micro cracking, and brittle fracture.

Duraiselvamet al. (2006) [93] have studied the cavitation erosion behaviour of nickel aluminide intermetallic composite, and TiC reinforced matrix composites coatings deposited on AISI 420 stainless steel by laser cladding process. The cavitation erosion of three different coatings was compared with heat-treated (tempering at 650°C) stainless steel specimen. The Ni-Al clad was prepared at 1.5 kW laser power, whereas Ni-Al-TiC claddings were developed at 1.5 kW and 2 kW laser powers. The developed claddings were examined for microstructure, surface roughness and microhardness. The average microhardness of the developed claddings was 385 $HV_{0.2}$ and 649 $HV_{0.2}$ for Ni-Al and Ni-Al-TiC claddings respectively. The microstructure analysis reveals that the partially melted clads were formed with parameters combination of low powder feed rate, low scanning speed and low power. The cladding with homogeneity and good metallurgical bonding was achieved at higher laser powers. Ni_3Al, NiAl and Fe_3Al intermetallic phase were found through XRD analysis of Ni-Al clad, whereas Ni_3Al, NiAl and TiC phases were found while XRD examination of Ni-Al-TiC clads. The CER of NiAl and NiAlTiC were 3.3 and 3.6 times that of the procured specimen and only 2.4 and 2.6 times more than of heat-treated specimen. There was no correlation was found between hardness and CER, but it was reported that high work hardenability has significantly improved CER.

Chiu et al. (2005) [94] have developed NiTi cladding on the AISI 316 stainless steel with the laser cladding process. The NiTi strip of thickness 0.2 mm was preplaced over the specimen before cladding. The cladding process was performed by using a higher power Nd: YAG laser. Both single and double layer specimens were fabricated, but due to the higher dilution in the range of 13-30% in single layer sample, the double layer (dilution below 10%) specimens were selected for the final examination. The hardness of the developed double-layer claddings was 700 HV, which was approximately 3 times higher than the substrate. The reason for higher hardness attributed to dissolution of elements like Cr, Fe, and N in the matrix confirmed via EDS analysis. The doubly cladded specimen possesses the highest elastic recovery while nanoindentation testing

and doubly cladded specimen have highest CER. The high hardness, high elastic recovery and cracks & porosity free claddings were assigned as the reason for the enchantment of CER.

Cheng et al. (2002) [95] have fabricated WC reinforced metal matrix composite (MMC) - cobalt and nickel claddings by laser cladding process on SS31603. The effect of laser power (0.5, 0.7, 0.9, and 1.1 kW), the volume fraction of WC (by varying clad thickness - 0.15 and 0.25 mm), and different matrix materials on CER were investigated. The average hardness in matrix region was in the range of 200-320 HV, in case of both the matrix materials (Co and Ni), whereas the hardness of WC particles was found in the range of 1500-1600 HV. The cavitation erosion testing of the developed claddings was carried out as per ASTM-G32-92 standards at the vibratory frequency of 20 kHz and peak to peak amplitude of 60 µm for 4 hours each sample. The CER was increased about 45 times by laser cladding of Co-WC powder on SS31603. The CER of the Co-WC cladding was more than Ni-WC because of lower stacking fault energy of the Co matrix.

2.2.15 Surface Modification for CER by Laser Surface Alloying

Wu et al. (2017) [96] has studied the effect of laser surface alloying with high entropy alloys (HEA) FeCoCRAlNiTi$_X$ on cavitation erosion-corrosion resistance of SS304 substrate. The combinations of coatings were prepared by varying the molar ratio of titanium in the range 0.5 to 2. The laser surface alloying was performed at constant laser parameters (laser power = 2 kW, overlapping ratio = 50%, scanning speed = 5 mm/s and spot diameter = 3 mm). The microhardness of the prepared coatings increases with an increase in the percentage of titanium, the microhardness HEA coating was found in the range of 615-730 HV, approximately 3.6 harder than of substrate. The reason for the increase in hardness was attributed to transformation to a two-phase structure composed of FCC and BCC phase into three-phase structure compose of FCC+BCC+IC (intermetallic compounds like Ti_2Ni and NiAl). The HEA coatings showed the better cavitation then SS-304 in distilled water because of higher deformation and fracture resistance due to the presence of intermetallic (IC's). Whereas, the presence of IC's reduced the corrosion resistance of the HEA coatings because IC's act as cathodic phases and that can reduce microcell corrosion in HEA coatings. The HEA possess poor CER in 3.5% NaCl solution. The comparison of CER of all the fabricated HEA coatings

in distilled water and NaCl solution are shown in Figure 2.8. The material removal mechanism during cavitation testing was surface fatigue and then the propagation of cracks. While testing the specimen in NaCl solution, the corrosion plays an important role. The corrosion effect weekend the grain boundaries and formation of various corrosion products, further that corrosion products were quickly washed away by the cavitation impact force.

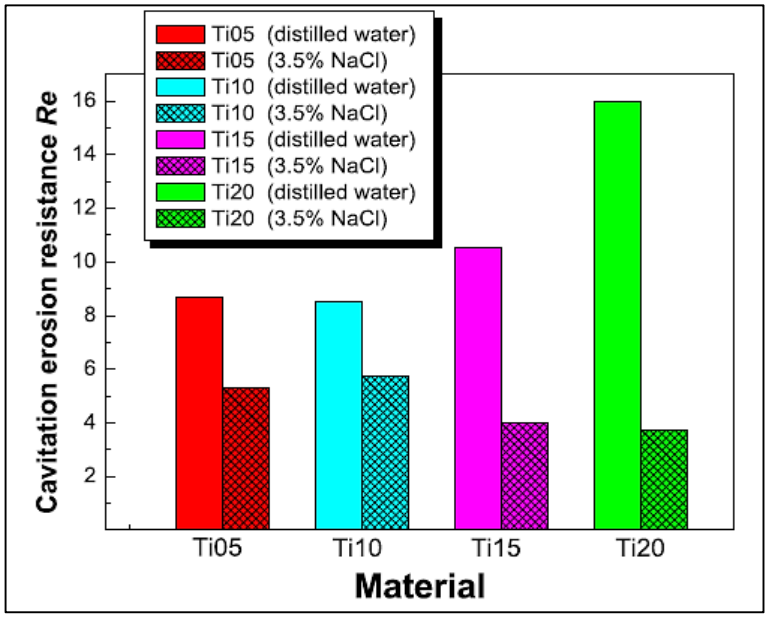

Figure 2.8: Comparison of CER of the HEA coating in distilled water and 3.5% NaCl solution

Girenet al. (2005) [97] have investigated the effect of alloying the surface of structural carbon steel and chromium steel with Mn, Ni, Cr, Nb, Co, Si, Mo, Ti and B on CER. The total of six experiments was performed by varying the composition elements mentioned above. The surface alloying process was carried out via argon laser. The experimental conditions were laser beam power of 6000 W, laser beam diameter-2.5 cm, focal length-20 cm, gas velocity-60 m/s, and sample velocity 0.5-0.8 cm/s. The thickness of the developed coatings was in the range of 0.4-0.6 mm. The refined microstructures were formed enriched with alloying elements. The microhardness of the developed coatings was in the range of 300-750 HV. The produced coating layers exhibit higher CER, but the developed microstructure of the coatings was not susceptible to plastic deformations, only confined to brittle fracture. In a few cases, the austenitic and ferrite matrix structures of the developed coatings showed superior CER

than of martensite structure. Whereas the hardness of the martensite structure is more, but higher hardness is also accompanied by higher brittleness and decline the ability to absorb energy. Hence, it was concluded that CER mainly dependent on work hardenability of material.

Lo et al. (2003) [98] have deposited fine WC powder (particle size 1µm) cladding on AISI 316 stainless steel substrate by high power Nd:YAG laser. The paste of WC powder was preplaced on the substrate. The five experiments were performed at different laser processing parameters. The laser power was varied between 1.5 to 2.10 kW and scanning speed between 20 to 35 m/s. The overlapping ratio and spot diameter were kept constant. The average thickness and microhardness of the developed claddings were 0.3 mm and 900-1200 HV. The maximum hardness of 1200 HV was achieved at laser power 1.5 kW and scanning speed 25 mm/s. However, the clads of 900 HV and 1000 HV hardness were formed at other parametric sets. The cladding developed at laser power 1.75 kW and scanning speed 20 mm/s, and having 1000 HV was reported as most favourable and that possesses 30 times higher CER than AIS 316 in 3.5% NaCl solution. The XRD spectrum of most favourable cladding reveals the presence of hard metal carbides phases and γ-FeCrNiW phases. It was concluded that higher hardness promotes the brittleness in the cladding layer and cause premature failure of cladding during cavitation. The presence of fine precipitated tungsten carbides in microstructure was attributed for excellent CER.

Cheng et al. (2001) [99] has fabricated ceramics (WC, SiC, TiC, Cr_2O_3, CrB_2, and $Cr3C_2$) reinforced coatings on UNS 31603 using a laser cladding technique. The slurry of powders was applied on the surface of the stainless steel, followed by laser heating. The Co_2 laser of 3.5 kW power was used for experimentation purpose. The laser scanning speed was varied at two levels (15 and 25 mm/s), whereas other parameters were kept constant (laser beam power- 1100 W, argon gas flow rate- 20 l/min and overlapping ratio- 50%). The average thickness of the deposited coatings was in the range of 0.1-0.2 mm. The details of metallurgical and mechanical properties of all developed coatings were summarized in Table 2.3.

Table 2.3: Mechanical and metallurgical properties of the developed coatings

S.no	Specimen Name	Microhardness (HV)	Phases	Dilution Percentage (%)
1	SS-316	200	γ-FeNiCr	-
2	WC	1800	γ-FeNiCr, WC,W_2C, $M_{23}C_6$ and M_7C_3	5
3	TiC	1600	γ-FeNiCr, $M_{23}C_6$	5
4	CrB_2	1400	γ-FeNiCr, CrB_2, CrB, and Fe_2B	20
5	SiC	800-1000	γ-FeNiCr, Fe_3Si,Cr_3C_2, $M_{23}C_6$ and M_7C_3	5
6	Cr_3C_2	900	γ-FeNiCr, Cr_3C_2, $M_{23}C_6$ and M_7C_3	5
7	Cr_2O_3	600	Cr_2O_3, $FeCr_2O_4$, and γ-FeNiCr	0

The CrB_2coatings have 9.4 times more CER than steel, highest among the all developed coatings, followed by WC (8.5 times CER), Cr_3C_2 (4.8 times CER) and SiC (2 times CER). The higher microhardness and high volume fraction was reason attributed for enhancement of CER.

2.2.16 Surface Modification for CER by Laser Surface Melting

Kwok et al. (2000) [100] has modified the surface of UNS S42000 martensitic stainless steel by melting the surface of steel with a CO_2 laser. The experiments were performed at five sets of parameters. The laser power and scanning speed were varied in the range of 1.1 to 1.7 kW and 5 to 25 mm/s respectively. The experiment carried out at laser power 1.7 kW and 25 mm/s scanning speed possess a maximum percentage of retained austenite (around 89.2%) after laser melting. Whereas, the specimen prepared at 5 mm/s scanning speed at the same laser power possess maximum hardness (600 HV). However, the maximum hardness of the specimen prepared at 25 mm/s was only 450 HV. The all the prepared specimen was tested for CER and electrochemical corrosion. The cavitation testing was performed for 4 hours on vibratory cavitation apparatus at 20 kHz vibratory frequency and 30 µm amplitude in 3.5% NaCl solution at pH 6. The specimen prepared at laser power 1.7 kW and 25 mm/s scanning speed exhibits 70 times higher CER then of UNS S42000 martensitic stainless steel. However, the significant increase in CER was observed in specimen prepared at other parameters. It was also concluded that the pitting potential of the steel increases with increase in austenite

volume fraction. Also, the volume fraction has a significant role in the enhancement of CER than hardness.

2.2.17 Post Processing or Heat Treatment Methods for CER Enhancement

Peng et al. (2018) [101] has investigated the effect of age hardening on CER of SUS630 stainless steel. The specimens were annealed at 1040°C for 30 min before age hardening at different temperatures (480°C, 550°C, 580°C and 620°C). The yield strength and hardness of SUS630 improved by 20.6% and 41.1% with age hardening at 480°C, respectively. However, with age hardening at 620°C, the yield strength and hardness was lowered by 14.7% and 2.7%, respectively. The cavitation erosion testing was carried out as per G-134 standards, on cavitation jet apparatus, specimens were kept at a standoff distance of 19 mm from a nozzle head, the inlet pressure of P_1 = 30 MPa, and outlet pressure of P_2 = 0.42 MPa was maintained so that the cavitation number of 0.014 was achieved. It was found that the CER decrease continuously as the annealing temperature increases. It was reported that CER is the function of various mechanical properties like elastic work ratio, hardness, and yield strength.

Wang et al. (2016) [102] has investigated the effect of heat treatment on developed atmospheric plasma spray (APS) coatings. The CoMoCrSi coatings was deposited on carbon steel at constant process parameters of APS (electric arc current- 620 A, electric arc current- 60 V, plasma gas flow rate (Ar) 35 Nl/min, plasma gas flow rate (H_2) 10 Nl/min, spray velocity- 300 mm/s, and standoff distance- 110 mm). The prepared sprayed coating was heat-treated at 800°C and 1000°C. The microhardness of the as-sprayed coating was 498±22 $HV_{0.3}$, whereas, after heat treatment at 800°C and 1000°C, the microhardness was increased to 685±21 $HV_{0.3}$ and 755±35 $HV_{0.3}$, respectively. After the heat treatment of developed coatings, the porosity of the coating decreased from 0.4% to 0.2%. The XRD analysis of the reveals that the peak intensity of laves phase of $CrSi_2$ increased after heat treatment. The CER of the heat-treated coating was found more than as-sprayed coatings. The surface roughness (Ra) of the coating before and after cavitation testing was 0.45 and 4.31 µm. The formation of laves phase and improved metallurgical bonding was found helpful in the enhancement of CER.

Zheng et al. (2015) [103] has explored the effect of heat treatment on cavitation-corrosion behaviour of HVOF sprayed Fe-based amorphous coatings. The HVOF

coatings were deposited at constant parameters (spraying distance-250 mm, travel velocity- 800 mm/s, feed rate- 20 g/mm, kerosene flow- 72 l/min, oxygen flow- 252 l/min and air flow-399 l/min) on austenitic stainless steel 304. The developed coatings were annealed in a tubular furnace for 1 hour at 500°C, 650°C, and 750°C. The average thickness and average hardness of the developed coatings was 450 µm and 750 HV, respectively. The microhardness of the developed coatings was significantly improved after the annealing process. The HVOF coating heat-treated at 750°C possesses a maximum hardness about 1000 HV. The XRD analysis exhibits that the amorphous phase of the developed coating was transformed into crystalline phase after heat treatment. The coatings heat-treated at 750°C and 650°C mainly contain M_7C_3, Fe_3B, and martensite, Fe_2C & $M_{23}(C,B)_6$ phase, respectively. The presence of those phase results in higher hardness. The coating heat-treated at 750°C possesses higher CER in distilled water, while deteriorate quickly in 3.5% NaCl solution. Whereas the coating heat-treated at 650°C was not recommended because of poor adhesion between coating and substrate. Also, the coatings heat-treated at 550°C, showed minimal improvement in CER.

Lin et al. (2015) [104] has investigated the effect of post-annealing on mechanical, metallurgical, and cavitation erosion behaviour of the Fe-based arc sprayed coating. The coating was deposited on a Stainless steel 1Cr18Ni9Ti substrate. The deposited coatings were annealed at 450, 550, and 650°C. The XRD analysis reveals that the amorphous phase was transformed into a fine crystalline phase, and heat treatment promoted the formation of borides and oxides phases. The SEM microstructure confirms that the porosity of the arc sprayed coating was reduced to 1% form 1.8% after post-annealing. The hardness of the deposited coatings was increased from 898±67 $HV_{0.1}$ to 1245±109 $HV_{0.1}$. The maximum hardness was reported after annealing at 650°C for 1 hour. The fracture toughness of the deposited coatings decreased with increase in annealing temperature, because of the reduction in grain size. It was found that CER of as- arc sprayed coatings was higher than heat-treated coatings, due to larger grain size and higher fracture toughness.

Kishor et al. (2015) [105] has explored the effect of thermomechanical processing (TMP) on CER of 13/4 martensitic stainless steel (MSS). The specimens were processed at 1000 & 1100°C temperature and $0.1s^{-1}$ and $0.01s^{-1}$ strain rates. The

prepared specimens were examined via SEM, XRD, and Vickers microhardness. The SEM micrographs reveal that 13/4 steel, (1100°C, $0.01s^{-1}$), and (1000°C, $0.01s^{-1}$) the average austenitic grains TMP specimens was 458 µm, 61 µm, and 21 µm, respectively. The XRD investigation reveals that the volume percentage of the ferrite phase decreased after TMP; the soft ferrite phase was converted into a hard martensitic phase. The increase of average microhardness confirms the presence of more hard phases in the processed steel. The microhardness of the 13/4 MSS, (1000°C, $0.01s^{-1}$), (1000°C, $0.1s^{-1}$), (1100°C, $0.01s^{-1}$), and (1100°C, $0.1s^{-1}$) was 300±2 HV, 400±15 HV, 433±3 HV, and 404±16 HV, respectively. The TMP specimens were tested for CER as per ASTM-G32. It was found that the CER of TMP at 1000°C, $0.1s^{-1}$ was 52% higher as compared to 13/4 MSS. The reason for higher CER was finer grain structure and higher hardness.

2.3 Statistical Analysis of Work Reported on Conventional Techniques Used

The researchers and academicians are very much concerned about the cavitation problem, and much has been carried out in the field of improving CER by surface engineering. As wear is a surface phenomenon, to utilize the hydro resources efficiently, the researchers of many countries of the world are giving attention to tackling this problem by using appropriate surface engineering method. The country China is more concerned about this problem and leads in terms of publications than any other country in the world. Almost 47.5% publications are from China, followed by India (17.5%), Germany (7.5%), Poland (7.5%), Columbia (5%), and other countries (15%) as shown in Figure 2.9 (a). The many processing techniques have been developed and used for coating/, to improve CER. The widely used technique for surface engineering, since 2000, are Thermal spraying (30%), followed by Laser cladding (25%), Post-processing technique (15%), Sputtering (12.5%), conventional welding (7.5%), Surface metallurgy (7.5%), Casting (2.5%) as shown in Figure 2.9 (b).

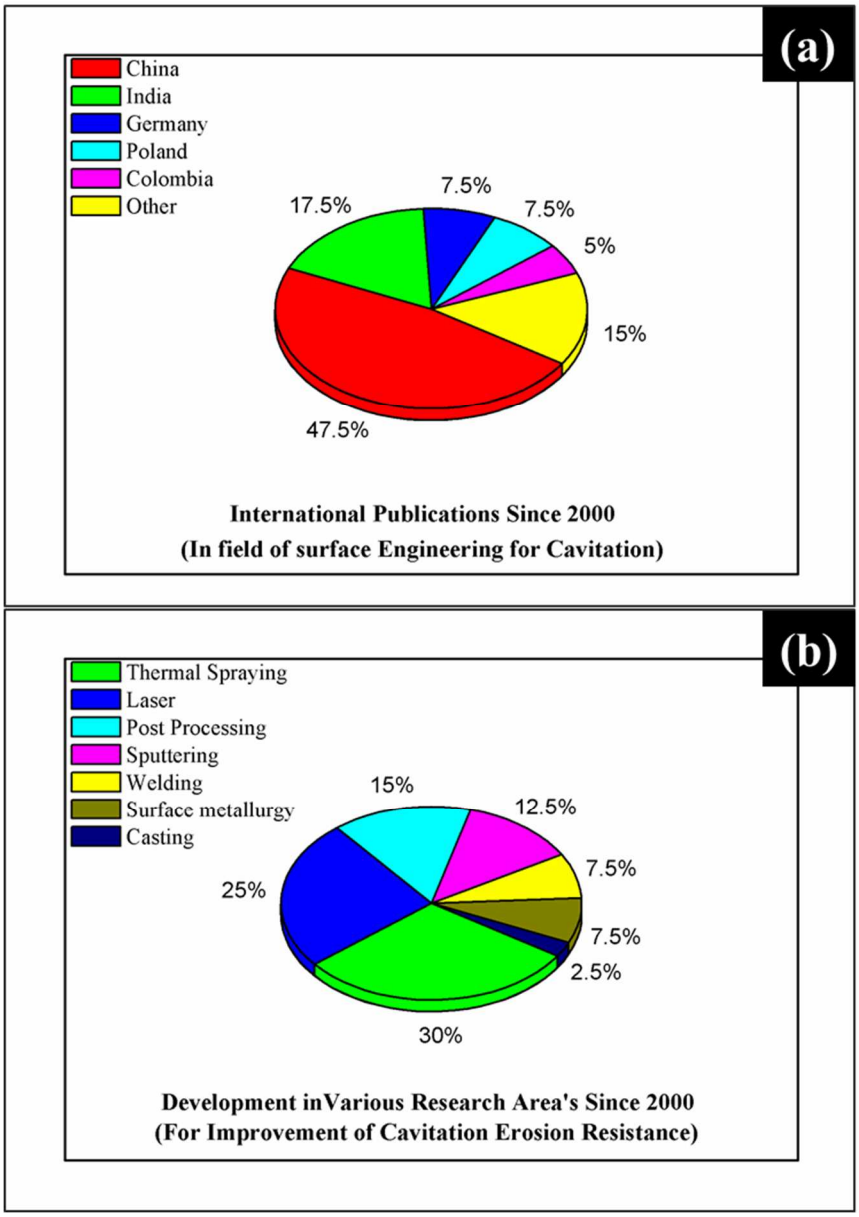

Figure 2.9: (a) Pie chart of percentage contribution of various countries in the field of cavitation resistance coatings/cladding & materials (b) Pie chart showing the percentage of research carried out by using various surface engineering techniques

2.4 Breakthrough and Development in the Field of Cladding Process through Microwave Hybrid Heating Technique

As mentioned in Chapter-1, the cladding process through microwave hybrid heating on the metallic substrate of metallic and non-metallic cladding materials is patented by Gupta and Sharma in 2010 **[48].** Many authors revealed that microwave cladding with hybrid heating has yield better properties than other processing methods. The authors

have worked on microwave cladding on different steel grade (SS-304, SS-316, and SS-420) with different metal matrix base (Ni-based and Co-based). In which many metal ceramics were reinforced like tungsten carbide, silicon carbide, alumina, and chromium carbide to enhance the hardness of the clad. Further, Investigations on so developed clads, showed, enhanced sliding wear resistance, more resistant to slurry erosion, high abrasive wear resistance and have less solid particle erosion **[106-111].** The few of the latest developments in the field of microwave claddings are discussed below:

Singh et al. (2019) **[112]** have developed Ni+ 20% Cr_7C_3 cladding of C6AMN substrate through microwave hybrid heating technique in multimode microwave of 2.45 GHz frequency and 1.1 kW power. The influence of microwave exposure time on the microstructure, fracture toughness, hardness and slurry erosion resistance was investigated. The four experiments were performed at an exposure time of 15 min (sample-1), 25 min (sample-2), 35 min (sample-3), and 45 min (sample-4). The layer of 1.2 mm thickness of mixed clad powder was preplaced on the substrate manually. The clad of average thickness 1.15 mm, 1.01 mm, 0.92 mm and 0.76 mm was achieved after an exposure time of 15 min, 25 min, 35 min and 45 min, respectively. The SEM images of microstructure reveal that proper clad formation took place after 35 min, whereas after 35 min the molten clad powder starts to move to the sides of the substrate, then the thickness of the clad layer reduces. The developed sample 4 exhibits the highest nanohardness (19.3-21 GPa) due to the presence of fine carbide particles. However, the nanohardness of sample 3 was 17-19.5 GPa. The fracture toughness of the developed clad was 11.2±0.56 and 9.8±0.49 MPa√m for sample 3 and sample 4, respectively. Sample 3 and sample 4 possess 29% and 45% higher slurry erosion resistance, respectively, in a slurry made up of silica sand. The erosion mechanism in CA6MN steel was plastic deformation. Whereas, the material loss was occurred due to ductile erosion of matrix, severe pull out of carbides, brittle fracture in sample 3. However, negligible plastic deformation was reported in case of sample 4, because of little matrix material at the top surface.

Babu et al. (2019) **[113]** has developed Ni-SiC composite claddings on SS316L through microwave hybrid heating technique. Total seven combinations of claddings were developed using different particles sizes (nano, micro and bimodal) and reinforcement weight percentage. The microstructure analysis showed that clads of the

average thickness of 600 µm was developed. The microhardness (550 $HV_{0.05}$) and fracture toughness (12.2 MPa√m) of the bimodal coating with 10% SiC (B10-5% nano-SiC & 5% micro SiC) was found highest among all other prepared coatings. The XRD analysis exhibits the presence of Ni, NiSi and SiC phases. The cavitation testing was carried as per ASTM-G32 with vibratory cavitation test apparatus at an ultrasonic frequency of 20 kHz with an amplitude of 50 µm and specimens were placed at 0.5 mm away from the tip of the ultrasonic horn. The CER of the developed claddings was compared with thermal sprayed stellite6 and WC10Co4Cr coatings and CA6NM steel. The B10 showed 5 times higher CER than SS316L. Also, the microwave synthesized claddings have outperformed the thermal sprayed stellite6 and WC10Co4Cr coatings. The surface topography of the fractured specimen was examined via SEM. The brittle mode of fracture was observed in thermal sprayed coatings. However, the mixed (ductile and brittle) mode fracture has occurred in bimodal claddings.

2.5 Statistical Analysis of Work Reported on Microwave Cladding

Microwave cladding has gained popularity in recent years; many research groups in different parts of the country (India) are exploring this cladding technique. In Figure 2.10 (a) all of the active research groups in India have been shown. Researchers in IIT-Roorkee and TIET- Patiala are exploring this novel technique much more than research groups of other organizations. Clads produced by this technique are tested for various applications as shown in Figure 2.10 (b). The tribological properties of the various metallic substrate have been investigated by developing composite clads through MHH by various authors from India as shown in Figure 2.10 (c). The used matrix materials and different reinforced materials for composite cladding through MHH by authors have been presented in Figure 2.10 (c) and Figure 2.10 (d) respectively.

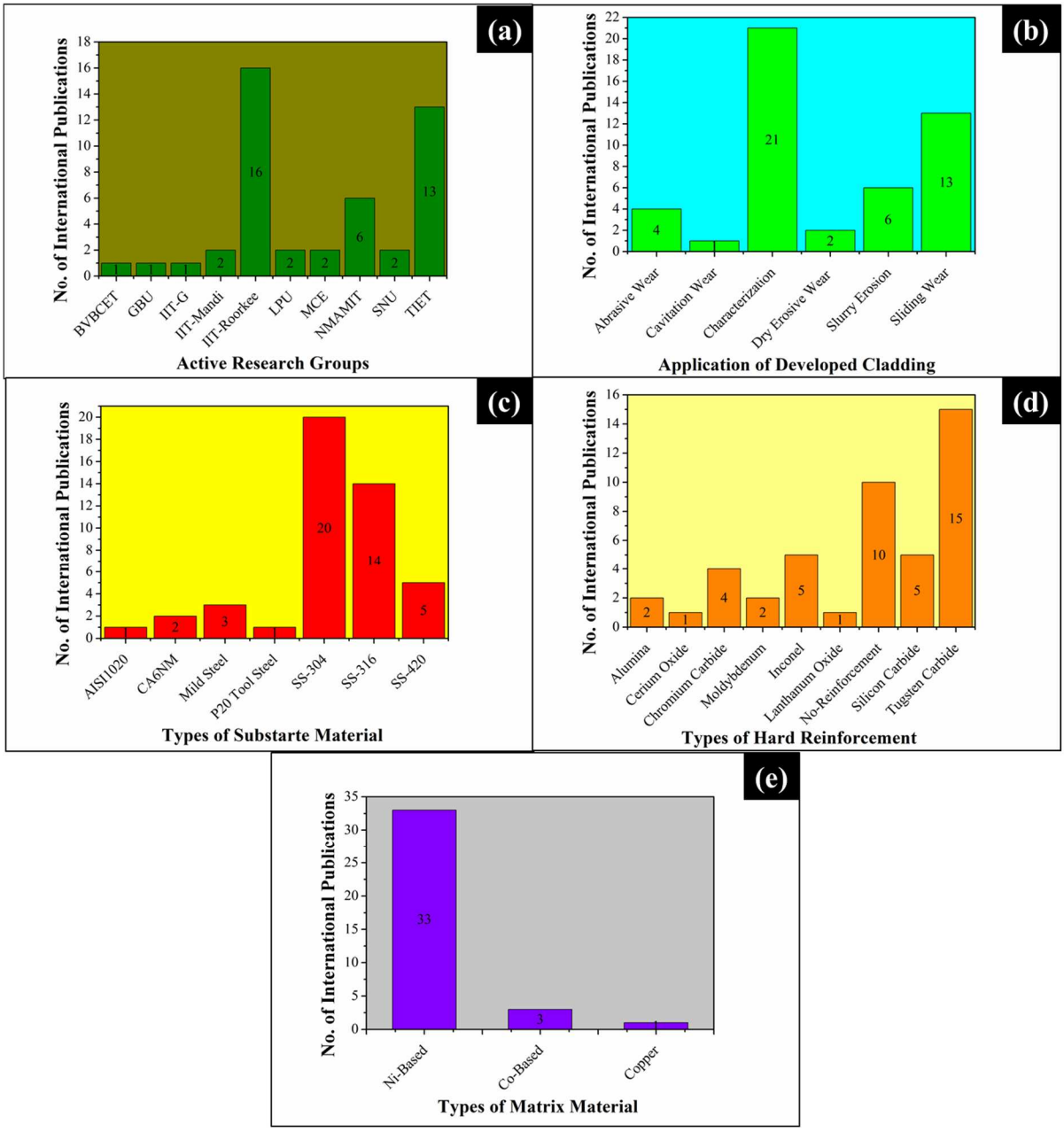

Figure 2.10: The bar chart showing (a) Active research groups exploring the microwave cladding technique; Different aspects of cladding with MHH (b) Application of claddings (c) Substrate material used (d) Hard reinforcement used (e) Matrix material used

Chapter 3

Research Gap & Problem Formulation

3.1 Introduction to Chapter

This chapter presents the literature gaps found during its survey. Based on these surveys, the research gaps were found and the formulation of the problem was developed. Further, based on problem formulation, the work plan was established to achieve the objectives of the present work.

3.2 Gaps in Literature

3.2.1 Conventional Coatings/Claddings and Microwave Cladding Technique

The extensive literature survey has been carried out on the different methods used for the development of coating/ claddings by using conventional sources of heating and microwave heating. The literature survey allowed the understanding of technologies and their mechanisms of processing with their limitations. A milestone was established in the year 1999, in the field of microwave processing of metallic materials. Since, a lot of research has been carried in multiple domains like joining of bulk metals, claddings of hard facing metallic powders on metallic substrate and sintering of powders, casting of metallic materials etc. Although, only sintering of powders process through this route has been commercialized. However, other processes are still in the investigation phase. The following research gaps are identified from the literature survey and these are as follows:

i. The thermal spray and laser cladding **[74-82]** are mainly the customary techniques preferred for surface modification of the substrate, which comes with many limitations.
ii. The researchers/academicians have developed clads/cast/sintered objects of metallic materials through hybrid heating route **[106-113]** MHH route and their tribological investigations have been carried out for sliding wear, dry erosive wear, abrasive wear and slurry erosion microwave. The literature review depicted that very less amount of work has been carried out in the field of cavitation erosion-resistant (CER) claddings through MHH.

iii. A limited amount of literature reveals parametric optimization (microwave exposure time, magnetron power and preheating temperature) of the MHH process **[112]** and monitoring of online temperature **[114]** variation during microwave processing has been reported.

iv. Modelling of the transient process (Microwaves material processing) is not focused on by the researcher **[64].**

v. The most of the real-life applications of developed cladding/coatings are focused on complicated geometries like hydropower plant components, biomedical implants and automobile components. Whereas no work has reported till date on such complicated geometries **[64]** by microwave technique.

3.2.2 Cavitation Testing Apparatus

Researchers extensively use the two methods for the cavitation erosion testing that are vibratory apparatus, and cavitation liquid jets apparatus **[115].** Whereas, the vibratory apparatus (Also known as acoustic cavitation apparatus) and cavitation liquid jet system are standardized by the American society of testing methods (ASTM) in the ASTM G-32-16 (its earlier version is known as G-32-10) and G-134-17 (its more previous version is known as G134-95), respectively **[116-117].**

In the case of materials and surface coatings/cladding comparative studies, ASTM G-32-16 is the most preferred in literature **[82,94,102],** Because the standard diameter & thickness of the sample, vibratory amplitude, specimen vibration frequency, test liquid, and its container dimensions are specified in standards documents **[116].** In this method, the sample is attached to the ultrasonic horn with the screw threads, which must be the integrated part of the sample.

However, in some hard composite coating/cladding technique, it's challenging to develop a screw thread type of specimens. So, the researcher has introduced the amendment in G-32-16 (Indirect Method). Instead of attaching the specimen with the horn, the specimen is placed opposite to the tip of the horn **[84,91,96].** Whereas it has been reported that in the direct method, bubbles cloud collapses in a hemispherical way however, during the indirect method, bubbles cloud collapses in a cylindrical way **[118-121].**

Due to more simplicity, the G-32-16 with the amendment is frequently used in the field of cavitation resistance coatings/claddings. As the researcher mentioned, cavitation is not only single phenomena, even pH level of water (corrosion) and silt content in water also responsible for enhancing the cavitation effect by making the material more prone to cavitation damage **[11].** Also, ASTM G-32-16 (Indirect Method) gives that more provision of testing the combined result of cavitation, corrosion, and silt erosion by just adding acid or base and silt particle to the test liquid **[76,103].** However, the limitation of the indirect method is that the additions of other mandatory test parameters, i.e., stand-off distance and immersion depth of specimen. Also, indirect cavitation method gaining importance recently, the pressure sensors are also being utilized by some authors to investigate the effect of different input conditions such as stand-off distance, amplitude, immersion depth of the horn inside the liquid and pulse on-off time of acoustic vibrations on pressure and impact force generated during bubbles explosion **[122].** Whereas no study was reported in the literature on the effect of a stand of distance (SOD), vibration amplitude, vibration frequency and immersion depth on cumulative mass loss & incubation time during cavitation performance of the prepared clads.

3.3 Research Objectives

Based on research gaps identified through the available literature survey, the proposed research plan was developed, and the various research objectives have been established, which are given below:

1. To develop and investigate the cavitation erosion-resistant cladding through MHH on austenitic stainless steel (SS-316) by using multimode domestic microwave oven of 2.45 GHz frequency.
2. To Characterize the so developed clads in various aspects like Metallurgical, Mechanical, Tribological and Fractographic analysis of worn material.
3. To study the effect of cavitation test parameters like the amplitude of vibration, Stand-off distance and immersion depth on cumulative mass loss and incubation time.

3.4 Proposed Plan

To achieve the proposed research objective on time, the stepwise research plan was developed. The flow chart of the anticipated plan for the research work is as shown in Figure 3.1. The work to be accomplished was divided into three phases:

Phase 1: Selection of cladding powder so as the desired properties would be successfully achieved.

Phase 2: Development of metal-ceramic composite cladding on the substrate via microwave hybrid heating technique and process parameters optimization.

Phase 3: Metallurgical, mechanical and tribological characterization of developed clads by using various toolings like SEM, OM, EDS, XRD, Vickers microhardness tester, UTM and Probe Sonicator.

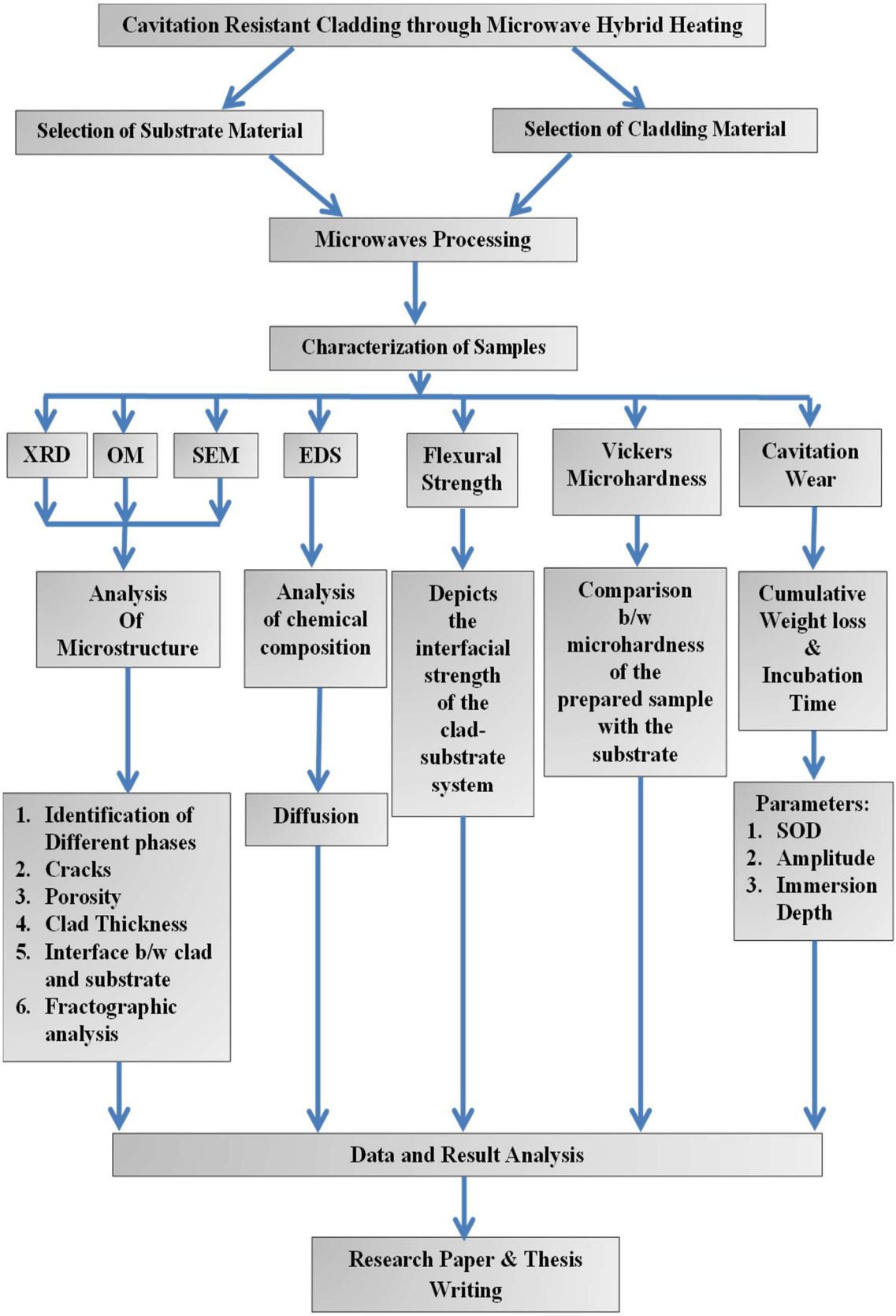

Figure 3.1: Flow chart of the work plan

Chapter 4

Materials Selection & Characterization

4.1 Introduction to Chapter

The selection of material itself is a very challenging task for tailoring the surface properties of poor CER substrate material. In this chapter, the material has been selected after considering the characteristics of the material and their behaviour with microwave radiations of low frequency. The characterization of the selected materials for current work has been presented in.

4.2 Material Selection

4.2.1 Selection of Substrate Material

The current work is mainly focused on the cavitation problem of hydropower plant components. The austenitic and martensitic stainless steel of different grades are extensively used materials in hydropower plant components **[11,14].** Hence, the austenitic stainless steel (SS-316) has been selected as a substrate material for present work. The austenitic stainless steel (SS-316) contains 2.0 to 3% Mo which can provide excellent resistance to pitting corrosion, when components of this material used in gas turbine plant and hydropower plant **[123]**. Consequently, turbine parts such as nozzles, buckets, seal rings of a Pelton turbine are fabricated or cast from these stainless steels and further, they heat-treated (hardened) to resist cavitation and sediment erosion **[6]**.

4.2.2 Selection of Cladding Material

In 1987, Bhagat et al. **[124]** reported that the cavitation incubation time increases logarithmically along with the microhardness of the material; their findings are shown in Figure 4.1. The resistance to cavitation also depends on the hardness and ductility of the materials, so that they can absorb the energy during the cavitation phenomenon. Therefore, the material must be less susceptible to cavitation damage. However, properties such as ductility and toughness generally have an adverse effect on the hardness of the material. Therefore, a combination of good ductility, high hardness and toughness could be achieved with composite materials, with a suitable choice of matrix

and reinforcing material [6]. As indicated, the composite can be more cavitation resistant if both the matrix and the hard reinforcement are selected to be:

i. Low strain-rate sensitivity (no ductile-to-brittle phase transformation).
ii. Work hardenability (low stacking fault energy) materials.
iii. Good interfacial bonding to allow subsurface micro-buckling of hard reinforcement.
iv. Moderate reinforcement volume fraction to allow larger inter particle distance.
v. Relatively large diameter reinforcement which may undergo plastic deformation without fracturing.
vi. Reinforcement normal to the surface.

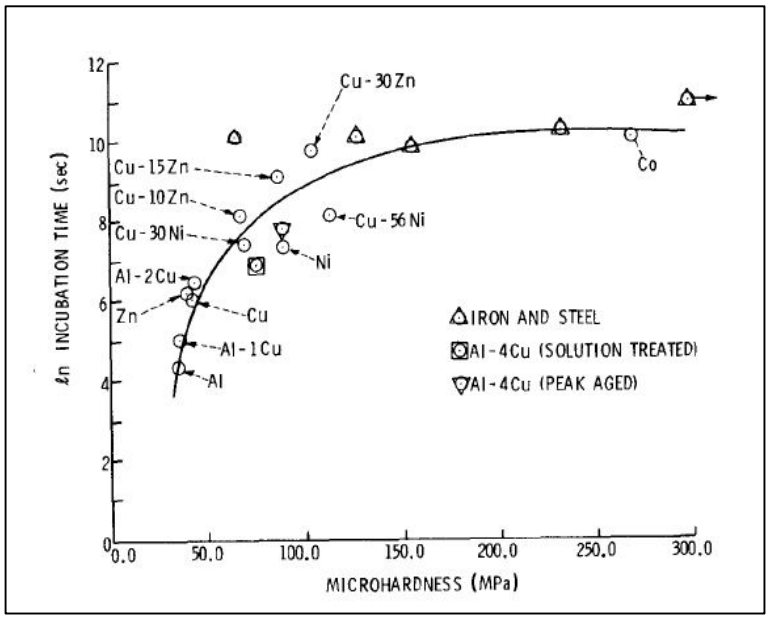

Figure 4.1: Dependence of cavitation resistance of several metals and alloy on their microhardness [124]

4.2.2.1 Selection of Matrix Material

The Fe-based alloy amorphous material is most attractive in terms matrix material for cavitation resistance due to the combination of excellent properties like good glass-forming ability (amorphous to crystalline phase transformation upon loading) [124], high hardness and relatively low material cost. However, Fe-based alloy exhibits poor corrosion resistance [103], but the Co and Ni-based alloy coatings can prove to be excellent against the corrosive environment [125]. However, Cobalt has a carcinogenic effect on humans, if it is inhaled, also have radioactive isotopes [87] and expensive as

compared to Fe-based materials. Also, if the comparison were made based on stacking fault energy, all three coating materials possess almost the same stacking fault energy **[126].** During earlier days, metals were difficult to handle with microwaves because their poor microwave absorption capacity, whereas in the current scenario, the processing of metallic material with a hybrid heating technique is not an impractical **[106].** Therefore, after analyzing the entire pro and cons a commercially available Ni-based alloy powder (EWAC-1004) was chosen as the matrix materials. Nickel and nickel-based alloys have been found to be resistive against wear, corrosion, high-temperature oxidation and they are commonly used in power generation, marine and aviation applications.

4.2.2.2 Selection of Hard Reinforcement

The function of reinforcement material is to provide better properties when added to the metal matrix. It is used to increase the hardness, toughness, and strength of the composite material. However, the refractory carbides, nitrides and borides possess required characteristics of the hard reinforcement. Also, in the area of microwave material processing some ceramics was known for its microwaves radiation absorption **[37].** Although, as per literature review the tungsten carbide (WC), silicon carbide (SiC), titanium carbide (TiC), chromium boride (CrB_2), titanium nitride (TiN), and Chromium nitride (CrN) are extensively used as hard reinforcements in development of cavitation erosion resistance claddings/coatings **[69,93,113].** Whereas chromium carbide (interstitial carbide) was utilized only in a few studies and boron carbide (covalent carbide) is yet to explore.

Since most of the ceramics materials are known for their infinite heat absorption capacity and poor thermal conductivity. However, interstitial carbides (tungsten carbide, chromium carbide and molybdenum carbide) exhibit the highest thermal conductivity **[127]** among the various types of carbides, and those properties make them suitable candidate as a hard reinforcement, for the development of metal matrix composite (MMC) cladding with MHH technique. Therefore, keeping all things mind, the commercially available Cr_3C_2 powder was chosen as one of the hard reinforcement for current work. The chromium carbide also has good corrosion and oxidation resistance up to 900°C **[127].**

In general coating/cladding and surface modification methods effectively increase resistance to cavitation erosion by suitable selection of coating materials. However, modified surface treatments or claddings/coatings may sustain a high and repeated micro jet. Sometimes the protective layer of the modified surface dissatisfied with delamination, due to the presence of negative charge micro particles in water (ultrapure, distilled or tap water) **[88].** Hence, the typical way of improving resistance to cavitation erosion means changing the inherent physical and chemical properties of the solid-liquid interface. Since the passive or oxide layer formation is very usual on the surface of the metals. The passive layer formation takes place in the presence of oxygen, and act as a barrier for ions to inhibit the diffusion of cations and anions inside the passive film, and then the substrate is protected from further corrosion. In a few studies, the formation of passive film was found useful in enchantment in CER. However, Hu et al. **[128]** reported that Inconel 625 alloy possesses higher CER than Inconel 600 alloy in tap water because of the denseness of the passive layer. However, Li et al. **[129]** have investigated the effect of passive film formation on the CER of the titanium. Also, Li et al. **[88]** in their other study reported that with the increase in molybdenum percentage in the casting of SS316L the accumulation negative charge increases in the passive layer, due to the higher electronegativity of molybdenum. Hence, during cavitation, the micro jet carrying high-velocity negative charge micro particles repels by like poles stern layer that ultimately helps in increasing CER. Molybdenum is also known for its excellent corrosion resistance, high melting point and hardness. Therefore, considering all aspects commercially available, Mo powder was chosen as other hard reinforcement for current work.

4.3 Characterization of Raw Material

Characterization of material is essential for understanding the behaviour of the material to be processed. In the present investigation, the characterizations of bulk materials were carried out using relevant techniques such as X-ray diffraction (XRD), scanning electron microscopy (SEM), optical microscope (OM), spectroscopy and energy dispersive spectroscopy (EDS).

4.3.1 Characterization of Bulk Austenitic Stainless Steel

As in received condition, the austenitic stainless steel (SS-316) was characterized to determine its purity. From the optical micrograph in Figure 4.2 (a), it is clear that procured material has a grain structure of pure austenitic stainless steel. The austenitic grains have a greyish appearance, and ferrite grains are tannish in colour. The average grain size was measured by using Micro Cam 4.0. *(Microstructure Image Analyzing Software, Make: Radical Scientific, India)* as per ISO 643 standard (Equivalent to ASTM E112-13 [130]), as shown in Figure 4.2 (b). The average grain size of the SS-316 came out to be approximately 12 µm *(Grain Size No.10).* The spectrometer (Make: Foundry Master) and microhardness tester *(Make: Meta-Tech, Dwell time: 20 s, Load: 300 g)* were utilized to evaluate the chemical composition and Vickers microhardness, respectively of SS-316. The results are presented in Table 4.1 and 4.2. Also, some other important physical and mechanical properties of SS-316 are tabulated in Table 4.2.

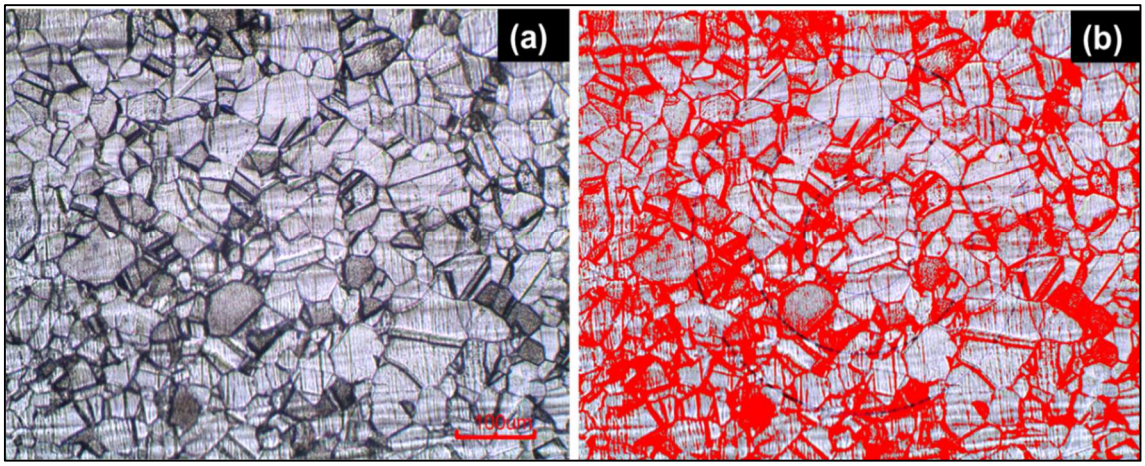

Figure 4.2: Microstructure of austenitic stainless steel (a) Optical micrograph at 100X (b) Grain size measurement of SS316 in Micro Cam 4.0.

Table 4.1: Chemical composition of SS-316 substrate

Chemical Elements									
C	**P**	**S**	**Co**	**Si**	**Mn**	**Mo**	**Ni**	**Cr**	**Fe**
0.0235	0.0510	0.0069	0.137	0.282	1.21	1.99	9.82	17.1	Bal.

The value of skin depth (D_S) for SS-316, in the temperature range of 1 K to 1800 K was calculated by using equation (1.4). The resistivity and wavelength are input variables,

the value of resistivity for concerned temperature range was collected from the literature [131], and wavelength (λ_0) of incident microwave radiation at 2.45 GHz frequency (f) was calculated by using Equation (4.1), which was came out to be 0.122 m.

$$\lambda_0 = \frac{c}{f} \text{ ---------- (4.1)}$$

Where, c is speed of light = $3.0*10^8$ m/s. From the calculated values, the temperature v/s skin depth plot has been prepared as shown in Fig. 4.3. The prepared line plot of the graph has been divided into three regions, as shown in Figure 4.3 (a). In region-1 temperature of the material is below room temperature (1-293 K), in region-2 the temperature of material is in the range of 293-1672 K and in region-3 the temperature is in the range of 1672-1727 K. From the plot, it is clear that in region-2, the skin depth of SS-316 increases exponentially with the rise in temperature. However, with the increase in temperature, the skin depth exhibits logarithmic behaviour in the region-1 and linear response in the region-3 as shown in the zoomed views in Figure 4.3 (b) & 4.3 (c), respectively.

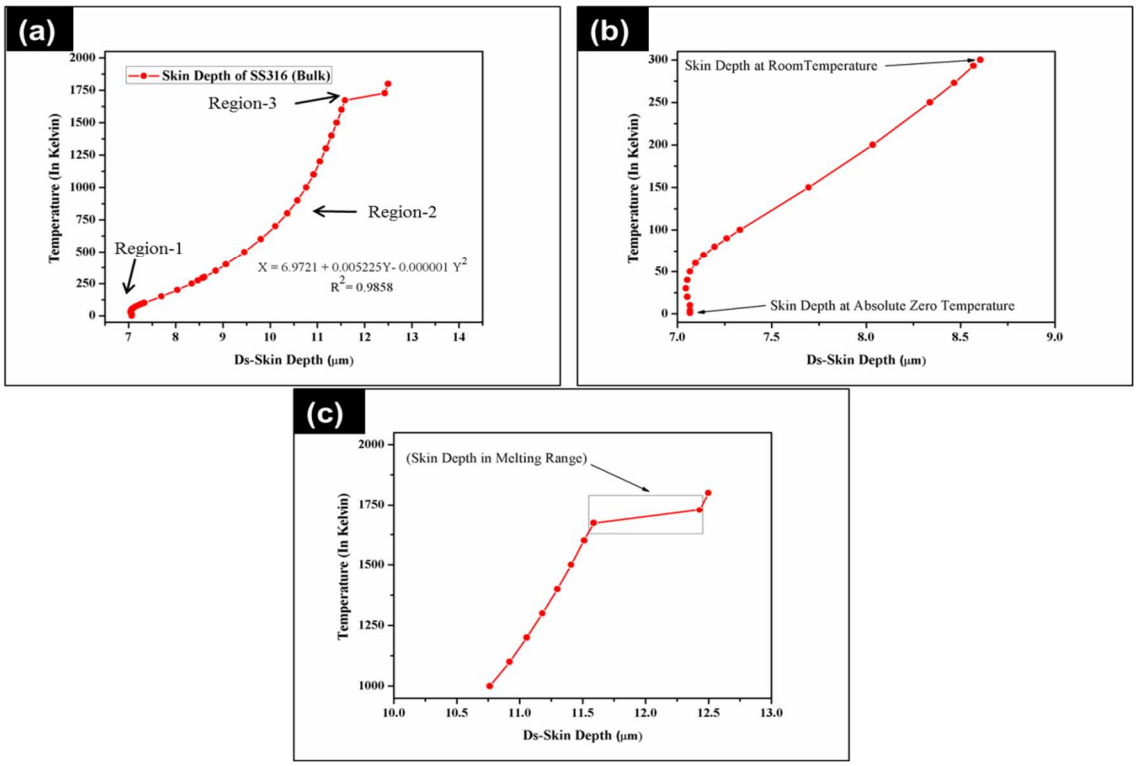

Figure 4.3: Temperature v/s skin depth plot for SS-316 showing (a) Behaviour (skin depth) of material in the temperature range of 1-1800 K (b) Enlarged view of region-1 (c) Enlarge view of region-3

4.3.2 Characterization of Ni-based EWAC Powder

A commercially available nickel-based (EWAC 1004EN) powder was procured form EWAC alloy limited *(Make: Larson & Toubro).* The received powder was characterized by using SEM, EDS and XRD to determine its purity. The typical morphology of Ni-based EWAC powder is illustrated in Figure 4.4 (a), which reveals the spherical morphology of Ni powder particles and approximately 40±10 µm particle size.

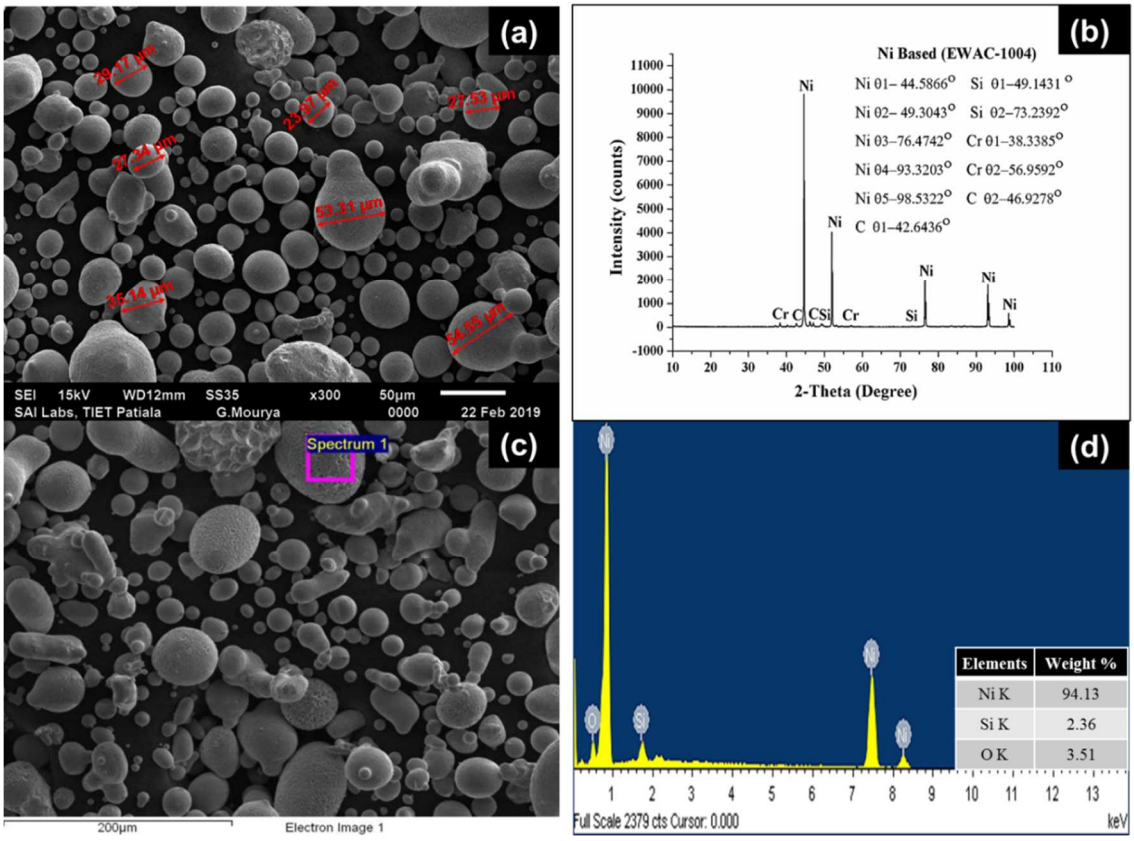

Figure 4.4: (a) SEM micrographs of EWAC powder (b) X-ray diffraction pattern of EWAC powder (c) SEM micrographs of the marked probe on EWAC powder (d) EDS of EWAC powder

Figure 4.4 (b) shows the typical X-ray diffraction spectrum of EWAC powder, which shows the presence of Ni as a dominant phase with small traces of Cr, Si and C elements. The chemical composition of raw Ni-based EWAC powder was also measured using an electron probe micro-analyzer *(Maker: JEOL 8600M)* device having 15 kV accelerating voltage, the marked probe is shown in Figure 4.4 (c), and EDS (electron dispersive spectrum) and chemical composition of EWAC powder are shown

in Figure 4.4 (d). Some other important physical and mechanical properties of EWAC powder are tabulated in Table 4.2.

As discussed in section 4.3.1 for calculation of skin depth for SS-316 material, similarly, the value of skin depth (D_S) for pure Ni-based powder, in the temperature range of 293 K to 1393 K was calculated by using Equation (1.4). The value of resistivity for different temperature range was collected from the literature **[132],** and wavelength of incident microwave radiation was kept as 0.122 m. From the calculated values of the skin depth, the temperature v/s skin depth plot has been prepared. The prepared line plot is shown in Figure 4.5. From the plot, it is clear that, the skin depth of Ni increases exponentially with the rise in temperature.

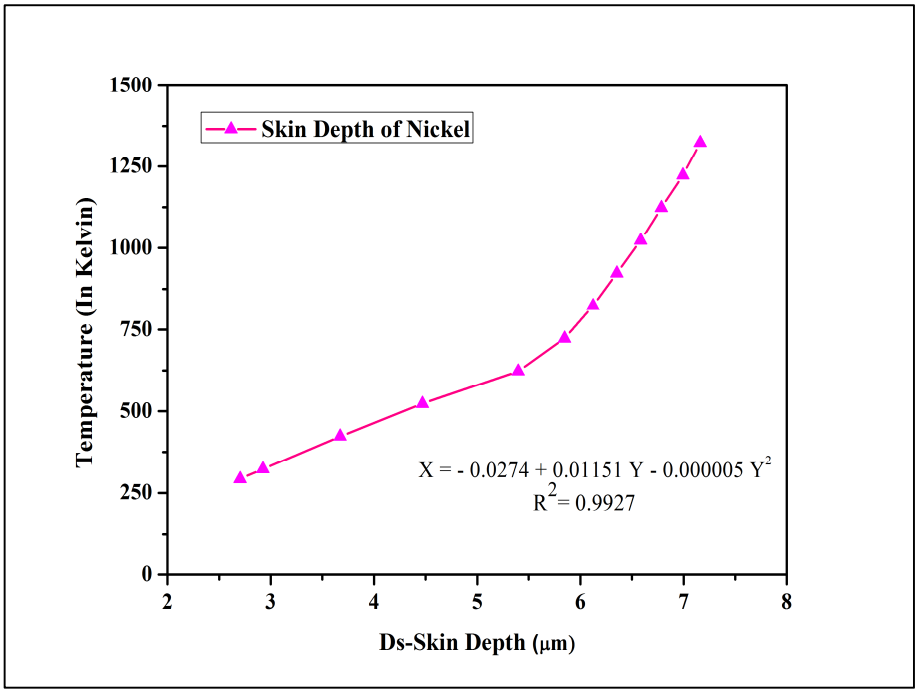

Figure 4.5: Temperature v/s skin depth plot for nickel material, showing the behaviour of skin depth in the temperature range of 293-1323 K

4.3.3 Characterization of Chromium Carbide Powder

A commercially available chromium carbide-based ceramic powder was procured from Ms. Shankar Pvt. Ltd. New Delhi. The SEM micrographs of powder have shown in Figure 4.6 (a). The powder exhibits the typical sharp edge morphology and the average particle size of 50 µm. The XRD spectrum of chromium carbide powder is as shown in Figure 4.6 (b), which reveals the presence of a dominant Cr_3C_2 phase. The chemical

composition of powder has been examined by EDS on the marked area on the particle, which is as shown in Figure 4.6 (c) and Figure 4.6 (d). Some important physical and mechanical properties of chromium carbide powder are summarized in Table 4.2.

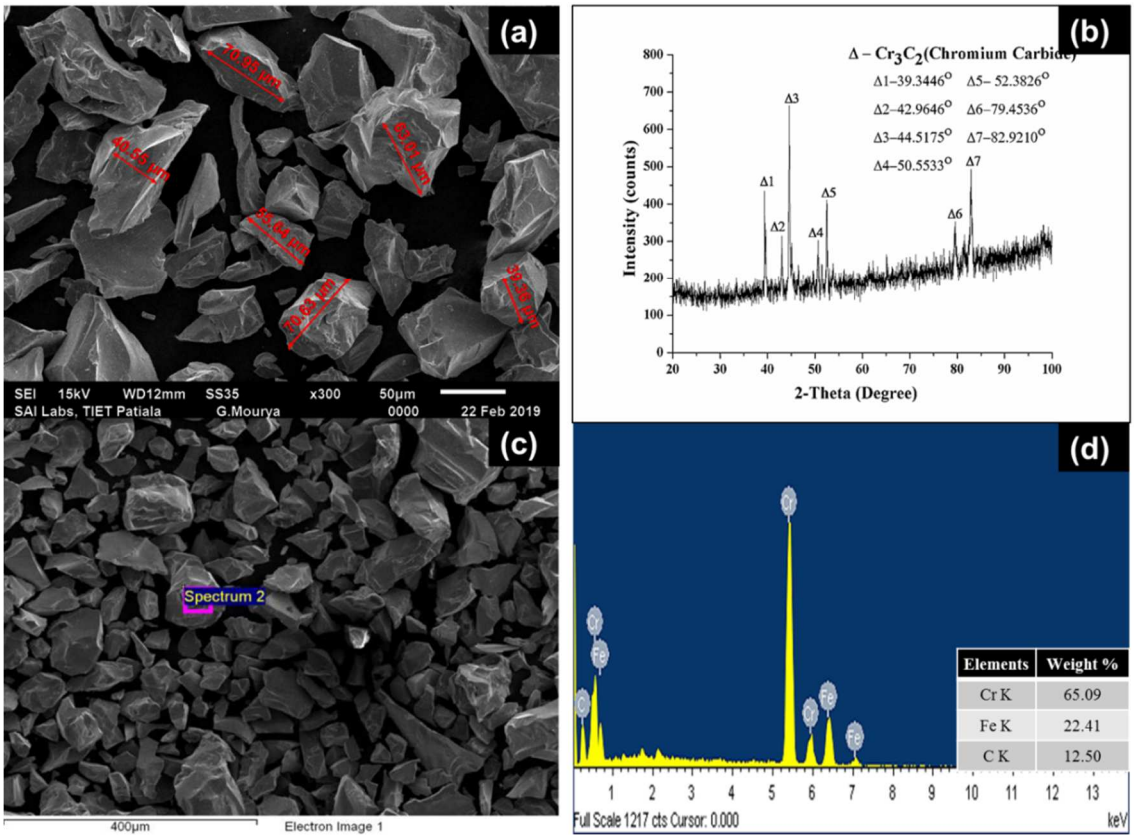

Figure 4.6: (a) SEM micrographs of Cr_3C_2 powder (b) X-ray diffraction pattern of Cr_3C_2 powder (c) SEM micrographs of marked probe on Cr_3C_2 powder (d) EDS of Cr_3C_2 powder

4.3.4 Characterization of Molybdenum Powder

A commercially available molybdenum powder was procured from Otto Kemi Pvt. Ltd. Mumbai. The SEM micrographs have shown in Figure 4.7 (a) exhibits the typical blocky rough morphology of molybdenum powder and the average particle size of 15 µm. An XRD spectrum of molybdenum powder is shown in Figure 4.7 (b), which reveals the presence of a dominant Mo phase. The chemical composition of powder has been examined by EDS on the marked area on the particle, which is as shown in Figure 4.7 (c) and Figure 4.7 (d). The few physical and mechanical properties of molybdenum powder are also tabulated in Table 4.2.

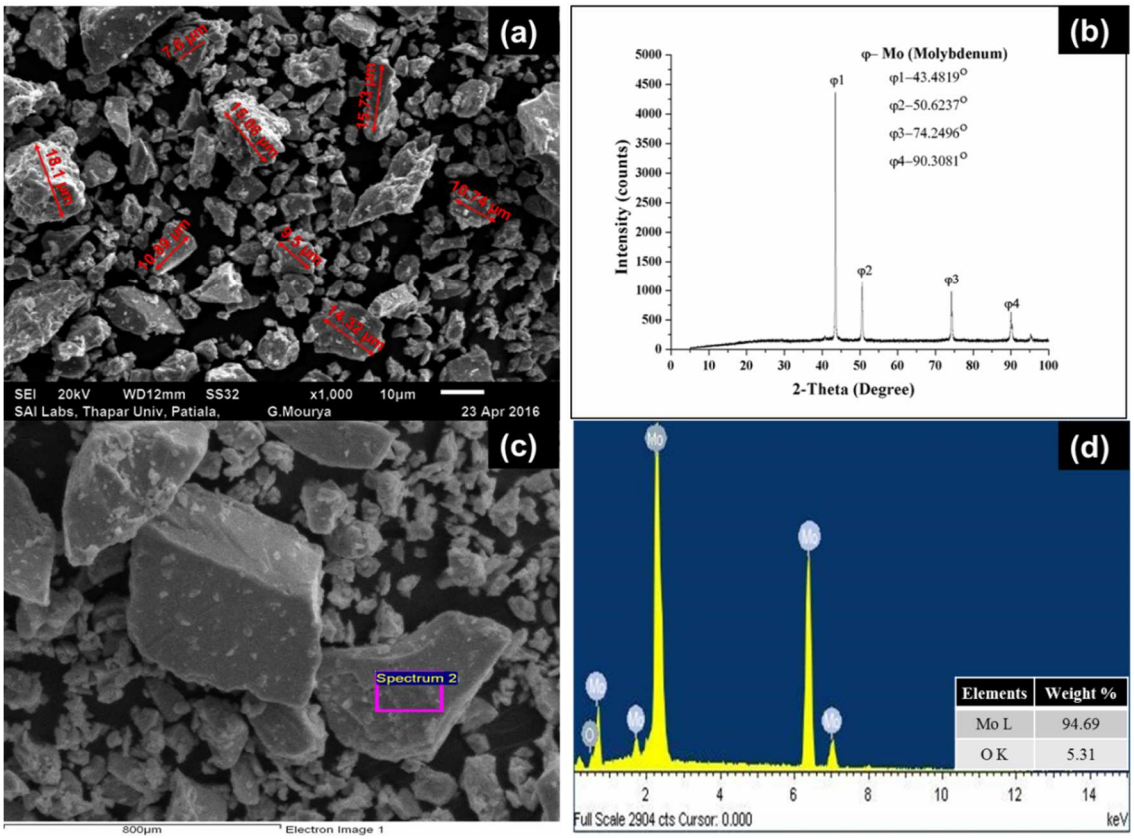

Figure 4.7: (a) SEM micrographs of Mo powder (b) X-ray diffraction pattern of Mo powder (c) SEM micrographs of the marked probe on Mo powder (d) EDS of Mo powder

As discussed in section 4.3.1 for calculation of skin depth for SS-316 material, similarly, the value of skin depth (D_S) for pure molybdenum, in the temperature range of 1 K to 2894 K was calculated by using Equation (1.4). The value of resistivity for different temperature range was collected from the literature **[133],** and wavelength of incident microwave radiation was kept as 0.122 m. From the calculated values of the skin depth, the temperature v/s skin depth plot has been prepared. The prepared line plot has been divided into three regions, as shown in Figure 4.8 (a). In region-1 temperature of the material is below room temperature (1-293 K), whereas in region-2 the temperature of material is in the range of 293-2600 K and in region-3 the temperature is in the range of 2600-2894 K. From the plot, it is clear that in region-2, the skin depth of Mo increases exponentially with the rise in temperature. However, with the increase in temperature the skin depth exhibits logarithmic behaviour in the region-1 and linear response in the region-3 as shown in the zoomed views in Figure 4.8 (b) & 4.8 (c), respectively.

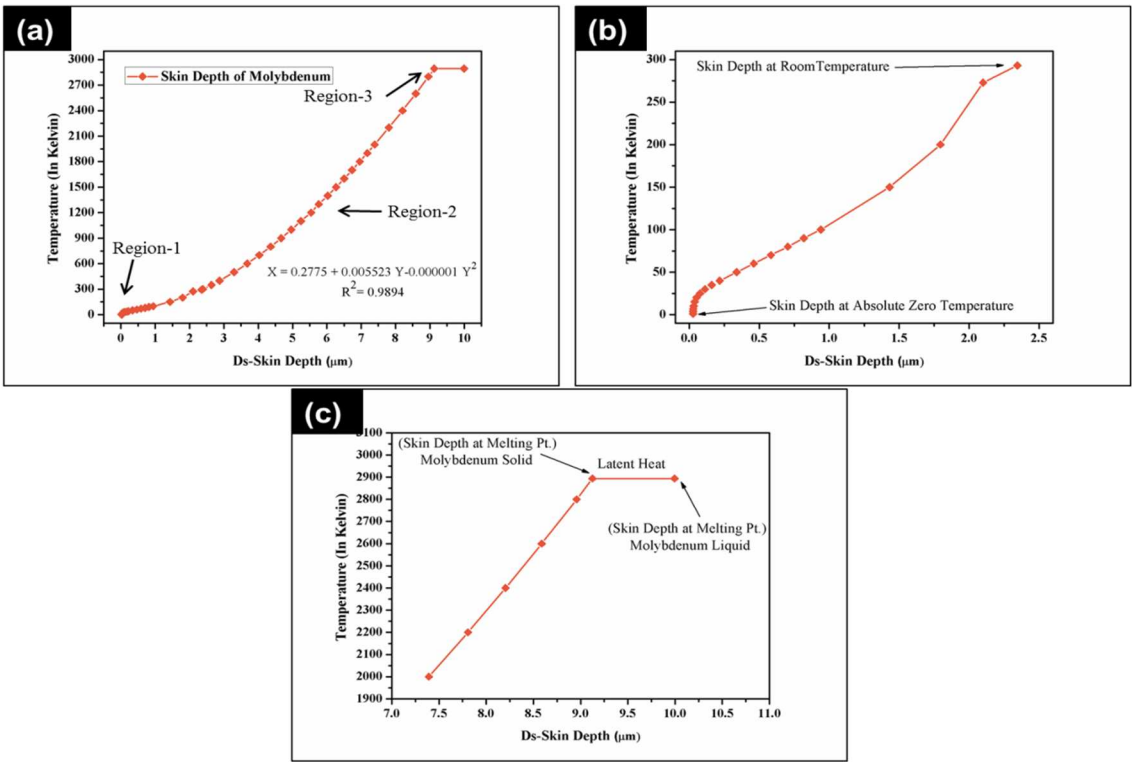

Figure 4.8: Temperature v/s skin depth plot for Mo showing (a) Behaviour (skin depth) of material in the temperature range of 1-293 K (b) Enlarged view of region-1 (c) Enlarge the view of region-3

Table 4.2: Physical properties of bulk material and raw powders

Properties	**Materials**			
	SS-316	**EWAC Powder**	**Cr_3C_2 Powder**	**Mo Powder**
Vickers Hardness (HV)	190±15	75[27]	476-1650[27]	140-280
Melting Point (°C)	1375-1400[131]	1455[135]	1810[127]	2617[137]
Thermal Conductivity (W/mK) at 293 K	13.31[131]	90[134]	19[127]	138[137]
Heat Capacity (j/kgK)	500[134]	461[134]	181[127]	277.5[137]
Destiny (kg/m^3)	7960	8910[134]	6740[127]	10220[137]
Fracture Toughness (Mpa√m)	112[136]	100[27]	5.1[27]	40[137]
Elastic Modulus (GPa)	190[136]	150[27]	15.5-24.5[27]	330[137]
Appearance	Grey	Silver With a Gold Tinge	Grey crystals	Dark Grey

Chapter 5

Experimental Procedure

5.1 Introduction to Chapter

This chapter includes a detailed of the experimental procedure followed in the current research work to achieve the proposed objectives. In the beginning of the chapter, prerequisite requires for the microwave cladding process has been discussed in detail. The initial trial has been carried to optimize the process parameters for the development of composite cladding through MHH process. The information and working principles of the equipment's or apparatus utilized for the metallurgical, mechanical and tribological characterization of the so developed clads are also discussed. In the last section, the experimental design for the cavitation erosion testing of so developed clad at varying test parameters has been explained.

5.2 Initial Preparation

Some mandatory preparation is required before performing the cladding process through microwave heating route is discussed as follows.

5.2.1 Powder Mixing and Preheating

Prior to the cladding process, the metal matrix powder and hard reinforcement powders must be mixed by using a suitable mixing process, so that, homogeneous properties **[138]** of the developed clads can be achieved and, the clad powder must be free from any moisture content, so that defect-free clads can be achieved. The presence of moisture in the clad region increases the probability of defects like porosity, hydrogen embrittlement **[139]**. So, in the present study, the mixing of the powder has been carried out via ball milling apparatus *(Model: SSI-165 Make: U-Tech)* at 80 rpm, the actual setup is shown in Figure 5.1 (a). Further, the mixed powder was placed in graphite coated crucible as shown in Figure 5.2 (b), the whole setup is preheated in a domestic microwave oven at 180°C using convection mode to avoid any possibility of the presence of any moisture content in the powder.

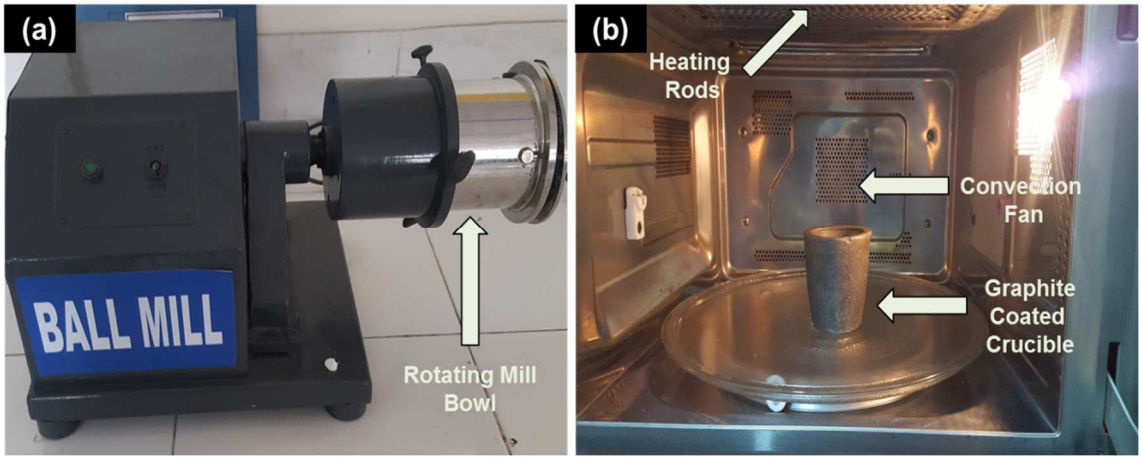

Figure 5.1 (a) Ball milling apparatus *(Photo Courtesy: FPM Lab, Chemical Engineering Department, TIET, Patiala)* (b) Graphite crucible placed in the microwave cavity *(Photo Courtesy: Surface Engineering & Tribology Research Lab, Mechanical Engineering Department, TIET, Patiala)*

5.2.2 Charcoal Grinding or Crushing

As discussed in the chapter-1, the charcoal is used as a susceptor material in microwave material processing for the hybrid heating mode. Hence, for the present study, the high-grade hard coke was crushed manually in a mortar by using pestle and wedge rammer as shown in Figure 5.3 (a), until the hard coke is completely turned into appropriate fine mesh charcoal powder. The condition or shape of hard coke before and after crushing or grinding is as shown in Figure 5.3 (b) and (c) respectively. The large particle sizes of the charcoal are not appropriate for the low frequency (2.45 GHz) microwave application. However, the skin depth of the charcoal (carbon) is greater than 35 µm at 2.45 GHz [63]. So, due to higher skin depth, the fine charcoal powder will work as very efficient susceptor in microwave material processing.

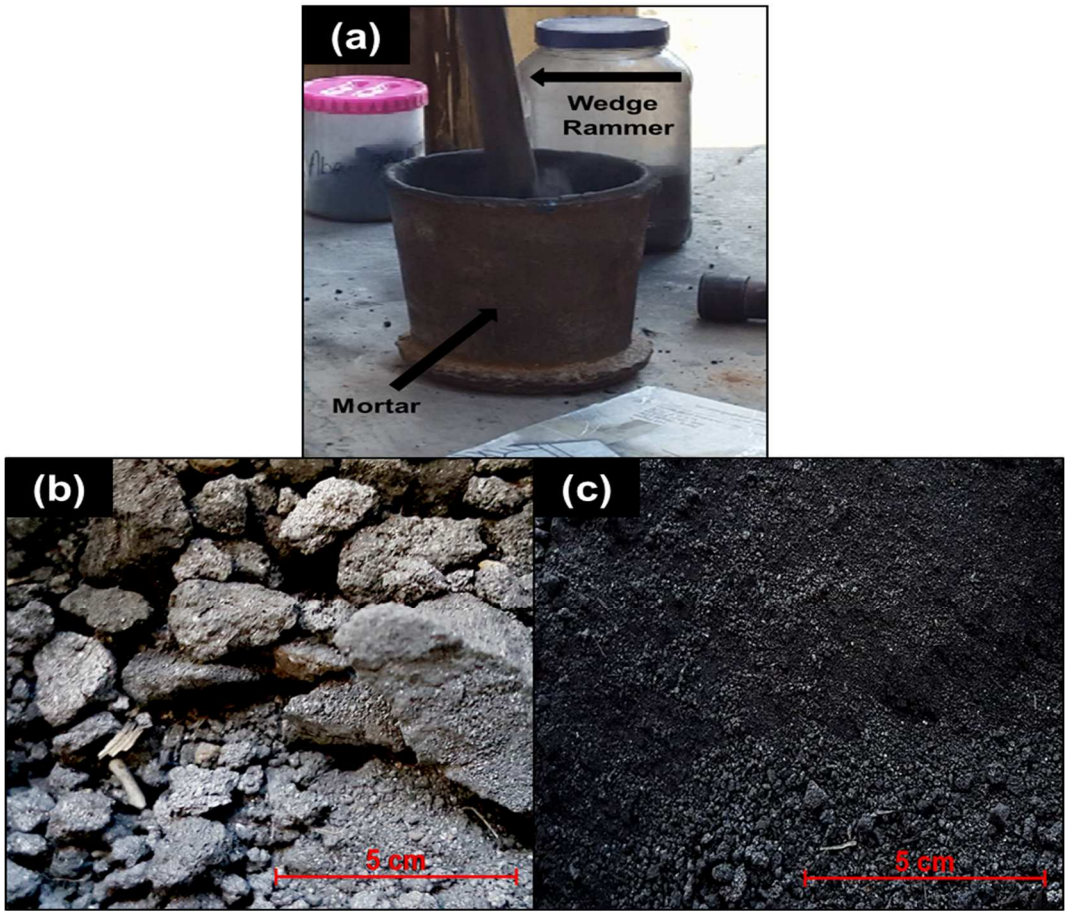

Figure 5.2: (a) The mortar and wedge rammer for hard coke grinding *(Photo Courtesy: Central Workshop, TIET, Patiala)*; The condition or shape of hard coke or charcoal (b) Before grinding (c) After grinding

5.2.3 Specimen Preparation

As received SS-316 material was in the form of 50*6 mm cross-section flat. The specimen of three different sizes (10 x 10 x 6 mm for metallurgical characterization, 15 x 15 x 6 mm for vibratory cavitation testing as per ASTM-G32-17, and 40 x 12 x 6 mm for flexural strength testing as per ASTM-C1161-13) has been prepared from the initial flat with the help of hand abrasive cutter as shown in Figure 5.3. After the abrasive cutting process, the burr has been removed from the specimen grinding. Prior to cladding, the top surface of the specimen has been grounded with the emery paper of grade 220 and 600. The purpose of the grounding is to remove the oxide layer if any. And, also to make the surface rough so that the clad layer will stick to the substrate strongly, due to the fact that roughness increases adhesion between two surfaces.

Figure 5.3: The hand abrasive cutter *(Courtesy: Machine Tool Design Lab, TIET, Patiala)*

5.3 Microwave Cladding Process and Parameters Optimization

5.3.1 Microwave Cladding Process

The microwaves of low frequency do not interact with all metals at room temperature. Therefore, processing of the metallic substrate with microwave heating is a challenging task. Hence, the microwave hybrid heating (MHH) technique was adopted for the current work. In the present study composite cladding of two different compositions of materials has been decided. The descriptions of the composition of the decided claddings are presented in Table 5.1.

Table 5.1: The description of the compositions, decided for microwave processed clads

S.No.	Description
1	60% Ni-based + 40 Cr_3C_2 (Ni-based/40Cr_3C_2)
2	60% Ni-based + 20 Cr_3C_2-20Mo (Ni-based/20Cr_3C_2-20Mo)

The cladding process of decided compositions has been carried out in a domestic microwave applicator of 2.45 GHz frequency at 900 Watt maximum available power. In the MHH technique, an appropriate susceptor is required, which can absorb microwaves irradiation at room temperature and further, transfers this heat by conduction/convection

to a mixture of metal powder. The charcoal powder has this characteristic and therefore, selected as a susceptor material in the present work.

To avoid the contamination of clad materials with charcoal powder, a thin sheet of alumina/graphite *(Make: VB Ceramics, Chennai/ S.D. Industries, Ahmedabad)* of 1mm thickness and of 99.7% purity has been used as a separator. The skin depth of pure alumina and graphite is about 12.5 cm and greater than 40 µm, respectively **[63,140]** and hence, alumina/graphite sheet is used as a separator. The schematic and actual cladding process with microwave hybrid heating is shown in Figure 5.4

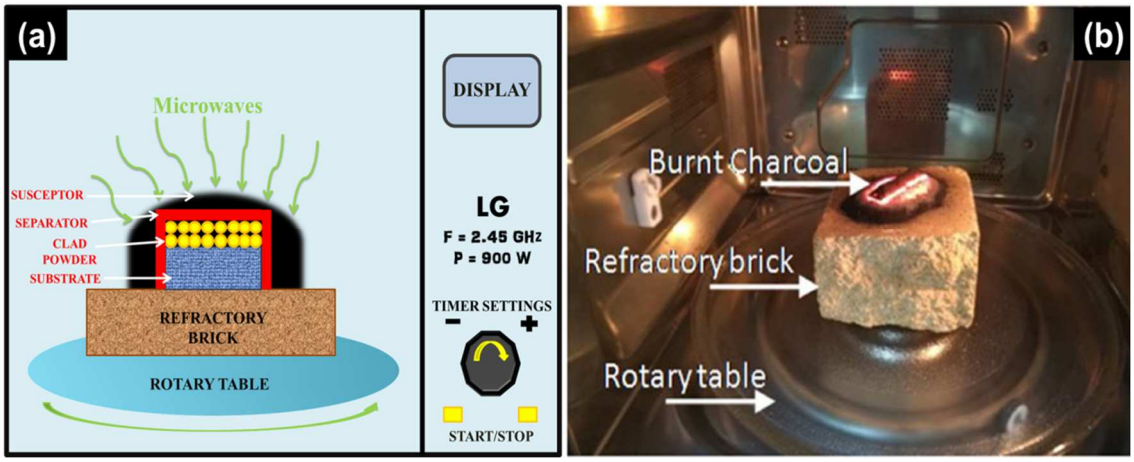

Figure 5.4: Cladding process through microwave hybrid heating (a) Schematic; (b) Actual setup *(Photo Courtesy: Surface Engineering and Tribology Research Lab, Mechanical Engineering Department, TIET, Patiala)*

5.3.2 Parameter Optimization for Cladding Process

As per literature, a number of parameters play a significant role in the successful development of the microwave processed clads as illustrated in the fishbone diagram shown Figure 5.5.

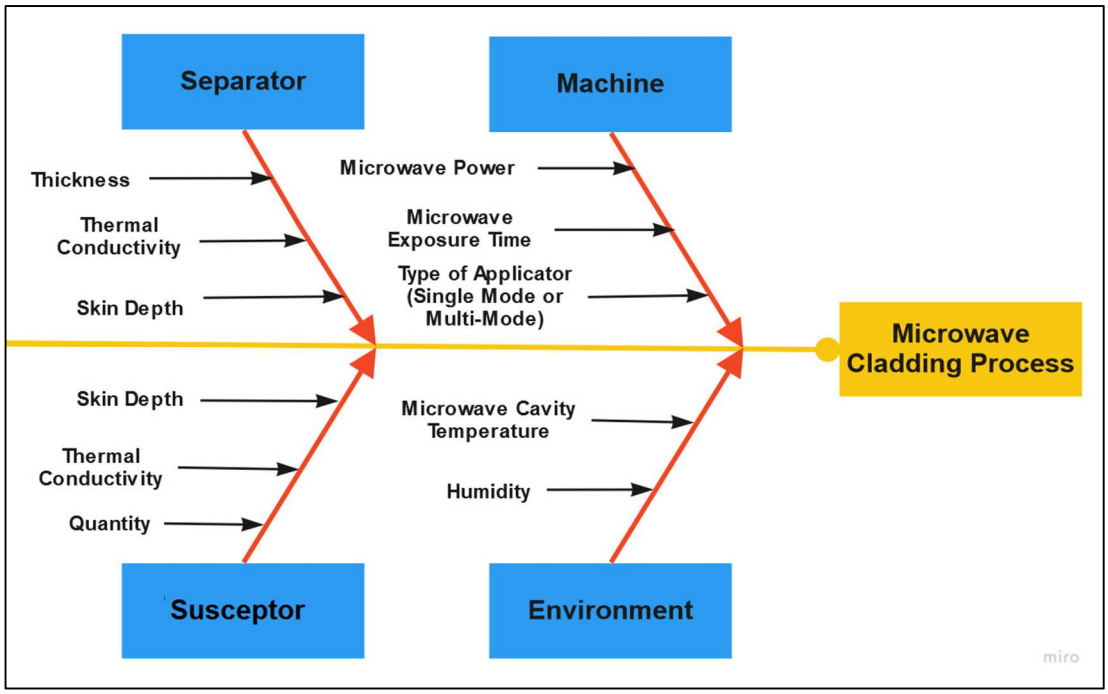

Figure 5.5: Fishbone diagram of parameter affecting microwave cladding process

For the present study, all parameters were kept constant during initial trials of cladding except microwave power and exposure time. The optimum processing time and power for microwave cladding have been decided through the number of pilot runs. It has been observed during entire exhaustive experimentation for the development of Ni-based/40Cr_3C_2 composite clad, that the minimum exposure microwave power 900 W is required to melt the powder material system and a partial amount of substrate material to cause the dilution for development of metallurgically bonded clads of these powder systems. The observations during the pilot run have been presented in Table 5.2. The charcoal (susceptor) temperature have been measured by using a portable infrared thermometer *(Model: Raynger 3i Plus Make: Raytek Corporation)* at different time intervals to get an understanding of processing time and power required to develop clads. The observation and reading recorded for Ni-based/40Cr_3C_2 composite clad during optimizing the processing time are presented in Table 5.3.

Table 5.2: Microwave processing parameters and their effect on Ni-based/40Cr_3C_2 composite cladding

Processing Time (In Seconds)	**Microwave Power (In Watt)**		
	540	**720**	**900**
120	Evaporation of moisture from charcoal	Heating of susceptor	Charcoal was red hot, heating of powder started
180	Partial heating of charcoal	Charcoal was red hot	Both powder and substrate was red hot
240	Charcoal was red hot	Heating of powder and substrate	Sintering of particles started
300	Heating of powder started	Both powder and substrate was hot	Melting of clad powder started
360	Both powder and substrate was hot	Sintering of particles started	Partially melted clad
420	Sintering of particles started, no clad formation	No melting of clad powder	Formation cladding layer with good interfacial bonding

The conclusion is drawn from the recorded temperature readings and raw material condition i.e. metallic powder present in clad completely reflect microwaves because of less skin depth of powder system used for the current work up to 120s of processing as schematically shown in Figure 5.7. However, it has been observed that clad powder and substrate was heated up from the charcoal via conventional modes of heat transfer. The charcoal reaches its maximum temperature of 837.3°C after 180s of microwaves exposure and it has been observed that coalescence between powder particles initiated and as schematically shown in Figure 5.7. This can be assuming that during 120s to 180s of exposure time of microwave radiations, the powder system attains critical temperature, where microwave radiations are get absorbed by the material system used. The charcoal powder turns into ash after 240s of microwaves exposure. Hence, the further rise in temperature of clad powder is solely possible due to absorption of microwaves irradiation. It has also observed that when clad powder starts absorbing microwaves, the sudden rise in temperature of powder owing to molecular heating and some un-melted particle is found in clad layer after 300s of microwaves exposure and the partially melted clad layer has formed in 360s. The 420s microwaves exposure the melted substrate is found due to an excessive rise in temperature and maximum dilution has been achieved. After, the successive pilot trials, the powder (Ni-based/40Cr_3C_2)

system again has been exposed to microwaves for 380s at 2.45 GHz frequency and 900 W power level to develop microwave clads. The possible microwaves material interaction versus different processing time is illustrated in Figure 5.6. The processing conditions and optimized parameters are summarized in Table 5.4.

Table 5.3: Observations and reading recorded while optimizing the processing time for Ni-based/40Cr_3C_2 composite clad

Test Run	**Exposure time (In Sec.)**	**Observations & Readings**	
		Observations	**Charcoal Avg.Temp. (In Degree Centigrade)**
1	15	Evaporation of moisture contents present in charcoal	102.3
2	30	Heating of substrate but powder remains unaffected.	250.5
3	60	Charcoal started transferring heat to substrate and substrate starts heating. Heating of powder started and charcoal became red hot.	443.7
4	120	Both powder and substrate became red hot.	721.1
5	180	Sintering of particles started	837.3
6	240	Charcoal completely turned in ash.	819.7
7	300	Melting of clad powder started.	796.4
8	360	Partially melted clad	779.7
9	380	Formation cladding layer	727.3
10	420	Complete melting of Substrate	721.1

Similarly, the extensive experimentation has been carried out for Ni-based/20Cr_3C_2-20Mo composite clad for the optimization of the processing parameters. The fully melted and metallurgically bonded clad of Ni-based/20Cr_3C_2-20Mo has been achieved in 420s at a 2.45 GHz frequency and 900 W power.

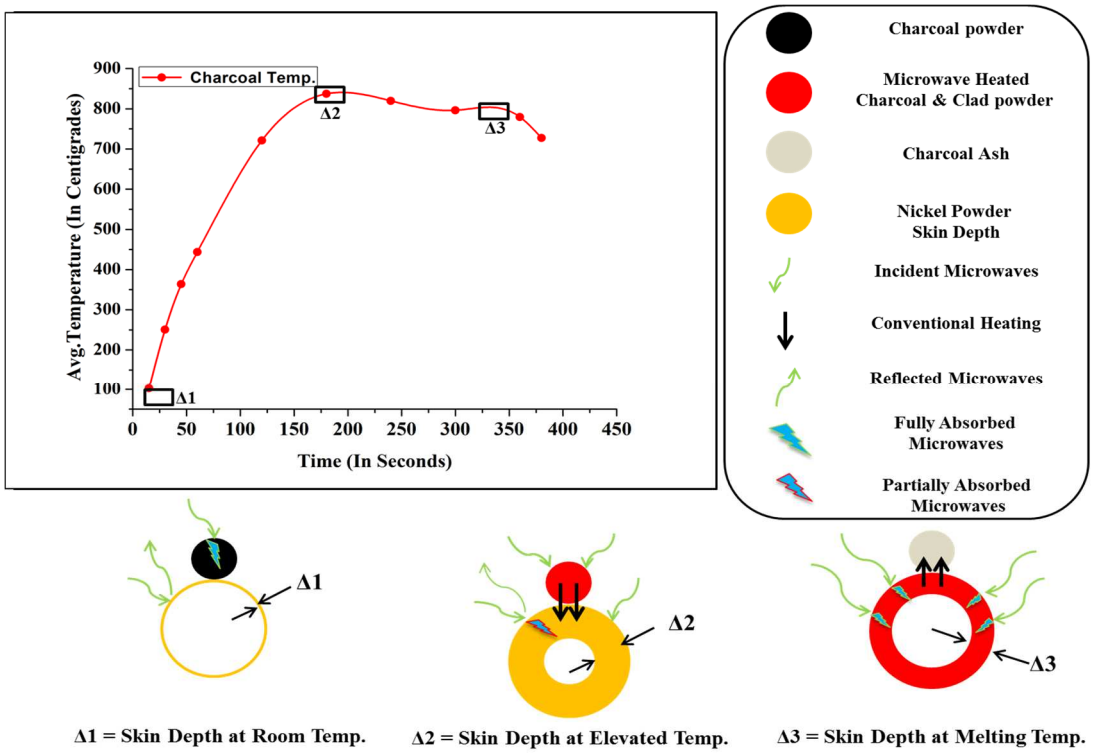

Figure 5.6: The schematic representation for possible material interaction of microwave radiation with the material at different temperatures

Table 5.4 The processing conditions and optimized process parameters used in microwave cladding process

Parameters	Description
Applicator	Multimode Domestic Microwave (Model: Charcoal, Make: LG)
Cladding Material	Ni-based/40Cr_3C_2 Ni-based/20Cr_3C_2-20Mo
Substrate Material	SS-316
Substrate Dimensions	10*10*6 mm
Exposure Power	900 Watt
Exposure Time	380seconds, 420Seconds
Frequency	2.45 GHz
Susceptor	Fine Charcoal Powder
Separator	Alumina substrate/ Graphite Sheet 1mm Thickness
Powder Preheating Temperature	180°C
Ambient Temperature	22°C

5.4 Clad Characterization

5.4.1 Low-Speed Saw Cutting

The developed clad specimens are sectioned along with the thickness with help of low speed saw cutter *(Model: MS-10 Make: Ducom)* as shown in Figure 5.7, which is also known as a diamond cutter. The diamond wafering blade is used for cutting of various hard materials. The very high quality (higher surface finish) cut with minimal deformation can be achieved, without much surface damage of the specimen. The same specimen will be utilized after polishing for scanning electron microscopy (SEM), optical microscopy (OM), and microhardness investigation.

Figure 5.7: Low speed saw unit *(Photo Courtesy: Surface Engineering and Tribology Research Lab, Mechanical Engineering Department, TIET, Patiala)*

5.4.2 Polishing Process

After cutting the samples transversally, they were grounded with the help of emery papers of grit size 100, 220, 600, and 800, respectively. The samples were polished to remove any type of contamination present on the surface of the cladding. The samples were then polished on a disc polisher, which consists of two rotating wheels are shown in Figure 5.9.

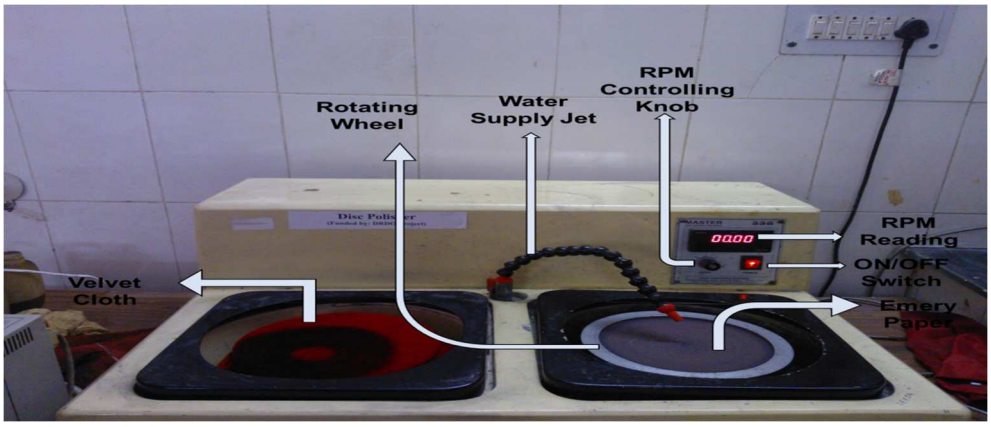

Figure 5.8 Disc polisher *(Photo Courtesy: Machine Tool Design Lab, Mechanical Engineering Department, TIET, Patiala)*

The first wheel was mounted with emery paper of fine grades starting from 1000 to 2000, and 3000 were used in series and second wheel was covered with soft velvet cloth over which diamond paste of particle size 1 µm was spread uniformly to get mirror-like surface without any scratches, so that microstructure of the sample can be examined easily via SEM. The diamond lapping compound was also sprayed on velvet cloth to hold diamond polishing paste on the cloth.

5.5 Microstructural Characterization

5.5.1 Scanning Electron Microscopy

After polishing process, the specimens were further examined for microstructure and chemical composition via scanning electron microscope (SEM) *(Model: JEOL JSM 650LV, Make: Oxford Instruments)* and energy-dispersive x-ray spectroscopy (EDS), respectively, the actual setup is shown in Figure 5.9 (a). The SEM produces images of a sample by scanning the surface of the sample with help of focused beam of high energy electrons. It is a type of electron microscope in which the electrons interact with atoms to reveal information about the sample regarding surface topography, morphology and crystallographic information at very high magnifications, in the range of 5-300000X. The SEM equipped with EDS is useful in finding the chemical composition of the sample. In the present study, the top surface and transverse section of prepared clad was characterized via backscatter electron (BSE) detector at 20 kV voltage. However, the procured powders or materials and clad specimen after cavitation testing were characterized by secondary electron imaging (SEI) at 20 kV voltage.

5.5.2 Optical Microscopy

The optical microscope, it is also known as the light microscope. The optical microscope uses visible light and a number of high magnification lenses to magnify the image of small samples. The optical microscope *(Model: RMM-8T Make: Radical Scientific Equipment)* with digital camera and image analyzing software Micro Cam 4.1 was used in the current study for the investigation of porosity and the indentation geometry on the developed clads after the microhardness testing. The installed microscope has the capability of taking images at four magnifications i.e. 40X, 100X, 400X and 1000X. The actual setup of the optical microscope is shown in Figure 5.9 (b)

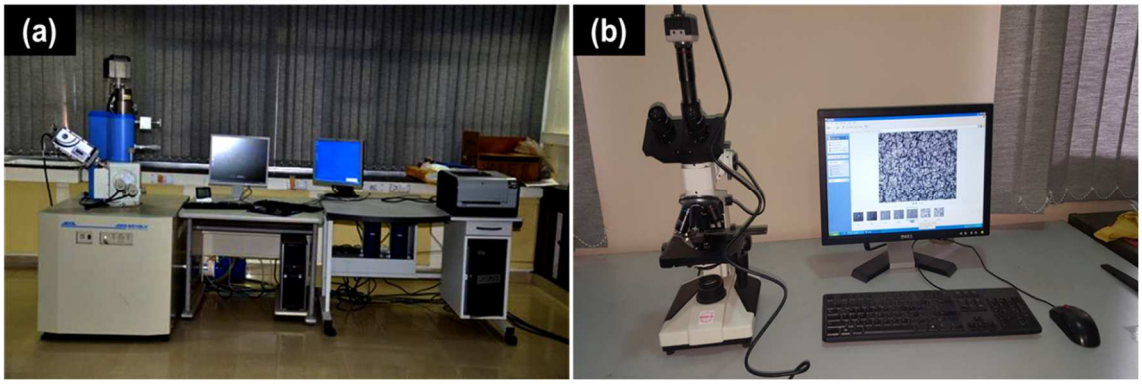

Figure 5.9: The actual setup of (a) Scanning electron microscopy *(Photo Courtesy: SAI Labs, TIET, Patiala)* (b) Trinocular optical microscope with a digital camera *(Photo Courtesy: Surface Engineering and Tribology Research Lab, Mechanical Engineering Department, TIET, Patiala)*

5.5.3 X-ray Diffraction

X-ray diffraction (XRD) is a non-destructive analytical technique designed to give detailed information about crystalline compounds, including detection and quantification of crystalline phases. It is the simplest and most economical technique available at the time. The X-rays are generated through cathode ray tube and they are directed towards the sample. When the incident rays interact with the sample, diffracted rays are produced, satisfying the condition of Bragg's Law ($n\lambda=2d\sin\theta$). These diffracted rays are then detected, processed and counted to get an XRD pattern. All the measurements were carried out at room temperature in the diffractometer using Cu-Kα radiations. The actual setup of the XRD machine *(Model: SmartLab 9 kW,*

Make: Rigaku Corporation), which was used in current work, is shown in Figure 5.10. The scan rate for XRD was set at 1° min-1 in the scan range of 10° to 100°. The raw data generated from the system was analyzed in Xpert high score software version 2.2, the JCPDS database available were used to identify the phases.

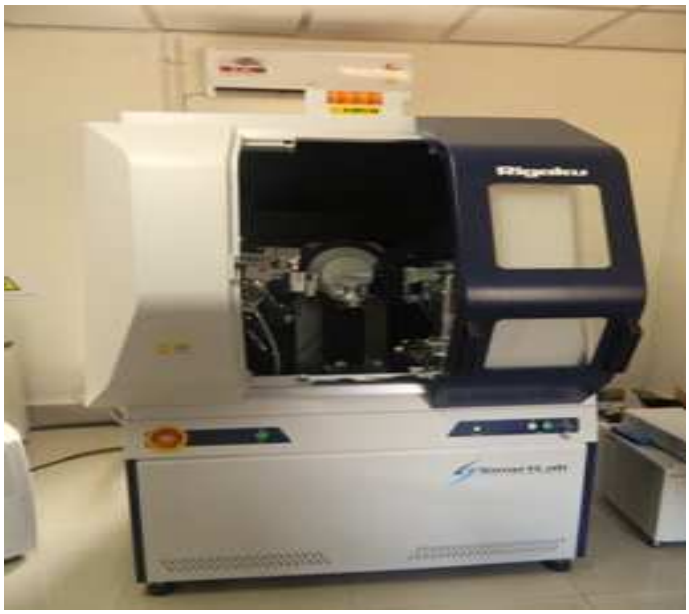

Figure 5.10 The actual setup of X-ray diffraction machine *(Photo Courtesy: AMRC, Indian Institute of Technology, Mandi)*

5.6 Mechanical Characterization

5.6.1 Micro-hardness Measurement

Microhardness investigation helps in establishing the structural properties correlation. Microhardness of the developed clad is monitored along its cross-section by using Vickers microhardness tester *(Make: MetaTech, Load Range: 5 g to 1 kg*), as shown in Figure 5.11 (a). The microhardness of prepared clads are measured by using 300 g normal load and 20s dwell time. The measurements are made at a distance of 50 µm starting from the clad top surface. Three measurements (100 µm left and 100 µm right) for each indentation have been taken for the measurement. Due to small specimen size, it was fitted into the fixture as shown in Figure 5.11 (b), while microhardness measurement, so that specimen doesn't topple during indentation loading or unloading.

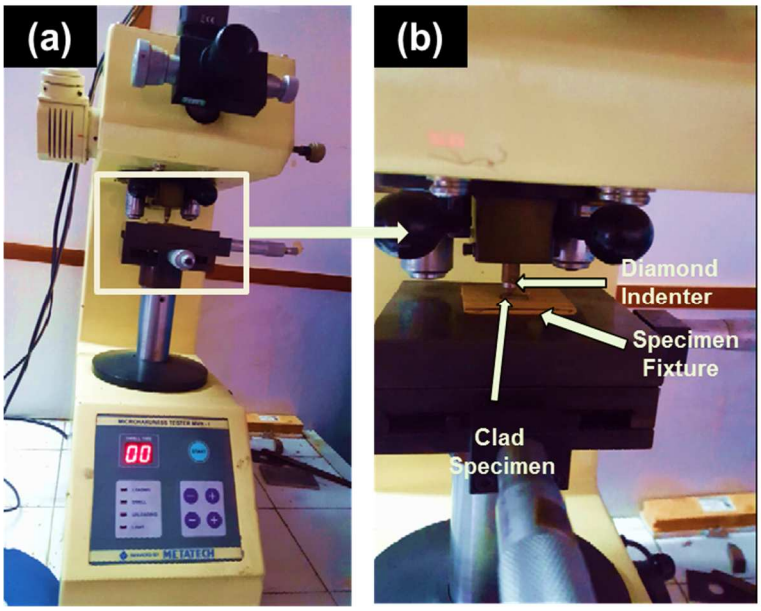

Figure 5.11: The actual setup of (a) Microhardness tester (b) Specimen fixture assembly for microhardness measurement *(Photo Courtesy: Advance Measurement Lab, Mechanical Engineering Department, TIET, Patiala)*

5.6.2 Flexural Strength Test or Three-Point Bend Test

The flexural performance of the developed clads was evaluated as per ASTM C1161-13 [141] using the universal testing machine *(Model: Z010, Make: Zwick/Roell)* as shown in Figure 5.12 (a). A three-point bend test setup as shown in Figure 5.12 (b) was employed on the UTM machine to evaluate the interfacial strength or peel of strength of the specimen. The flexural strength of the specimen significantly affects the structural, mechanical and wear performance of the coatings/claddings on metallic substrates. The size of the specimen to be tested was kept as 40 mm x 12 mm x 6 mm. During testing the specimen acts like a simply supported beam, 5.12 (c). The three-point bend test was carried out at a deformation rate of 0.5 mm per min. The flexural strength (F_s) of the samples has been calculated using Equation 5.1.

$$F_s=\frac{3\times P\times L}{2\times w\times t^2} \text{ ----------(5.1)}$$

Where; P=maximum load in Newton;

L = span length in mm;

w = width of the specimen in mm;

t =thickness of the specimen in mm.

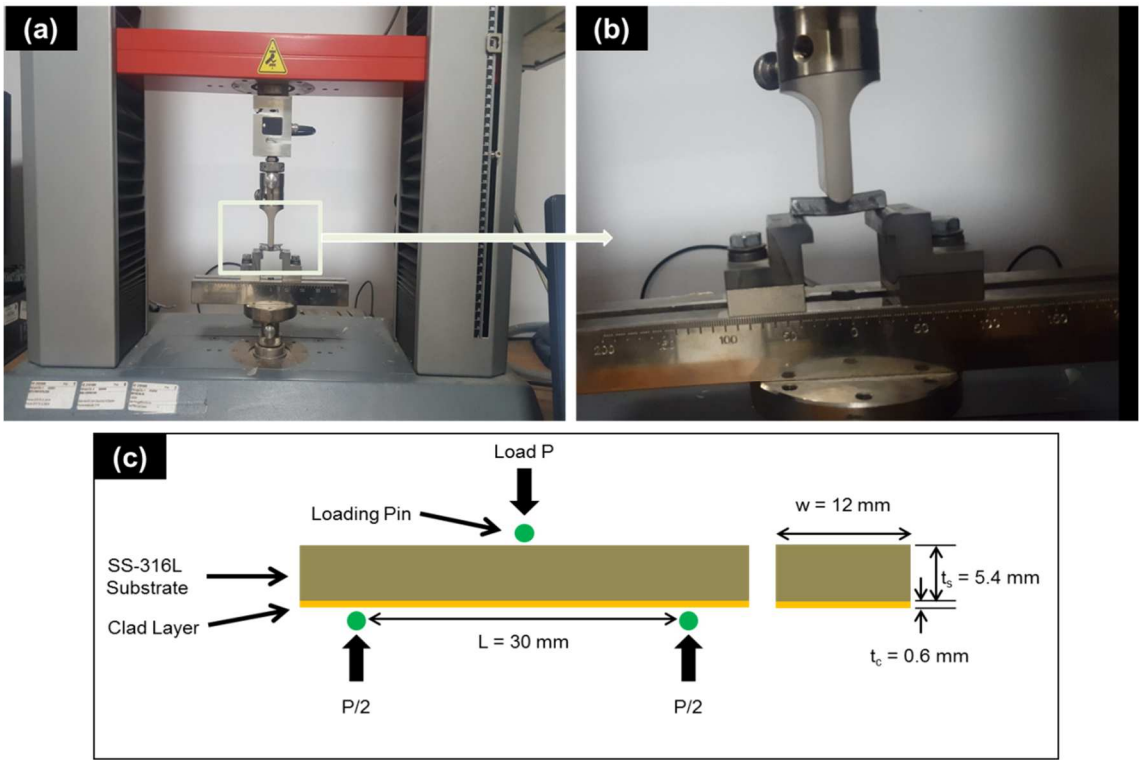

Figure 5.12: The actual setup of (a) UTM (Universal Testing Machine) (b) Fixture assembly for three points bend test *(Photo Courtesy: PDC Lab, Chemical Engineering Department, TIET, Patiala);* (c) The schematic of three points bend test

5.7 Tribological Characterization

5.7.1 Vibratory Cavitation Erosion Testing

The cavitation erosion testing of the developed clads has been carried as per modified ASTM-G32-16 method, which is also known as the indirect cavitation testing method. In this method, the clads specimen is placed opposite to the tip of the horn and stream of the bubble is ejected towards the surface of the clad and when it explodes, it generates impact force on the surface of the material and causes stress generation as well as material removal. The square samples of area 15 mm x 15 mm & thickness 6 mm (if coated thickness around 7-7.5 mm) were used as specimens for the cavitation erosion testing. The samples were polished up to 0.2 µm R_q (mean square roughness) value, as mentioned in the ASTM G-32-16 the R_q value of the surface before testing must be less than 0.8 µm. The same polishing procedure was followed, as mentioned in section 5.4.2. After polishing, specimens are tested using probe Sonicator *(Model: Samkoon, Make: Kamtronics Technology Pvt. Ltd.)* as shown in Figure 5.13 for indirect acoustic

cavitation. The schematic of the indirect vibratory cavitation method is shown in Figure 5.14. The specifications of the apparatus utilized for cavitation erosion testing are tabulated in Table 5.5.

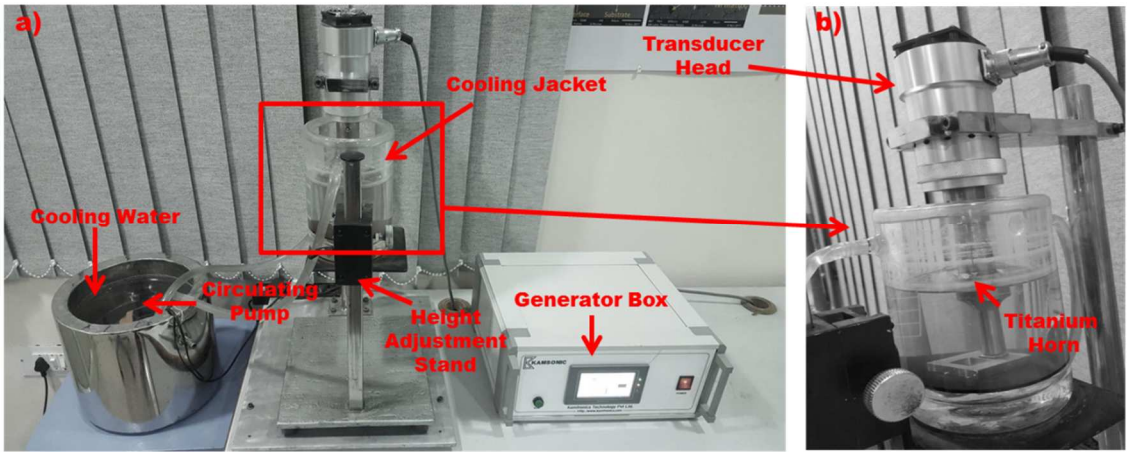

Figure 5.13 The actual setup of (a) Cavitation probe sonicator (b) Titanium Horn and transducer head assembly *(Photo Courtesy: Surface Engineering and Tribology Research Lab, Mechanical Engineering Department, TIET, Patiala)*

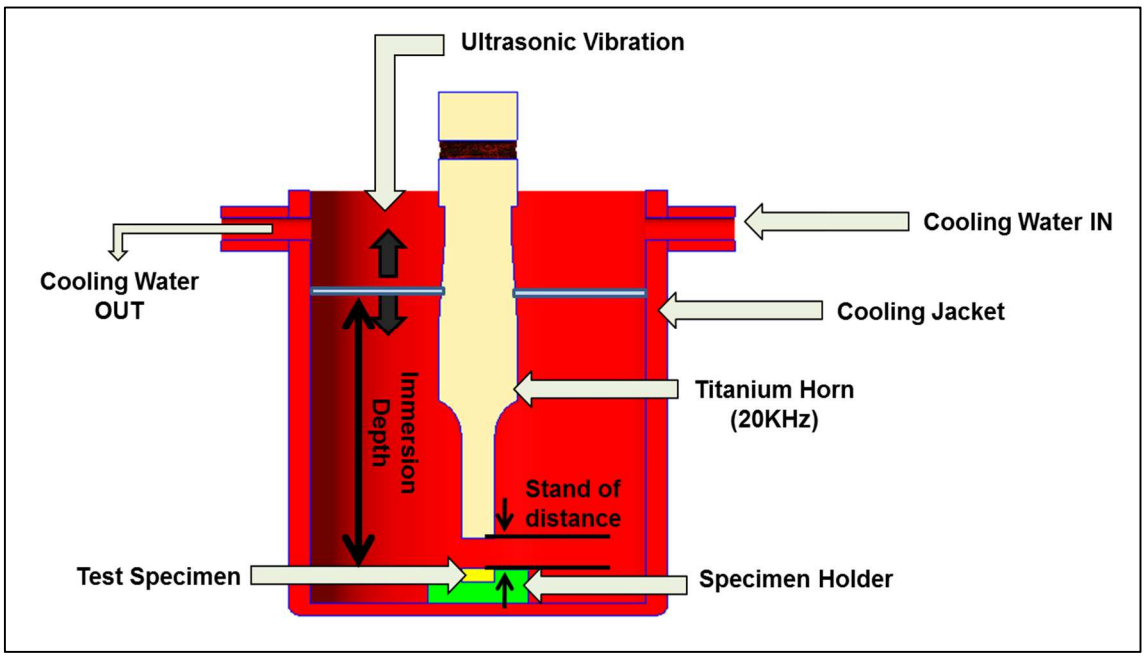

Figure 5.14: The schematic of indirect acoustic/vibratory cavitation apparatus

Table 5.5 The specification of the probe sonicator

Parameters	Description
Test setup	Acoustic/Vibratory Cavitation System (ASTM-G32-16)
Maximum Power	200 W
Frequency	20±0.1 kHz
Horn Material	Titanium
Horn Diameter	15 mm
Amplitude Range	35 to 70 µm
Water Temperature	25±5°C

The cavitation Testing for each specimen has been carried out for 6 hours and mass loss in the specimens due to cavitation erosion has been measured after every fixed interval of time using the weighing balance of least count 0.1 mg *(Model: CAS220, Make: CAS global).*

5.7.2 Experimental Design to Study the Effect of Cavitation Test Parameter on Cumulative Mass loss and Incubation Time

With the efficient design of experiments, we can obtain the maximum information from experimentation by with least effort which gives us the valid conclusion for our research purpose. In a crude way, we can say that the design of experiment methods is utilized for minimizing the count of experiments to attain the optimal conclusion. It also provides us with the connection between the response, which is our dependent variable and the several parameters (which is independent variables) levels. It also gives us a chance to examine the individual impacts of each factor as well as their interactions. In the current study, the three independent parameters were selected for cavitation erosion testing, all three parameters (Stand of distance, Amplitude and Immersion depth) was varied at three levels each. Therefore, the Taguchi L9 orthogonal array has been selected for the experimentation purpose. Table 5.6 shows the parameters variation for cavitation erosion testing. Whereas the complete experimental plan (L9 orthogonal array) for cavitation erosion testing was generated by using Minitab 17.0 is presented in Table 5.7. Total 27 experiments have been carried out in the current study, 9 each for SS-316, Ni-based/40Cr_3C_2 clads, and Ni-based/20Cr_3C_2-20Mo clads. The effect of cavitation test parameters on cumulative mass loss and incubation time has been studied.

Table 5.6 Factor and their levels for cavitation erosion testing

Parameters	Units	Levels		
		1	**2**	**3**
Stand of Distance	mm	0.5	1	1.5
Amplitude	µm	40	50	60
Immersion Depth	mm	80	100	120

Table 5.7 Experimental plan for cavitation erosion testing (Taguchi L9 array)

Experiment No.	Stand-of-Distance (mm)	Amplitude (µm)	Immersion depth (mm)
1	0.5	40	80
2	0.5	50	100
3	0.5	60	120
4	1	40	100
5	1	50	120
6	1	60	80
7	1.5	40	120
8	1.5	50	80
9	1.5	60	120

5.7.3 Surface Roughness Measurement

The surface roughness has an influence on several tribological characteristics, like friction, wear, and tear. However, the cavitation erosion resistance of the material, considerably affected by initial surface roughness **[142-143].** Hence, in the current study, the initial surface of the polished clads before cavitation erosion testing were measured via surface profilometer *(Model: SJ-400 Make: Mitutoyo)* and later, it has been utilized to measure the surface roughness of the eroded specimens to compare and confirm the severity of the damage. The monitor of the actual setup is shown in Figure 5.15 (a) and stylus and fixture assembly is shown in Figure 5.15 (b). The surface roughness measurement has been carried as per JIS 2001 standards at 4 mm sampling length and 0.8 mm cut-off length. The Gaussian filter has been applied to the measured profile to remove the waviness from the generated data.

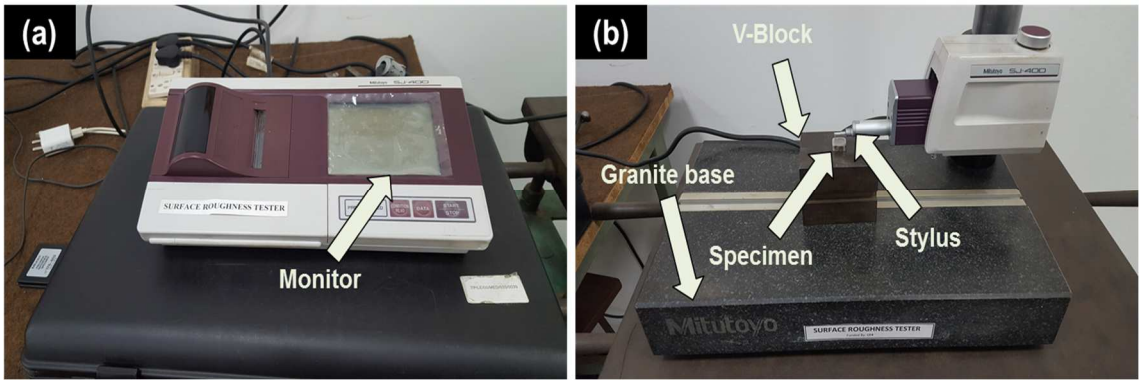

Figure 5.15 The actual setup of (a) Monitor of surface profilometer (b) Stylus and specimen fixture *(Photo Courtesy: Metrology Lab, Mechanical Engineering Department, TIET, Patiala)*

Chapter 6

Metallurgical and Mechanical Characterizations: Results & Discussion

6.1 Introduction to Chapter

The microstructure characterization of the developed clads has been presented in this chapter. The microstructure characterization has been carried out in terms of solidification growth and their pattern, elemental analysis, phase analysis, porosity, cracking, flexural and microhardness of the developed clads at optimized processing parameters of microwave hybrid heating. The morphology, porosity, hardness, and metallurgical bonding of clads with substrate, influence the functional (cavitation erosion) performance of clads.

6.2 Microstructure Characterization of Developed Composite Clads

6.2.1 Microstructural Characterization of Ni-based/40Cr_3C_2 Composite Clad

The clad of approximate 600 µm thickness has been developed through microwave cladding process and clear distinctive clad-substrate interface region can be seen through BSE (Backscatter electron) image, as shown in Figure 6.1 (a). The developed clad is free from all visible type of the solidification and interfacial cracks. The grain refinement has been observed in the thin layer formed just beneath the clad layer, which is due to the re-solidified substrate. It can be clearly seen in the microstructure, that the grey phase is equitably dispersed in white phase matrix. The enlarged view is shown in Figure 6.1 (b) reveals that the particles of the grey phase are of different size and shapes, which are randomly oriented in the white phase matrix. The solid solution of partially agglomerated carbides and columnar dendrite can be observed in the liquid solution of the metallic matrix from Figure 6.1 (c). The similar kind of structures was also reported by Gupta et al. **[27],** Cheng et al. **[99]**, and Zafar et al. **[144]**, while microwave cladding of Ni+20%$Cr_{23}C_6$ powder, laser cladding of Cr_3C_2 powder, microwave cladding of Inconel 718 alloy powder, respectively.

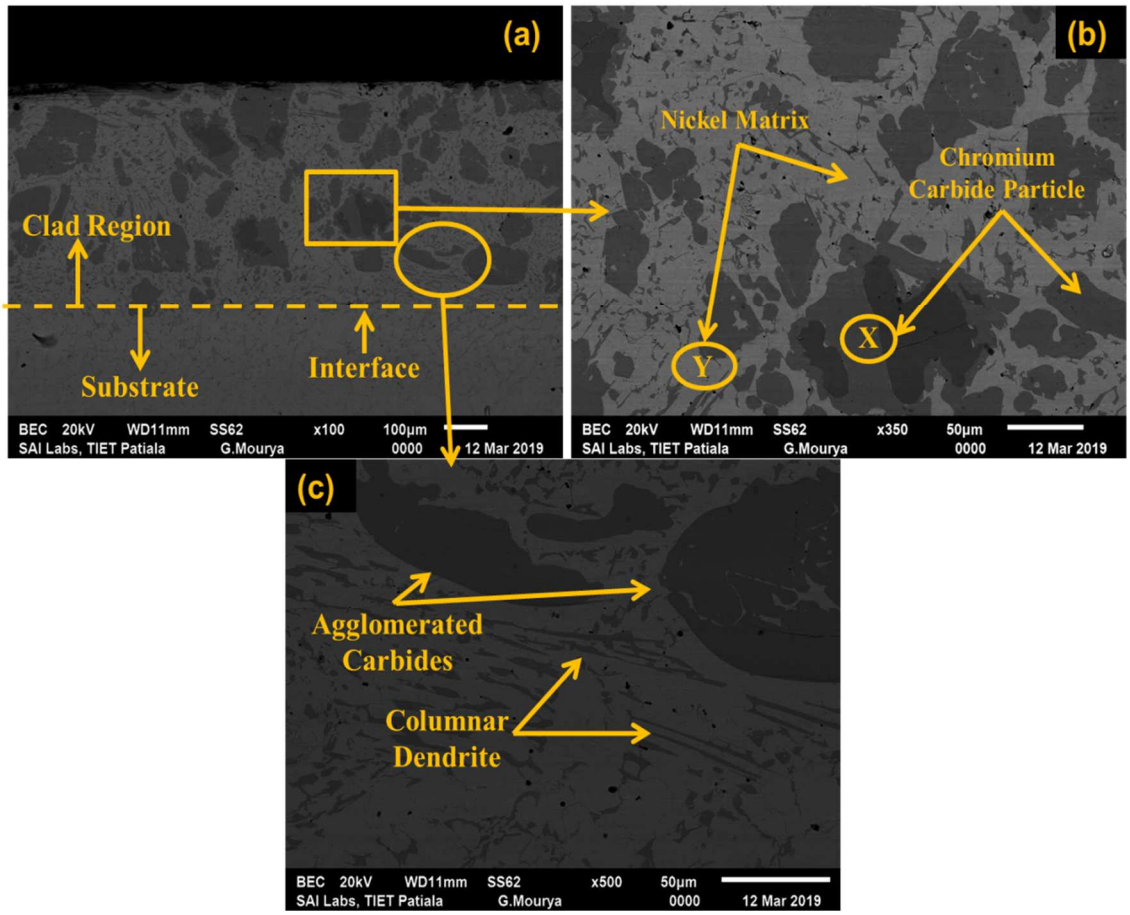

Figure 6.1: Typical BSE image of the developed Ni-based/40Cr_3C_2 composite clad showing (a) Transverse section (b) Enlarged view & locations of EDS analysis (c) Agglomerated carbides & Columnar Dendrite

However, the formation of partially agglomerated carbides and columnar dendrite is due to the fact that, as in microwave cladding process, the composite clad powder is preplaced over the metallic substrate, and the melting point of the major constituent nickel is lower than the refractory carbides used as reinforced. Due to the non-uniform rise of temperature in the powder system, because of their different physical properties, ultimately the thermal imbalance takes place inside the clad layer, and that generated localized melt pool current or convection currents in the clad layer. The localized current is further responsible for the partial agglomeration and columnar structure formation of the higher melting point particles (refractory carbides) in the soft matrix phase **[134]** and are equally distributed in the matrix phase (white region).

6.2.2 Elemental Study of Ni-based/40Cr_3C_2 Composite Clad

To verify and determine the presence of different elements in white and gray region as marked in Figure 6.1 (b), the energy dispersive spectroscopy has been carried out on these. The results of EDS show that, the grey phase (X) belongs to chromium carbide rich, while, white phase (Y) is nickel rich regions. Whereas, the Fe was found in a significant amount at both phases, it should be noted that, the clad raw powders don't contain any Fe element. Hence, the increase of Fe in the clad region is clear evidence of partial dilution of the substrate in the clad and vice-versa. The EDS analysis results of locations X and Y showed in Figure 6.1 (b) are presented in Figure 6.2 (a) & (b).

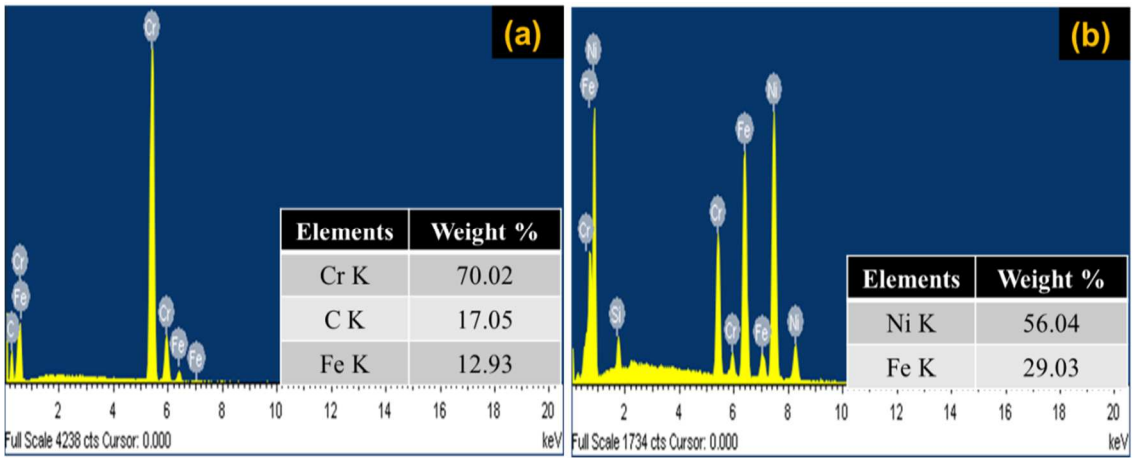

Figure 6.2: Energy dispersive spectrum of (a) Location X (b) Location Y

The area mapping also has been carried out to see the distribution of different elements in the clad region to get a better understanding of different phases formed and possible reasons for the formation of these. The area selected for area mapping is shown in Figure 6.3 (a). The results of area mapping shows, that grey phases are enriched with Cr and C elements and confirms the chromium carbide phase as shown in Figure 6.3 (b & c). The white region of clad microstructure mainly consists of Ni, O, Fe, and Si as shown in Figure 5 (d, e, f & g), respectively. The existences of Fe in the clad region favour and authenticate the claim of minimal dilution of a substrate (SS-316) and metallurgical bonding between the clad (Ni+40 Cr_3C_2) region and a substrate. The presence of O is due to the processing is carried out in an atmospheric environment.

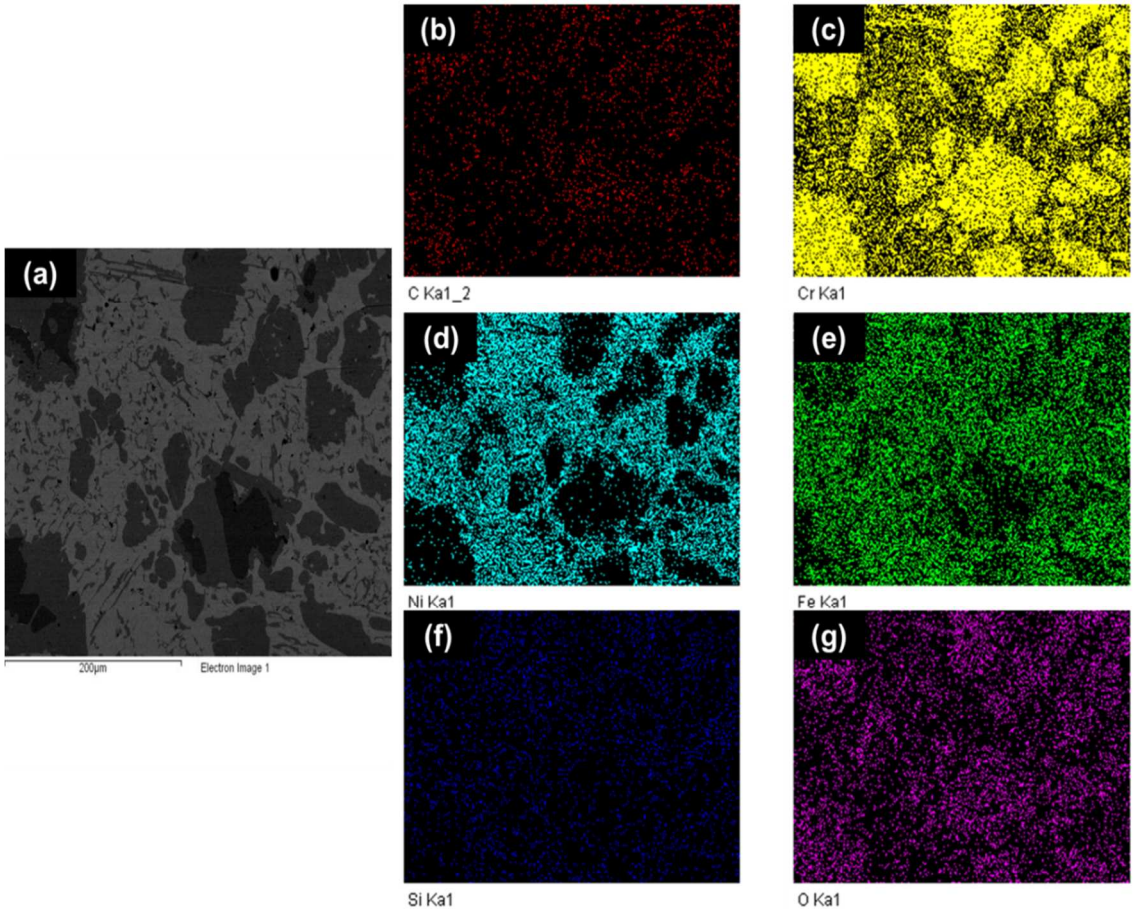

Figure 6.3 EDX area mapping of Ni-based/40Cr_3C_2 composite cladding (a) Region selected for area mapping (b) Carbon (c) Chromium (d) Nickel (e) Iron (f) Silicon (g) Oxygen

6.2.3 Microstructural Characterization of Ni-based/20Cr_3C_2-20Mo Composite Clad

The BSE image of the transverse section of the developed Ni-based/20Cr_3C_2-20Mo clad is illustrated in Figure 6.4 (a). The clad of the average thickness of 750 µm has been developed at the optimized processing parameters. The steep thermal gradient is not exist during microwave cladding process, owing to which clads are free from visible defects solidification defects like porosity, cracks etc.

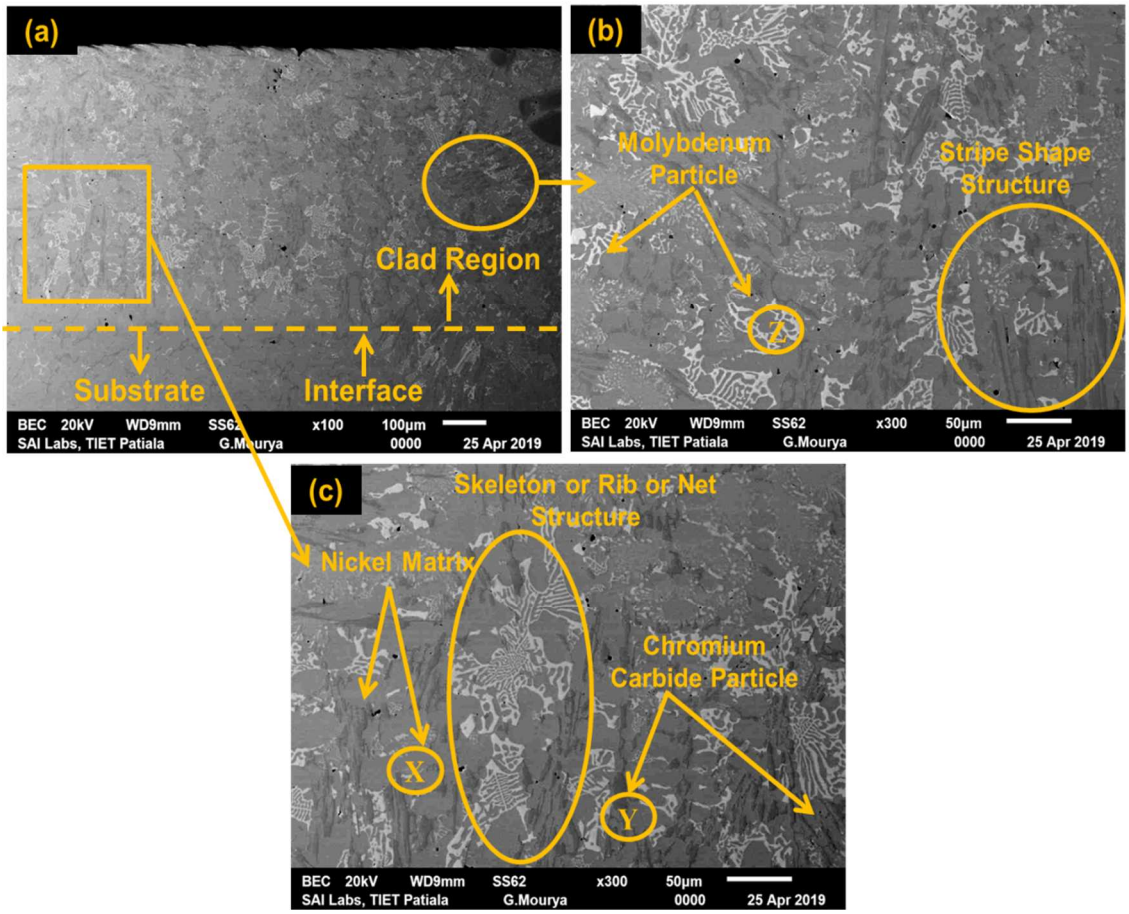

Figure 6.4: Typical BSE image of the developed Ni-based/20Cr_3C_2-20Mo composite clad showing (a) Transverse section (b) Enlarged view of stripe type dark phase uniformly dispersed in white phase matrix & location Z of EDS analysis (c) Skeleton-type or rib or net type light grey phase equally distributed in white phase matrix & locations X and Y of EDS analysis

In enlarged view, shown in Figure 6.4 (b) & (c), it has been observed that the microstructure of developed clad is consist of the light grey skeleton phase (Z) and stripe-like dark phase (Y), which are uniformly dispersed in the white matrix phase (X). The skeleton-type phase, which is also known as net-like or rib-like microstructure, the similar phase was reported by Hou et al. **[145]**and Ferreira et al.**[146],** while the development of Ni-based alloy coatings on steel substrate by using PTA welding process. It has been concluded that the presence of molybdenum in the Ni-base alloy cladding, increases the nucleation rate, as the melting temperature of Mo (2612°C) is higher than that of Ni-based alloy powder (1323°C), when the clad started cooling form the liquid state, the Mo precipitation begins first in the melt pool, which further

promotes the non-spontaneous nucleation. Hence, net-like or rib-like or skeleton-like morphology was observed in Mo-modified Ni-based alloy cladding. However, the plate-like or stripe-like morphology of carbide was observed in Mo-Free Ni-based coatings. Also, Li et al. [147] reported that the formations of stripe dark like structure take place due to poor solubility of C in Ni solution, during the development of Cr_3C_2 reinforced Ni_3Al matrix composite cladding via welding technique. Moreover, the stripe-like $M_{23}C_6$ and M_7C_3 are formed easily in the nickel matrix, because of lower Gibbs free energy.

6.2.4 Elemental Study of Ni-based/20Cr_3C_2-20Mo Composite Clad

To determine the different elementary components of different phases present in the microstructure of developed Ni-based/20Cr_3C_2-20Mo composite clad, the EDS is performed at different locations X, Y and Z as shown in Figure 6.4 (b) & (c), respectively.

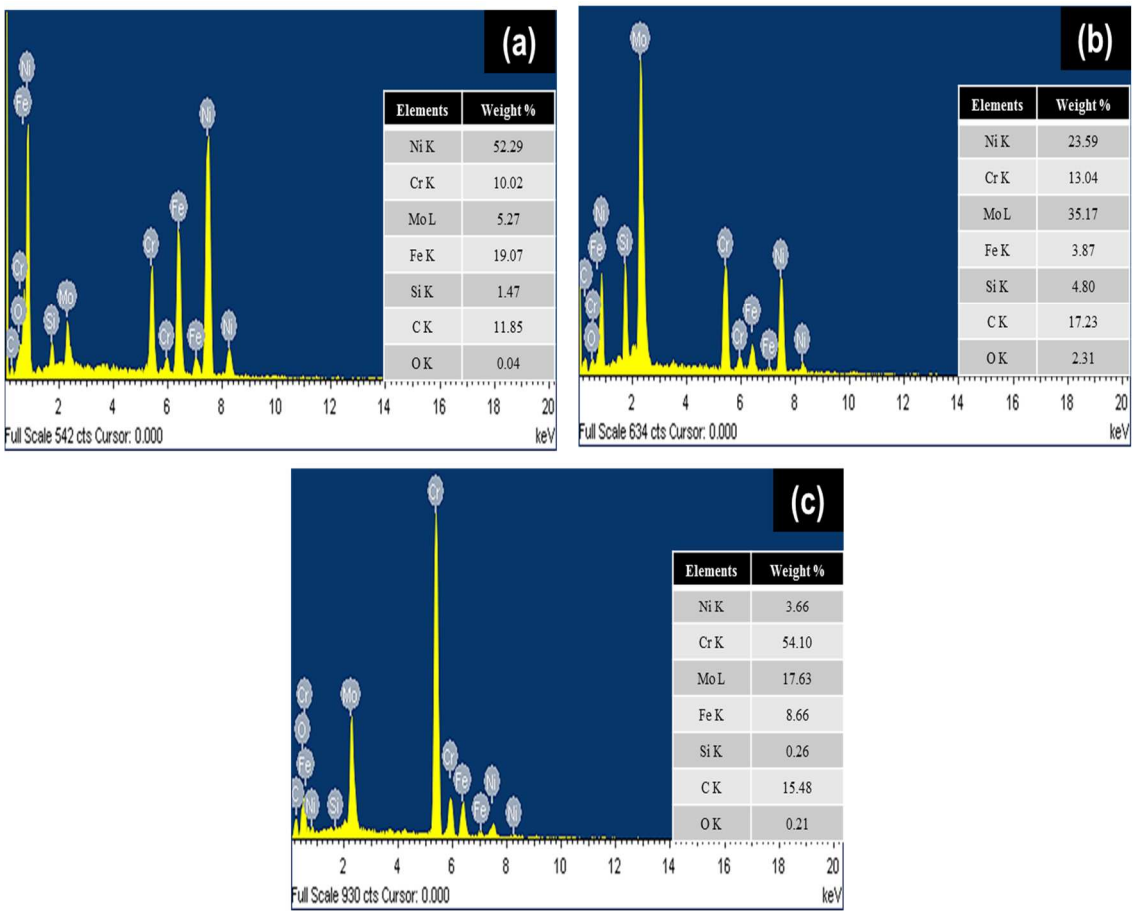

Figure 6.5: EDS spectra of (a) Location X (b) Location Y (c) Location Z

The area selected at location X is enriched with Ni, where Fe, Cr, Mo, Si, O, C are present in small amounts. Hence, the presence of Ni at X location confirms, that the location X is a nickel rich matrix. Similarly, the elemental analysis results at location Y and Z shows that light grey phase (Z) is molybdenum rich and dark grey phase (Y) is chromium carbide rich. However, Cr and C are found in considerable amount with Mo and vice-versa and Mo is also known for increasing the weight fraction of carbide in the Ni-rich dendrite solution **[145].** The evaluated EDS spectra of location X, location Y, and location Z are presented in Figure 6.5 (a), (b) and (c), respectively.

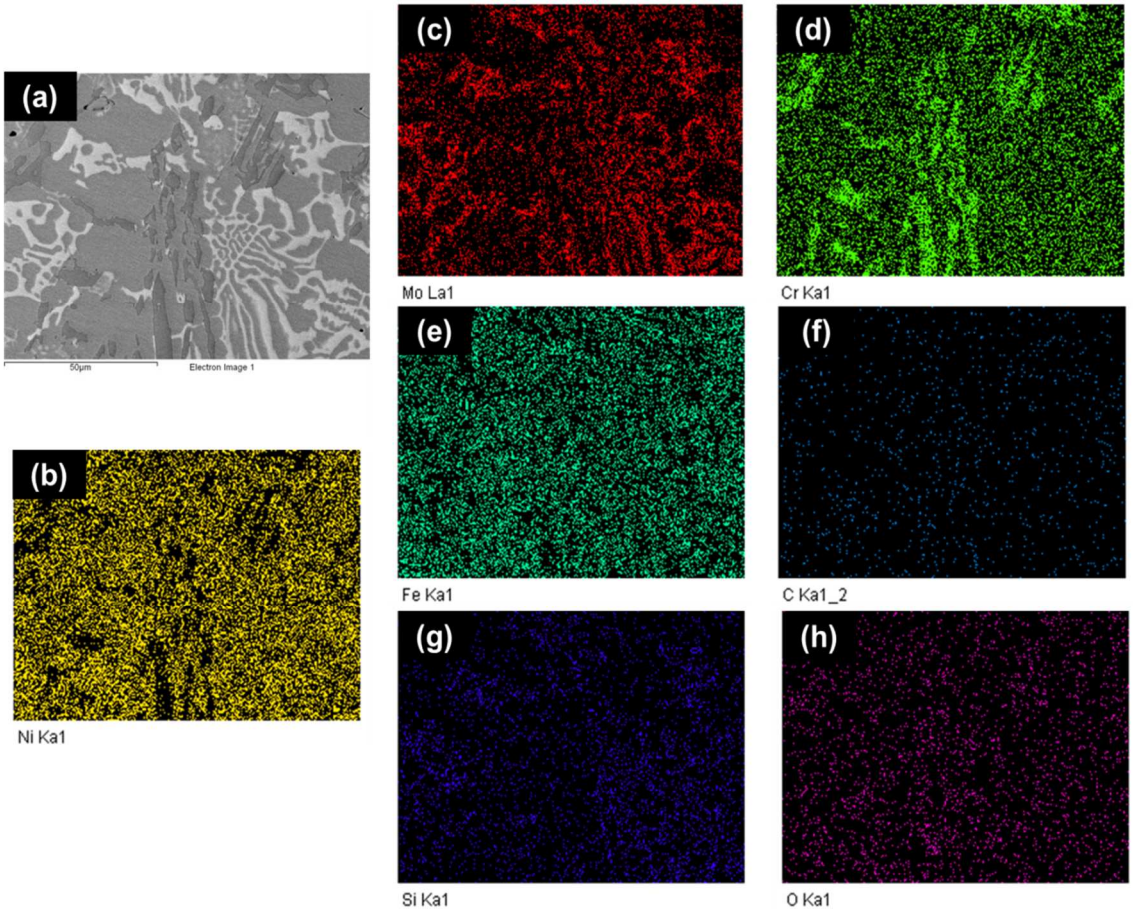

Figure 6.6: EDX area mapping of Ni-based/20Cr_3C_2-20Mo composite cladding (a) Cladding Micrograph (area selected for elemental mapping) (b) Nickel (c) Molybdenum (d) Chromium (e) Iron (f) Carbon (g) Silicon (h) Oxygen

The area mapping of the Ni-based/20Cr_3C_2-20Mo composite clad has been done on BSE image as illustrated in Figure 6.6 (a), to study the distribution of various elements in the clad region to acquire appropriate knowledge of various phases formed while microwave cladding process. Further, to find out the possible causes for the following

phase's formation. The area mapping results showed in Figure 6.6 (b) exhibits that the nickel is evenly distributed in the white phase, which confirms i.e. nickel matrix. The light grey phase is shown in Figure 6.6 (c) is Mo particles, and the Fe particles are consistently distributed over the region as visible in Figure 6.6 (d). Whereas from Figure 6.6 (e), it can be seen that Mo locations are enriched with chromium, as it was known that solubility of Cr in Ni-rich dendritic solution is poor till 1000°C, and Mo increases the nucleation rate, hence the Cr was found at Mo sites **[145,148].** However, the presence of Fe in the clad region justifies the claim of partial dilution of the substrate into the clad region. The clad region also consists of C, Si, and O as shown in Figure 6.6 (f, g, and h); the presence of O in the clad region due to the microwave cladding process has been carried out in the atmospheric conditions. It is visible from the area mapping that the oxygen is uniformly dispersed in the nickel matrix.

6.3 Porosity Study of Developed Composite Clads

6.3.1 Porosity Results of Ni-based/40Cr_3C_2 Composite Clad

The presence of pores in the developed clads is one of the major defects, it decreases the ductility, fatigue strength and ultimately affects the functionality of the clad **[149]**. It has been reported that the CER of the coatings/claddings decreases with the increase in porosity **[150]**. The goal of the current study is to develop defect-free clads, the porosity analysis of Ni-based/40Cr_3C_2 has been carried out on three randomly selected fields as per ASTM-B276 standards. The optical micrographs of the selected fields are shown in Figure 6.7 (a), (b) and (c), respectively. Whereas, the red spots visible in optical micrographs represent pores in the clad region. The evaluated results (number of pores and the percentage of porosity), for each area, are presented in Table 6.1. The average porosity in the Ni-based/40Cr_3C_2 clad came out to be 1.67 %. However, Santa et al. **[82]** reported the similar type of coatings with the HVOF technique, the porosity developed HVOF coatings was found about 2-5 times higher and Knotek et al. **[151]** had reported 7% porosity in plasma-sprayed Ni+Cr_3C_2 coating. Whereas Gupta et al. **[27]** reported that the porosity of 20% chromium carbide reinforced Ni-based microwave cladding on stainless steel was 0.90% only. However, in the current study it has been found slightly higher as compared to 20% Cr_3C_2, it might be due to the higher percentage of reinforcement in the cladding (higher percentage of reinforcement cause thermal imbalance inside the clad during heating, and while solidification the formation of

cracks and pores takes place due to different temperature of reinforcement and matrix phase) and poor solubility of C in the Ni matrix. But still, the cladding developed via microwave cladding route has significantly less porosity as compared to other processes like sputtering and thermal spraying. The reason for less porosity is attributed to volumetric and uniform heating by microwaves.

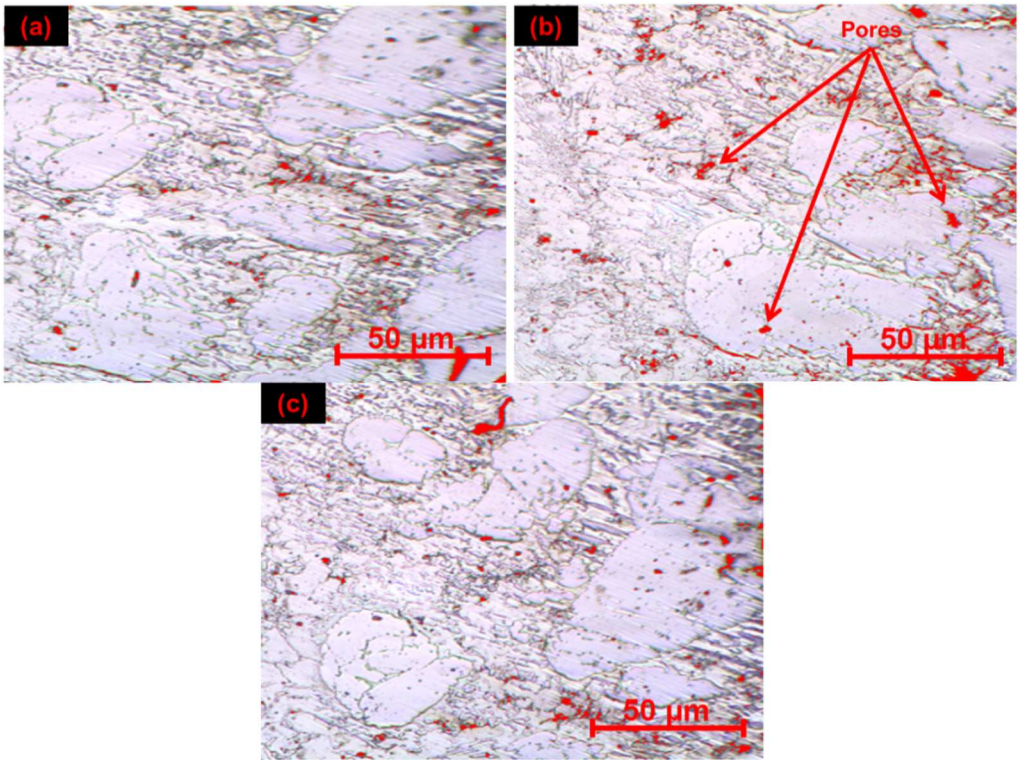

Figure 6.7: The optical micrographs at 100X magnification showing pores in (a) Field a (b) Field b (c) Field c

Table 6.1: The results of porosity analysis of Ni-based/40Cr_3C_2 composite clad

Fields	Total Pores	Pore %
(a)	597	0.97
(b)	1420	2.67
(c)	654	1.39
Average	890.33	1.67

6.3.2 Porosity Results of Ni-based/20Cr_3C_2-20Mo Composite Clad

The similar porosity investigation of Ni-based/20Cr_3C_2-20Mo composite clad has also been done on three arbitrary chosen fields. The optical micrographs of the selected

fields are represented in Figure 6.8 (a), (b) and (c), separately. While the red spots appeared in optical micrographs signifies pores in the developed clad. The evaluated results (number of pores and the percentage of porosity), for each area, are presented in Table 6.2. The average porosity in the Ni-based/20Cr_3C_2-20Mo clad came out to be 0.26 %. However, the clad developed by microwave cladding route possess very less porosity. Whereas in case of Ni-based/20Cr_3C_2-20Mo composite clad, the significantly less porosity was observed due to the smaller size of Mo powder particles (<15 µm), though the average particle size of the EWAC1004 and chromium carbide powder was 40 µm and 50 µm, respectively. The similar phenomena of reduction in porosity was observed by Ding et al. [74], while using nanoparticle size WC-12Co, in place of conventional WC-12Co in HVOF coating on SS-304 substrate. The reason attributed to lower porosity is that nanostructured WC-12Co particles allow sufficient growth for denser microstructure. Whereas reason for low porosity in microwave processed clad is a low thermal gradient in the setup of microwave cladding and lower solidification rate because the clads was allowed to solidify at room temperature.

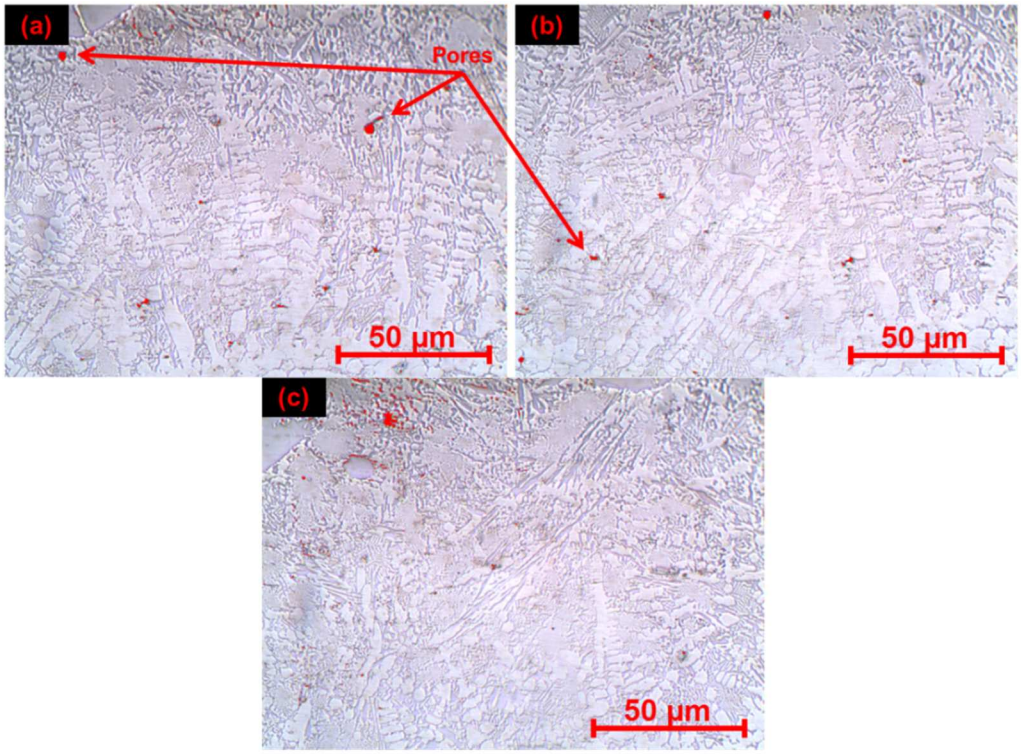

Figure 6.8: The optical micrographs at 100X magnification showing pores in (a) Field a (b) Field b (c) Field c

Table 6.2: The results of porosity analysis of Ni-based/20Cr_3C_2-20Mo Composite Clad

Fields	Total Pores	Pore %
(a)	582	0.46
(b)	116	0.13
(c)	192	0.19
Average	296.66	0.26

6.4 X-Ray Diffraction Evaluation of Composite Clads

6.4.1 X-Ray Diffraction Results of Ni-Based/40Cr_3C_2 Composite Clad

The XRD spectrum of developed clad is presented in Figure 6.9. The phases detected in the developed clads by XRD are Ni_3Cr_2 (44.3012°), $Cr_{23}C_6$ (51.6876°), SiC (71.5235°), Cr_3Ni_2SiC (75.9201°), NiO_2 (82.7391°) and Ni_3Fe (97.4319). During melting of the matrix material, the Cr_3C_2 particles and Cr present in EWAC powder get partially diluted in the molten pool, therefore the Cr and C content will increase in the liquid solution of Ni **[152]**, and C has poor solubility in Ni liquid solution **[147]**. Hence, the formation of the intermetallic Ni_3Cr_2 phase takes place due to the reaction between Ni and Cr at elevated temperature. Whereas, the chromium carbide formation takes place due reaction between remaining Cr and C, but $Cr_{23}C_6$ phase was formed due to less Gibb free energy of $Cr_{23}C_6$ among the all other chromium carbides (Cr_3C_2 and Cr_7C_3) phases **[153]**. Due to the presence of Si in EWAC powder and base material the SiC phase has formed and Cr_3Ni_2SiC phase is formed due reaction of Si, Cr present in EWAC powder and free C in the molten pool at elevated temperature **[154]**. The presence of Ni_3Fe confirms the metallurgical bonding between the clad and the substrate region because no Fe was present initially in the clad powder; the only source of Fe is substrate **[27]**. However, the presence of NiO_2 is due to the processing is carried out in an atmospheric environment.

The quantitative assessment of the different phases formed in Ni-based/40Cr_3C_2 composite clad has been done by using the normalized intensity ratio (NIR) method and results have been presented in Table 6.3. The NIR of the phase-1 has been calculated by using Equation 6.1. This equation has been utilized by Gupta et al. **[106]** for quantitative assessment of relative phase intestines of phase formed in EWAC clad deposited on

austenitic stainless steel. Where I_1, I_2, I_3 and I_N is the intensities or counts of the 1st, 2nd, 3rd and Nth phases, respectively, and the back ground intensity is denoted by I_{back}.

$$NIR_1 = \frac{I_1 - I_{back}}{I_1 + I_2 + I_3 + \cdots\ldots I_N + -NI_{back}} \text{----------(6.1)}$$

However, the NIR don't give the exact proportion of phase present in the clad, though during the solidification of clad at the room temperature, almost 48.33 % of chromium carbide formed ($Cr_{23}C_6$) due to the reaction between Cr and C. Whereas, other major carbides formed are SiC (13.83%) and Cr_3Ni_2SiC (13.63%), while presence of intermetallic Ni_3Cr_2 (15.50%) and Ni_3Fe (7.99%) in substantial amount, validate the metallurgical bonding between substrate and clad. The nickel has high oxidation resistance at elevated temperature [107], hence the only a small amount of NiO_2 (1.66%) formed due to the reaction between Ni and O at elevated temperature.

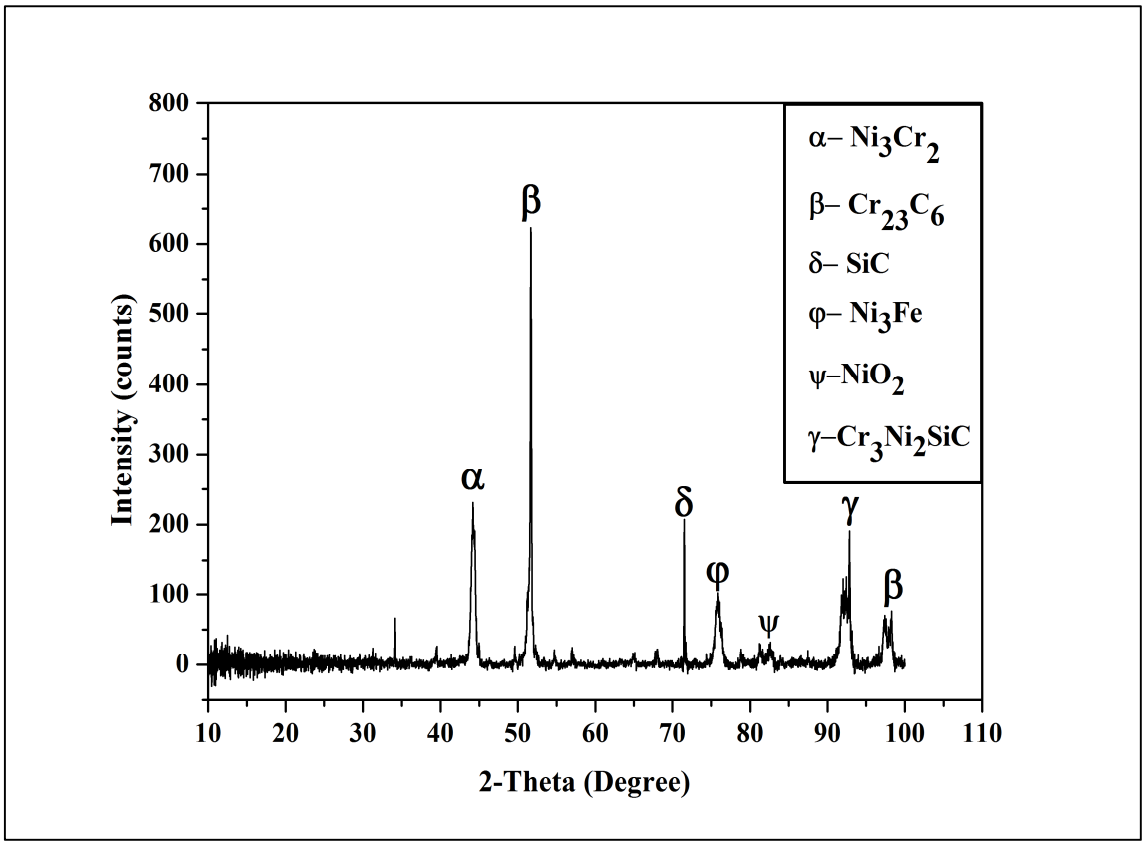

Figure 6.9: The XRD spectra of Ni-based/40Cr_3C_2 composite clad

Table 6.3: Relative phase intensities in Ni-based/40Cr_3C_2 composite clad

S.No.	Phase	I_1	I_2	I_3	I_4	I_5	I_6	I_7	I_{back}	NIR (%)
1	Ni_3Cr_2	238	-	-	-	-	-	-	15	15.50
2	$Cr_{23}C_6$	-	627	-	-	-	-	83	15	48.33
3	SiC	-	-	214	-	-	-	-	15	13.83
4	Ni_3Fe	-	-	-	130	-	-	-	15	7.99
5	NiO_2	-	-	-	-	39	-	-	15	1.66
6	Cr_3Ni_2SiC	-	-	-	-	-	212	-	15	13.69

6.4.2 X-Ray Diffraction Results of Ni-Based/20Cr_3C_2-20Mo Composite Clad

The XRD analysis of developed Ni-Based/20Cr_3C_2-20Mo composite clad has been carried out. The XRD spectra of the Ni-Based/20Cr_3C_2-20Mo composite clad is presented in Figure 6.10. The results of the spectra disclose the existence of FeMoCr (39.8670°), $MoSi_2$ (39.8670°), $NiMo_4C$ (41.3970°), $MoNi_4$ (43.4682°), Ni_3Fe (44.3484°), Cr_2Ni_3 (51.6966°), Mo_2C (54.6958°), FeCr (75.7806°), $Cr_{23}C_6$(75.7806°) and Cr_3Si (78.4196°) phases in the clad region. This is may be due to fact that, at high temperature heating of the clad powder, Ni, Mo, Cr, and Si react to form $MoSi_2$ and Cr_3Si **[155-156]**. The formation of $Cr_{23}C_6$ precipitate was observed due to the reaction between Cr and C during solidification of clad **[153]**. As the clad powders originally contain no Fe, so the presence of the various intermetallic phases FeMoCr, FeCr, and Ni_3Fe indicate the dilution of clad with the substrate and support the claim of minimal dilution of the substrate. The formation of FeMoCr phase-only possible during the reaction of Fe, Mo, and Cr at high temperature, which must be followed by furnace cooling **[157]**, and microwave cladding setup has the capability of rapid heating and slow cooling. The formation of the following carbide $NiMo_4C$ and Mo_2C is a good indication of anti-wear clad. The Cr_2Ni_3 confirm the reaction of main constituents of the substrate and clad powder system at elevated temperature.

The qualitative analysis of the Ni-based/20Cr_3C_2-20Mo composite clad has been carried by using the NIR method. The results of the quantitative analysis have been presented in Table 6.4. According to NIR results, the prime most constituents in the clad are Cr_2Ni_3 (67.30%), Ni_3Fe (14.43%), and $Cr_{23}C_6$ (8.57%). Where many other carbide phase and intermetallic phase are a presence in small quantities, which may ultimately help in properties enhancement of cladding.

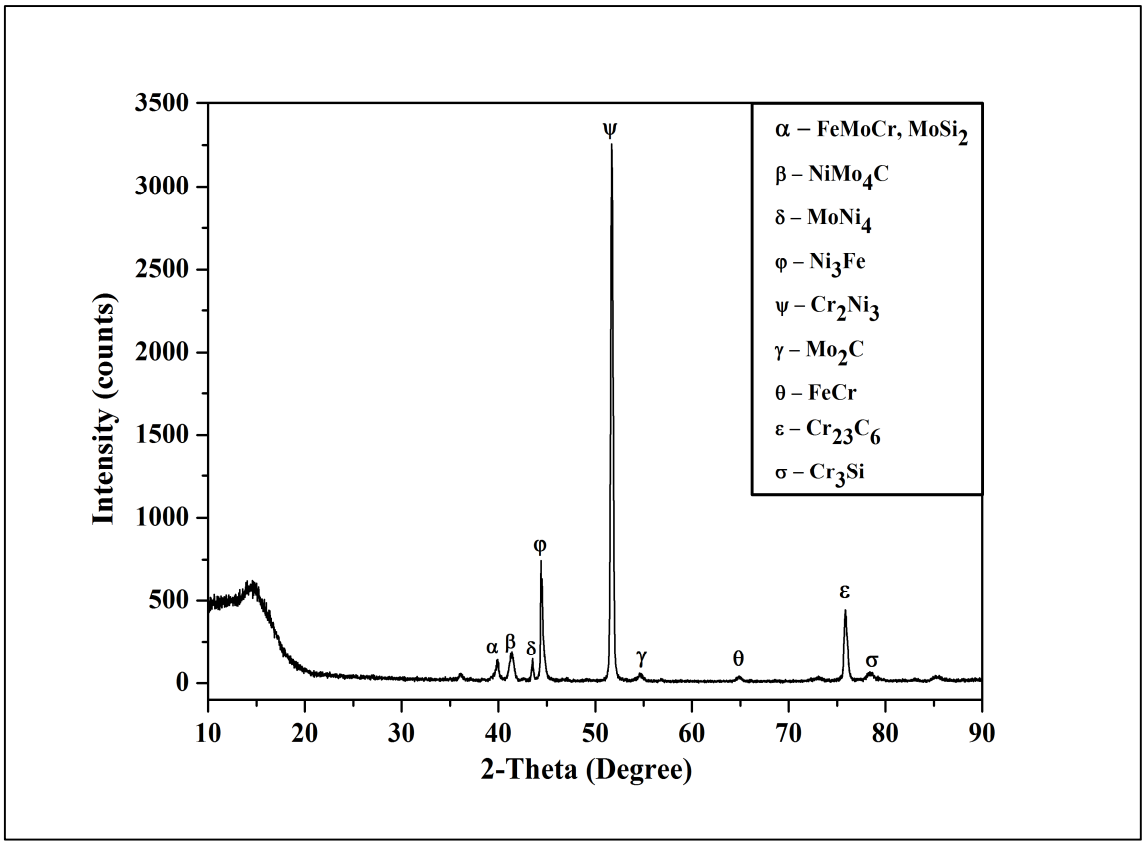

Figure 6.10: The XRD spectra of Ni-based/20Cr_3C_2-20Mo composite clad

Table 6.4: Relative phase intensities in Ni-based/20Cr_3C_2-20Mo composite clad

S.No.	Phase	I_1	I_2	I_3	I_4	I_5	I_6	I_7	I_8	I_9	I_{back}	NIR
1	FeMoCr, $MoSi_2$	112	-	-	-	-	-	-	-	-	20	1.91
2	$NiMo_4C$	-	183	-	-	-	-		-	-	20	3.40
3	$MoNi_4$	-	-	102	-	-	-	-	-	-	20	1.71
4	Ni_3Fe	-	-	-	712	-	-	-	-	-	20	14.43
5	Cr_2Ni_3	-	-	-	-	3246	-	-	-	-	20	67.30
6	Mo_2C	-	-	-	-	-	66	-	-	-	20	0.95
7	FeCr	-	-	-	-	-	-	33	-	-	20	0.27
8	$Cr_{23}C_6$	-	-	-	-	-	-	-	431	-	20	8.57
9	Cr_3Si	-	-	-	-	-	-	-	-	88	20	1.41

6.5 Micro-hardness Estimation of Developed Composite Clads

6.5.1 Micro-hardness Results of Ni-Based/40Cr_3C_2 Composite Clad

The microhardness influences the functional characteristics of the clad layer like wear and friction. The microhardness of the developed clad is monitored along its cross-section. The microhardness of the clad region increases by the uniform dispersion of chromium carbide particles in the clad region. The observed average value of microhardness of the clad region is 605±80 $HV_{0.3}$, which means that the clad is almost three times harder than the substrate. The mean of recorded values of Vickers microhardness and their standard deviation has been presented in Figure 6.11. The microhardness values show non-uniformity, which is due to the presence of soft to hard phases in the clad region. The optical micrograph of microhardness indentation on Ni-based/40Cr_3C_2 composite clad region is shown in Figure 6.12 (a). It has been observed that hardness of carbide particle is more than 1600 $HV_{0.3}$; the morphology of indent on carbide particle is shown in Figure 6.12 (b), whereas the hardness of Ni-matrix is more than 450 $HV_{0.3}$. The morphology of indent of the substrate region and nickel matrix is shown in Figure 6.12 (c) and (d), respectively.

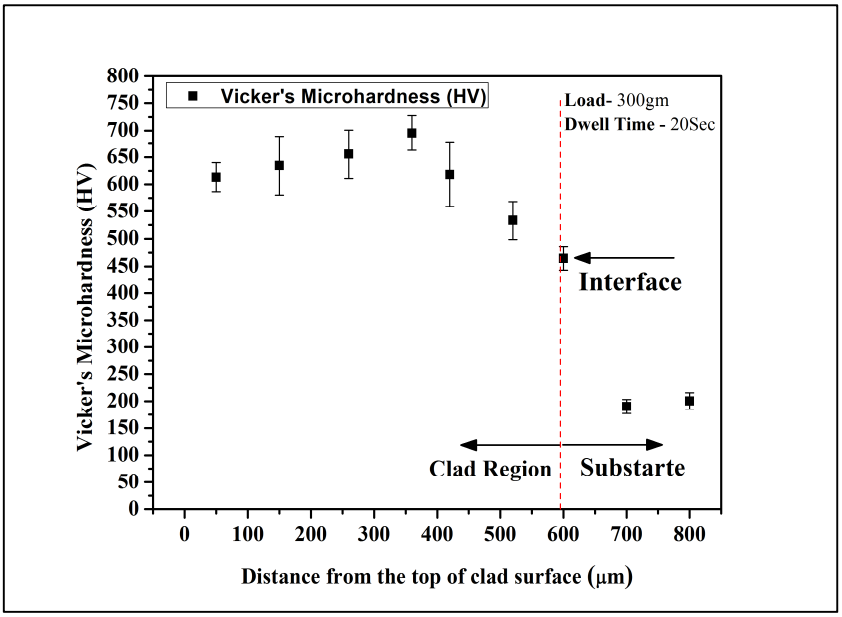

Figure 6.11: Scatter plot of microhardness values of Ni-based/40Cr_3C_2 clad at different locations

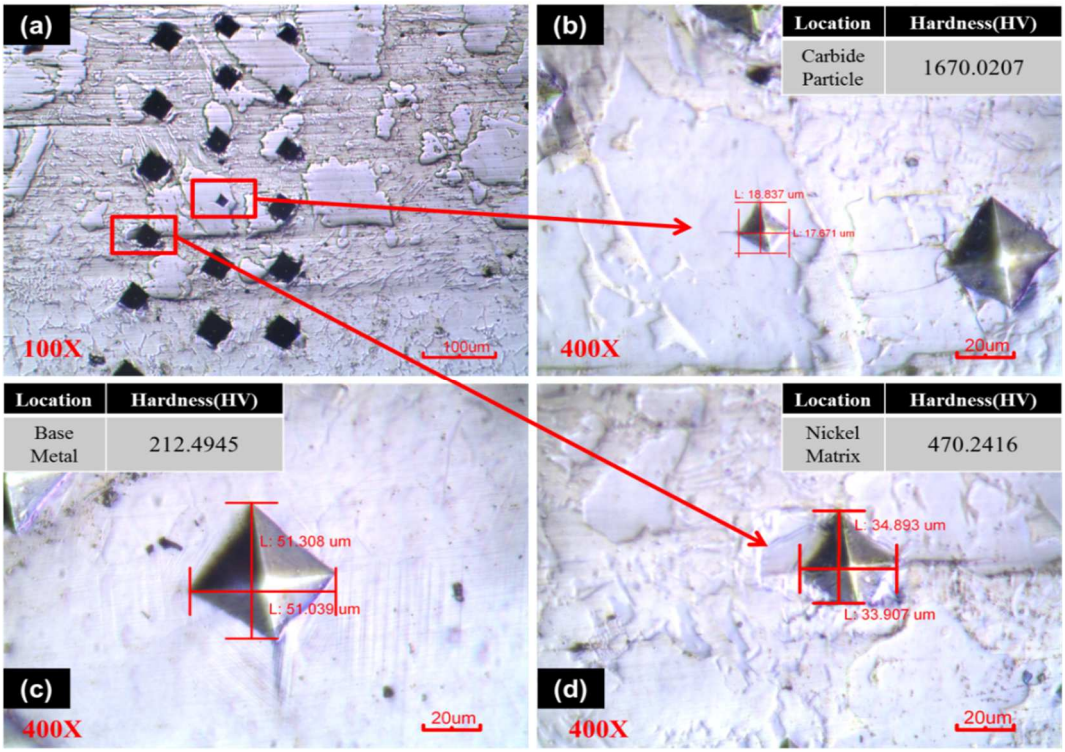

Figure 6.12: Optical micrographs showing (a) Microhardness indentation on Ni-based/40Cr_3C_2 clad (b) Morphology of indent on carbide particle (c) Morphology on indent on SS316 (d) Morphology on indent on nickel matrix

6.5.2 Micro-hardness Results of Ni-Based/20Cr_3C_2-20Mo Composite Clad

The microhardness investigation of the developed Ni-based/20Cr_3C_2-20Mocomposite clads was performed to verify the fact that the presence of hard carbide phases like $Cr_{23}C_6$, Ni_2Mo_4C, and Mo_2C increases the microhardness of the clad. It was witnessed that the average value of microhardness at the top of clad was 681±30 $HV_{0.3}$. The average microhardness in the clad region is 3.5 times more than that of SS-316 substrate (190±15 $HV_{0.3}$). The minor standard deviation that can be seen in the readings shown in scatter plot (Figure 6.13) is due to the existence of hard carbide phases as well as soft intermetallic simultaneously in the clad region. The microhardness at molybdenum phase was recorded around 340 $HV_{0.3}$. The optical image of indentation carried out on clad, interface and substrate region is shown in Figure 6.14 (a), whereas the optical micrograph of an enlarged view of microhardness indents on Ni-Based/20Cr_3C_2-20Mo composite clad region is shown in Figure 6.14 (b). The morphology of indents on the substrate and molybdenum region is shown in Figure 6.14 (c) and 6.14 (d), respectively.

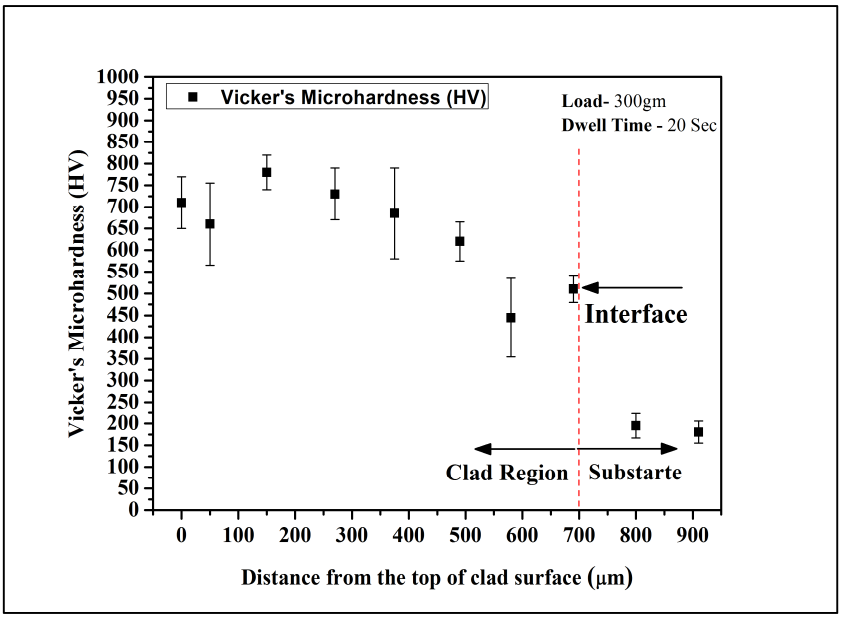

Figure 6.13: Scatter plot of microhardness values of Ni-based/20Cr_3C_2-20Mo clad at different locations

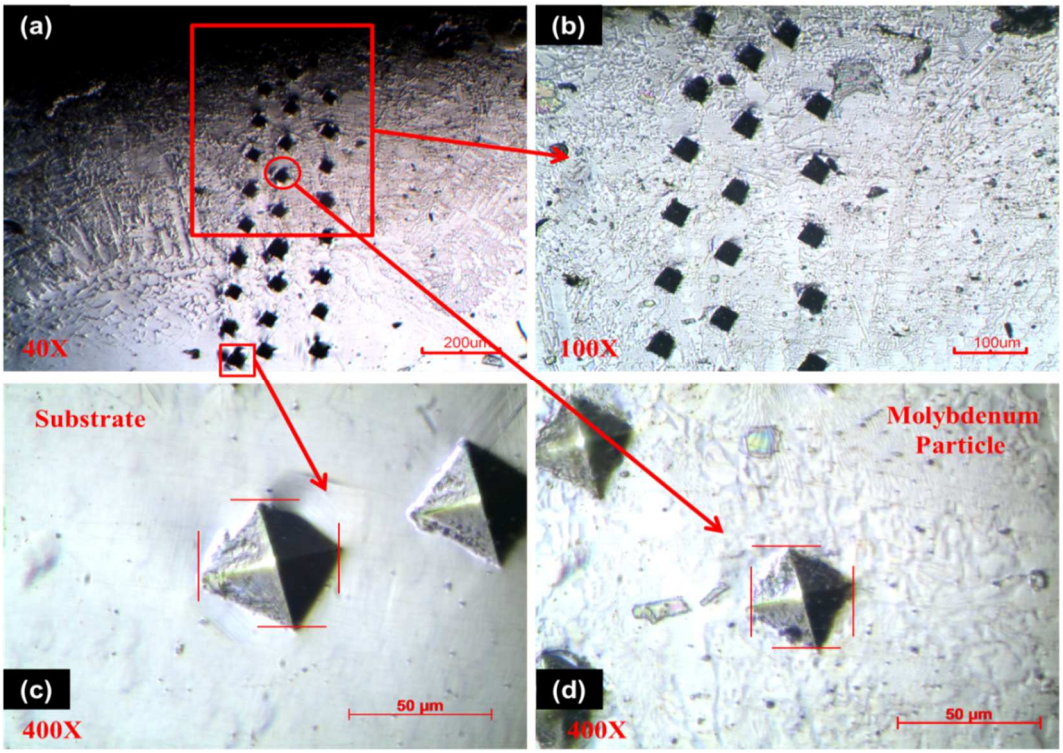

Figure 6.14: Optical micrographs showing (a) Microhardness indentation on Ni-based/20Cr_3C_2-20Mo clad, interface and substrate (b) Enlarged view of microhardness on clad region (c) Morphology on indent on SS316 (d) Morphology on indent on Mo particle

6.6 Flexural Strength Examination of Microwave Processed Composite Clads

6.6.1 Flexural Strength Results of Ni-Based/40Cr_3C_2 Composite Clad

The flexural strength is one of the most important properties of many mechanical components. The flexural strength of the microwave processed Ni-Based/40Cr_3C_2 composite clad has been performed as per *ASTM-C1161-13*, to verify the metallurgical bonding between clad and substrate. The results of load-deformation characteristics are illustrated in Figure 6.15 (a). The entire load-deformation characteristics are sub-divided into three segments as illustrated in Figure 6.15 (b).

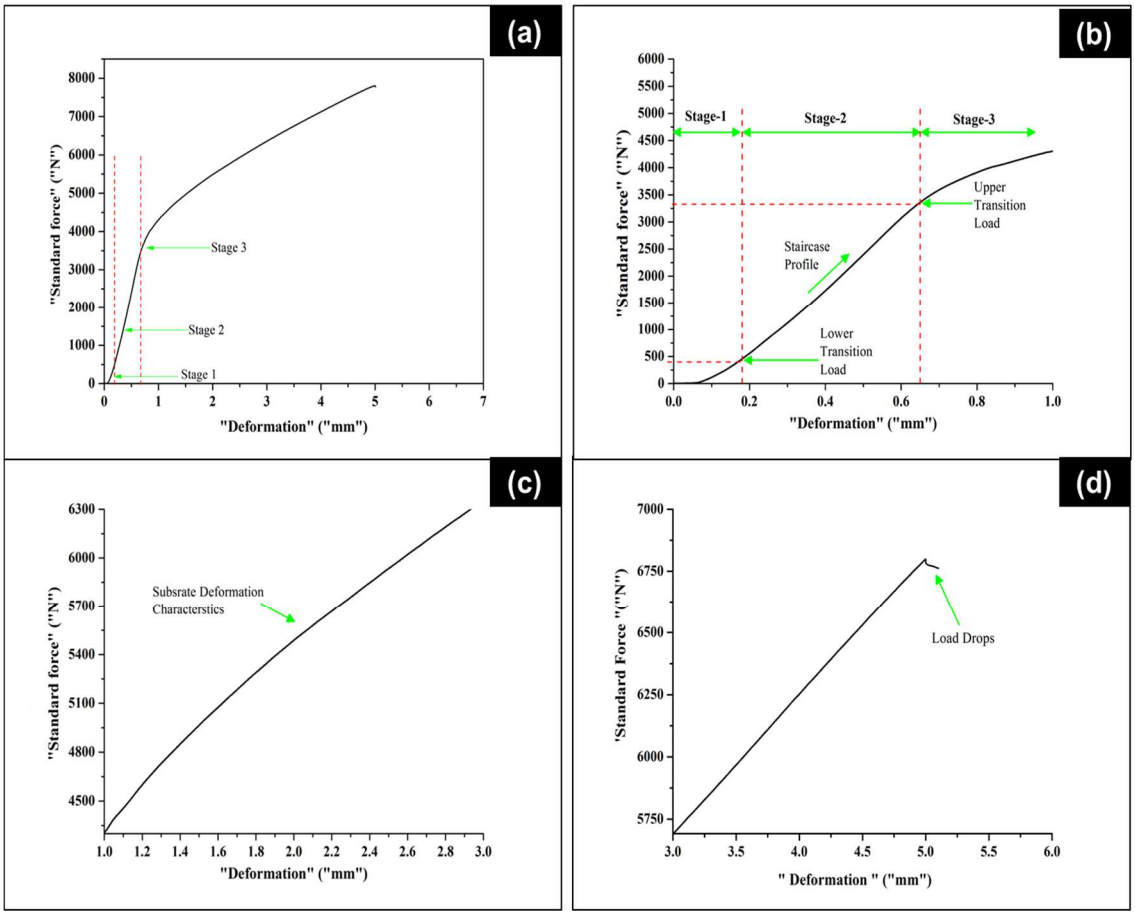

Figure 6.15: (a) Load vs. deformation characteristics of microwave processed Ni-Based/40Cr_3C_2 composite clad during a peel-of-strength test or 3-point bend test: Expanded views of the of clad characteristics (b) Up to 1 mm deformation (c) Between 1 to 3 mm deformation (d) Onwards 3 mm deformation

The first segment exhibits the behaviour of clad up to 1 mm deformation (stage-I), the second segment exhibits the behaviour of clad between 1 to 3 mm deformation (stage-II), and the third region exhibits the behaviour of clad and load drop characteristics deformation 3 mm onwards (stage-III). In stage-I, the Ni-based/40Cr_3C_2 composite clad possess consistent load vs. deformation characteristics up to ~632 N of the force. Further, there is an abrupt rise in force from ~632 N to ~3211 N, which is corresponding to deformation of 0.63 mm at the end of stage-II as shown in Figure 6.15 (b). These two loads are designated as lower transition load and upper transition load. Afterwards, load-deformation characteristics follow stage-III; have known as substrate deformation characteristics (Figure 6.15 (b) stage-III).

Further, the initial 1 mm deformation was rescaled and presented in Figure 4.15 (b), it was observed that up to lower transition load, the Ni-based/40Cr_3C_2 composite clad exhibits elastic behaviour and underwent deformation of 0.18 mm. However, with the constantly increasing load, the micro-cracks start forming on the top of the clad surface as observed from constant load-deformation at lower transition load ~632 N in the present case. During this stage, the hard carbide present in clad the starts absorbing the load and exhibit strong load-deformation properties as shown in stage-II. This deformation stage can be described as the beginning of plastic deformation in the clad. However, at this stage, the micro-cracks begin to develop and reduce the induced stresses, as shown by the staircase profile in Figure 6.15 (b).

These small bends caused the reinforced phase to separate from the matrix, causing larger cracks. However, if the load is increased beyond the upper transition load value (in this case ~ 3211 N), greater plastic deformation will occur and the cracks will spread to the depth of the clad, and the clad will fail when the load is shifted on the SS-316 substrate. Stage-III (Figure 6.15 (c)) shows the progressive deformation of the substrate. In addition, the load was stopped, when the load began to fall (Figure 6.15 (d)). The maximum flexural value of microwave processed Ni-Based/40Cr_3C_2 composite clad was observed as 813.229 MPa. The observations of the complete study are tabulated in Table 6.5.

Table 6.5: Observations recorded during three-point bend test of microwave processed Ni-Based/40Cr_3C_2 composite clad

Sample set	Lower transition load (N)	Upper transition load (N)	Deformation at upper transition load (mm)	Flexural strength (MPa)	Maximum load (N)	Maximum deformation (mm)
Ni-40% Cr_3C_2	632	3211	0.63	813.229	7807	5.02

Further, to examine the Ni-Based/40Cr_3C_2 composite clad failure mode, fractographic analysis of three-point bend tested clad specimen was performed using SEM. However, the top view and side view of a fractured test specimen of Ni-Based/40Cr_3C_2 composite clad is shown in Figure 6.16 (a) and (b).

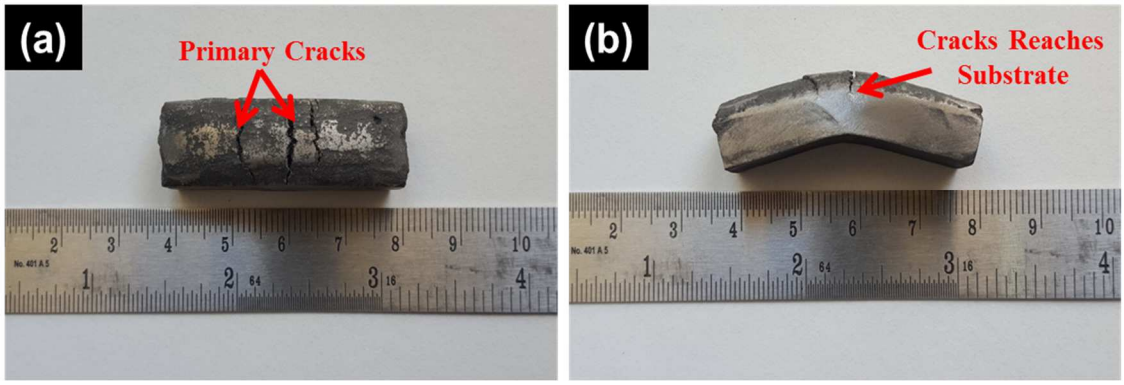

Figure 6.16: Photographs of the fractured clad specimen after three points bend test of showing (a) Top view of Ni-Based/40Cr_3C_2 composite clad (b) Side view of Ni-Based/40Cr_3C_2 composite clad

The SEM images are shown in Figure 6.16 (a) and (b) exhibits that during loading on the surface of the clad generates multidirectional macro cracks in the clad. The cracks spread in to the depth of the clad up to the interface via primary cracks as loading progress. Whereas, the Ni-Based/40Cr_3C_2 composite clad possess higher ductility, as a result of the presence of Ni in the matrix. However, the hard reinforce carbide particle, due to their brittle nature, act as crack origination point, between reinforcement and matrix phase. The carbides detached from the matrix phase shown in Figure 6.17 (c). As a detachment of carbide from matrix phase occurs during loading above the lower transition load. The ductile Ni matrix resists the crack formation up to the stage-I of loading, but later in stage-II or stage-III, cracks scattered in the matrix and secondary

micro-cracks appear as shown in Fig. 6.17 (c). However, the carbide particles were still visible firmly embedded in the matrix. The formation of secondary cracks in the Ni matrix phase, during tensile loading, indicates the debonding of the matrix phase.

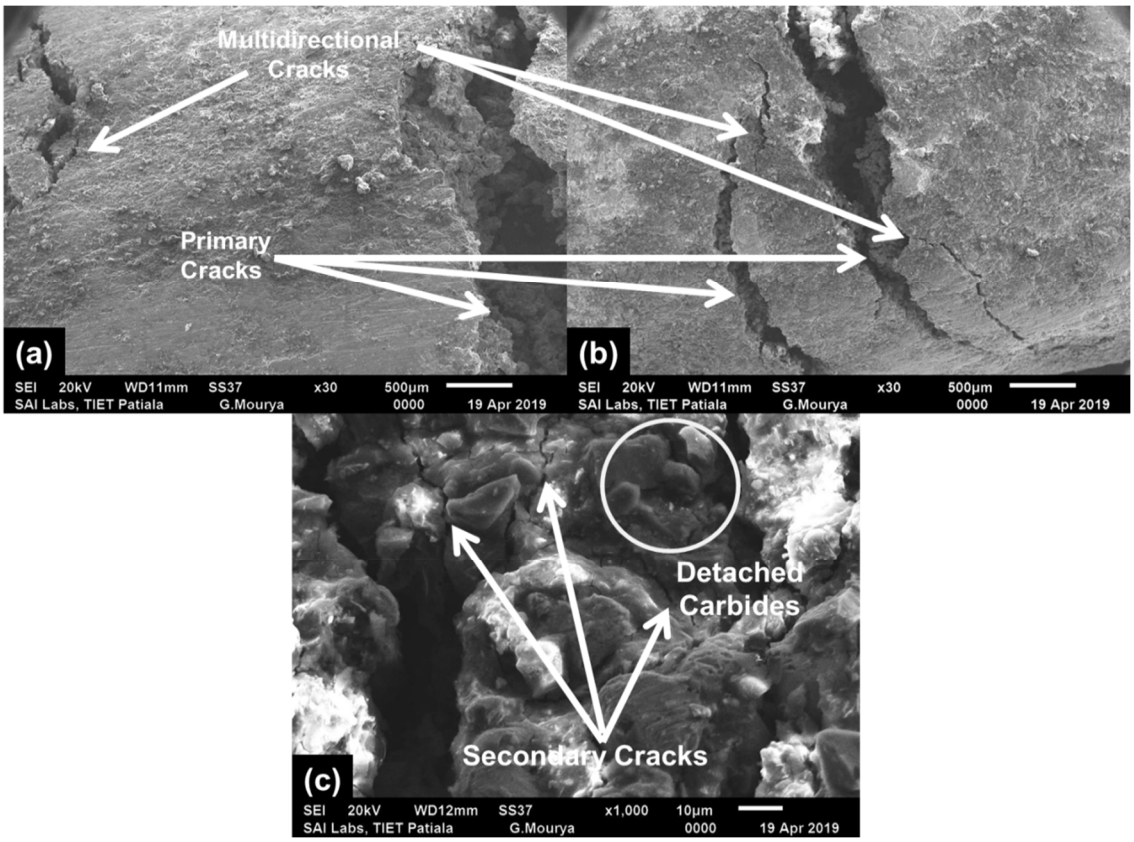

Figure 6.17 SEM micrographs of the fractured specimen of Ni-Based/40Cr_3C_2 composite clad after three-point bend test showing (a) Multidirectional Cracks (b) Primary cracks (c) Secondary cracks

6.6.2 Flexural Strength Results of Ni-Based/20Cr_3C_2-20Mo Composite Clad

Similarly, the three-point bend test has been carried out to examine the flexure behaviour developed Ni-based/20Cr_3C_2-20Mo composite clad. The load vs. deformation characteristics of Ni-based/20Cr_3C_2-20Mo composite clad is illustrated in Figure 6.18 (a). For the exhaustive study the load vs. deformation characteristics curve was divided into three stages as shown in Figure 6.18 (b), (c) and (d).

During stage-I, uniform load-deformation behaviour was observed up to ~ 577 N of the load for Ni-based/20Cr_3C_2-20Mo clad. Further, in stage-I, there was a sharp increase in load from ~ 577 N to ~ 3760 N with deformation of 0.63 mm. Till the stage-2 clad

exhibits, elastic behaviour Ni-based/20Cr_3C_2-20Mo clad and only microcracks were observed on the top of the clad. During this stage, plastic deformation in the clad just starts as the hard carbides in the clad takes the load and due to which sharp increase in load-deformation characteristics can be observed in Figure 6.18 (b). The minor cracks which were formed in stage-II propagate as the load increases and turn into a major crack in stage-III. During stage-III, more plastic deformation in the clad occurs and the clad gets failed with an increase in load as the load is shifted to the SS-316 substrate. As the load is shifted to the substrate, the substrate deformation characteristics are shown in Figure 6.1 (c), due to that the load drop is observed in the load vs. deformation characteristics curve as shown in Figure 6.18 (d). It was observed that the average value of the flexural strength of Ni based/20Cr_3C_2-20Mo was 708.76 MPa.

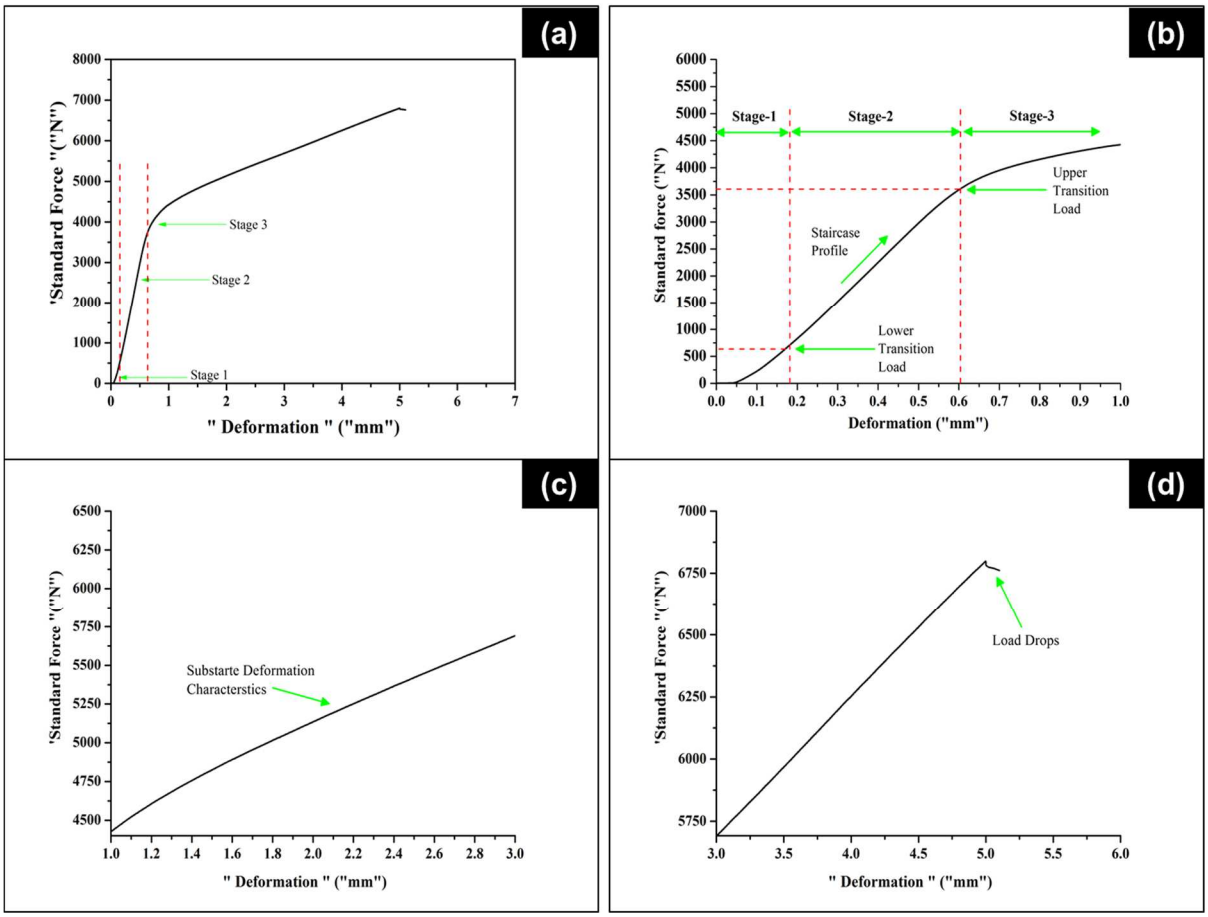

Figure 6.18: (a) Load vs. deformation characteristics of microwave processed Ni-Based/20Cr_3C_2-20Mo composite clad during a peel-of-strength test or 3-point bend test: Expanded views of the of clad characteristics (b) Up to 1 mm deformation (c) Between 1 to 3 mm deformation (d) Onwards 3 mm deformation

The observations recorded during the load-deformation characteristics complete study are presented in Table 6.6. The fractographic study of the flexural tested Ni-based/20Cr_3C_2-20Mo composite clad was carried out using SEM. However, the photographs of the top view and side view of a fractured test specimen of Ni-Based/20Cr_3C_2-20Mo composite clad are shown in Figure 6.19 (a) and (b).

Table 6.6 Observations recorded during three points bend test of microwave processed Ni-Based/20Cr_3C_2-20Mo composite clad

Sample set	Lower transition load (N)	Upper transition load (N)	Deformation at upper transition load (mm)	Flexural strength (MPa)	Maximum load (N)	Maximum deformation (mm)
Ni-20% Cr_3C_2-20Mo	577.69	3760	0.63	708.76	6804.16	5.11

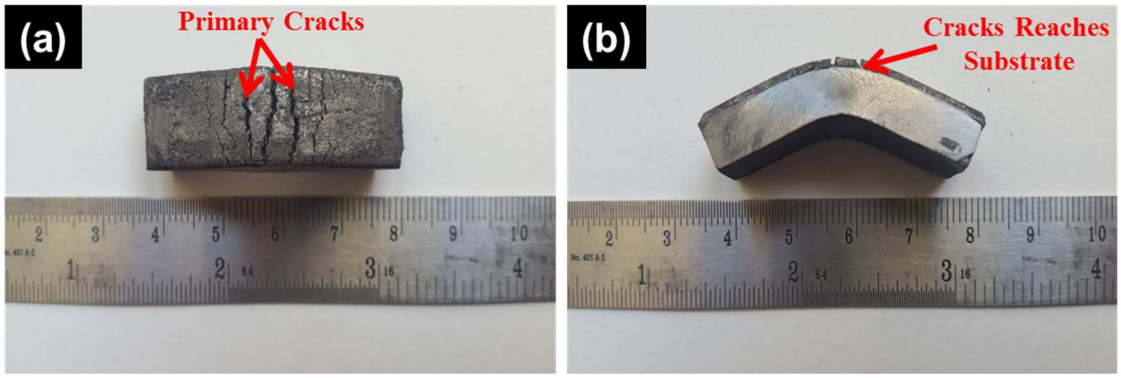

Figure 6.19 Photographs of the fractured clad specimen after three points bend test of showing (a) Top view of Ni-Based/20Cr_3C_2-20Mo composite clad (b) Side view of Ni-Based/20Cr_3C_2-20Mo composite clad

The SEM micrographs illustrated in Fig. 4.20 (a), (b), and (c), which reveals the formation of primary cracks, secondary cracks and detached carbides during flexural testing. These primary cracks grew under continuous loading and reach the substrate. However, one interesting observation was found during flexural testing that, clad layers did not get peeled off from the substrate, which confirms the presence of metallurgical bonding between the substrate and the clad layer.

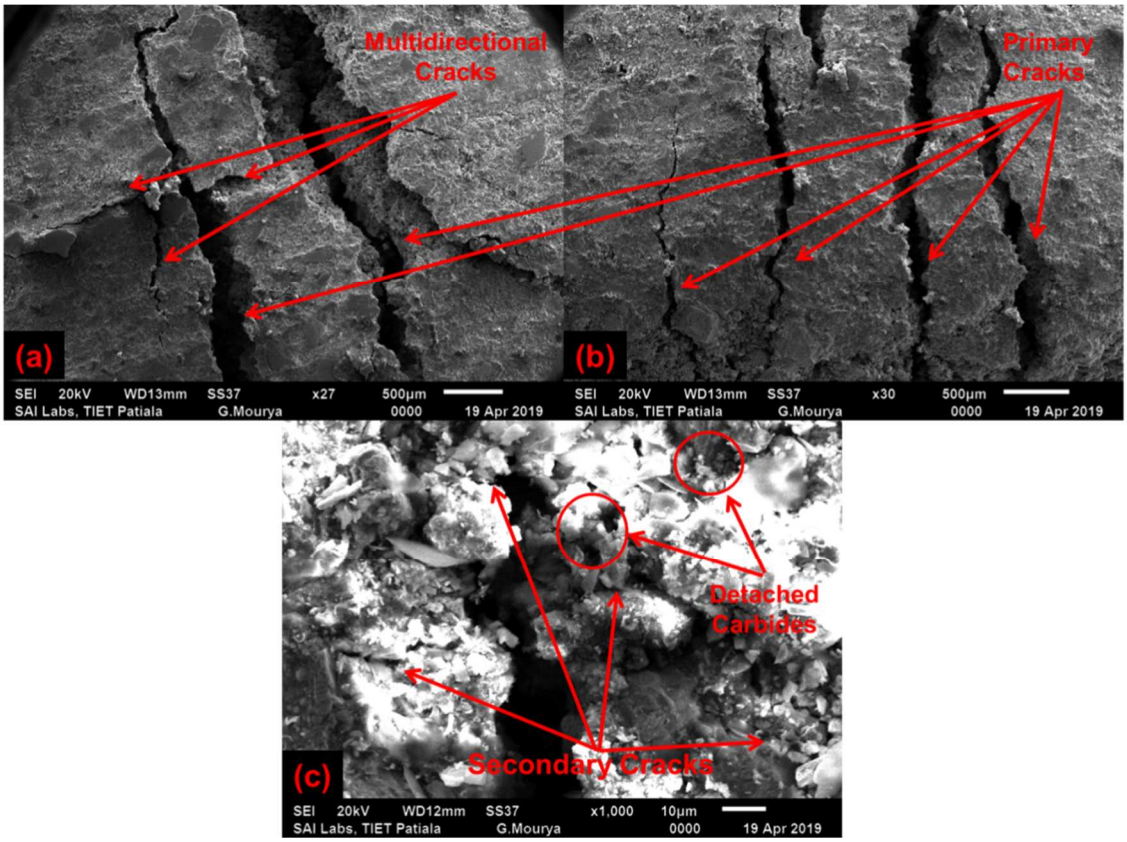

Figure 6.20 SEM micrographs of the fractured specimen of Ni-Based/20Cr_3C_2-20Mo composite clad after three-point bend test showing (a) Multidirectional Cracks (b) Primary cracks (c) Secondary cracks

Chapter 7

Functional Characterization: Results & Discussion

7.1 Introduction to Chapter

This chapter presents the results of the functional characterization of the microwave processed clads. The initial sections present the results of cavitation erosion parametric study of SS-316, Ni-based/40Cr_3C_2 clad, Ni-based/20Cr_3C_2-20Mo clad in terms of weight loss. Further, the effect of various parameters on cavitation erosion behaviour has been discussed in detail. The following sections report the fractographic analysis of the worn surfaces was carried out using SEM to know the mechanism of failure. Whereas the last section represents the results of a comparative study of physical, mechanical, metallurgical and tribological properties of various materials has been incorporated.

7.2 Results of Parametric Study of Cavitation Erosion Behaviour of SS-316 and Developed Clads

The Cavitation erosion testing was conducted, according to the Taguchi L9 orthogonal array on the stainless steel-316 substrate and on developed Ni-based/40Cr_3C_2 & Ni-based/20Cr_3C_2-20Mo composite clads. The experimental results obtained in terms of cumulative mass loss (CML) or cumulative weight loss (CWL) were further converted in other terms like cumulative volume loss (CVL), cavitation erosion rate (CER); mean depth of erosion (MDE), means erosion rate (MER), and incubation time (IBT), so that the results of various tested materials can be effectively compared. The calculation of the above-mentioned terms has been carried using the following relations (as per ASTM G32-17 Standards):

i. **Volume loss or CVL (mm^3)** = $\frac{\Delta W}{\rho} \times 1000$, Where, ΔW is weight loss in mg and ρ is density in g/cm^3.

ii. **CER (mg/h)** = $\frac{\Delta W}{\Delta t}$, Where, ΔW is weight loss in mg and Δt is time interval in hours.

iii. **MDE (µm) =** $\frac{\Delta W}{10\times\rho\times A}$ **,** and **MER (µm/h) =** $\frac{\Delta W}{10\times\rho\times A\times\Delta t}$ **,** Where, ΔW is weight loss in mg, ρ is the density of the material in g/cm^3, A is the area of eroded specimen in cm^2 (In current study it is taken equal to area of the ultrasonic horn, Diameter of horn = 1.5 cm and area = πr^2 = 1.77 cm^2 or 176.7 mm^2).

iv. **IBT (Minutes/Hours) =** Incubation period is the initial stage of the cavitation erosion, where the cavitation erosion is zero or very small as compared to later stages. Till incubation period, material under cavitation testing possesses higher resistance to impingement jets. In the present study, the period up to which, only 10% weight loss has occurred is taken as the incubation period, because initially, the material possesses a lower cavitation erosion rate.

7.2.1 Results of Parametric Study of Cavitation Erosion Behaviour of SS-316

The cavitation erosion testing has been carried out, according to Taguchi L9 orthogonal array (with optimization goal- larger is better). The Taguchi L9 orthogonal array has four columns, where three columns are assigned to each parameter or control factor (SOD-standoff distance, AMP-Amplitude and IMD-immersion depth) and the fourth column is assigned to the error. The experimental results of cavitation testing of stainless steel-316 are tabulated in Table 7.1.

Table 7.1: Cavitation erosion study experimentation results or response data for SS-316

Run Order	SOD (mm)	AMP (µm)	IMD (mm)	CML (mg)	CVL (mm^3)	CER (mg/h)	MDE (µm)	MDER(µm/h)	IBT (Min)
1	0.5	40	80	18.3	2.3	3.0	8.2	1.4	86.36
2	0.5	50	100	19.3	2.4	3.2	8.7	1.4	87.8
3	0.5	60	120	21.4	2.7	3.6	9.7	1.6	48.8
4	1	40	100	13.4	1.7	2.2	6.0	1.0	94.7
5	1	50	120	14.1	1.8	2.4	6.4	1.1	90.2
6	1	60	80	21.0	2.6	3.5	9.5	1.6	64.1
7	1.5	40	120	5.3	0.7	0.9	2.4	0.4	174.8
8	1.5	50	80	13.1	1.6	2.2	5.9	1.0	89.5
9	1.5	60	100	14.4	1.8	2.4	6.5	1.1	90.8

The highest mass loss in SS-316 has occurred at test parameters set-3 (SOD- 0.5 mm, AMP- 60 µm and IMD- 120 mm). At test, parameter set-3 the SS-316 has an incubation

period of 48.8 minutes and mean erosion rate of 1.6µm/h. However, out of all measured and calculated responses, the cumulative mass loss was selected as the response variable for statistical analysis and mathematical modelling, although it is a most commonly used response variable in cavitation studies by researchers. The plot of cumulative mass loss as a function of cavitation erosion test time for all 9 stainless steel-316 specimens is shown in Figure 7.1; it reveals that with the increase in cavitation erosion time the CER increases drastically. The steady or constant erosion rate has been observed in the initial phase, or till cavitation erosion testing of 2 hours. Whereas many steep slopes also have been observed in the plot after 2 hours of cavitation erosion, this confirms the higher erosion rate at later stages during cavitation phenomena.

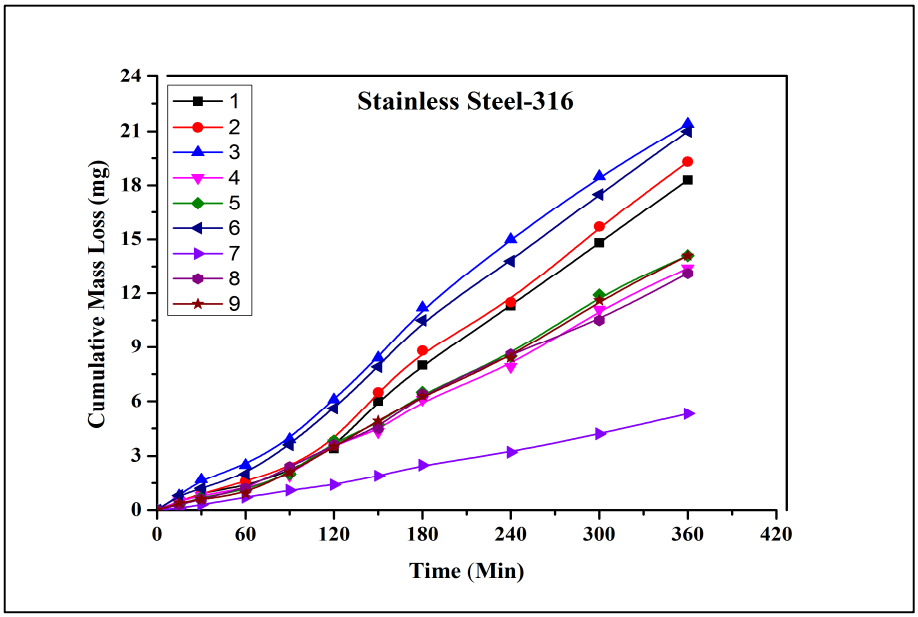

Figure 7.1 Cumulative mass loss as a function of cavitation erosion test time (SS-316)

7.2.2 Results of Statistical Analysis of Cavitation Erosion Behaviour of SS-316

The main effect plot of test parameters is shown in Figure 7.2. In the main effect plot if the line is near to horizontal axis the parameter of control factor has less effect on the response. Where, if the line is more incline with a horizontal axis that mean factor have a significant effect on the response.

Figure 7.2 reveals that the SOD and AMP have a more significant effect on mass loss of SS-316 because the lines are more incline form the horizontal axis. Also, it has been observed that the with the increase in SOD the mass loss in SS-316 decreases

drastically, and with the increase of AMP, the mass loss increases sharply, whereas with the increase in IMD the mass loss has decreased a little. However, the average mass loss of 15.5 mg has been observed in SS-316.

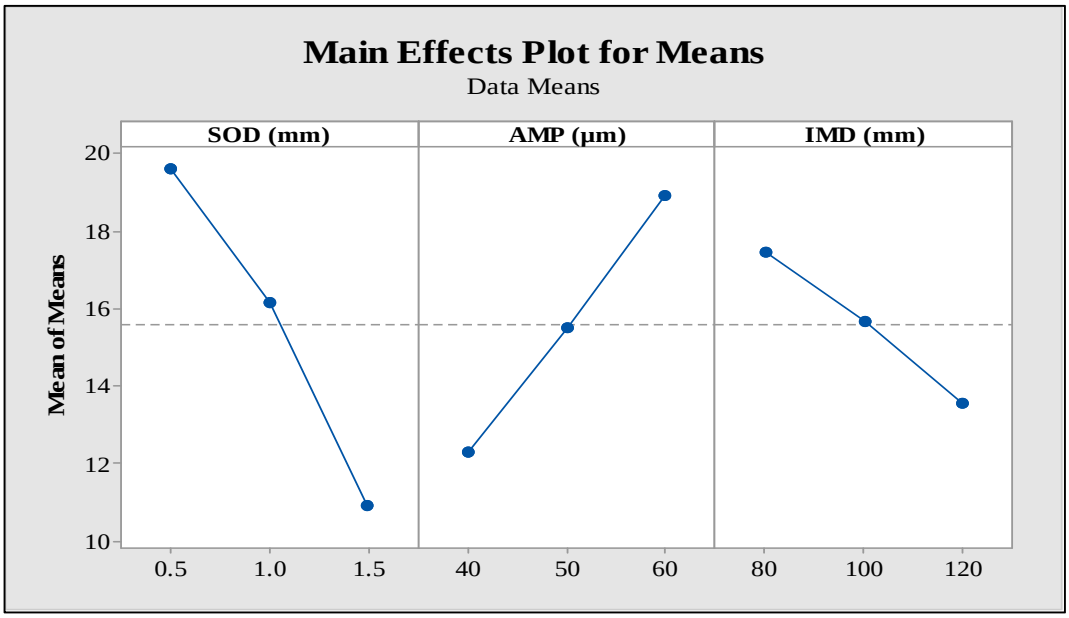

Figure 7.2: Main effect plots for cumulative weight loss for SS-316

Further, the Analysis of Variance (ANOVA) has been performed to identify the significance of the test parameters on cumulative mass loss (cavitation erosion of the material) or which test parameter is critically important for the response. The analysis has been carried out at a 95% confidence level. Hence, the parameter with a p-value less than 0.05 will be considered as a significant parameter. The analysis has been performed using Minitab 17.0 software. Table 7.2 shows the obtained ANOVA results for mass loss in SS-316. It is observed from the ANOVA table that all the test parameters or control factors have a significant effect of the response and important role in mass loss of the SS-316. However, the contribution of SOD, AMP and IMD in mass loss of SS-316 is 56.34%, 32.16%, and 11.02%, respectively. The immersion depth has less effect on mass loss as compared to standoff distance and amplitude. Moreover, the cavitation erosion is difficult phenomena and it is not fully understood yet, because many other factors influence it, and it works simultaneously. These factors include target material properties, frequency of the ultrasonic horn, the temperature of test liquid and machine error. Where the error is least influenced by the selected control factors in the current study, it might be due to the fact that, in current study the cavitation testing

has been carried out for 6 hours (360 Minutes) at 20 kHz frequency, which is almost 360×20000 = 7200000 cycles, hence the influence of machine error, if any, is suppressed due to a large number of cycles. The SOD is the most influential parameter for mass loss of the SS-316 and that can be seen from the second last column of Table 7.2.

Table 7.2: ANOVA table for CML (SS-316) - Taguchi L9 Array Analysis at 95% confidence level

Source	DF	Seq SS	Adj SS	Adj MS	F	P	Percentage Contribution
SOD (mm)	2	115.358	115.358	57.6788	122.59	0.008	56.34
AMP (µm)	2	65.858	65.858	32.9288	69.99	0.014	32.16
IMD (mm)	2	22.566	22.566	11.283	23.98	0.04	11.02
Residual Error	2	0.941	0.941	0.4705			0.45
Total	8	204.722					

The Response table for mass loss of SS-316, the mean value of the mass loss at the different levels is listed in Table 7.3. The response helps in the analysis of the effect of test parameters or control factors based on delta statistics. Where, the delta statistics depend on the highest mean value minus the lowest mean value of the individual factors. Also, the delta grades are assigned to factors on the basis of these values. A larger delta value stands for rank 1, the second largest for rank 2 and so on. In the current case, the most in dominating factor for mass loss of SS-316 are standoff distance (SOD) and amplitude (AMP), the delta value for SOD and AMP are 8.71 and 3.87, respectively.

Table 7.3: Response table for CML (SS-316)

Level	SOD (mm)	AMP (µm)	IMD (mm)
1	19.63	12.29	17.46
2	16.17	15.5	15.67
3	10.92	18.92	13.58
Delta	8.71	6.63	3.87
Rank	1	2	3

Further, the mathematical modelling of the mass loss has been done; the linear fit regression equation has been developed using Minitab 17.0. The obtained ANOVA table of regression analysis is presented in Table 7.4. All three parameters have a

significant effect on mass loss. The percentage contribution of SOD (55.56%) and AMP (32.15%) is relatively higher as compared to IMD (11.00%), which can be seen from the last column of Table 7.4. And the 1.27% contribution of error has been observed, which might be due to many uncontrollable factors like temperature rise in test liquid during cavitation erosion testing or machine error like fluctuation in frequency or amplitude. The Equation 7.1 can be used to compute the mass loss in stainless steel-316 at varying cavitation test parameters.

Table 7.4: ANOVA table for CML of SS-316 – Regression Analysis at a 95% confidence level

Source	DF	Adj SS	Adj MS	F	P	Percentage Contribution
SOD (mm)	1	113.753	113.753	217.9	0	55.56
AMP (µm)	1	65.836	65.836	126.11	0	32.15
IMD (mm)	1	22.523	22.523	43.14	0.001	11.00
Residual Error	5	2.61	0.522			1.27
Total	8	204.722				

$$\textbf{\textit{CML (mg)}} = 17.40 - 8.708 \times SOD + 0.3312 \times AMP - 0.0969 \times IMD \text{-----(7.1)}$$

The model summary of the regression equation is tabulated in Table 7.5, the R^2 (R-Square) value of the model is 98.72%, and it means that the developed regression model can fit into the 98.72% of the data points or the 98.72% data points are close to the developed linear equation. The R^2 (Predicted) came out to be 96.13%, which mean that the prepared mathematical model has an accuracy of results prediction up to 96.13%.

Table 7.5: Regression model summary for mass loss of SS-316

Model Summary			
S	**R-Sq**	**R-Sq(Adj)**	**R-Sq(Pred)**
0.722529	98.72%	97.96%	96.13%

The optimization of the test parameter is required to get the desired output. Hence, after the mathematical modelling, the optimization of test parameters has been done by using delta statistics, considering the delta value as shown in the response table (Table 7.3), as the goal of the current work is to maximize the response (mass loss). And Table 7.3 exhibits that, the average mass loss is maximum at 0.5 mm SOD, 60 µm AMP and 80 mm IMD i.e. 19.63 mg, 18.92 mg, and 17.46 mg, respectively. Therefore, the 0.5 mm

SOD, 60 µm AMP, and 80 mm IMD is chosen as the optimum test parameters. Thereafter the prediction calculation at a 95% confidence level for mass loss at optimal parameter has been done; the prediction model summary at optimal test parameters is tabulated in Table 7.6. Table 7.6 reveals that values of the mass loss at optimal values must lies between 22.7 to 27.8 mg. These values can be further utilized to compare the results of the confirmatory or validatory experiments.

Table 7.6: Predicted values for mass loss of SS-316 at a 95% confidence level

Prediction Model Summary			
Variable Input (SOD-0.5 mm, AMP-60 µm, IMD-80 mm)			
Fit	**SE Fit**	**95% CI**	**95% PI**
25.1736	0.564827	(23.7217, 26.6255)	(22.8161, 27.5311)

7.2.3 Results of Parametric study of Cavitation Erosion Behaviour of Ni-Based/40Cr_3C_2 Composite Clad

Similarly, the developed Ni-based/40Cr_3C_2 composite clad has been examined for cavitation erosion behaviour. The total 9 experiments have performed, according to L9 Taguchi orthogonal array. The results gained from the parametric study of developed Ni-based/40Cr_3C_2 composite clad are presented in Table 7.7. It can be observed from the experimental results that maximum mass loss of 2.8 mg has occurred at parametric set-3, at that particular parameters set the Ni-based/40Cr_3C_2 composite clad has an incubation period of 287.42 minutes and mean erosion rate of 0.21 µm per hour.

Table 7.7: Cavitation erosion study experimentation results or response data for Ni-based/40Cr_3C_2 composite clad

Run Order	**SOD (mm)**	**AMP (µm)**	**IMD (mm)**	**CML (mg)**	**CVL (mm^3)**	**CER (mg/h)**	**MDE (µm)**	**MDER(µm/h)**	**IBT (Min)**
1	0.5	40	80	2.4	0.30	0.40	1.09	0.18	319.4
2	0.5	50	100	2.5	0.31	0.42	1.13	0.19	300.8
3	0.5	60	120	2.9	0.35	0.47	1.27	0.21	278.42
4	1	40	100	1.7	0.21	0.28	0.77	0.13	>360
5	1	50	120	1.8	0.23	0.30	0.81	0.14	>360
6	1	60	80	2.8	0.35	0.47	1.27	0.21	280.8
7	1.5	40	120	0.6	0.08	0.10	0.27	0.05	>360
8	1.5	50	80	1.7	0.21	0.28	0.77	0.13	>360
9	1.5	60	100	1.8	0.23	0.30	0.81	0.14	>360

The Figure 7.3 shows that cumulative mass loss as a function of cavitation exposure time, the Ni-based/40Cr_3C_2 composite clad exhibits steady-state erosion till 120 minutes at parameters set-3, where the steady-state erosion period at other parametric sets is even more. Moreover, the mass loss in the developed Ni-based/40Cr_3C_2 composite clad is lesser as compared to SS-316 at all experimental conditions. Where the few experimental conditions are found not that appropriate to cause significant damage to the developed Ni-based/40Cr_3C_2 composite clad in the 6 hours of cavitation erosion testing. The Ni-based/40Cr_3C_2 composite clad exhibits 7.6 time lesser mass loss as compared to SS-316 at same experimental conditions.

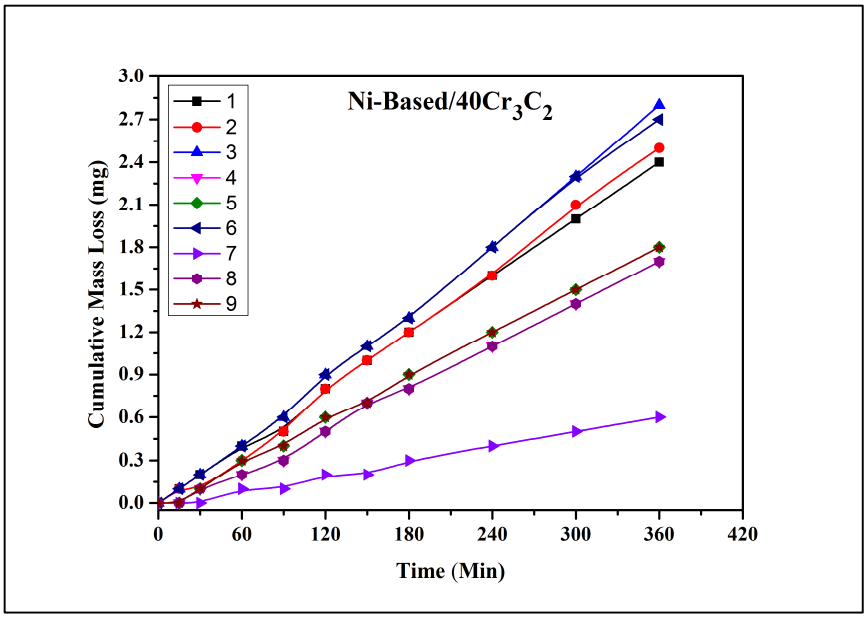

Figure 7.3: Cumulative mass loss as a function of cavitation erosion test time (Ni-based/ 40Cr_3C_2 composite clad)

7.2.4 Results of Statistical Analysis of Cavitation Erosion Behaviour of Ni-Based/40Cr_3C_2 Composite Clad

Figure 7.4 shows the graphical effect of all three test parameters. From Figure 7.4, it can be observed that with the increase of SOD the mass loss decreases drastically, whereas with the increase in AMP the abrupt increase in the mass loss was observed. However, the minimal decrease in mass loss has been observed from the main effect plot with the increase of IMD.

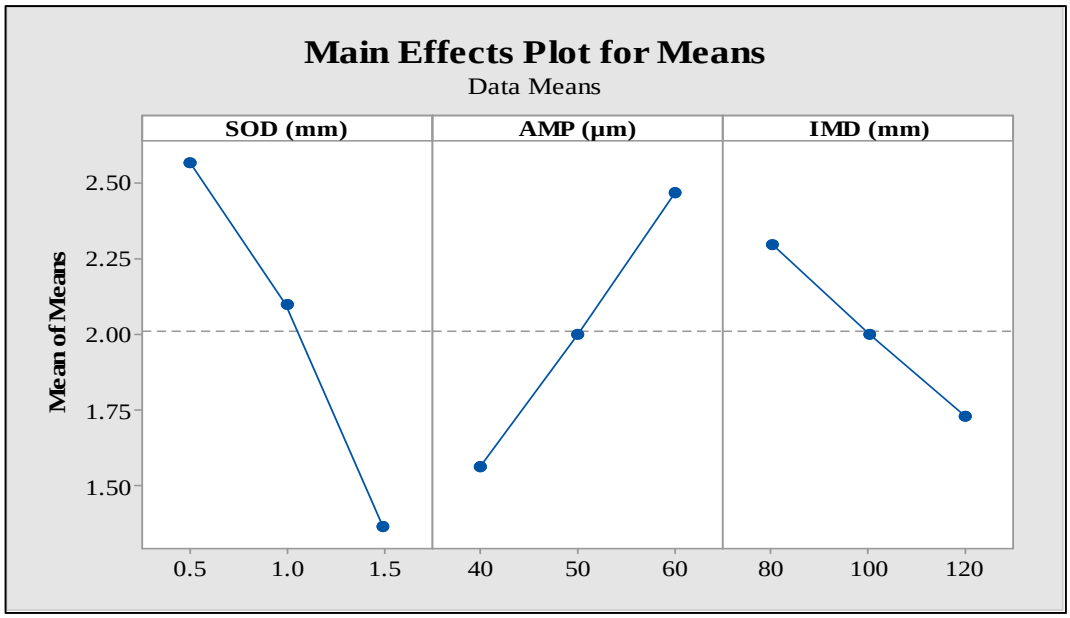

Figure 7.4: Main effect plots for cumulative weight loss for Ni-based/40Cr_3C_2 composite clad

The cavitation testing results of Ni-based/40Cr_3C_2 composite clad was analyzed statistically by using Minitab 17.0. The purpose of statistical analysis is to figure out which tests parameter has significantly affected the cavitation erosion characteristics or response (mass loss). The statistical analysis has been carried out at 95% confidence level. Table 7.8 shows the results of ANOVA analysis of CML of Ni-based/40Cr_3C_2 composite clad. From the ANOVA table, it has been observed that all of three test parameters are statistically and physically significant, as the p-value of all three test parameters is less than 0.05. The percentage influence of SOD on response is more as compare to AMP and IMD, as the percentage contribution of SOD is 56.16%, where the percentage contribution of AMP and IMD is 31.09% and 12.33%, respectively. Where, the percentage influence of the error is only 0.39%, which might be due to experimental fluctuations like temperature rise of test liquid while cavitation erosion testing or weighing machine error). It has been reported that the temperature of test liquid significant affects the cavitation erosion of the material **[158].**

Table 7.8: ANOVA table for CML (Ni-based/40Cr_3C_2) - Taguchi L9 Array Analysis at 95% confidence level

Source	DF	Seq SS	Adj SS	Adj MS	F	P	Percentage Contribution
SOD (mm)	2	2.19556	2.19556	1.09778	141.14	0.007	56.16
AMP (µm)	2	1.21556	1.21556	0.60778	78.14	0.013	31.09
IMD (mm)	2	0.48222	0.48222	0.24111	31	0.031	12.33
Residual Error	2	0.01556	0.01556	0.00778			0.39
Total	8	3.90889					

Further, the results are examined via delta statistics, the results of delta analysis are tabulated in Table 7.9. The procedure of the delta analysis was already discussed in section 7.2.2. In the current case, the delta value of the SOD is higher (1.2) as compared to AMP (0.9) and IMD (0.5). Hence, it confirms that the SOD has more effect on mass loss during cavitation erosion testing of Ni-based/40Cr_3C_2 composite clad, followed by AMP and IMD.

Table 7.9: Response table for CML (Ni-based/40Cr_3C_2 composite clad)

Level	SOD (mm)	AMP (µm)	IMD (mm)
1	2.567	1.567	2.3
2	2.1	2	2
3	1.367	2.467	1.733
Delta	1.2	0.9	0.567
Rank	1	2	3

To set up the relation between mass loss and test parameter, the mathematical modelling of the mass loss has been done; the linear regression has been developed by regression analysis at 95% confidence level. The obtained ANOVA results of regression analysis are presented in Table 7.10. According to the analysis, the most important parameter with respect to mass loss during cavitation erosion testing is SOD (55.25%), followed by AMP (31.08%) and IMD (12.33%).

Table 7.10: ANOVA table for CML of Ni-based/40Cr_3C_2 composite clad– Regression Analysis at a 95% confidence level

Source	DF	Adj SS	Adj MS	F	P	Percentage Contribution
SOD (mm)	1	2.16	2.16	206.81	0	55.25
AMP (µm)	1	1.215	1.215	116.33	0	31.08
IMD (mm)	1	0.48167	0.48167	46.12	0.001	12.33
Residual Error	5	0.05222	0.01044			1.33
Total	8	3.90889				

The following Equation (7.2) has been developed with an R^2 of 98.66% for mass loss of Ni-based/40Cr_3C_2 composite clad as a response variable using the least square method in Minitab 17.0. The summary of the prepared mathematical model is tabulated in Table 7.11. The developed model has R^2 (predicted) 96.18%, which mean the developed model, can predict 96.18% correct results in future, within the same domain.

$$\boldsymbol{CML\ (mg)} = 2.378 - 1.2 \times SOD + 0.045 \times AMP - 0.01417 \times IMD \text{---------(7.2)}$$

Table 7.11: Regression model summary for mass loss of Ni-based/40Cr_3C_2 composite clad

Model Summary			
S	**R-Sq**	**R-Sq(Adj)**	**R-Sq(Pred)**
0.102198	98.66%	97.86%	96.18%

As the goal of the current work is to maximize the response or mass loss, hence it is required to perform the cavitation testing at the optimized test parameters and it is clear from the response table (Table 7.9) that the average mass loss is maximum at 0.5 mm SOD, 60 µm AMP and 80 mm IMD i.e.2.5 mg, 2.4 mg, 2.3 mg, respectively.

Hence, 0.5 mm SOD, 60 µm AMP and 80 mm IMD was come out to be optimum cavitation erosion test parameters. The prediction calculation has been carried out at optimum parameters in Minitab 17.0 software at 95% confidence level. The predication modelling details are summarized in Table 7.12. As per prediction calculations at the optimized experimental condition, the value of mass loss must lies between 3.01 to 3.6 mg for Ni-based/40Cr_3C_2 composite clad. To verify the prediction, model the

confirmatory experiments have been carried out and the results of confirmatory experiments are presented in section 7.3.

Table 7.12: Predicted values for mass loss of Ni-based/40Cr_3C_2 at a 95% confidence interval

Prediction Model Summary			
Variable Input (SOD-0.5 mm, AMP-60 µm, IMD-80 mm)			
Fit	**SE Fit**	**95% CI**	**95% PI**
3.34444	0.0798919	(3.13908, 3.54981)	(3.01099, 3.67790)

7.2.5 Results of Parametric study of Cavitation Erosion Behaviour of Ni-Based/20Cr_3C_2-20Mo Composite Clad

Similarly, the experimental cavitation erosion testing was conducted, according to Taguchi L9 design plan for Ni-based/20Cr_3C_2-20Mo composite clad to assess the effect of cavitation test parameters SOD, AMP, and IMD on the CML of the Ni-based/20Cr_3C_2-20Mo composite clad. Table 7.13 illustrates the experimental results of the CML, CVL, CER, MDE, MDER and IBT. It has been observed that the maximum mass loss has occurred at test parameters set-3, which is 1.6 mg. The mean erosion rate at those particular experimental conditions is 0.12 µm per hour. The incubation period for Ni-based/20Cr_3C_2-20Mo composite clad at all experimental conditions is more than the 360 minutes or 6 hours.

Table 7.13: Cavitation erosion study experimentation results or response data for Ni-based/20Cr_3C_2-20Mo composite clad

Run Order	**SOD (mm)**	**AMP (µm)**	**IMD (mm)**	**CML (mg)**	**CVL (mm^3)**	**CER (mg/h)**	**MDE (µm)**	**MDER (µm/h)**	**IBT (Min)**
1	0.5	40	80	1.2	0.14	0.20	0.59	0.10	>360
2	0.5	50	100	1.4	0.16	0.23	0.69	0.12	>360
3	0.5	60	120	1.6	0.18	0.27	0.79	0.13	>360
4	1	40	100	0.7	0.08	0.12	0.35	0.06	>360
5	1	50	120	0.9	0.10	0.15	0.44	0.07	>360
6	1	60	80	1.2	0.14	0.20	0.59	0.10	>360
7	1.5	40	120	0.2	0.02	0.03	0.10	0.02	>360
8	1.5	50	80	0.5	0.06	0.08	0.25	0.04	>360
9	1.5	60	100	0.6	0.07	0.10	0.30	0.05	>360

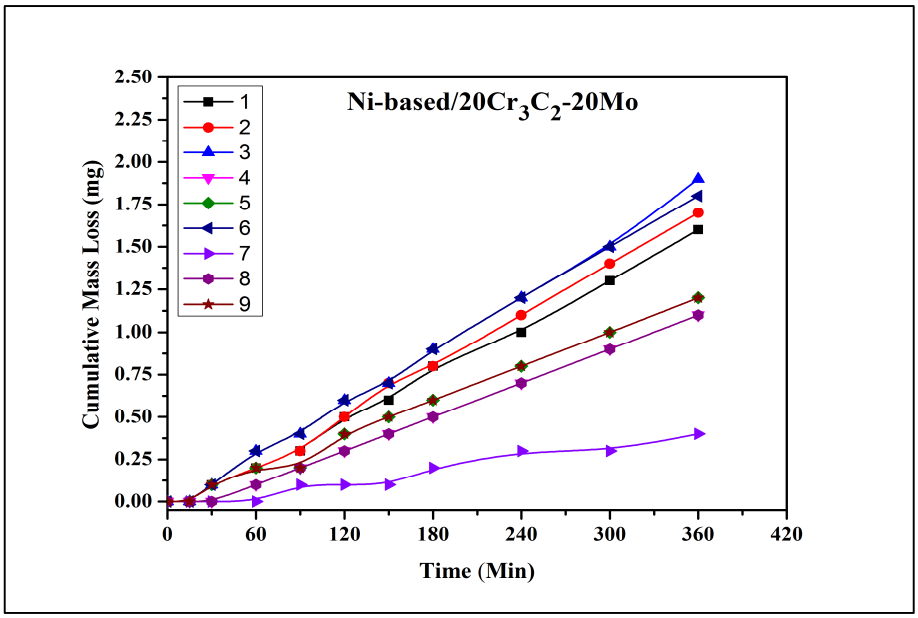

Figure 7.5: Cumulative mass loss as a function of cavitation erosion test time (Ni-based/ 20Cr_3C_2-20Mo composite clad)

The results of cumulative mass loss of Ni-based/20Cr_3C_2-20Mo composite clad with respect to cavitation time during cavitation erosion experiments are shown in Figure 7.5. From the plot shown in Figure 7.5, it can be seen that the no mass loss was observed in the developed Ni-based/20Cr_3C_2-20Mo composite clad up to half-hour of cavitation testing, whereas at experimental conditions 7, 8, and 9 no mass loss has been observed until 30 min, 60 min, and 60 min of cavitation erosion testing, respectively.

7.2.6 Results of Statistical Analysis of Cavitation Erosion Behaviour of Ni-Based/20Cr_3C_2-20Mo Composite Clad

The varying effect of the cavitation test parameter on mass loss is illustrated in Figure 7.6, the main effect plots of the cavitation test parameters reveal that the mass loss decrease with the increase in SOD and IMD, whereas with the increase in AMP the decrease in mass loss was observed. The all main effect plots also show that the main effect in mass loss is due to the SOD and Amp, where the very little effect of immersion depth on the mass loss.

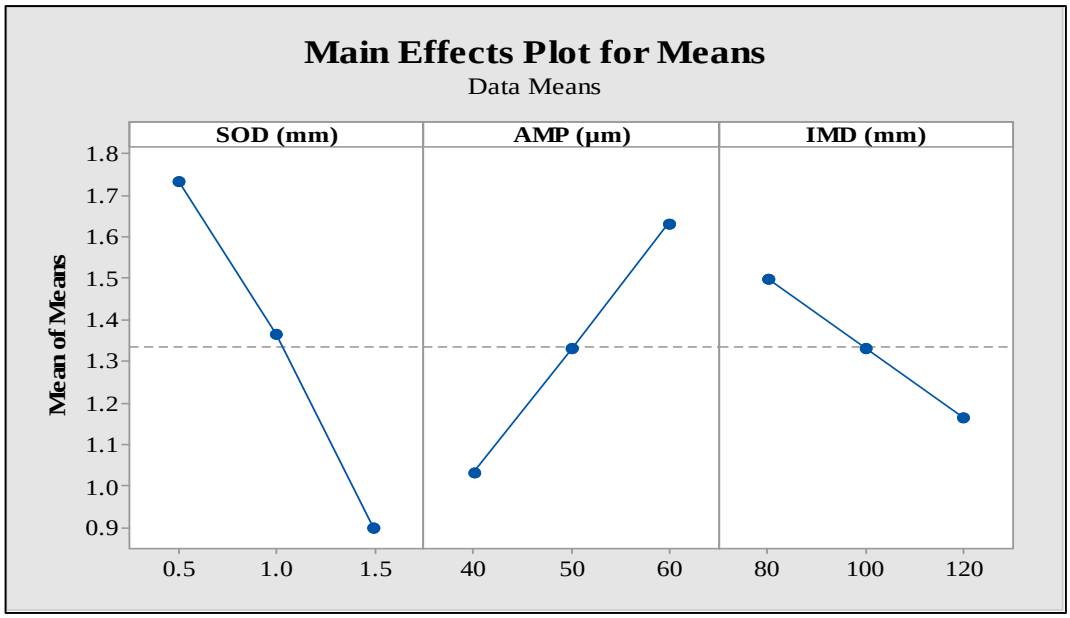

Figure 7.6: Main effect plots for cumulative weight loss for Ni-based/20Cr_3C_2-20Mo composite clad

To determine the statistical significance of the cavitation test parameters on mass loss of Ni-based/20Cr_3C_2-20Mo composite clad the ANOVA has performed at a confidence interval of 95%. The results of ANOVA for mass loss of Ni-based/20Cr_3C_2-20Mo composite clad are presented in Table 7.14. It can also be observed from the ANOVA table that all the selected test parameters are significant as the p-value for the all the test parameters is less than 0.05 and the SOD, AMP, and IMD affect the mass loss by 59.46%, 30.68%, and 9.46%, respectively.

Table 7.14: ANOVA table for CML (Ni-based/20Cr_3C_2-20Mo) - Taguchi L9 Array Analysis at 95% confidence level

Source	DF	Seq SS	Adj SS	Adj MS	F	P	Percentage Contribution
SOD (mm)	2	1.04667	1.04667	0.523333	157	0.006	59.46
AMP (µm)	2	0.54	0.54	0.27	81	0.012	30.68
IMD (mm)	2	0.16667	0.16667	0.083333	25	0.038	9.46
Residual Error	2	0.00667	0.00667	0.003333			0.37
Total	8	1.76					

The experimental results are further analyzed by using delta statistics method. The results of delta analysis are tabulated in Table 7.15.

Table 7.15: Response table for CML (Ni-based/20Cr_3C_2-20Mo composite clad)

Level	SOD (mm)	AMP (µm)	IMD (mm)
1	1.7333	1.0333	1.5
2	1.3667	1.3333	1.3333
3	0.9	1.6333	1.1667
Delta	0.8333	0.6	0.3333

The delta statistical analysis computes the difference between an average of response at the highest levels minus and averages of response at lowest levels, then the final delta values are obtained. The highest delta value is given as the rank 1, and the following values are given rank 2 and rank, so on. The delta values of SOD, AMP, and IMD are 0.83, 0.6 and 0.33, respectively. As the delta value of the SOD in highest, which mean the SOD have highest significance on the mass loss, followed by Amp and IMD.

After studying the effect of test cavitation test parameters, the mathematically modelling has been done, to develop the relation between response and the control variables. Therefore, the regression analysis has been carried out at a 95% confidence interval by using the least square method in Minitab 17.0 software. The obtained ANOVA results of the regression analysis are presented in Table 7.16. The following Equation (7.3) has been developed with R^2 of 99.34 %, and R^2 (predicted) of 97.87%. The model summary of the regression analysis is tabulated in Table 7.17.

$$\boldsymbol{CML\ (mg)} = 1.5 - 0.8333\ \times SOD + 0.030 \times AMP - 0.00833\ \times IM \text{--------(7.3)}$$

Table 7.16: ANOVA table for CML of Ni-based/20Cr_3C_2-20Mo composite clad– Regression Analysis at a 95% confidence level

Source	DF	Adj SS	Adj MS	F	P	Percentage Contribution
SOD (mm)	1	1.04167	1.04167	446.43	0	59.18
AMP (µm)	1	0.54	0.54	231.43	0	30.68
IMD (mm)	1	0.16667	0.16667	71.43	0	9.46
Residual Error	5	0.01167	0.00233			0.66
Total	8	1.76				

Table 7.17: Regression model summary for mass loss of Ni-based/20Cr_3C_2-20Mo composite clad

Model Summary			
S	**R-Sq**	**R-Sq(Adj)**	**R-Sq(Pred)**
0.048306	99.34%	98.94%	97.87%

The typical researcher would do experiments to obtain particular results from the processing or testing; nominal is better, lower is better, and higher is better. The mass loss in the Ni-based/20Cr_3C_2-20Mo composite clad is the response parameter used in this case. Hence, the goal of the current work is to maximize the response. Therefore, the optimization has been carried by using a delta response table (Table 7.15). On the basis of the delta analysis results, the 0.5 mm SOD, 60 mm AMP, and 80 mm came out to be optimum cavitation test parameter, for maximizing the mass loss.

Further, the prediction calculation has been carried out at optimum cavitation test parameters at a confidence level of 95%. The prediction model summary is tabulated in Table 7.18. As per prediction results, the mass loss of Ni-based/20Cr_3C_2-20Mo composite clad at optimum cavitation test condition must lie between 2.05 to 2.37, then the prepared mathematical model will consider as valid.

Table 7.18: Predicted values for mass loss of Ni-based/20Cr_3C_2-20Mo composite clad at a 95% confidence interval

Prediction Model Summary			
Variable Input (SOD-0.5 mm, AMP-60 µm, IMD-80 mm)			
Fit	**SE Fit**	**95% CI**	**95% PI**
2.21667	0.0377614	(2.11960, 2.31374)	(2.05906, 2.37428)

7.3 Effect of Test Parameters on Cavitation Erosion Behaviour of Materials

7.3.1 Effect of Stand of Distance on Cavitation Erosion Behaviour of Materials

The standoff distance can be defined as the distance between the ultrasonic horn and the specimen surface. The generated cavitation bubbles are directed downwards surface direction and are transported in the direction acoustic waves towards the specimen surface. And during fluctuation in pressure due to change direction of movement of the

ultrasonic horn the reversal of bubbles growth will take place and ultimately they explode and cause the formation of high-velocity micro jets and micro-jets impingement on material surface cause material damage [159]. However, it has been observed from the main effect plots shown in Figure 7.2, 7.4 and 7.6 that with the increase in standoff distance between the ultrasonic horn and specimen surface, the average mass loss in the specimens has decreased. At 0.5 mm SOD the shockwave produced by the ultrasonic horn has sufficient energy to direct most of the formed vapour bubble too wards specimen surface as shown in Figure 7.7 (a) and (b). Whereas at 1 mm SOD, that same shockwave energy is not that sufficient to transport the all cavitation bubble near to the specimen surface, the some of the bubbles get escaped from the bubbles stream as illustrated in Figure 7.7 (b).

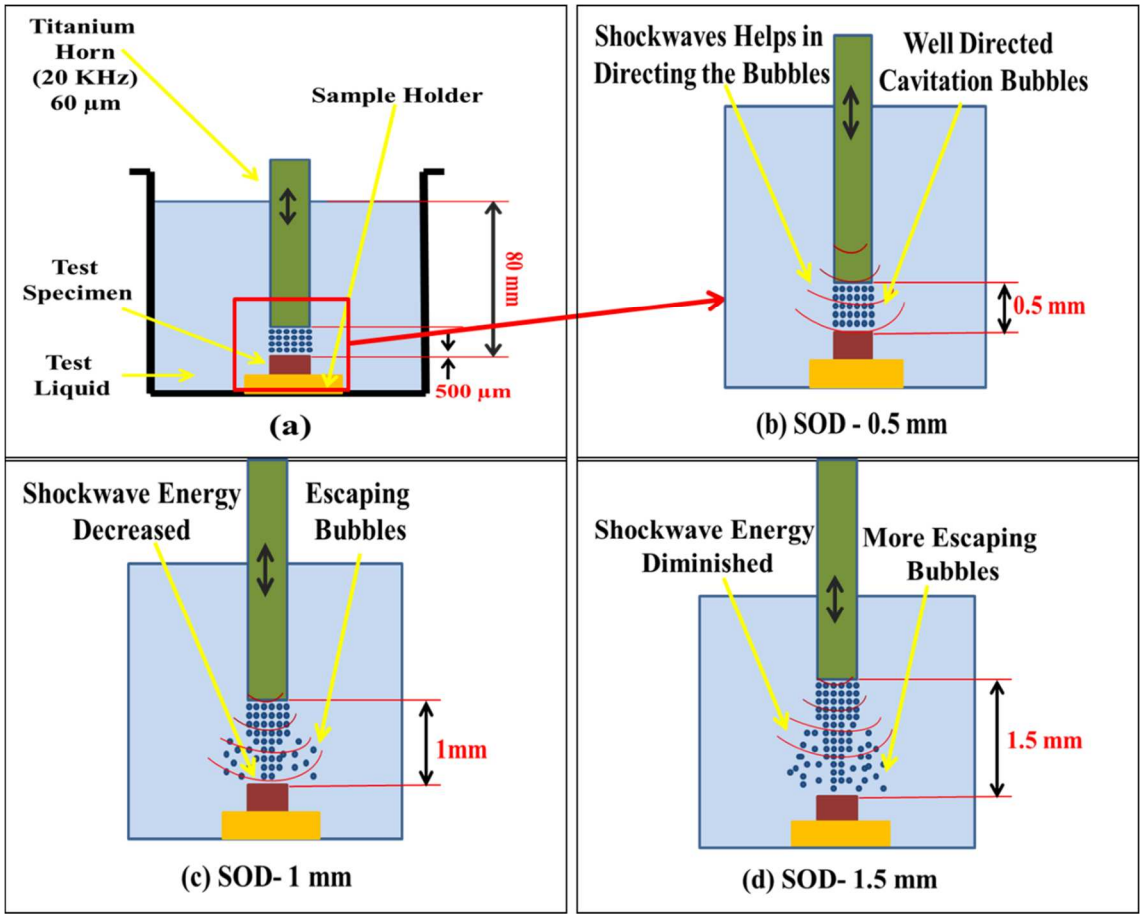

Figure 7.7 Schematic of (a) Cavitation bubbles behaviour at 0.5 mm SOD, 60 µm AMP and 80 mm IMD (b) Acoustic bubbles behaviour at 0.5 mm SOD (c) Acoustic bubbles behaviour at 1 mm SOD (d) Acoustic bubbles behaviour at 1.5 mm SOD

Hence due to the fewer bubbles near the surface of the specimen, the fewer micro-jets will form near the surface of the specimen and the lesser damage to material and less average mass loss & higher incubation period have been observed as compared to 0.5 mm SOD. Similarly, when the SOD is 1.5 mm the more vapour bubbles will escape forming the bubbles stream as shown in Figure 7.7 (d) because the shockwave energy almost got diminished. Therefore, very less mass loss and very large incubation period have been observed at 1.5 mm SOD. It also has been reported that with the increase of SOD the shockwave velocity will decrease, which results in smaller pressure pulse, lesser acoustic pressure and low impact energy. Therefore, less material loss will take place in the specimen under cavitation erosion testing **[119, 160].**

7.3.2 Effect of Amplitude on Cavitation Erosion Behaviour of Materials

The intensity of the cavitation bubble collapse is strongly influenced by the amplitude of ultrasonic horn vibration. Figure 7.2, 7.4 and 7.6 shows the effect of amplitude on mass loss on the SS-316, Ni-based/40Cr_3C_2 composite clad, Ni-based/20Cr_3C_2-20Mo composite clad at a vibratory frequency of 20 kHz. The amplitude of vibration can be directly related to the number of vapour bubbles generated and the intensity of the collapse pressure. Due to the smaller negative cycles, the cavitation bubble grows smaller and less intense when they collapse, while in larger negative cycles the cavitation bubble grows larger, and collapse at higher pressure when the pressure is recovered to a certain value, above vapour pressure at that particular temperature **[161].** Hence, in the current study, at larger amplitude 60 µm, it has been observed that the more vapour bubbles have formed due to large negative cycle and high velocity of the ultrasonic horn velocity as shown in Figure 7.8 (a) and (b). Therefore, large mass loss and smaller incubation period in materials have been observed. However, at the 50 µm amplitude, due to the medium negative cycle, the moderate number of vapour bubbles has formed as shown in Figure 7.8 (c), therefore, the less average mass loss and moderate incubation period have been observed. When the amplitude is 40 µm, the very few vapour bubbles will form due to the very small negative cycle as shown in Figure 7.8 (d). Hence, very little mass loss and large incubation period have been observed at the 40 µm amplitude.

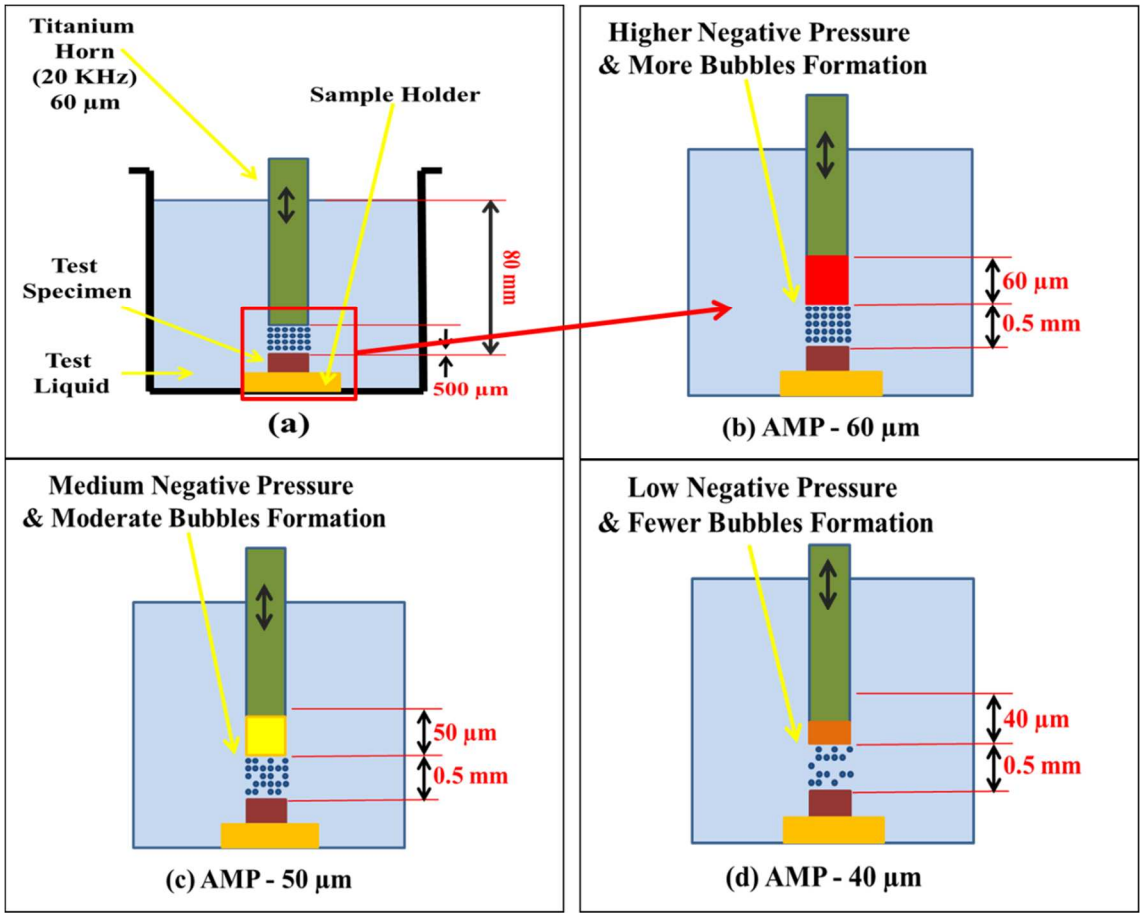

Figure 7.8 Schematic of (a) Cavitation bubbles behaviour at 0.5 mm SOD, 60 µm AMP and 80 mm IMD (b) Acoustic bubbles behaviour at 60 µm AMP (c) Acoustic bubbles behaviour at 50 µm AMP (d) Acoustic bubbles behaviour at 40 µm AMP

7.3.3 Effect of Immersion Depth on Cavitation Erosion Behaviour of Materials

Figure 7.2, 7.4 and 7.8 shows the influence of the depth of the horns immersed into the test liquid. Experimental results reveal that at an immersion depth of 80 mm, the larger mass loss has been observed than at 100 mm and 120 mm. The increase in cavitation bubbles strongly depends on the static fluid pressure. At higher static pressures, the acoustic pressure amplitude must be greater to create negative pressure for bubble growth. Therefore, it is more difficult to facilitate the growth of bubbles by introducing more test liquid into the container [119]. Hence, in the present work when the immersion depth is 80 mm the static pressure is 78.31 Pa, which is less compares to static pressure at an immersion depth of 100 mm (97.38 Pa) and 120 mm (117.76 Pa). Therefore, the more average mass loss has been observed at 80 mm IMD as compared to 100 and 120 mm IMD. The reason attributed to the lesser mass loss at 100 mm and

120 mm is less bubble formation at higher immersion depth. The schematics of the cavitation bubble behaviour at a varying immersion depth of the ultrasonic horn are shown in Figure 7.9 (a-d).

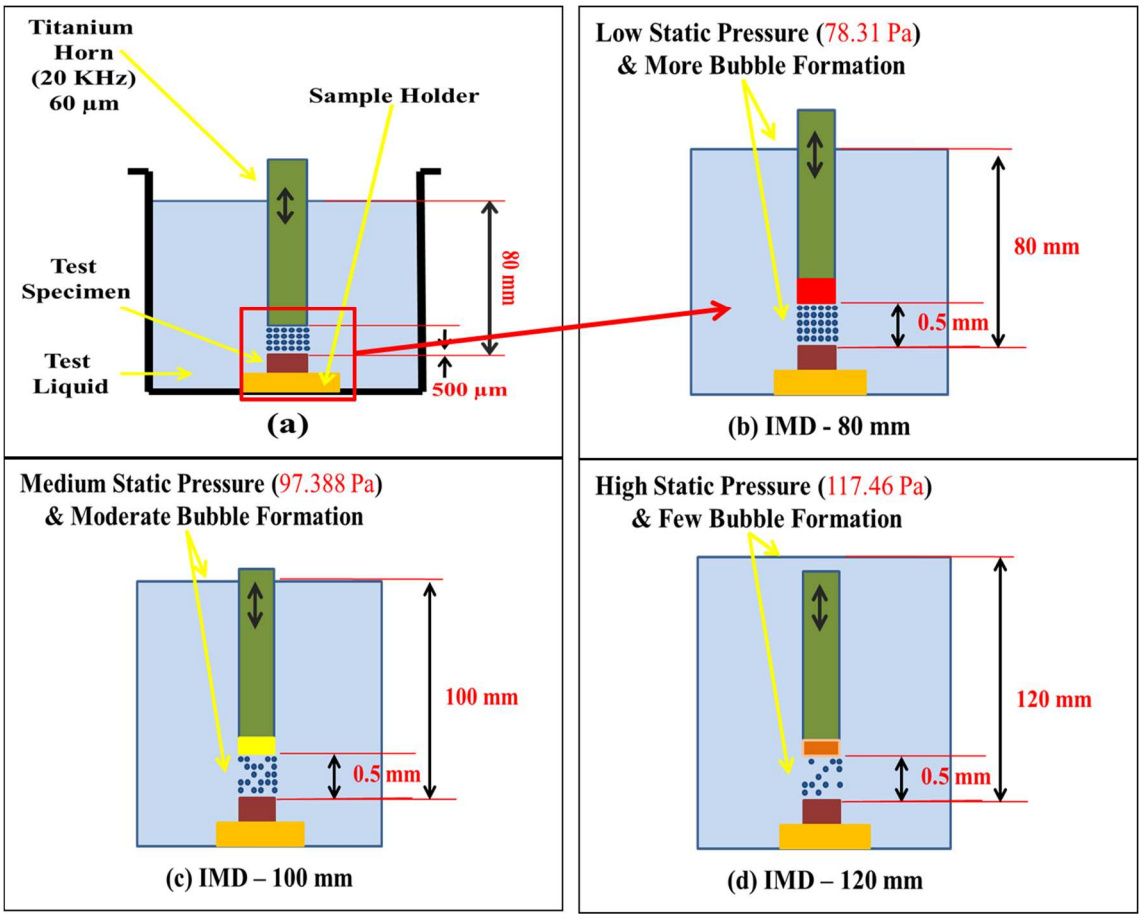

Figure 7.9: Schematic of (a) Cavitation bubbles behaviour at 0.5 mm SOD, 60 µm AMP and 80 mm IMD (b) Acoustic bubbles behaviour at 80 mm IMD (c) Acoustic bubbles behaviour at 100 mm IMD (d) Acoustic bubbles behaviour at 120 mm IMD

7.4 Fractrographic Analysis of Worn Surfaces of Materials

To extensively analyze the cavitation erosion mechanism, the fractographic analysis of the eroded specimens has been carried out. The results of the fractographic analysis of SS-316, Ni-based/40Cr_3C_2 composite clad and Ni-based/20Cr_3C_2-20Mo composite clad are presented in section 7.4.1, 7.4.2 and 7.4.3, respectively.

7.4.1 Fractographic Analysis of Worn Surface of SS-316 Specimens

Figure 7.10 (a) shows the surface topography of the SS-316 before cavitation erosion, as it can be seen that the surface is well polished and starch free before the cavitation erosion testing. Where Figure 7.10 (b), (c), and (d) show the surface of eroded SS-316 specimen, which was tested at parametric set-3, 5, and 7, respectively.

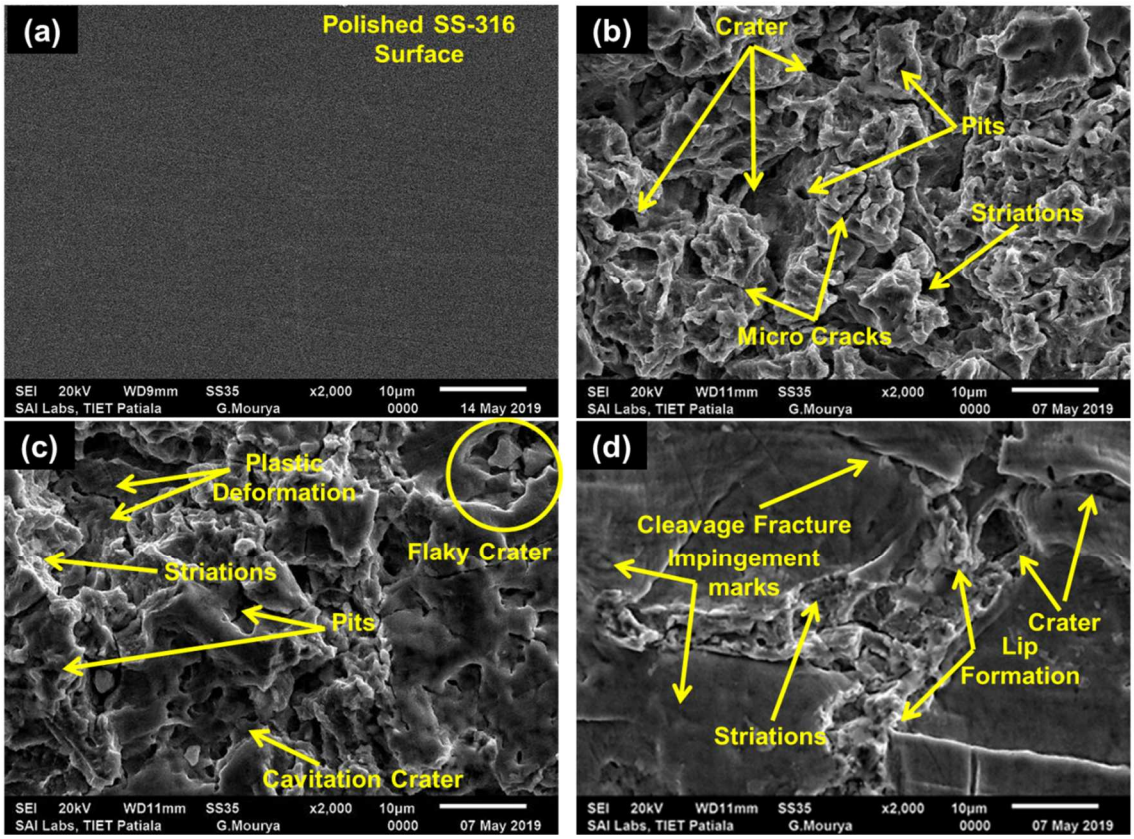

Figure 7.10: Typical SEM Micrographs showing surface topography of SS-316 (a) Before cavitation erosion (b) After cavitation erosion at 0.5 mm SOD, 60 µm AMP & 120 mm IMD (c) After cavitation erosion at 1 mm SOD, 50 µm AMP & 120 mm IMD (d) After cavitation erosion at 1.5 mm SOD, 40 µm AMP & 120 mm IMD

Figure 7.10 (b) reveals that, at parametric conditions no.3, the SS-316 was severely damaged by the vapour bubbles during cavitation erosion testing for 6 hours. Therefore, the large number of wide crater, pits, micro cracks and striations has been observed through the SEM micrograph. The presence of striation and micro-cracks confirms that the SS-316 got damaged due to heavy impact loading on SS-316, because of the explosion of the cavitation bubbles, which initially leads to plastic deformation and at later stages when the impact energy is more than the material capacity, the material

fracture will occur. Whereas Figure 7.10 (c) reveals that moderate amount damage in the form pits, flaky craters, cavitation crater and striation has occurred in stainless steel specimen at parameter set no. 5, as the SOD has increased and amplitude has decreased, the fewer and less intense vapour bubbles will able to reach the specimen surface. However, on the specimen tested at parametric set no.7 (1.5 mm SOD, 40 µm, and 120 mm) the cleavage marks, impingement marks of impingement jet, small carter; fatigue striation and lip formation have been observed. From the Figure 7.10 (d), it has been clear that the material is under initial stages of cavitation erosion and due to the fact that, at larger SOD only few vapour bubbles will able to reach specimen surface, the most of the get escape from the sides. Hence, the localized cavitation erosion in the middle of the specimen has been observed.

7.4.2 Fractographic Analysis of Worn Surface of Ni-Based/40Cr_3C_2 Composite Clad Specimens

Figure 7.11 (a) shows the well-polished and scratch-free top surface of the developed Ni-Based/40Cr_3C_2 composite clad, the chromium carbide particles are uniformly dispersed in the Ni-matrix. Where, Figure 7.11 (b) of the top surface microwave processed Ni-Based/40Cr_3C_2 composite clad, showing the mixed mode of both brittle and ductile fracture tested at parametric set no.3. The matrix region of the clad is covered with small craters, striations and plastically deformed lips. At the same time, the explosion of cavitation bubbles has induced cracks in the hard carbide phase and intermetallic phase present in the clad. Whereas at the parametric set no.5, the severity of damage is less, therefore, only a few micro-cracks, minor pits, small extruded lips impingement marks, ploughing marks and fracture carbide can be seen from the Figure 7.11 (c). The crack formation along with the carbide phase and cleavage fracture has been observed in the specimen tested at parametric set no.7. From the Figure 7.11 (d), it is clear that impingement jet lacks sufficient amount of impact energy to cause considerable damage to microwave processed Ni-Based/40Cr_3C_2 composite clad, hence only localized carbide fracture, few impingement marks and pits in the matrix has been observed. According to mass loss results, the microwave processed Ni-Based/40Cr_3C_2 composite clad exhibits better CER, further the SEM micrographs confirms the same, the cavitation damage in the microwave processed Ni-Based/40Cr_3C_2 composite clad is little as compared to SS-316.

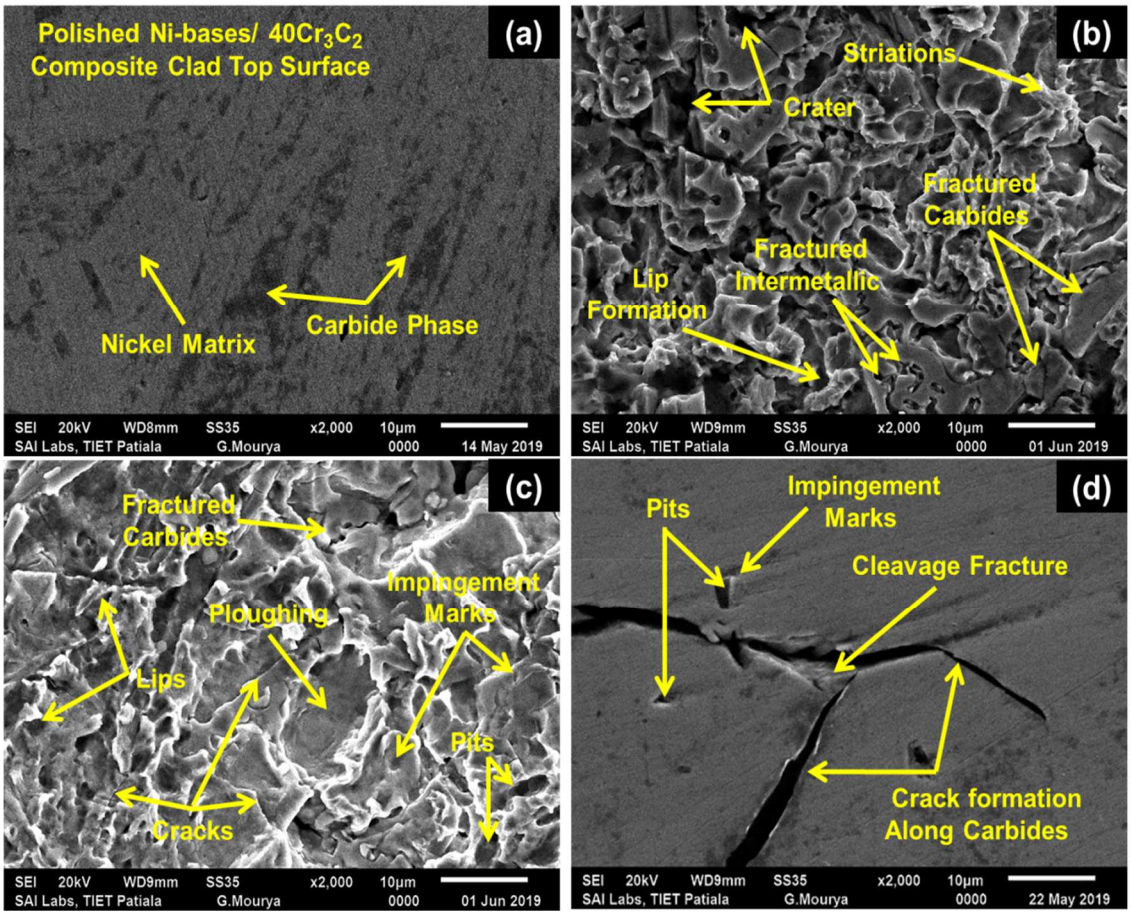

Figure 7.11: Typical SEM Micrographs showing surface topography of Ni-based/40Cr_3C_2 composite clad (a) Before cavitation erosion (b) After cavitation erosion at 0.5 mm SOD, 60 µm AMP & 120 mm IMD (c) After cavitation erosion at 1 mm SOD, 50 µm AMP & 120 mm IMD (d) After cavitation erosion at 1.5 mm SOD, 40 µm AMP & 120 mm IMD

7.4.3 Fractographic Analysis of Worn Surface of Ni-Based/20Cr_3C_2-20Mo Composite Clad Specimens

Similarly, the fractographic analysis of the worn Ni-Based/20Cr_3C_2-20Mo composite clad has been carried out. The surface topography of polished and scratch-free of the top surface of the Ni-Based/20Cr_3C_2-20Mo composite clad is presented in Figure 7.12 (a), the uniformly dispersed dark grey carbide particle and light grey molybdenum particles, is easily visible from the SEM micrograph (Figure 7.12 (a)). Where, Figure 7.12 (b), (c) and (d), shows the fractured surface of the Ni-Based/20Cr_3C_2-20Mo composite clad, tested at parameters set-3, 5 and 7, respectively.

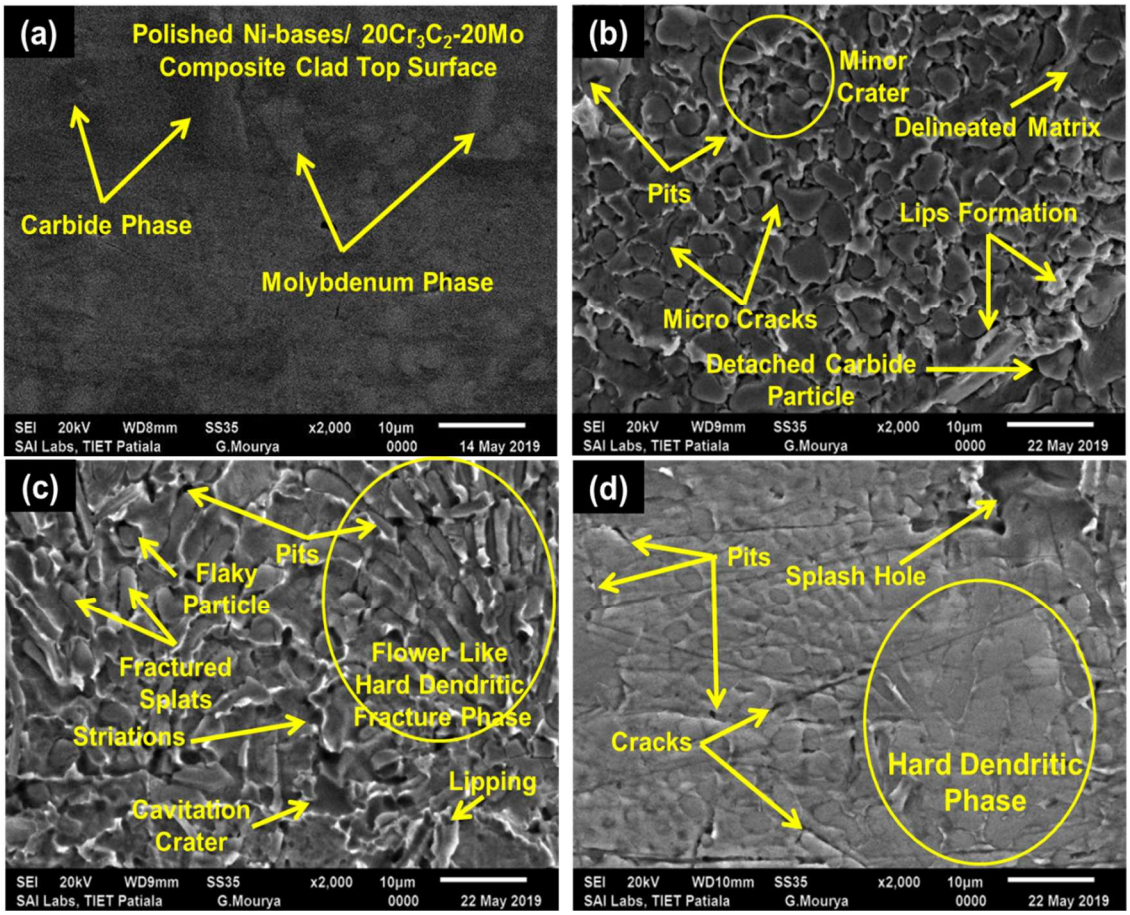

Figure 7.12: Typical SEM Micrographs showing surface topography of Ni-based/20Cr_3C_2-20Mo composite clad (a) Before cavitation erosion (b) After cavitation erosion at 0.5 mm SOD, 60 µm AMP & 120 mm IMD (c) After cavitation erosion at 1 mm SOD, 50 µm AMP & 120 mm IMD (d) After cavitation erosion at 1.5 mm SOD, 40 µm AMP & 120 mm IMD

The pure brittle mode of fracture has taken place at parametric set-3; the fracture morphology consists of the minor crater, pits in the matrix, lipping and micro-cracking of Mo enrich Ni-matrix as shown in Figure 7.12 (b). The few detached carbide particles also have been observed in the SEM micrograph. Comparably, the severity of the damage at the parametric set-5 is less, and minimal at parametric set-7 as observable from Figure 7.12 (c) and (d), where the mode of fracture in the Ni-Based/20Cr_3C_2-20Mo composite clad is brittle at all the experimental conditions. However, Figure 7.12 (c) exhibits that during cavitation vapour bubbles explosion the generated impact energy absorbed by Mo enrich Ni- matrix and partially transferred to carbide particle. Hence, the flower-like dendritic fracture in the hard matrix phase has been observed as

illustrated in Figure 7.12 (c), and the fracture morphology consists of small pits, flaky particles, fractured splats, striations and lipping in the matrix region due to surface fatigue and cavitation crater (approximately of bubble shape). Where, only a few minor cracks, micro pits and particularly one splashes hole (empty cavity left by detached reinforcement particle) are observed in the SEM micrograph (Figure 7.12 (d)) of specimen tested at parametric set-7. As per mass loss results in the Ni-based/20Cr_3C_2-20Mo composite clad exhibits 11.2 times less mass loss as compare to SS-316 and the fractographic analysis results confirm the same because minor damage to the clad region has been observed through SEM micrographs.

7.5 Results of Confirmatory or Validatory Experiments

The confirmatory experiments have been performed at optimized cavitation test parameters (0.5 mm SOD, 60 µm AMP, and 80 mm IMD). The result shows that the maximum mass loss of 23.9 mg has been observed in the SS-316 specimen, the mass loss observed in the SS-316 is within the range of the statistical predicted value of mass loss for the SS-316 at optimized parameters. Also, the mass loss of both Ni-based/40Cr_3C_2 composite clad (3.3 mg) and Ni-based/20Cr_3C_2-20Mo composite clad (2.1 mg) is also in the statistically predicted range. For the comparison purpose, the cavitation erosion study of EWAC coating and heat-treated SS-316 has been carried out. The heat treatment (tempering) of the SS-316 has been performed using microwave hybrid heating technique; firstly, the SS-316 was heated up to lower critical temperature and then allowed to cool at room temperature. Basically, the purpose of this heat treatment is to homogenize the steel specimen. The microstructure of the homogenize SS-316 is shown in Figure 7.13 (a), the graphical representation of grain size measurement is shown in Figure 7.13 (b), the average grain size of the homogenized SS-316 is 15.9 µm. The mass loss in heat-treated SS-316 (15.5 mg) is 1.5 times lesser as compared to SS-316. The reason attributed to a reduction in mass loss is the increase of grain size and increase in toughness (as tempering is known for enhancement of toughness).

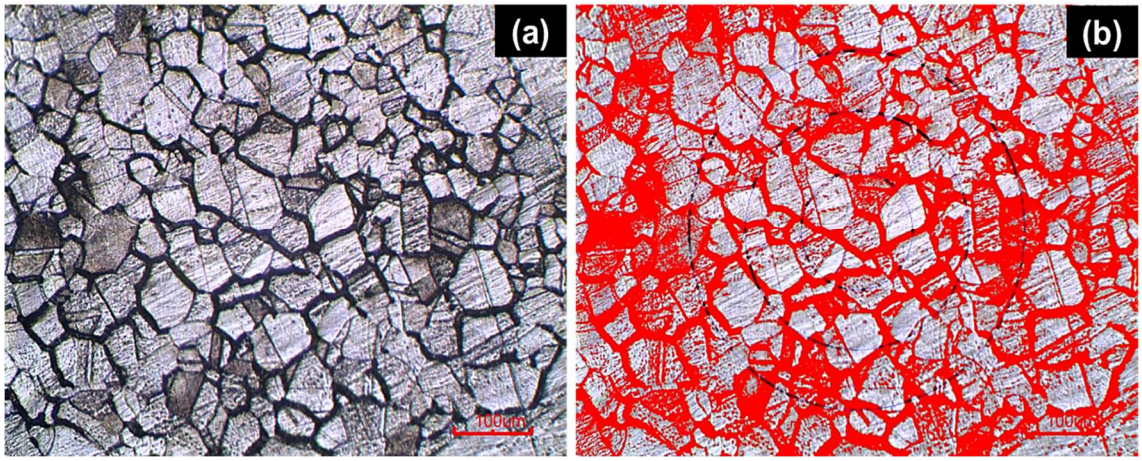

Figure 7.13: Microstructure of heat-treated austenitic stainless steel (a) Optical micrograph at 100X (b) Grain size measurement of SS-316 in Micro Cam 4.0.

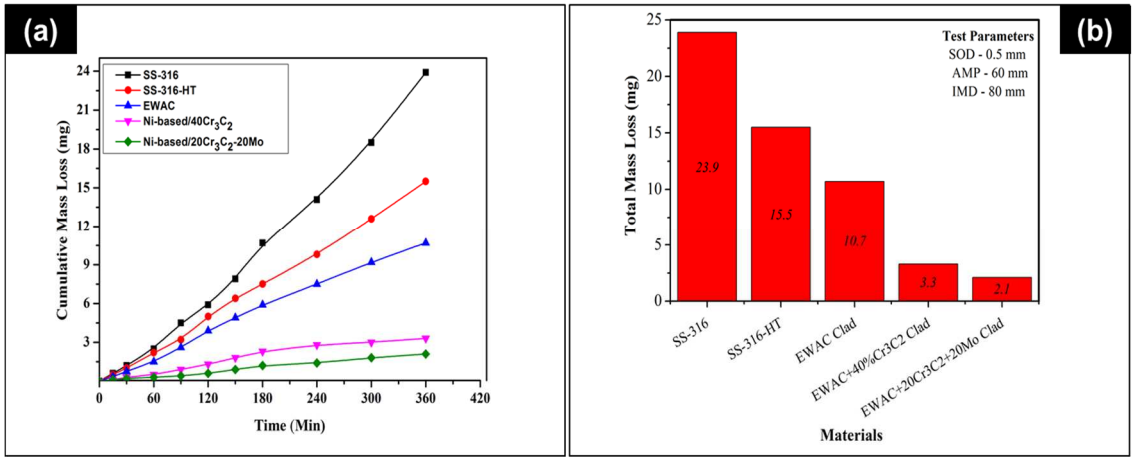

Figure 7.14: (a) Cumulative mass loss vs. cavitation erosion time plot for various materials (b) Bar graph showing total mass loss in the base material, heat treated base material and developed EWAC & Ni-based composite clad

Whereas the mass loss in EWAC coating is found 2.2 times lesser as compared to SS-316, the reason attributed for the reduction in mass loss is that the nickel has hardenability and toughness property, when it is added as an alloying element. However, the results of cumulative mass loss in cavitation erosion study of SS-316, SS-316-HT, EWAC clad, Ni-based/40Cr_3C_2 composite clad and Ni-based/20Cr_3C_2-20Mo composite clad is presented in Figure 7.14 (a). Also, total mass loss occurred in different materials and developed clads in shown in Figure 7.14 (b).

7.6 Results of Comparative study of Physical, Mechanical, Metallurgical and Tribological Properties of Base Material and clads

7.6.1 Results of Density of Base Material and Clads

To efficiently compare the developed clads and base material, the normalized cavitation erosion resistance (NCER) is the suitable term. And for the calculation of NCER, the density of the material must be known. Therefore, the density calculation of the developed clads and base material has been carried out as per the Archimedes principle. The density of the EWAC clad was come out to be highest 8.91g/cm^3 as the density of pure nickel is higher as compared to stainless steel and chromium carbide. However, the results of density are presented graphically in Figure 7.15.

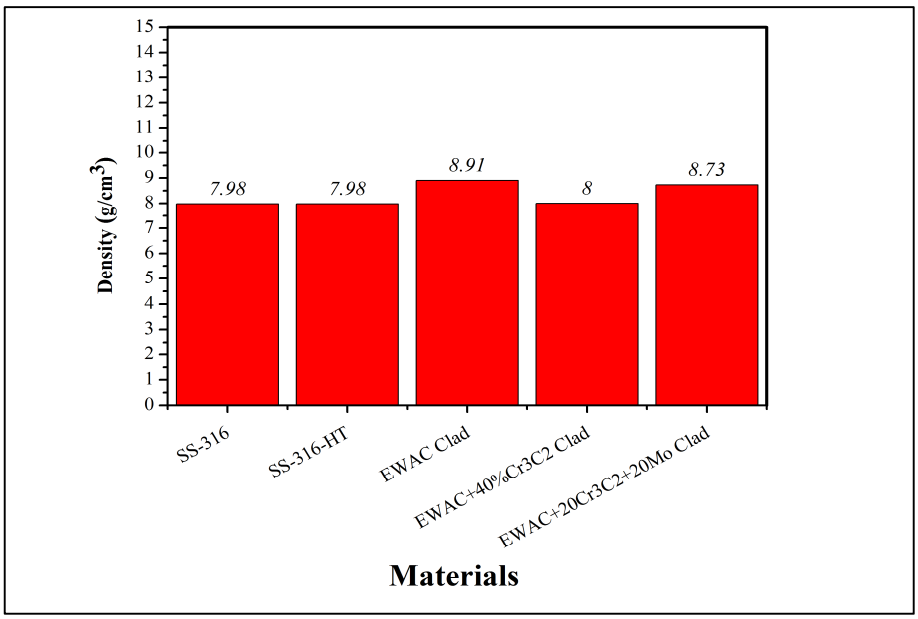

Figure 7.15: Comparison of density of base material and microwave developed clads

7.6.2 Results of Comparative Study of Micro-hardness of Various Materials and Clads

The hardness of the material plays a vital role in the enhancement of the CER **[124].** The average microhardness of the base material (SS-316) is 190±15 $HV_{0.3}$. However, the average microhardness of the heat-treated steel specimen is less as compared to as-received material i.e. 170±10 $HV_{0.3}$, as tempering is known for the reduction in brittleness and hardness, but it helps in increasing toughness of the material. And

toughness is a suitable property for the high CER. The average microhardness of the microwave proceeded EWAC clad is 304±48 $HV_{0.3}$ **[106],** which is almost 1.6 times as compared to the base material. Whereas the average microhardness of the developed Ni-based/40Cr_3C_2 composite clad is 605±80 $HV_{0.3}$ and Ni-based/20Cr_3C_2-20Mo composite clad is 681±30 $HV_{0.3}$. The microhardness of the Ni-based/40Cr_3C_2 and Ni-based/20Cr_3C_2-20Mo composite clad is approximately 3 and 3.5 times better than that of the stainless steel substrate, respectively. The average Vickers microhardness values for each material and clad with standard deviation is shown in Figure 7.16.

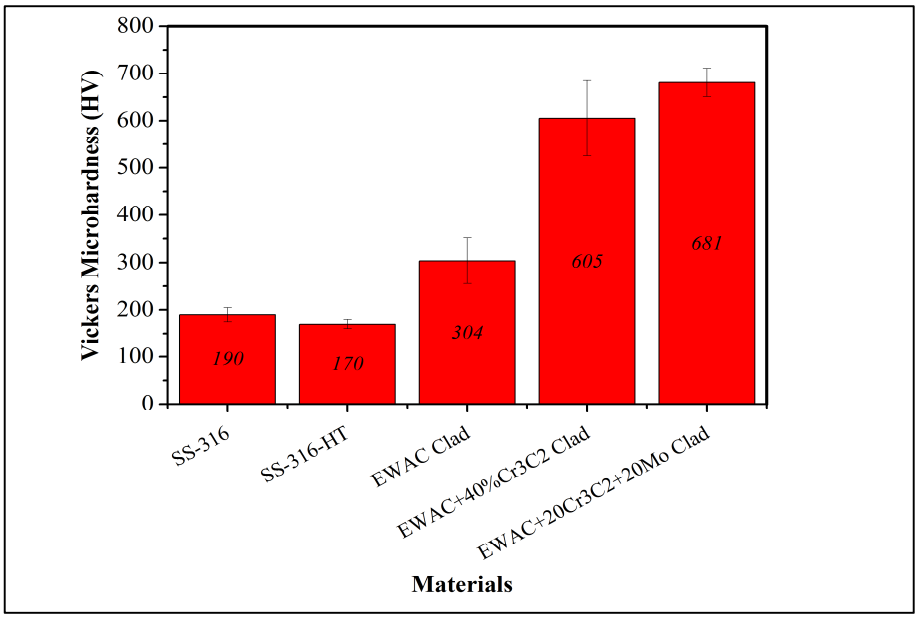

Figure 7.16: Comparison of microhardness of base material and microwave developed clads

7.6.3 Results of Comparative Study of Incubation Time and Normalized Cavitation Erosion Resistance of Various Materials and Clads

It was observed from the above cavitation erosion study that all developed clads exhibits excellent CER than SS-316 substrate under a different set of parameters. It has been seen that all developed clads perform better at optimized (highest cavitation erosion and mass loss) parametric conditions of 0.5 mm SOD, 60 µm AMP, and 80 mm IMD. However, to select the best possible composition of the microwave developed clads from the present developed clads. The comparison study between different materials and clads has also been carried out and the results are shown in Figure 7.17 and 7.18. The comparison has been carried out on the basis of incubation time and

NCER. The term incubation time already has been explained in section 7.2, where NCER can be calculated by using Equation (7.4)

$$NCER = (MDER)^{-1} \text{----------(7.4)}$$

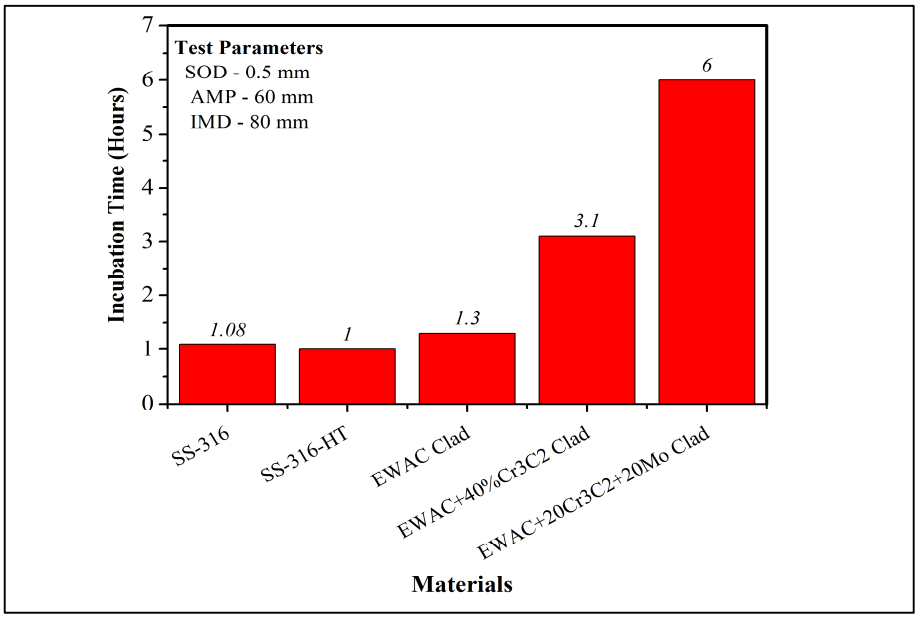

Figure 7.17: Incubation time of developed clads with respect to as received SS-316

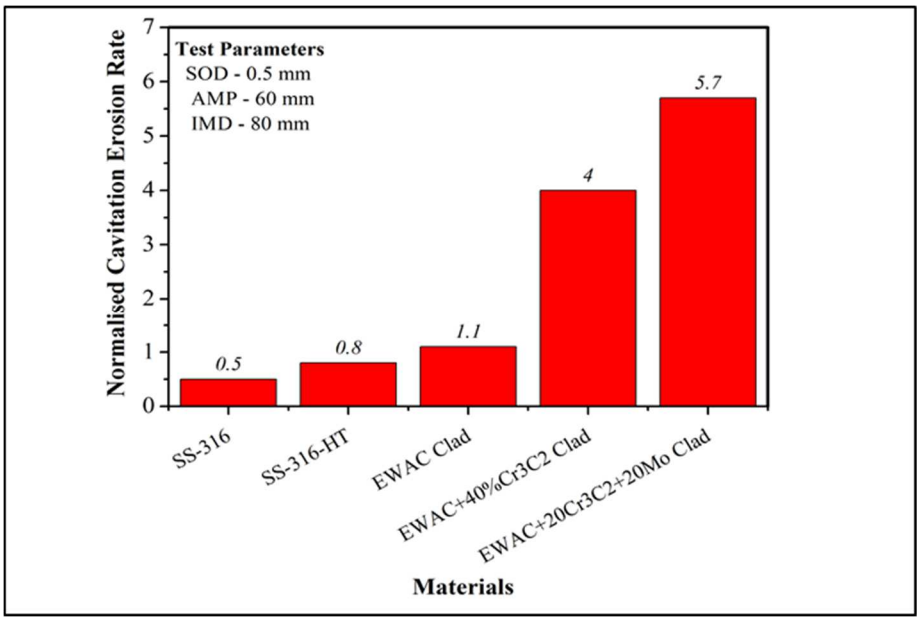

Figure 7.18: Normalized cavitation erosion resistance or rate of the developed clads with respect to the base material (SS-316)

From the Figure 7.17, it can be observed that the microwave process Ni-based/20Cr_3C_2-20Mo composite clad possess highest incubation period of about 6 hours, followed by Ni-based/40Cr_3C_2 composite clad (3.1 hours), EWAC clad (1.3 hours), SS-316-HT (1 hour), and SS-316 (1.08 hours). The reason attributed to the higher incubation period is the lower porosity, crack-free microstructure, good metallurgical bonding with the substrate and higher hardness of the developed clads. Therefore, the cavitation erosion resistance of the developed Ni-based/20Cr_3C_2-20Mo composite clad have 5.7 times CER resistance and Ni-based/40Cr_3C_2 composite clad possess 4 times higher CER than SS-316 substrate. Moreover, SS-316-HT has performed slightly better as compared to as-received SS-316.

7.6.4 Fractographic Study of Various Materials and Clads

The fractography study of the eroded materials and developed clad, tested at 0.5 mm SOD, 60 µm AMP, and 80 mm IMD was carried out using SEM/EDS to understand its cavitation erosion mechanism. Figure 7.19 (a, b) shows the SEM and EDS of surface morphology of eroded SS-316 after cavitation erosion testing. The surface of the specimen after vibratory cavitation to be obscured by a 50 µm size deep craters, fatigue cracks, micro tunnels, plastically deformed zone and plastically defamed particles. The presence of these features indicates plastic deformation and surface fatigue as the primary degradation mechanism.

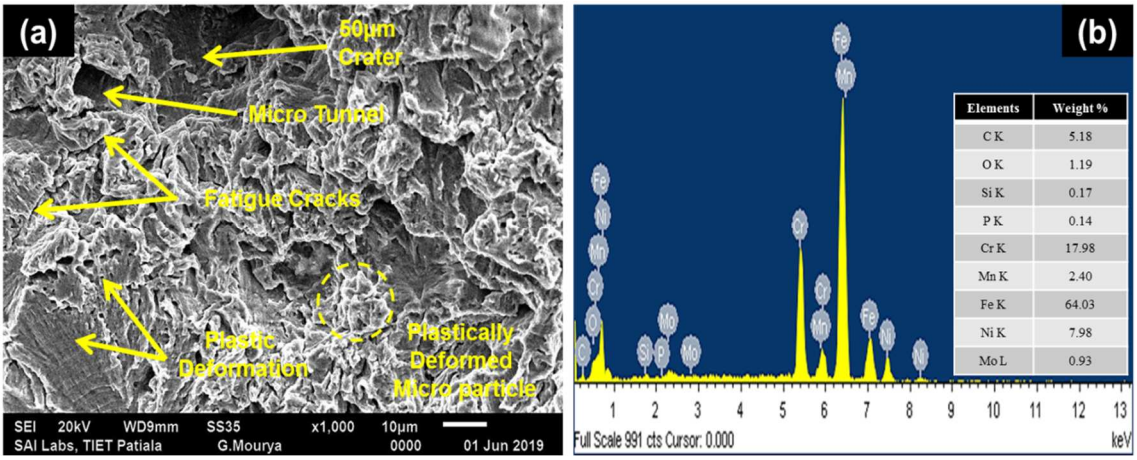

Figure 7.19: (a, b) Typical SEM micrograph along with EDS showing surface morphology of eroded SS-316 after cavitation erosion for 6 h

Whereas a large number of crater, pits, striations in the locality of plastically deformed lips and fatigue cracks in the grain boundaries region has been observed on the surface of the SS-316-HT as shown in Figure 7.21 (a), and the EDS spectra of the SS-316-HT is shown in the Figure 7.21 (b).

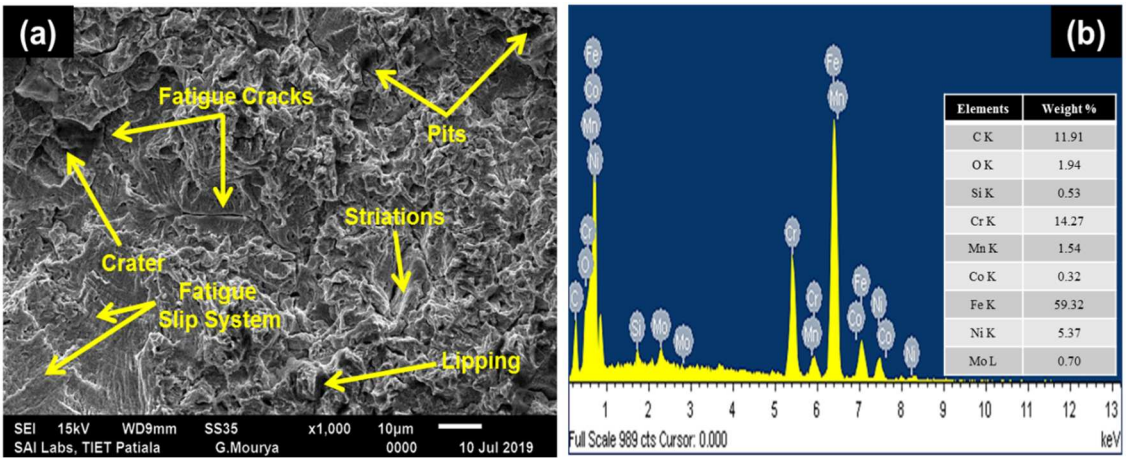

Figure 7.20: (a, b) Typical SEM micrograph along with EDS showing surface morphology of eroded SS-316-HT after cavitation erosion for 6 h

Figure 7.21 (a) and (b) shows the typical morphological features and EDS spectra of the surface of the EWAC clad after cavitation erosion of 6h in distilled water. Figure 7.21 (a) also shows that the carters with a diameter of 10 µm at the corner, along with several splashed particles at the top of erosion surface of the cladding.

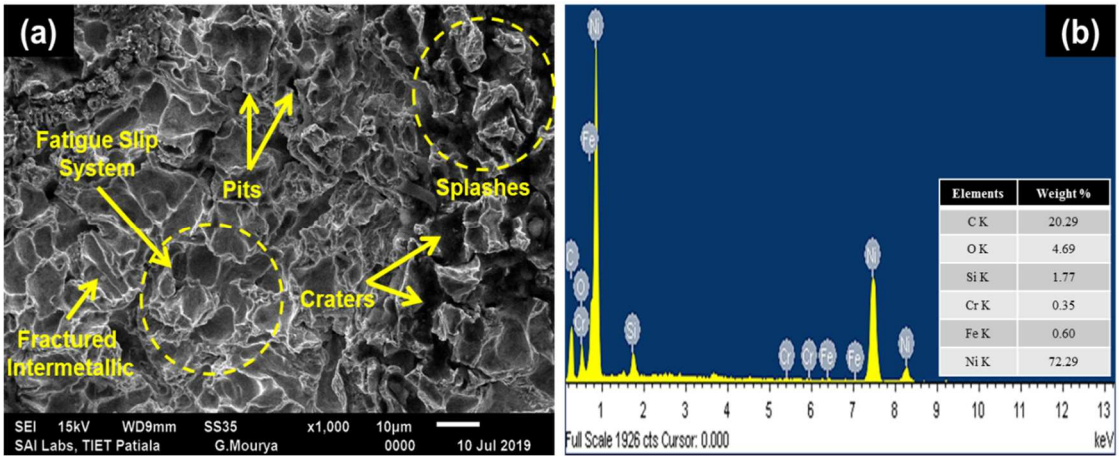

Figure 7.21: (a, b) Typical SEM micrograph along with EDS showing surface morphology of eroded EWAC clad after cavitation erosion for 6 h

As shown in Figure 7.21 (a), the pits, fractured intermetallic and large fatigue slip system are detected on the eroded surface, suggesting cavitation erosive damage of the EWAC clad in distilled water is of mixed-mode (ductile plus partially brittle).

After 6 hours of cavitation erosion testing, it was observed that the surface of Ni-based/40Cr_3C_2 composite clad was considerably damaged by impact energy of shock waves (Figure 7.22 (a)), the EDS of the eroded Ni-based/40Cr_3C_2 specimen is present in Figure 7.22 (b). Surface morphology Ni-based/40Cr_3C_2 composite clad specifics craters, pits, fractured carbides, extruded lips and fractured intermetallic. The presence of these features validates the mixed mode of fracture (ductile fracture of matrix and brittle fracture of carbide particles).

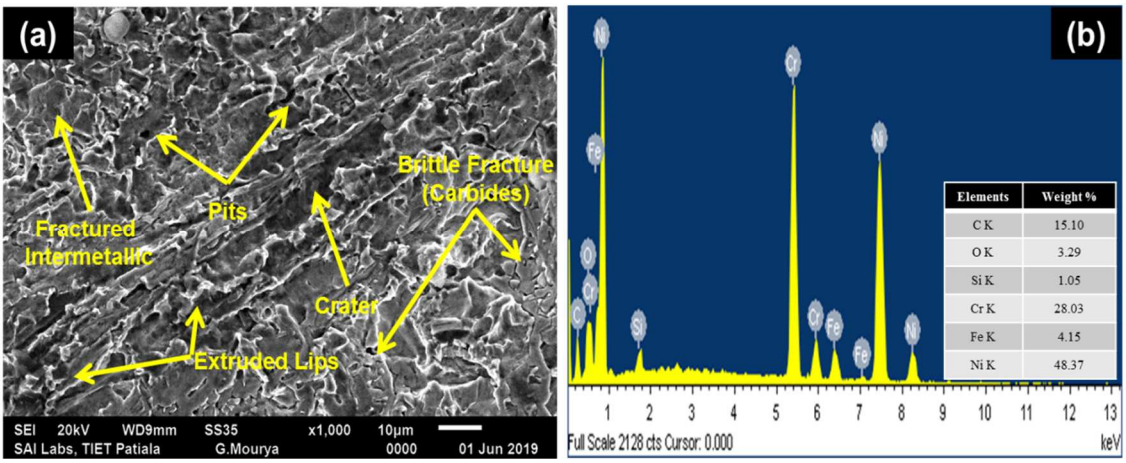

Figure 7.22: (a, b) Typical SEM micrograph along with EDS showing surface morphology of eroded Ni-based/40Cr_3C_2 composite clad after cavitation erosion for 6 h

Figure 7.23 (a) shows that the matrix has experienced extensive fatigue cracks and craters. During the cavitation erosion process, the surface of the Ni-based/20Cr_3C_2-20Mo composite clad was impinged by micro jets many times. Blow and damage caused by vapour bubbles explosion, resulting in the removal of the reinforcement particles (detached particles) from the matrix and products subjected to splashes as shown in Figure 7.23 (a). Whereas some unaffected clad region can also be observed from the SEM micrograph shown in Figure 7.23 (a). The EDS analysis results of Ni-based/20Cr_3C_2-20Mo composite clad is illustrated in Figure 7.23 (b). Also, the presence of significant amount of oxygen has been seen in the EDS spectra of fractured base material and developed microwave clads, which is due to the fact that, during final stage explosion of vapour bubbles the inside temperature of the bubbles nuclei reaches more

than 5000 K at 20 kHz [162], therefore, the molecules of H_2O, breakdown and form H_2 and O_2, further this oxygen will react with the surface of the specimen, under cavitation erosion testing.

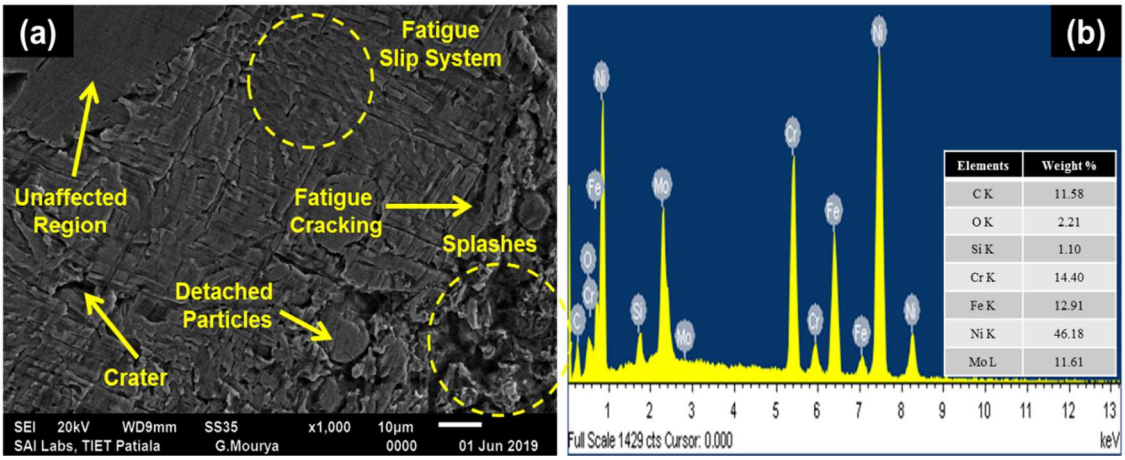

Figure 7.23: (a, b) Typical SEM micrograph along with EDS showing surface morphology of eroded Ni-based/20Cr_3C_2-20Mo composite clad after cavitation erosion for 6 h

7.6.5 Results of Comparative Surface Roughness of Various Materials after Cavitation Erosion Testing

The severity of damage is also confirmed by surface roughness testing by a surface profilometer. The initial roughness of the SS- 316 specimen before testing was 0.03 µm. The measured roughness (R) profiles of SS-316 specimens before and after testing are shown in Figure 2.4 (a) and (b). However, the deep craters and pits found in the roughness data. The R_q (mean square roughness) value of the SS-316 after cavitation testing found was 8 µm. Whereas, the R_q value of the SS-316-HT, EWAC clad, Ni-based/40Cr_3C_2 clad and Ni-based/20Cr_3C_2-20Mo clad surface after cavitation erosion testing is 5.48 µm, 5.28 µm, 3.18 µm and 2.83 µm, espectively. Higher R_q value in case of SS-316 after cavitation erosion confirms that cavitation damage to the material is more intense in case of SS-316 as compared to microwave developed composite clads. The measured R-profile of SS-316-HT, EWAC clad, Ni-based/40Cr_3C_2 clad and Ni-based/20Cr_3C_2-20Mo clad is shown in Figure 2.25 (a), (b), (c) and (d).

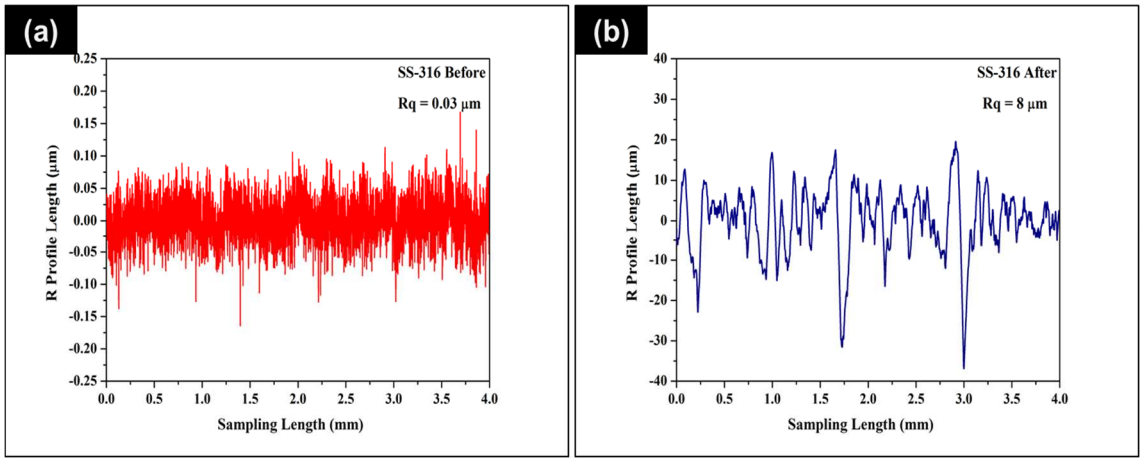

Figure 2.24: The measured surface roughness profiles of (a) SS-316 before cavitation erosion testing (b) SS-316 after cavitation erosion testing of 6 h

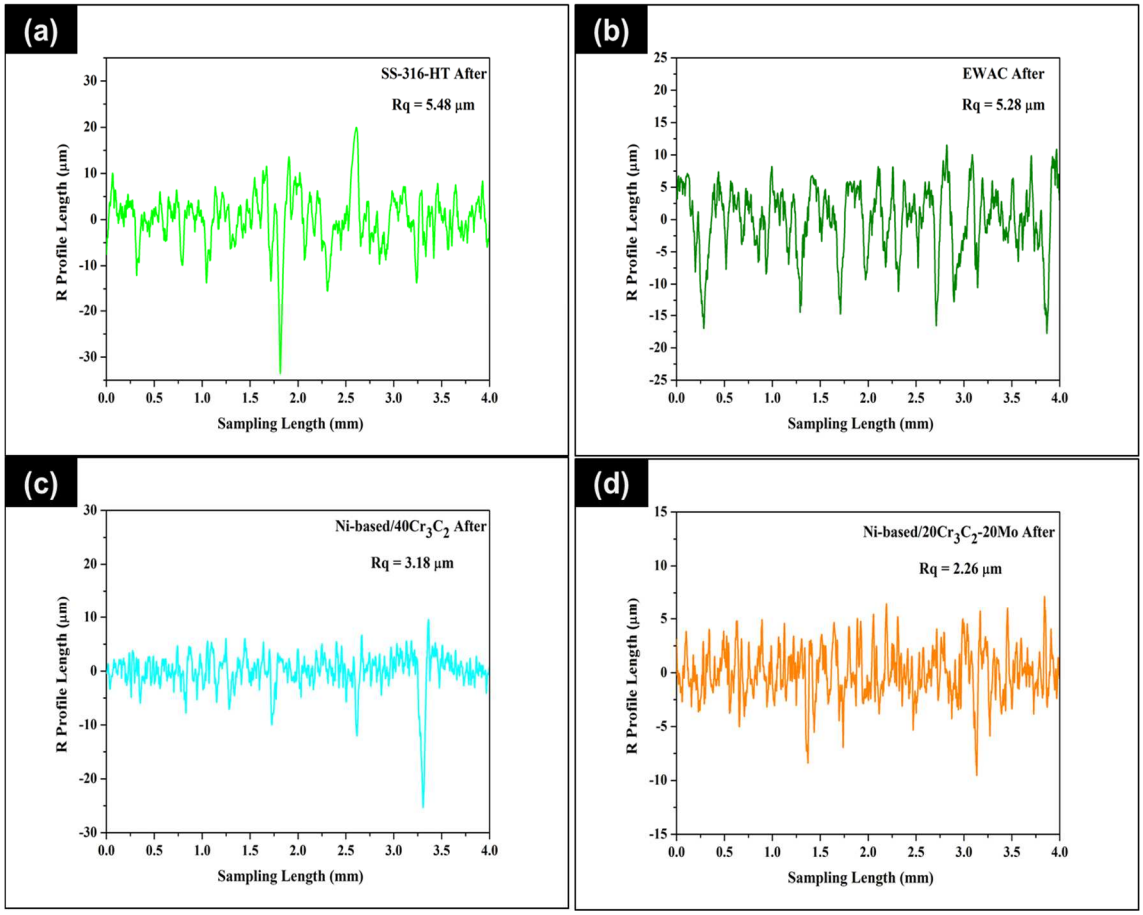

Figure 2.25: The measured surface roughness profiles of (a) SS-316-HT after cavitation erosion testing (b) EWAC clad after cavitation erosion testing of 6 h
(c) Ni-based/40Cr_3C_2 composite clad after cavitation erosion testing of 6 h
(d) Ni-based/20Cr_3C_2-20Mo composite clad after cavitation erosion testing of 6 h

Chapter 8

Conclusion & Suggestion for Future Work

8.1 Introduction to Chapter

This chapter presents the major conclusions drawn from the current study, followed by suggestions for future work in this area. The motivation of the present research work involved, the development cavitation erosion resistance microwave processed Ni-based/40Cr_3C_2 and Ni-based/20Cr_3C_2-20Mo composite clads on austenitic stainless steel (SS-316) substrate by using a 2.45 GHz frequency and 900 Watt power in a domestic microwave oven at optimization process parameters. In addition, the developed microwave processed Ni-based/40Cr_3C_2 and Ni-based/20Cr_3C_2-20Mo composite clads was subjected to different characterization techniques and the main conclusions of this study are summarized below.

8.2 Conclusion

8.2.1 Metallurgical and Mechanical Characterization of the Microwave Processed Clads

The developed microwave processed Ni-based/40Cr_3C_2 and Ni-based/20Cr_3C_2-20Mo composite clads were characterized by various metallurgical and mechanical characterization technique like SEM (Microstructural Investigation), EDS (Elemental Composition), XRD (Phase Quantification and Qualification), OM (Optical Microscopy), Vickers Microhardness Tester (Microhardness) and UTM (Flexure Strength or Peel of Strength), the major conclusions drawn from the results are as follows:

1. The microstructural investigation revealed that the processed Ni-based/40Cr_3C_2 and Ni-based/20Cr_3C_2-20Mo composite clads of approximately 600 µm and 750 µm thickness respectively were developed on SS-316 substrate through microwave hybrid heating technique in 380 Seconds and 420 Seconds, at optimized processing parameters. It was observed that microwave power directly affects the processing time required development of the composite clads. As the power level increased, the processing time was reduced.

2. The agglomerated carbides and columnar dendrite in the liquid solution of the Ni have been found through the microstructural investigation of Ni-based/40Cr_3C_2 composite cladding, the carbide particles are uniformly distributed in the Ni-matrix and this was further confirmed by the EDS point and area mapping.
3. Whereas the microstructure of the Ni-based/20Cr_3C_2-20Mo composite clad composed of skeleton-like or net-like or rib-like, where, Mo precipitate and stripe-like chromium carbide particle in the liquid solution the Ni.
4. The developed composite clads are almost free from all types of cracks (interfacial and solidification cracks) and pores. As the clear interfaces are visible from the SEM micrographs of the microwave processed clads, which is due to the volumetric or uniform heating of the microwaves.
5. The porosity analysis reveals that the Ni-based/40Cr_3C_2 and Ni-based/20Cr_3C_2-20Mo composite clads have only 1.67% and 0.26% porosity, which was significantly less as compared to the conventionally used claddings or coatings processes.
6. The XRD analysis of the various microwave processed Ni-based/40Cr_3C_2 composite clad revealed the formation of various intermetallics phase (Ni_3C_2 & Ni_3Fe), carbides phase (SiC, $Cr_{23}C_6$), and complex carbide phase (Cr_3Ni_2SiC), which is due to the intense microwaves heating. Further, NIR analysis results reveal that the $Cr_{23}C_6$ (48.33%) in the main content present the Ni-based/40Cr_3C_2 composite clad, which formed due to the reaction between Cr and C because Ni has poor C absorption capacity and $Cr_{23}C_6$ phase have lowest Gibbs free energy.
7. The presence of hard carbides particles such as Mo_2C, $NiMo_4C$, and $C_{23}C_6$ phases inside the Ni-based/20Cr_3C_2-20Mo composite clad, and the existence of other phases like FeMoCr, $MoSi_2$, Cr_3Si, Ni_3Cr_2 like in Ni-based/20Cr_3C_2-20Mo composite clad are responsible for the increase in microhardness of the developed clads. The NIR analysis results reveal that the major has present in the Ni-based/20Cr_3C_2-20Mo composite clad is Ni_3Cr_2 (67.30%), which was formed due to the reaction between Cr and Ni. However, the presence of Ni_3Fe phase in both developed clads confirms the metallurgical bonding between the substrate and clads.
8. The results of the Vicker's microhardness of the microwave processed Ni-based/40Cr_3C_2 and Ni-based/20Cr_3C_2-20Mo composite clads exhibits 3 (605±80 $HV_{0.3}$) and 3.5 (681±30 $HV_{0.3}$) time higher microhardness than that of

substrate SS-316 (190±15 $HV_{0.3}$). The reason attributed to the higher hardness is the formation of the various intermetallic and carbides in the clad region due to the microwave heating.

9. The partial dilution of the substrate with the clad and vice-versa, resulting in a higher flexural strength of these developed composite clads. The value of flexural strength in the case of Ni-based/40Cr_3C_2 and Ni-based/20Cr_3C_2-20Mo composite clads was 813.229 MPa and 708.76 MPa.
10. The fractographic analysis of specimens tested for the flexural strength showed that the clad layer was still attached to the substrate during the bending test, despite cracking in the substrate. The primary cracks during loading, occurred in the clad layers and these cracks increased under continuous loading and ultimately reaches to the substrate. Hence, the developed microwave processed clads possess appropriate bonding with the substrate.

8.2.2 Functional Characterization of the Microwave Processed Clads

To evaluate the cavitation erosion resistance of the microwave processed composite clads, the parametric study using vibratory cavitation test apparatus in distilled water using Taguchi L9 orthogonal array was performed separately for the SS-316, Ni-based/40Cr_3C_2 and Ni-based/20Cr_3C_2-20Mo composite clads, the major conclusions drawn from the study are discussed below:

1. The varying stand-of-distance, amplitude and immersion depth significantly affects the mass loss in the SS-316 substrate and developed composite clads. It was observed that with the increase of SOD and immersion depth, the mass loss decrease, whereas with the increase of amplitude the mass loss in the specimens increases.
2. The ANOVA analysis of all three parametric studies of cavitation erosion testing was performed at 95% confidence level, the results of the ANOVA analysis reveals that the SOD between specimen and ultrasonic horn have 56.16 to 59.46% percentage contribution in the change in the mass loss, whereas the amplitude and immersion depth of the ultrasonic horn in the test liquid has only 30.68 to 32.16% and 9.26 to 12.23% contribution in the parameters affecting mass loss.
3. The reason attributed to the lower mass loss at higher SOD is that with an increase of SOD the shockwave velocity will decrease, which results in smaller pressure

pulse, lesser acoustic pressure and low impact energy of the impingement jets. Therefore, the material damage will decrease as well as the mass loss.

4. However, the large mass loss was observed at the higher amplitude due to the fact that higher amplitude generates the larger negative cycles, the cavitation bubble grows larger, and collapse at higher pressure and cause of severe damage to the material under cavitation erosion testing.
5. Whereas the reason attributed to the lesser mass loss at higher immersion depth is lesser bubble formation at higher immersion depth, due to higher static pressure, and the larger amplitude is required to create more negative pressure, therefore, less bubble formation and fewer impingement jets & less material damage was observed.
6. The parameter optimization as per the optimization goal higher is the better was carried out using delta statistics response table. The optimized parameters were come out as 0.5 mm SOD, 60 µm amplitude and 80 mm immersion depth.
7. The regression equations were developed for the mass loss in SS-316, Ni-based/40Cr_3C_2 and Ni-based/20Cr_3C_2-20Mo clad. Thereafter, the prediction analysis was performed at 95% confidence level to predict the results of the confirmatory experiments, which was performed at the optimized parameters.
8. The results of confirmatory experiments reveal that the developed mathematical models are valid as the results of mass loss lie between within the predicted intervals.
9. The average mass loss of the developed Ni-based/40Cr_3C_2 and Ni-based/20Cr_3C_2-20Mo composite clads are 7.6 and 11.2 times lesser as compared to SS-316 substrate at same parametric conditions.
10. The fractographic analysis of the eroded surface of SS-316, Ni-based/40Cr_3C_2 and Ni-based/20Cr_3C_2-20Mo clads specimens tested at parametric set 3, 5 and 7 carried out via SEM. From the SEM micrographs, it was clear that the specimens tested at parametric set-3 were more severe damage as compared to other 2 sets.
11. The surface morphology of the eroded SS-316 specimens consists of pits, craters, striations, micro cracks, cavitation crater, flaky crater, plastically deformed region and lips, impingement marks, and cleavage fracture. The presence of these features indicates plastic deformation and surface fatigue as the primary degradation mechanism.

12. Whereas the surface morphology of the eroded Ni-based/40Cr_3C_2 composite clad consists of fractured carbides, fractured intermetallic, plastically deformed lips in matrix region, crater, striations, impingement marks, ploughing and pits, this indicates the dual-mode of fracture of the Ni-based/40Cr3C2 composite clad.
13. The mode of failure of the Ni-based/20Cr_3C_2-20Mo composite clad is brittle due to the higher average hardness of the clad region. The surface morphology consists of detached particles, micro-cracks, flower-like hard dendritic phase and flaky particles.

8.2.3 Comparative study of the various materials and developed clads

The comparison between the SS-316, SS-316-HT, EWAC clad, Ni-based/40Cr_3C_2 and Ni-based/20Cr_3C_2-20Mo composite clad on the basis of hardness, incubation time, normalized cavitation erosion resistance (at optimized test parameters SOD = 0.5 mm, AMP = 60 µm and IMD = 80 mm), surface roughness after cavitation erosion testing and fractographic analysis of the worn materials and clads was carried out, the main conclusion of the study are discussed below.

1. The Ni-based/20Cr_3C_2-20Mo composite clad exhibits higher incubation period (6 hours) as compared to Ni-based/40Cr_3C_2 composite clad, which can resistance cavitation erosion up to 3.1 hours. However, the EWAC clad, SS-316-HT and SS-316 can resist cavitation erosion up to only 1.3, 1 and 1.08 hours respectively.
2. The Ni-based/20Cr_3C_2-20Mo composite clad (5.7) have highest CER, followed by Ni-based/40Cr_3C_2 composite clad (4), EWAC clad (1.1), SS-316-HT (0.8) and SS-316 substrate (0.5). The reason attributed to the higher CER is the higher microhardness, good metallurgical bonding between clad and substrate, and cracks free & porosity-free microstructure of the microwave processed clads. Whereas the reason attributed to the higher CER in the SS-316-HT as compared to the SS-316 (despite having higher hardness), is the uniform and residual stresses free microstructure.
3. The result of the surface roughness testing reveals that the R_q value was significantly higher on the SS-316 (8 µm), which confirms that the severity of the damage in the SS-316 is higher. Hence, the mass loss in the SS-316 was found higher than microwave processed clads.

4. The fractographic analysis of the specimens exhibits that the cause of failure in the SS-316 and SS-316-HT was surface fatigue, where the cause of failure in the EWAC clad was surface fatigue and brittle cracking. Moreover, the composite clad had failed due to brittle fracture & ploughing of the carbides and plastic deformation of the matrix.

8.3 Suggestions for Future Work

Several studies have been performed on the development and characterization of microwave processed clads, but there is still plenty of room for improvement for research in microwave processing of materials. Some suggestions for future work are listed below:

1. An industrial microwave oven can be used to develop the clads in order to reduce the processing time.
2. Mathematical modelling can be carried out to develop the relation between microwave processing time for the development of the appropriate clad by varying microwave processing parameters like microwave power level, dimensions of the substrate, thickness of the separator, quantity of susceptor and preheating time.
3. The functionally graded materials (FGM) can be examined under cavitation environment.
4. The effect of cavitation erosion on the phase transformation of the microwave processed clads can be studied in the future.
5. The percentage of reinforcement can be furthered optimized to achieve better cavitation resistance.
6. The simulation of the transient process (Microwave cladding) using COMSOL MULTIPHYSICS can be one of the future scope.
7. The tribocorrosion (cavitation erosion testing in the corrosive environment) study of the microwave processed clads can be done in the future.

List of References

[1] I. Yuksel, H. Arman, I.H. Demirel, **As A Clean, Sustainable and Renewable Energy — Hydropower in Turkey**, MATEC Web Conf. 120 (2017) 1–5.

[2] Iea.org. (2019). **Global Energy & CO_2 Status Report: CO_2 emissions**. [online] Available at: https://www.iea.org/geco/emissions/ [Accessed 15 Aug. 2019].

[3] M. Bilgili, A. Ozbek, B. Sahin, A. Kahraman, **An Overview of Renewable Electric Power Capacity and Progress in New Technologies in the World**, Renew. Sustain. Energy Rev. 49 (2015) 323-334.

[4] M. Bilgili, H. Bilirgen, A. Ozbek, F. Ekinci, T. Demirdelen, **The Role of Hydropower Installations for Sustainable Energy Development in Turkey and the World**, Renew. Energy. 126 (2018) 755–764.

[5] S.A. Ali, S. Aadhar, H.L. Shah, V. Mishra**, Projected Increase in Hydropower Production in India Under Climate Change**, Nat. Res. 8 (2018) 1–12.

[6] U. Dorji, R. Ghomashchi, **Hydro Turbine Failure Mechanisms: An Overview**, Eng. Fail. Anal. 44 (2014) 136–147.

[7] **Executive Summary Power Sector May 2018 Report,** Central Electricity Authority, Ministry of Power, Govt. of India. 31 May 2018. Retrieved on 14 Sep 2018.

[8] **Physical Progress (Achievements),** Ministry of New and Renewable Energy, Govt. of India. Retrieved on 18 July 2018.

[9] **Repairengineering.com. (2019). Cavitation.** [online] Available at: http://www.repairengineering.com/cavitation.html [Accessed 19 Jul. 2019].

[10] S. Li, **Tiny Bubbles Challenge Giant Turbines: Three Gorges Puzzle**, Interface Focus. 5 (2015) 1–25.

[11] M. Kumari Padhy, R.P. Saini, **A Review On Silt Erosion In Hydro Turbines**, Renew. Sustain. Energy. 12 (2008) 1974–1987.

[12] R. Singh, S.K. Tiwari, S.K. Mishra, **Cavitation Erosion in Hydraulic Turbine Components and Mitigation by Coatings: Current Status and Future Needs**, J. Mater. Eng. Perform. 21 (2012) 1539–1551.

[13] S. Verlinski, H. Levonyan, A. Tyagunov, D. Tarasov, **Failure Analysis and Crack Estimation in a Hydro Runner**, Int. J. Pure Appl. Math. 119 (2018) 12841–12848.

[14] D. Momcilovic, Z. Odanovic, R. Mitrovic, I. Atanasovska, **Failure Analysis of Hydraulic Turbine Shaft**, Eng. Fail. Anal. 20 (2012) 54–66.

[15] B.K. Sreedhar, S.K. Albert, A.B. Pandit, **Cavitation Damage: Theory and Measurements – A Review**, Wear. 372–373 (2017) 177–196.

[16] A. Kumar, K. Govil, G. Dwivedi, M. Chhabra, **Problems Associated with Hydraulic Turbines**, In: Adv. Intell. Syst. Comput., Springer Singapore, (2018) 621–632.

[17] P. Kumar, R.P. Saini, **Study of Cavitation in Hydro Turbines — A Review**, Renew. Sustain. Energy. 14 (2010) 374–383.

[18] X. Escaler, E. Egusquiza, M. Farhat, **Detection of Cavitation in Hydraulic Turbines**, Mech. Syst. Signal Process. 20 (2006) 983–1007.

[19] K. Holmberg, A. Mathews**, Coatings Tribology**, 2nd Edition, Elsevier B.V., 1994

[20] J.R. Davis, **Surface Engineering For Corrosion and Wear Resistance**, 1st Edition, ASM International, 2001.

[21] G. Bolelli, L. Berger, T. Börner, H. Koivuluoto, L. Lusvarghi, C. Lyphout, N. Markocsan, V. Matikainen, P. Nylén, P. Sassatelli, R. Trache, P. Vuoristo, **Tribology of HVOF- And HVAF-Sprayed WC – 10Co4Cr Hard Metal Coatings: A Comparative Assessment**, Surf. Coat. Technol. 265 (2015) 125–144.

[22] S. Watanabe, T. Tajiri, N. Sakoda, J. Amano, **Fatigue Cracks in HVOF Thermally Sprayed WC-Co Coatings**, J. Therm. Spray Technol. 7 (1998) 93–96.

[23] D. Kekes, P. Psyllaki, M. Vardavoulias, **Wear Micro-Mechanisms of Composite WC-Co/Cr-NiCrFeBSiC Coatings. Part I: Dry Sliding**, Tribol. Ind. 36 (2014) 361–374.

[24] S. Zhou, X. Zeng, Q. Hu, Y. Huang, **Analysis of Crack Behavior for Ni-Based WC Composite Coatings by Laser Cladding and Crack-Free Realization**, Appl. Surf. Sci. 255 (2008) 1646–1653.

[25] G.R. Mirshekari, S. Daee, S.F. Bonabi, M.R. Tavakoli, A. Shafyei, M. Safaei, **Effect of Interlayers on the Microstructure and Wear Resistance of Stellite 6 Coatings Deposited on AISI 420 Stainless Steel by GTAW Technique**, Surfaces and Interfaces. 9 (2017) 79–92.

[26] T. Burakowki, T. Wierzchon, **Surface Engineering of Metals**, 1st Edition, CRC Press LLC, 1999.

[27] D. Gupta, P.M. Bhovi, A. Kumar, S. Dutta**, Development and Characterization of Microwave Composite Cladding**, J. Manuf. Process. 14 (2012) 243–249.

[28] S. Zafar, A.K. Sharma, **Prediction of Tribological Behaviour of WC-12Co Nanostructured Microwave Clad through ANN**, Tribol. Online. 11 (2016) 333–340.

[29] A.M. Hebbale, M.S. Srinath, **Microstructural Investigation of Ni-Based Cladding Developed on Austenitic SS-304 Through Microwave Irradiation**, Integr. Med. Res. 5 (2016) 293–301.

[30] S. Kaushal, D. Singh, D. Gupta, **Processing of Ni–WC–Cr_3C_2-Based Metal Matrix Composite Cladding on SS-316L Substrate Through Microwave Irradiation**, J. Compos. Mater. 53 (2018) 1023–1032.

[31] M. Oghbaei, O. Mirzaee, **Microwave versus Conventional Sintering: A Review of Fundamentals, Advantages and Applications**, J. Alloys Compd. 494 (2010) 175–189.

[32] D. Keyson, D.P. Volanti, L.S. Cavalcante, A.Z. Sim, **Domestic Microwave Oven Adapted for Fast Heat Treatment**, J. Mater. Process. Technol. 189 (2007) 316–319.

[33] R.J. Lauf, D.W. Bible, A.C. Johnson, C.A. Everliegh, **2-18 GHz Broadband Microwave Heating Systems**. Microwave Journal 36 (1993) 24–27.

[34] E.T. Thostenson, T. Chou, **Microwave Processing: Fundamentals and Applications**, Compos. Part A. 30 (1999) 1055–1071.

[35] P.K. Bajpai, I. Singh, J. Madaan, **Joining of Natural Fiber Reinforced Composites Using Microwave Energy: Experimental and Finite Element Study**, Mater. Des. 35 (2012) 596–602.

[36] J.A. Menéndez, A. Arenillas, B. Fidalgo, Y. Fernández, L. Zubizarreta, E.G. Calvo, J.M. Bermúdez, **Microwave Heating Processes Involving Carbon Materials**, Fuel Process. Technol. 91 (2010) 1–8.

[37] D. Agrawal, **Latest Global Developments in Microwave Materials Processing**, Mater. Res. Innov. 8917 (2016) 2–8.

[38] S. Singh, D. Gupta, V. Jain, **Recent applications of microwaves in materials joining and surface coatings**, Proc IMechE Part B J Eng. Manuf. 1 (2015) 1–15.

[39] A. Ahmed, E. Siores**, Microwave Joining of 48 % Alumina ± 32 % Zirconia ± 20 % Silica Ceramics**, J. Mater. Process. Technol. 118 (2001) 88–95.

[40] R.W. Bruce, A.W. Fliflet, H.E. Huey, C. Stephenson, **Microwave Sintering and Melting of Titanium Powder for Low-Cost Processing**, Key Eng. Mater. 436 (2010) 131–140.

[41] R.T. Giberson, M.A. Sanders, **The Real Benefits of Microwave-assisted Processing Go beyond Time Savings**, Microsc Microanal. 15 (2019) 29–30.

[42] S. Singh, D. Gupta, V. Jain, A.K. Sharma, **Microwave Processing of Materials and Applications in Manufacturing Industries: A Review**, Mater. Manuf. Process. 30 (2015) 1–29.

[43] R. Roy, D. Agrawal, J. Cheng, **Full Sintering of Powdered-Metal Bodies In A Microwave Field**, Nature. 399 (1999) 668–670.

[44] G. Sethi, A. Upadhyaya, D. Agarwal, **Microwave and Conventional Sintering of Premixed and Pre-alloyed Cu-12Sn Bronze**, Sci. Sinter. 35 (2003) 49–65.

[45] M. Wai Leong Eugene, Wong Gupta, **Simultaneously Improving Strength and Ductility of Magnesium using Nano-size SiC Particulates and Microwaves**, Adv. Eng. Mater. 8 (2006) 735–740.

[46] K. Ishizaki, K. Nagata, T. Hayashi, **Production of Pig Iron from Magnetite Ore – Coal Composite**, ISIJ Int. 46 (2006) 1403–1409.

[47] M.S. Srinath, A.K. Sharma, P. Kumar, **A new approach to joining of bulk copper using microwave energy**, Mater. Des. 32 (2011) 2685–2694.

[48] D. Gupta, A.K. Sharma, **A method of cladding-coating of metallic and non-metallic powders on metallic substrate by microwave irradiation**. Indian Patent application 527/Del, 2010.

[49] D. Gupta, A.K. Sharma, **Copper Coating on Austenitic Stainless Steel Using Microwave Hybrid Heating**, J. Process Mech. Eng. Downloaded. 226 (2011) 132–141.

[50] S. Kaushal, D. Singh, D. Gupta, H. Bhowmick, **On Development and Characterization of Microwave Processed Ni + 30 % SiC Based Composite Clads**, Mater. Today Proc. 5 (2018) 27718–27725.

[51] S. Singh, R. Singh, D. Gupta, V. Jain, **Preliminary Metallurgical and Mechanical Investigations of Microwave Processed Hastelloy Joints**, J. Manufacturing Sci. Eng. 139 (2018) 1–5.

[52] S. Singh, D. Gupta, V. Jain, **Novel Microwave Composite Casting Process: Theory, Feasibility and Characterization**, Mater. Des. 111 (2016) 51–59.

[53] R.R. Mishra, A.K. Sharma, **On Mechanism of In-Situ Microwave Casting of Aluminium Alloy 7039 and Cast Microstructure**, Mater. Des. 112 (2016) 97–106.

[54] S. Kaushal, D. Gupta, H. Bhowmick**, An approach for functionally graded cladding of composite material on austenitic stainless steel substrate through microwave heating**, J. Compos. Mater. 52 (2017) 301–312.

[55] M.K. Singh, S. Zafar, **Development and Characterization of Compression Moulding**, J. Cell. Plast. 0 (2019) 1–19.

[56] A. Borrel, M.D. Salvador, **Advanced Ceramic Material Sintered by Microwave Technology**, in: Sinter. Technol. Method Appl., 2018: pp. 1–22.

[57] D.E. Clark, D.C. Folz, J.K. West, **Processing Materials with Microwave Energy**, Mater. Sci. Eng. A287 (2000) 153–158.

[58] D. Demirskyi, D. Agrawal, A. Ragulya, **Densification Kinetics of Powdered Copper Under Single-Mode and Multimode Microwave Sintering**, Mater. Lett. 64 (2010) 1433–1436.

[59] E. Binner, E. Lester, S. Kingman, C. Dodds, J. Robinson, P. Wardle, J.P. Mathews, **A Review of Microwave Coal Processing**, J. Microw. Power Electromagn. Energy. 48 (2014) 35–60.

[60] A.K. Sharma, R. Krishnamurthy, **Microwave Processing of Sprayed Alumina Composite for Enhanced Performance**, J. Eur. Ceram. Soc. 22 (2002) 2849–2860.

[61] M.S. Spotz, **Thermal Stability of Ceramics Materials in Microwave Heating**, J. Am. Ceram. Soc. 78 (1995) 1041–1048.

[62] J. Lasri, P.D. Ramesh, L. Scha, **Energy Conversion During Microwave Sintering of a Multiphase Ceramic Surrounded by a Susceptor**, J. Am. Ceram. Soc. 83 (2000) 1465–1468.

[63] R.R. Mishra, A.K. Sharma, **Microwave – Material Interaction Phenomena: Heating Mechanisms, Challenges and Opportunities in Material Processing**, Compos. PART A. 81 (2016) 78–97.

[64] R.R. Mishra, A.K. Sharma, **A Review of Research Trends in Microwave Processing of Metal-Based Materials and Opportunities in Microwave Metal Casting**, Crit. Rev. Solid State Mater. Sci. 41 (2016) 217–255.

[65] A. Mondal, A. Upadhyaya, D. Agrawal, **Effect of Heating Mode and Copper Content on the Densification of W-Cu Alloys**, Indian J. Of Materials Sci. 2013 (2013) 1–7.

[66] S.S. Panda, V. Singh, A. Upadhyaya, D. Agrawal, **Sintering Response of Austenitic (316L) and Ferritic (434L) Stainless Steel Consolidated in Conventional and Microwave Furnaces**, Scr. Mater. 54 (2006) 2179–2183.

[67] J. Lin, Z. Wang, J. Cheng, M. Kang, X. Fu, S. Hong, **Evaluation of cavitation erosion resistance of arc-sprayed Fe-based amorphous/ nanocrystalline coatings in NaCl solution**, Results Phys. 12 (2019) 597–602.

[68] J. Lin, Z. Wang, P. Lin, J. Cheng, X. Zhang, S. Hong, **Microstructure and Cavitation Erosion Behavior of FeNiCrBSiNbW Coating Prepared by Twin Wires Arc Spraying Process**, Surf. Coat. Technol. 240 (2014) 432–436.

[69] A. Krella, **Cavitation Erosion of TiN and CrN Coatings Deposited on Different Substrates**, Wear. 297 (2013) 992–997.

[70] A. Krella, **An Experimental Parameter of Cavitation Erosion Resistance for TiN Coatings**, Wear. 270 (2011) 252–257.

[71] L.M. Yang, A.K. Tieu, D.P. Dunne, S.W. Huang, H.J. Li, D. Wexler, Z.Y. Jiang, **Cavitation Erosion Resistance of NiTi Thin Films Produced by Filtered Arc Deposition**, Wear. 267 (2009) 233–243.

[72] M. Hajian, A. Abdollah-zadeh, S.S. Rezaei-nejad, H. Assadi, S.M.M. Hadavi, **Improvement in Cavitation Erosion Resistance of AISI 316L Stainless Steel by Friction Stir Processing**, Appl. Surf. Sci. 308 (2014) 184–192.

[73] H.S. Grewal, A. Agrawal, H. Singh, H.S. Arora, **Cavitation Erosion Studies on Friction Stir Processed Hydroturbine Steel**, Trans. Indian Inst. Met. 65 (2012) 731–734.

[74] X. Ding, D. Ke, C. Yuan, Z. Ding, X. Cheng, **Microstructure and Cavitation Erosion Resistance of HVOF Deposited WC-Co Coatings with Different Sized WC**, Coatings. 8 (2018) 307.

[75] H.J. Amarendra, M.S. Pratap, S. Karthik, M.S. Punitha Kumara, H.C. Rajath, H. Ranjith, S. V Shubhatunga, **Combined Slurry and Cavitation Erosion Resistance of Surface Modified SS410 Stainless Steel**, Mater. Sci. Eng. 330. 330 (2018) 1–7.

[76] X. Ding, X.C.C. Yuan, J. Shi, **Structure of Micro-nano WC-10Co4Cr Coating and Cavitation Erosion Resistance in NaCl Solution**, Chinese J. Mech. Eng. 30 (2017) 1239–1247.

[77] L. Qiao, Y. Wu, S. Hong, J. Zhang, W. Shi, Y. Zheng, **Relationships between Spray Parameters, Microstructures** a**nd Ultrasonic Cavitation Erosion Behavior of HVOF sprayed Fe-based Amorphous/Nanocrystalline Coatings**, Ultrason. - Sonochemistry. 39 (2017) 39–46.

[78] S. Lavigne, F. Pougoum, S. Savoie, L. Martinu, J.E. Klemberg-Sapieha, R. Schulz, **Cavitation Erosion Behavior of HVOF CaviTec Coatings**, Wear. 386–387 (2017) 90–98.

[79] R.K. Kumar, M. Kamaraj, S. Seetharamu, T. Pramod, P. Sampathkumaran**, Effect of Spray Particle Velocity on Cavitation Erosion Resistance Characteristics of HVOF and HVAF Processed 86WC-10Co4Cr Hydro Turbine Coatings**, J. Therm. Spray Technol. (2016).

[80] S. Hong, Y. Wu, J. Zhang, Y. Zheng, Y. Qin, J. Lin, **Ultrasonic Cavitation Erosion of High-Velocity Oxygen-Fuel (HVOF) Sprayed Near-Nanostructured WC-10Co-4Cr Coating in NaCl Solution**, Ultrason. Sonochem. 26 (2015) 87–92.

[81] D. Kekes, P. Psyllaki, M. Vardavoulias, G. Vekinis, **Wear Micro-Mechanisms of Composite WC-Co/Cr-NiCrFeBSiC Coatings. Part II: Cavitation Erosion**, Tribol. Ind. 36 (2014) 375–383.

[82] J.F. Santa, L.A. Espitia, J.A. Blanco, S.A. Romo, A. Toro, **Slurry and Cavitation Erosion Resistance of Thermal Spray Coatings**, Wear. 267 (2009) 160–167.

[83] S. Jiang, H. Ding, J. Xu, **Cavitation Erosion Resistance of Sputter-Deposited Cr_3Si Film on Stainless Steel**, J. Tribol. 139 (2016) 014501.

[84] S. Momeni, W. Tillmann, M. Pohl, **Composite Cavitation Resistant PVD Coatings Based on NiTi thin films**, JMADE. 110 (2016) 830–838.

[85] S.A. Romo, J.F. Santa, J.E. Giraldo, A. Toro, **Cavitation and High-Velocity Slurry Erosion Resistance of Welded Stellite 6 Alloy**, Tribol. Int. 47 (2012) 16–24.

[86] F.T. Cheng, K.H. Lo, H.C. Man, **NiTi Cladding on Stainless Steel by TIG Surfacing Process Part I. Cavitation Erosion Behavior**, Surf. Coatings Technol. 172 (2003) 308–315.

[87] B.K. Sreedhar, S.K. Albert, A.B. Pandit, **Improving Cavitation Erosion Resistance of Austenitic Stainless Steel in Liquid Sodium by Hardfacing – Comparison of Ni and Co-Based Deposits**, Wear. 342–343 (2015) 92–99.

[88] D.G. Li, D.R. Chen, P. Liang, **Enhancement of Cavitation Erosion Resistance of 316L Stainless Steel by Adding Molybdenum**, Ultrason. Sonochem. 35 (2017) 375–381.

[89] M. Bitzer, N. Rauhut, G. Mauer, M. Bram, R. Vaßen, H.P. Buchkremer, D. Stöver, M. Pohl, **Cavitation-Resistant NiTi Coatings Produced by Low-Pressure Plasma Spraying (LPPS)**, Wear. 328–329 (2015) 369–377.

[90] S. Zhang, S. Wang, C.L. Wu, C.H. Zhang, M. Guan, J.Z. Tan, **Cavitation Erosion and Erosion-Corrosion Resistance of Austenitic Stainless Steel by Plasma Transferred Arc Welding**, Eng. Fail. Anal. 76 (2017) 115–124.

[91] R. Singh, D. Kumar, S.K. Mishra, S.K. Tiwari, **Laser Cladding of Stellite 6 on Stainless Steel to Enhance Solid Particle Erosion and Cavitation Resistance**, Surf. Coatings Technol. 251 (2014) 87–97.

[92] C.P. Paul, B.K. Gandhi, P. Bhargava, D.K. Dwivedi, L.M. Kukreja, **Cobalt-Free Laser Cladding on AISI Type 316L Stainless Steel for Improved Cavitation and Slurry Erosion Wear Behavior**, ASM Int. 23 (2014) 4463–4471.

[93] M. Duraiselvam, R. Galun, V. Wesling, B.L. Mordike, R. Reiter, J. Oligmüller, **Cavitation Erosion Resistance of AISI 420 Martensitic Stainless Steel Laser-Clad with Nickel Aluminide Intermetallic Composites and Matrix Composites with TiC Reinforcement**, Surf. Coat. Technol. 201 (2006) 1289–1295.

[94] K.Y. Chiu, F.T. Cheng, H.C. Man, **Laser Cladding of Austenitic Stainless Steel using NiTi Strips for Resisting Cavitation Erosion**, Mater. Sci. Eng. A. 402 (2005) 126–134.

[95] F.T. Cheng, C.T. Kwok, H.C. Man, **Cavitation Erosion Resistance of Stainless Steel Laser-Clad with WC-Reinforced MMC**, Mater. Lett. 57 (2002) 969–974.

[96] C.L. Wu, S. Zhang, C.H. Zhang, H. Zhang, S.Y. Dong, **Phase Evolution and Cavitation Erosion-Corrosion Behavior of FeCoCrAlNiTix High Entropy Alloy Coatings on 304 Stainless Steel by Laser Surface Alloying**, J. Alloys Compd. 698 (2017) 761–770.

[97] B.G. Gire, M. Szkodo, J. Steller, **Cavitation Erosion of Some Laser-Produced Iron-Base Corrosion-Resistant Alloys**, Wear. 258 (2005) 614–622.

[98] K.H. Lo, F.T. Cheng, C.T. Kwok, H.C. Man, **Improvement of Cavitation Erosion Resistance of AISI 316 Stainless Steel by Laser Surface Alloying Using Fine WC Powder**, Surf. Coat. Technol. 165 (2003) 258–267.

[99] F.T. Cheng, C.T. Kwok, H.C. Man**, Laser Surfacing of S31603 Stainless Steel with Engineering Ceramics for Cavitation Erosion Resistance**, Surf. Coatings Technol. 139 (2001) 14–24.

[100] C.T. Kwok, H.C. Man, F.T. Cheng, **Cavitation Erosion and Pitting Corrosion Behaviour of Laser Surface-Melted Martensitic Stainless Steel UNS S42000**, Surf. Coatings Technol. 126 (2000) 238–255.

[101] K. Peng, C. Kang, G. Li, K. Matsuda, H. Soyama, **Effect of Heat Treatment on the Cavitation Erosion Resistance of Stainless Steel**, Mater. Corros. 69 (2018) 536–544.

[102] Y. Wang, J. Liu, N. Kang, G. Darut, T. Poirier, J. Stella, H. Liao, M.P. Planche, **Cavitation Erosion of Plasma-Sprayed CoMoCrCSi Coatings**, Tribol. Int. 102 (2016) 429–435.

[103] Z.B. Zheng, Y.G. Zheng, W.H. Sun, J.Q. Wang, **Effect of Heat Treatment on the Structure, Cavitation Erosion and Erosion-Corrosion Behavior of Fe-Based Amorphous Coatings**, Tribology Int. 90 (2015) 393–403.

[104] J. Lin, Z. Wang, P. Lin, J. Cheng, X. Zhang, S. Hong, **Effects of Post Annealing on the Microstructure, Mechanical Properties and Cavitation Erosion Behavior of Arc-Sprayed FeNiCrBSiNbW Coatings**, Mater. Des. 65 (2015) 1035–1040.

[105] B. Kishor, G.P. Chaudhari, S.K. Nath, **Cavitation Erosion of Thermo mechanically Processed 13/4 Martensitic Stainless Steel**, Wear. 319 (2014) 150–159.

[106] D. Gupta, A. K. Sharma, **Development and Microstructural Characterization of Microwave Cladding on Austenitic Stainless Steel**, Surf. Coat. Technol 205 (2011) 5147–5155.

[107] S. Kaushal, V. Sirohi, D. Gupta, **Processing and Characterization of Composite Cladding through Microwave Heating On Martensitic Steel**, J Mater. Des. Appl 232 (2015) 80–86.

[108] S. Zafar, A. Kumar, **Abrasive and Erosive Wear Behavior of Nanometric WC – 12Co Microwave Clads**, Wear 346 (347) (2016) 29–45.

[109] A. M. Hebbale, M. S. Srinath, **Taguchi Analysis On Erosive Wear Behavior of Cobalt Based Microwave Cladding On Stainless Steel AISI-420**, Measurement 99 (2017) 98–107.

[110] S. Kaushal, D. Gupta, H. Bhowmick, **On Surface Modification of Austenitic Stainless Steel Using Microwave Processed Ni/Cr_3C_2 Composite Cladding**, Surf. Eng. 34 (2018) 809–817.

[111] B. Singh, S. Kaushal, D. Gupta, H. Bhowmick, **On Development and Dry Sliding Wear Behavior of Microwave Processed Ni / Al_2O_3 Composite Clad**, J. Tribol 140 (2018) 1–8.

[112] B. Singh, S. Zafar, **Effect of Microwave Exposure Time on Microstructure and Slurry Erosion Behavior of Ni + 20% Cr_7C_3 Composite Clads**, Wear. 426–427 (2019) 491–500.

[113] A. Babu, H.S. Arora, H. Singh, H.S. Grewal, **Microwave Synthesized Composite Claddings with Enhanced Cavitation Erosion Resistance**, Wear. 422–423 (2019) 242–251.

[114] Lingappa S.M, Srinath M.S, Amarendra H.J, **An Experimental Investigation to Find the Critical (Coupling) Temperature in Microwave Hybrid Heating of Bulk Metallic Materials**, Mater. Res. Express. 4 (2017) 1–12.

[115] A.K. Krella, D.E. Zakrzewska, **Cavitation Erosion – Phenomenon and Test Rigs**, Adv. Mater. Sci. 18 (2018) 15–26.

[116] ASTM G32-16, **Standard Test Method for Cavitation Erosion Using Vibratory Apparatus**, ASTM International, West Conshohocken, PA, 2016.

[117] ASTM G134-17, **Standard Test Method for Erosion of Solid Materials by Cavitating Liquid Jet**, ASTM International, West Conshohocken, PA, 2017.

[118] I. Hansoon, K. Aage, **The Dynamics of Cavity Clusters in Ultrasonic (Vibratory) Cavitation Erosion**, J. Appl. Phys. 51 (1980) 4651–4658.

[119] A. Arbor, G. Hammitt, **Effect of Separation Distance on Cavitation Erosion of Vibratory and Stationary Specimens: In A Vibratory Facility**, Wear. 102 (1985) 211–225.

[120] I. Ibanez, M. Hodnett, B. Zeqiri, M.N. Frota, **Correlating Inertial Acoustic Cavitation Emissions with Material Erosion Resistance**, Phys. Procedia. 87 (2016) 16–23.

[121] I. Lazar, I. Bordeasu, M.O. Popoviciu, I. Mitelea, T. Bena, L.M. Micu, **Considerations Regarding the Erosion Mechanism of Vibratory Cavitation**, Mater. Sci. Eng. 393 (2018) 1–8.

[122] M.S. Vohra, N.A. Prasanth, W.L. Tan, S.H. Yeo, **Analysis of Impact Load Induced by Ultrasonic Cavitation Bubble Collapse Using Thin Film Pressure Sensors**, Int. J. Mech. Ind. Eng. 11 (2017) 1815–1820.

[123] ASTM A276 / A276M-17, **Standard Specification for Stainless Steel Bars and Shapes, ASTM International**, West Conshohocken, PA, 2017.

[124] Ram B. Bhagat, **Cavitation Erosion of Composites - A Materials Perspective**, J. Mater. Sci. 6 (1987) 1473–1475.

[125] E. Sadeghimeresht, N. Markocsan, P. Nylén, **Microstructural Characteristics and Corrosion Behavior of HVAF- and HVOF-sprayed Fe-based coatings**, Surf. Coat. Technol. 318 (2017) 365–373.

[126] M. Muzyk, Z. Pakieła, K.J. Kurzydłowski, **Generalized Stacking Fault Energies of Aluminum Alloys–Density Functional Theory Calculations**, Metals (Basel). 8 (2018) 823.

[127] Hugh O. Pierson, **Handbook of Refractory Carbides and Nitrides, William Andrew Publishing**, 1996, Pages 100-117.

[128] H.X. Hu, Y.G. Zheng, C.P. Qin, **Comparison of Inconel 625 and Inconel 600 in Resistance to Cavitation Erosion and Jet Impingement Erosion**, Nucl. Eng. Des. 240 (2010) 2721–2730.

[129] D.G. Li, J.D. Wang, D.R. Chen, P. Liang, **Ultrasonic Cavitation Erosion of Ti in 0.35% NaCl Solution with Bubbling Oxygen and Nitrogen**, Ultrason. Sonochem. 26 (2015) 99–110.

[130] ASTM E112-13, **Standard Test Methods for Determining Average Grain Size**, ASTM International, West Conshohocken, PA, 2013.

[131] C.Y. Ho, T.K. Chu, American Iron and Steel Institute: **Electrical Resistivity and Thermal Conductivity of Nine Selected AISI Stainless Steels**: in: and others (Ed.), Thermo- Physical and Electronic Properties: Vol. 45 of CINDAS report: Purdue University, 1977.

[132] R.W. Powell, R.P. Tye, M.J. Hickman, **The Thermal Conductivity of Nickel**, Int. J. Heat Mass Transf. 8 (1965) 679–688.

[133] P.D. Desai, T.K. Chu, H.M. James, C.Y. Ho**, Electrical Resistivity of Ta, Mo, Hf, W, and Zn**., J. Phys. Ref. Data. 13 (1984) 1069-1094.

[134] A.K. Sharma, D. Gupta, **On Microstructure and Flexural Strength of Metal-Ceramic Composite Cladding Developed Through Microwave Heating**, Appl. Surf. Sci. 258 (2012) 5583–5592.

[135] W.D. Callisister, G.R. David, **Materials Science and Engineering: An Introduction**, 10th Edition: John Wiley & Sons, Inc, 2010.

[136] AZoM.com. (2019). **Properties: Molybdenum (Mo) - Properties, Applications**. [online] Available at: https://www.azom.com/properties.aspx?ArticleID=616 [Accessed 15 Jul. 2019].

[137] AZoM.com. (2019). **Properties: Stainless Steel - Grade 316 (UNS S31600).** [online] Available at: https://www.azom.com/properties.aspx?ArticleID=863 [Accessed 15 Jul. 2019].

[138] K. Chu, C. Jia, X. Liang, H. Chen, **Effect of Powder Mixing Process On the Microstructure and Thermal Conductivity of Al/Diamond Composites Fabricated by Spark Plasma Sintering**, Rare Met. 29 (2010) 86–91.

[139] P.E. Carrion, A. Soltani-Tehrani, N. Phan, N. Shamsaei, **Powder Recycling Effects on the Tensile and Fatigue Behavior of Additively Manufactured Ti-6Al-4V Parts**, Jom. 71 (2019) 963–973.

[140] rfcafe.com (2019). **Conductor Bulk Resistivity & Skin Depths at High Frequencies Microwave RF.** Available at: http://www.rfcafe.com/references/ electrical /cond-high-freq.htm [Accessed 16 Jul. 2019].

[141] ASTM C1161-13, **Standard Test Method for Flexural Strength of Advanced Ceramics at Ambient Temperature**, ASTM International, West Conshohocken, PA, 2013.

[142] J. Lin, Z. Wang, J. Cheng, M. Kang, X. Fu, S. Hong, **Effect of Initial Surface Roughness on Cavitation Erosion Resistance of Arc-Sprayed Fe-based Amorphous/Nanocrystalline Coatings,** Coatings. 7 (2017) 2001-2009.

[143] H.S. Kirols, D. Kevorkov, A. Uihlein, M. Medraj, **The Effect of Initial Surface Roughness on Water Droplet Erosion Behaviour**, Wear. 342–343 (2015) 198–209.

[144] S. Zafar, A.K. Sharma, **Development and Microstructural Characterization of Inconel Cladding on Stainless Steel Through Microwave Irradiation**, J. Mech. Eng. 3 (2013) 9–16.

[145] Q.Y. Hou, Y.Z. He, Q.A. Zhang, J.S. Gao, **Influence of Molybdenum on the Microstructure and Wear Resistance of Nickel-Based Alloy Coating Obtained by Plasma Transferred Arc Process**, Mater. Des. 28 (2007) 1982–1987.

[146] L. da S. Ferreira, K. Graf, A. Scheid, **Microstructure and Properties of Nickel-based C276 Alloy Coatings by PTA on AISI 316L and API 5L X70 Steel Substrates**, Mater. Res. 18 (2015) 212–221.

[147] S. Li, D. Feng, H. Luo, **Microstructure and Abrasive Wear Performance of Chromium Carbide Reinforced Ni_3Al Matrix Composite Coating**, Surf. Coatings Technol. 201 (2007) 4542–4546.

[148] M. Kosugi, N.C. Tso, J.M. Sanchez**, First-Principles Calculation of the Ni-Cr Phase Diagram**, Solid State Ionics 32/33. 33 (1989) 714–720.

[149] S.N. Aqida, M.I. Ghazali, J. Hashim, **Effect of Porosity on Mechanical Properties of Metal Matrix Composite: An Overview**, J. Teknol. 40 (2013) 17–32.

[150] T. Pramod, R.K. Kumar, S. Seetharamu, M. Kamaraj, **Effect of Porosity on Cavitation Erosion Resistance of HVOF Processed Tungsten Carbide Coatings**, Int. J. Adv. Mech. Eng. 4 (2014) 307–314.

[151] O. Knotek, R. Elsing, H. -R. Heintz, **On Plasma Sprayed WSi_2 and Cr_3C_2–Ni Coatings**, J. Vac. Sci. Technol. A Vacuum, Surfaces, Film. 3 (2002) 2490–2493.

[152] C. Pan, H. Wang, H. Wang, Q. Chang, H. Wang, **Microstructure and Thermal Physical Parameters of Ni60-Cr_3C_2 Composite Coating by Laser Cladding**, J. Wuhan Univ. Technol. Mater. Sci. Ed. 25 (2010) 991–995.

[153] S. Anthonysamy, K. Ananthasivan, I. Kaliappan, V. Chandramouli, P.R. Vasudeva Rao, C.K. Mathews, K.T. Jacob, **Gibbs Energies of Formation of Chromium Carbides**, Metall. Mater. Trans. A Phys. Metall. Mater. Sci. 27 (1996) 1919–1924.

[154] D. Bhattacharyya, J. Davis, M. Drew, R.P. Harrison, L. Edwards, **Characterization of Complex Carbide-Silicide Precipitates in a Ni-Cr-Mo-Fe-Si Alloy Modified by Welding**, Mater. Charact. 105 (2015) 118–128.

[155] E.G. Colgan, B.Y. Tsaur, J.W. Mayer, **Phase Formation in Cr-Si Thin-Film Interactions**, Appl. Phys. Lett. 37 (1980) 938–940.

[156] H. Okamoto, **Mo-Si (Molybdenum-Silicon),** J. Phase Equilibria Diffus. 32 (2011) 176.

[157] H. Masumoto, M. Hinai, S. Sawaya, **Damping Capacity and Pitting Corrosion Resistance of Fe-Mo-Cr Alloys**, Trans. Japan Inst. Met. 27 (1986) 401–407.

[158] A.P. Nagalingam, S.H. Yeo, **Effects of Ambient Pressure and Fluid Temperature in Ultrasonic Cavitation Machining**, Int. J. Adv. Manuf. Technol. 98 (2018) 2883–2894.

[159] P.R. Birkin, D.G. Offin, C.J.B. Vian, T.G. Leighton, **Multiple Observations of Cavitation Cluster Dynamics Close to an Ultrasonic Horn Tip**, J. Acoust. Soc. Am. 130 (2011) 3379–3388.

[160] J. Mago, S. Bansal, D. Gupta, V. Jain, **Investigation of Erosion and Pressure for Direct and Indirect Acoustic Cavitation Testing**, J. Emerg. Technol. Innov. Res. 6 (2019) 468–476.

[161] S. Merouani, O. Hamdaoui, Y. Rezgui, M. Guemini, **Effects of Ultrasound Frequency and Acoustic Amplitude on the Size of Sonochemically Active Bubbles-Theoretical Study**, Ultrason. Sonochem. 20 (2013) 815–819.

[162] K. Yasui, **Acoustic Cavitation and Bubble Dynamics**, Springer International Publishing, Cham, 2018.

Visible Output

List of Publications in International Conference:

- **Jonty Mago**, Sandeep Bansal, Dheeraj Gupta, Vivek Jain, "**Investigation of Erosion and Pressure for Direct and In-Direct Acoustic Cavitation Testing**". Presented at International Conference on Trends in Science, Engineering & Management (**ICTSEM-2019**) held in July 2019 at Gulzar Group of Institutes, Ludhiana, India. (Published in JETIR Vol.6, Issue 5, pp468-476, May-2019)

- Sandeep Bansal, **Jonty Mago**, Dheeraj Gupta, Vivek Jain, "**Microstructural Characteristics of Microwave Processed Ni-10%Cr_3C_2 Composite Cladding**". Presented at International Conference on Trends in Science, Engineering & Management (**ICTSEM-2019**) held in July 2019 at Gulzar Group of Institutes, Ludhiana, India. (Published in JETIR Vol.6, Issue 5, pp463-467, May-2019)

- **Jonty Mago,** Sandeep Bansal, Dheeraj Gupta, Vivek Jain, "**On Metallurgical and Mechanical Characterization of Ni/Cr_3C_2 Cladding Through Microwave Heating**" Presented at International Conference on Smart and Sustainable developments in Materials, Manufacturing, and Energy (**SME-2019**), NMAM Institute of Technology, Udupi, Karnataka, India.

Thesis_Jonty Mago_801785006

ORIGINALITY REPORT

10%	3%	8%	5%
SIMILARITY INDEX	INTERNET SOURCES	PUBLICATIONS	STUDENT PAPERS

PRIMARY SOURCES

1	Apurbba Kumar Sharma, Dheeraj Gupta. "On microstructure and flexural strength of metal–ceramic composite cladding developed through microwave heating", Applied Surface Science, 2012 Publication	1%
2	Dorji, Ugyen, and Reza Ghomashchi. "Hydro turbine failure mechanisms: An overview", Engineering Failure Analysis, 2014. Publication	<1%
3	Submitted to Caledonian College of Engineering Student Paper	<1%
4	Submitted to University of East London Student Paper	<1%
5	Z.B. Zheng, Y.G. Zheng, W.H. Sun, J.Q. Wang. "Effect of heat treatment on the structure, cavitation erosion and erosion–corrosion behavior of Fe-based amorphous coatings", Tribology International, 2015 Publication	<1%